

Laboratory Surface and Solid State Astrochemistry of
Biomolecular Precursors on Grain Mimics

Ali Ghith Moussa Abdulgalil

Submitted for the degree of Doctor of Philosophy

Heriot-Watt University

School of Engineering and Physical Sciences

October 2013

The copyright in this thesis is owned by the author. Any quotation from the thesis or use of any of the information contained in it must acknowledge this thesis as the source of the quotation or information.

ABSTRACT

The existence of water (H_2O) and acetonitrile (CH_3CN) in various extraterrestrial environments attracts considerable attention as both molecules are crucial to understanding the genesis of life. This thesis involves investigations of the physical and chemical interactions of CH_3CN and H_2O ices condensed on an amorphous silica surface using ultrahigh vacuum-based surface science methods (reflection-absorption infrared spectroscopy, temperature programmed desorption, proton- and electron-irradiation experiments) in an effort to understand how such molecules will behave when they are processed by radiation and heat in space environments.

The thermal behaviour of CH_3CN on H_2O and on the silica surface is governed by a balance of intermolecular forces and shows evidence for wetting of the silica surface (formation of a distinct first adsorption layer before multilayer growth) and of dewetting or island formation on the H_2O surface (multilayer growth for all CH_3CN exposures). This illustrates the importance of the substrate in determining the solid state growth morphology.

Physical and chemical processes induced by 250 to 500 eV electrons have been investigated in the CH_3CN and H_2O systems. Such interactions promote only desorption from both CH_3CN and H_2O ice surfaces. 200 keV protons irradiation experiments of CH_3CN ices, conducted by collaborators in Italy, in contrast showed evidence for chemical reactions in the solid CH_3CN . Quantitative measurements of desorption and reaction cross-sections are used to reconcile this stark contrast.

The impact of such processes in relation to H_2O on astrophysics is investigated through simple numerical simulations using results derived from this work.

Acknowledgments

This thesis would never have been written without the enormous support and assistance of many people who so generously shared their knowledge with me.

First of all, I would like to express my sincere gratitude to my primary supervisor, Prof. Martin McCoustra. His continuous help, guidance and support made this work possible. I am deeply moved by Prof. McCoustra's patience with correcting my thesis word by word. I am also very grateful to my second supervisor Prof. Kenneth McKendrick for his help, advice and encouragement on many aspects.

I am grateful to Dr. Mark Collings and Dr. Jérôme Lasne for all of their valuable comments and their efforts making my thesis understandable. A special thank goes to John Thrower (previous PhD student) who trained me to utilise the Beam Rig and analysis my data. I am also grateful for the support from my colleagues in the surface astrochemistry group; Victoria Frankland (previous PhD student), Demian Marchione, and Alexander Rosu-Finsen. Furthermore, I would like to thank all of the M.Sc, MChem, and B.Sc students that I have worked with on this project; Lars Finger, Elizabeth Hall, Kylie Beasley, Alexandre Vinck, Alain Aprahamian, and Steven Campbell. For their advices and help in solving any technical issues, I would like to express my appreciation to Alan Barton, Ian Drummond, and Paul Allan, along with all the technicians in the electronics workshop. Thanks are also extended to the staff and colleagues at the Institute of Chemical Sciences. I would like to acknowledge; Dr. François Dulieu from l'Observatoire de Paris et de l'Université for his contribution in TPD analysis of the CH₃CN, Dr. Maria Elisabetta Palumbo and Dr. Farahjabeen Islam from Osservatorio Astrofisico di Catania for providing me with the proton irradiation data in Chapter 5 of my thesis. For their financial support, I would like to acknowledge the Libyan Cultural Affairs – London.

Last but not the least; I would like to thank my family, parents, wife, brothers, and sisters for supporting me spiritually during my PhD course.

DECLARATION STATEMENT

(Research Thesis Submission Form should be placed here)

TABLE OF CONTENTS

CHAPTER 1 – Introduction	1
1. Introduction	2
1.1 Interstellar Medium (ISM)	2
<i>1.1.1 Chemical Composition of Interstellar Matter</i>	6
<i>1.1.2 Formation of Interstellar Ice</i>	9
<i>1.1.3 Cosmic Rays and Radiation Fields in The ISM</i>	10
<i>1.1.3.1 Cosmic Rays</i>	10
<i>1.1.3.2 Ultraviolet Radiation</i>	12
<i>1.1.3.3 Secondary Electrons</i>	13
1.2 Interstellar Molecules	13
1.3 Chemistry of the ISM	16
<i>1.3.1 Gas-phase Chemistry</i>	16
<i>1.3.2 Grain Surface Chemistry</i>	19
1.4 Review of Experimental and Theoretical Studies of ISM Chemistry	20
<i>1.4.1 Gas-phase Model</i>	20
<i>1.4.2 Dust Grain Model</i>	21
1.5 Grain Mimics	23
1.6 Thesis Outline	24
1.7 References	26
CHAPTER – 2 Experimental	31
2.1 Introduction	32
2.2 Experimental	36
2.2.1 UHV Chamber (Beam Rig)	36

2.2.1.1	<i>UHV Chamber and Pumping System</i>	36
2.2.1.2	<i>Pressure Measurements</i>	39
2.2.1.3	<i>The Molecular Beam Source</i>	40
2.2.1.4	<i>Sample Manipulation and Mounting</i>	42
2.2.1.5	<i>Temperature Calibration</i>	44
2.2.2	Experimental Techniques and Instrumentation	46
2.2.2.1	<i>Temperature-programmed Desorption (TPD)</i>	48
2.2.2.2	<i>Reflection-absorption Infrared Spectroscopy (RAIRS)</i>	53
2.2.2.3	<i>Electron-stimulated Desorption (ESD)</i>	59
2.2.3	Sample Preparation	62
2.2.4	Computational Methods	64
2.2.4.1	<i>The Chemical Kinetics Simulator (CKS)</i>	64
2.2.4.2	<i>HyperChem®</i>	65
2.2.4.3	<i>SRIM/TRIM</i>	66
2.3	References	67
CHAPTER – 3 Desorption of ASW Adsorbed on Amorphous SiO₂		69
3.1	Introduction	70
3.2	Water (H₂O)	70
3.2.1	<i>Phases of H₂O Ice</i>	71
3.2.2	<i>H₂O Isotopologues</i>	72
3.2.3	<i>Formation of Interstellar Water</i>	73
3.3	Thermal Desorption of ASW Adsorbed on Amorphous SiO₂	76
3.3.1	<i>Experimental Procedure</i>	76
3.3.2	<i>Results and Discussion</i>	78
3.4	Non-thermal Desorption of ASW Adsorbed on Amorphous SiO₂	86

3.4.1	<i>Experimental Procedure</i>	86
3.4.2	<i>Results and Discussion</i>	87
3.5	Modelling of Water Abundance in the Interstellar Clouds	91
3.5.2	<i>Results and Discussion</i>	99
3.5.3	<i>Comparison of the model and the observations</i>	109
3.6	Conclusion and Astrophysical Implications	111
3.7	References	113
	CHAPTER – 4 Surface Science of Acetonitrile on Model Grain Surfaces	118
4.1	Introduction	119
4.2	Acetonitrile (CH₃CN)	119
4.3	Experimental Procedure	123
4.4	Results and Discussion	124
4.4.1	<i>TPD of CH₃CN</i>	124
4.4.1.1	<i>CH₃CN Adsorbed on Amorphous SiO₂</i>	124
4.4.1.1.1	<i>Sub-monolayer and Monolayer Analysis</i>	125
4.4.1.1.2	<i>Multilayer Analysis</i>	128
4.4.1.2	<i>TPD of CH₃CN Adsorbed on ASW</i>	133
4.4.2	<i>RAIRS of CH₃CN</i>	133
4.4.2.1	<i>CH₃CN Adsorbed on Amorphous SiO₂</i>	133
4.4.2.2	<i>CH₃CN Adsorbed on ASW</i>	139
4.4.2.3	<i>Annealed CH₃CN / ASW</i>	147
4.5	Conclusions	150
4.6	References	153
	CHAPTER – 5 Low Energy Electron Promoted Desorption of CH₃CN	157
5.1	Introduction	158

5.2	Chemistry of Acetonitrile	158
5.3	Experimental Procedure	160
5.3.1	<i>Electron Irradiation Experiments</i>	160
5.3.2	<i>Proton Irradiation Experiments</i>	161
5.4	Results and Discussion	163
5.4.1	<i>Low Energy Electron Processing of CH₃CN</i>	163
5.4.1.1	<i>Irradiated CH₃CN Adsorbed on ASW</i>	163
5.4.1.2	<i>Irradiated CH₃CN Adsorbed on Amorphous SiO₂</i>	172
5.4.1.3	<i>Interactions of Solid CH₃CN with Low Energy Electrons</i>	178
5.4.2	<i>Proton Processing of CH₃CN</i>	183
5.4.3	<i>Impact of Electron and Proton Irradiation on Solid CH₃CN</i>	190
5.5	Conclusions and Astrophysical Implications	193
5.6	References	196
	CHAPTER – 6 Conclusions	201
6.1	Introduction	202
6.2	Summary	202
6.2.1	<i>Chapter 3</i>	202
6.2.2	<i>Chapter 4</i>	203
6.2.3	<i>Chapter 5</i>	204
6.3	Future Outlook	205
6.4	References	207

GLOSSARY

ASW – Amorphous Solid Water
AFM – Atomic Force Microscopic
c-ASW – Compact Amorphous Solid Water
CKS – Chemical Kinetics Simulator
CR – Cosmic Rays
CSW – Crystalline Solid Water
DEA – Dissociative Electron Attachment
DFT – Density Functional Theory
DC – Direct Current
EPD – Electron-promoted Desorption
ESD – Electron-stimulated Desorption
FTIR – Fourier Transform Infrared
FUV – Far Ultraviolet
HDA – High Density Amorphous
HK – Habenschaden-Küppers
HOPG – Highly Oriented Pyrolytic Graphite
HV – High Vacuum
I_c – Crystalline ice
IP – Ionization Potential
IR – Infrared
ISM – Interstellar Medium
ISO – Infrared Space Observatory
ISRF – Interstellar Radiation Field
LDA – Low Density Amorphous
LEA – Leading Edge Analysis
LO – Longitudinal Optical
MCT – Mercury Cadmium Telluride
MO – Molecular Orbital
MGR – Menzel-Gomer-Redhead
NMR - Nuclear Magnetic Resonance
OFHC – Oxygen Free High Conductivity
PAHs – Polycyclic Aromatic Hydrocarbons

PANHs – Polycyclic Aromatic Nitrogen-containing Hydrocarbons
p-ASW – Porous Amorphous Solid Water
PSD – Photon-stimulated desorption
QCM – Quartz Crystal Microbalance
QMS – Quadrupole Mass Spectrometer
RAIRS – Reflection Absorption Infrared Spectroscopy
RF – Radio Frequency
RGA – Residual Gas Analysis
RHF – Restricted Hartree-Fock
SEM – Scanning Electron Microscope
SEM – Secondary Electron Multiplier
SRIM/TRIM – Stopping and Range of Ions in Matter/Transport of Ions in Matter
STM – Scanning Tunnelling Microscopy
SWAS – Submillimeter Wave Astronomy Satellite
TIRS – Transmittance Infrared Spectroscopy
TO – Transverse Optical
TPD – Temperature-programmed Desorption
UHV – Ultrahigh Vacuum
UMIST – University of Manchester Institute of Science and Technology
UV – Ultraviolet
VUV – Vacuum Ultraviolet

CHAPTER 1 – Introduction

Contents

1. Introduction	2
1.1 Interstellar Medium (ISM)	2
<i>1.1.1 Chemical Composition of Interstellar Matter</i>	6
<i>1.1.2 Formation of Interstellar Ice</i>	9
<i>1.1.3 Cosmic Rays and Radiation Fields in The ISM</i>	10
<i>1.1.3.1 Cosmic Rays</i>	10
<i>1.1.3.2 Ultraviolet Radiation</i>	12
<i>1.1.3.3 Secondary Electrons</i>	13
1.2 Interstellar Molecules	13
1.3 Chemistry of the ISM	16
<i>1.3.1 Gas-phase Chemistry</i>	16
<i>1.3.2 Grain Surface Chemistry</i>	19
1.4 Review of Experimental and Theoretical Studies of ISM Chemistry	20
<i>1.4.1 Gas-phase Model</i>	20
<i>1.4.2 Dust Grain Model</i>	21
1.5 Grain Mimics	23
1.6 Thesis Outline	24
1.7 References	26

1. Introduction

1.1 Interstellar Medium (ISM)

The regions between stars are not completely empty as most people think; there is matter in these regions. The first evidence for this interstellar matter emerged in 1876 when William Herschel noted that there are small dark regions in the sky where the stars were completely absent. These were difficult to explain and drove him to call them “black holes” [1]. In 1904, the German astronomer Johannes Hartmann deduced the presence of this matter from the stationary Ca II H and K lines at 396.8 and 393.3 nm using the Tautenburg 2 m telescope in Thuringia, Germany (see **Figure 1.1**) [2].

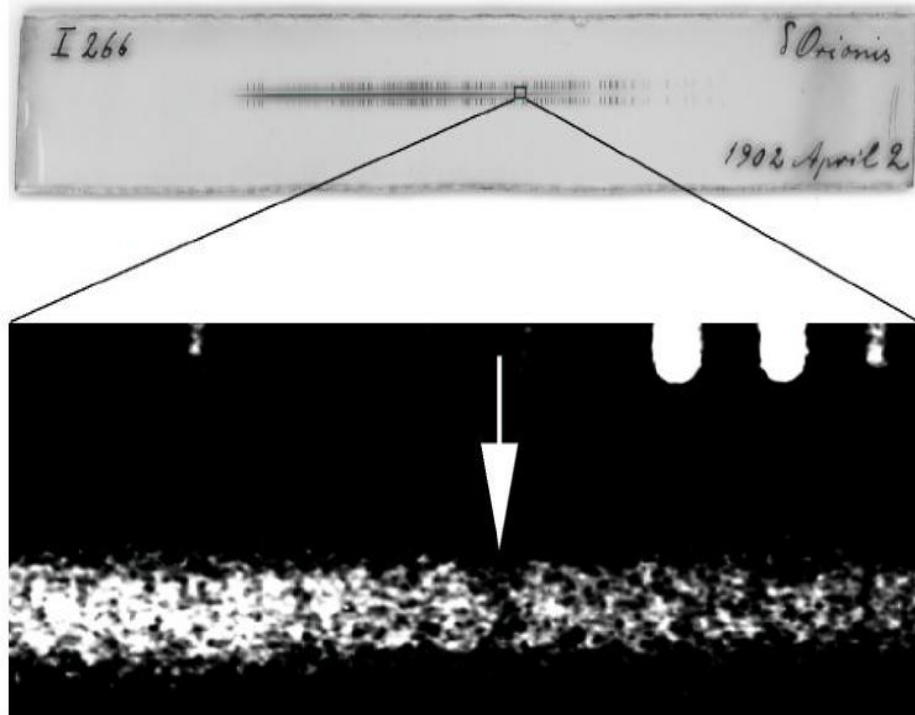


Figure 1.1: The first observation of interstellar matter described in the stationary Ca II H and K lines in a radial velocity spectrogram of δ Orion is taken by Hartmann in the winter months February 1901 and March 1902 [2].

The existence of the interstellar clouds had been confirmed in 1930, when Trumpler reported that material fills these clouds [3]. His observations were based on investigations of open cluster properties. He concluded that the light from isolated

clusters is gradually dimmed, as it propagates through interstellar space, by the obscuring effect of the interstellar material. Significantly, the exact agent causing this general obscuration was due to the presence of tiny particles of dust [3]. The interstellar medium is now recognised to exist in several forms; intercloud regions, diffuse clouds, the H II region, dense clouds, and translucent clouds. Intercloud regions have a low density of hydrogen (typically $n_{\text{H}} < 1 \text{ cm}^{-3}$). The diffuse clouds ($T = 50 - 100 \text{ K}$) have parallel-plane layers (sheet-like) structures [4]. They are dominated by atomic hydrogen with a density of about $10\text{-}10^2 \text{ atoms/cm}^3$ and are penetrated by visible radiation. In diffuse clouds the most common forms of nitrogen are N^0 and N^+ . The H II regions ($n_{\text{H}} = 10^2 - 10^3 \text{ cm}^{-3}$) are dominated by the H^+ ion. **Figure 1.2** shows photographs of the three types of the interstellar clouds [5-7].

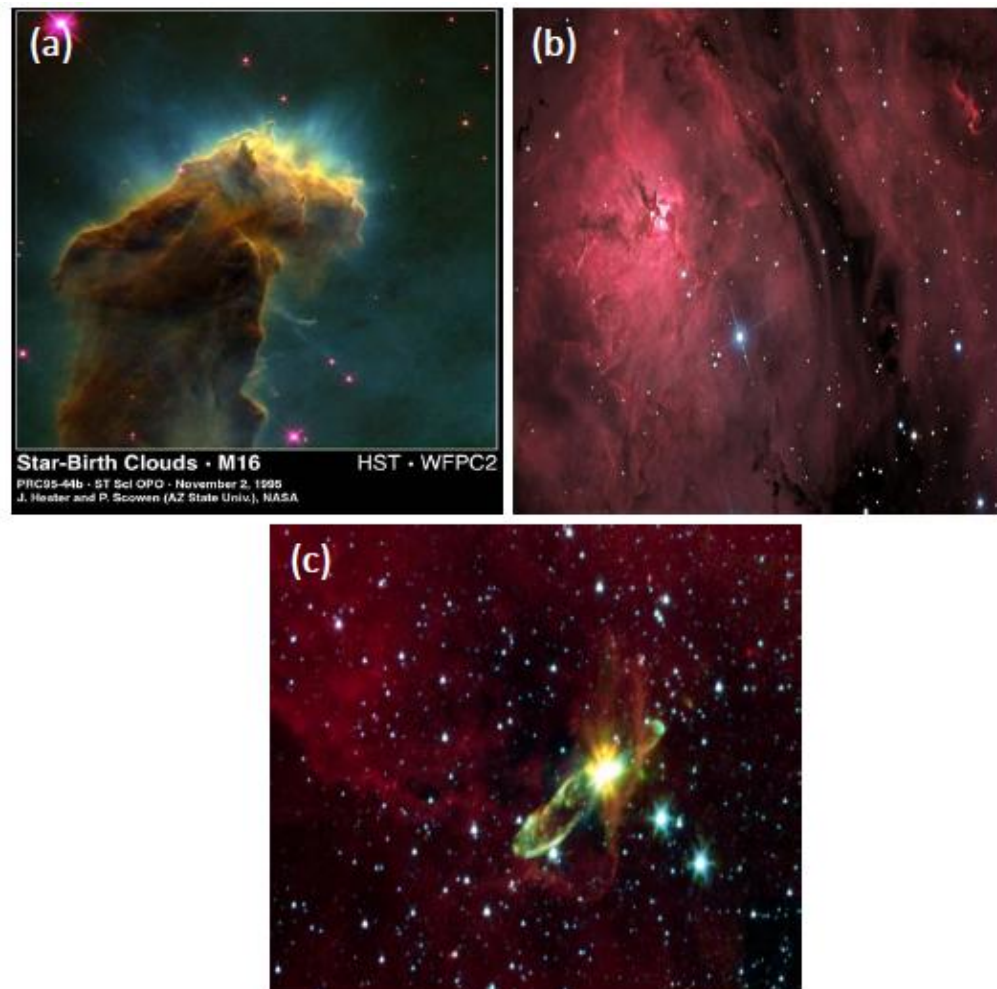


Figure 1.2: Interstellar gas clouds pictures as shown: (a) Eagle Nebula (dense clouds) represents dark clouds of cool molecular hydrogen gas and dust [5], (b) M8 – The Lagoon Nebula (diffuse clouds) and Open Cluster BLM [6], and (c) The HH 46/47 (translucent clouds) [7].

Dense clouds (also called dark or molecular clouds) are characterised by their ability to absorb starlight leading to the starlight being blocked. The magnitude of the light being absorbed by dust grains is known as a visual extinction (typical dense clouds have a magnitude of visual extinction, $A_v \geq 5$). It is also hypothesised that much of the production of complex molecules is found to occur within dense clouds. They can also be characterised by low temperatures, often as low as 10 K, high gas densities (typically $10^4 - 10^6$ atoms cm^{-3}), and a prevalence of hydrogen in molecular form ($n_{\text{H}_2} 10^5 - 10^6$ molecules cm^{-3}). Although, the dark clouds act as a shield to starlight, they are penetrated by some UV radiation and by stellar winds from stars in their neighbourhood. An intermediate between diffuse and dense clouds is the so-called translucent cloud, which contains both atomic and molecular gases [8]. The dust grains present in these molecular clouds are also responsible for the reddening of the light emitted by background and embedded stars. The reddening can be described through the interstellar radiation field curve (see **Figure 1.3**) [9], which defines the distribution of electromagnetic radiation flux with wavelength across the radio, microwave, infrared (IR), visible (V), ultraviolet (UV) and vacuum ultraviolet (VUV).

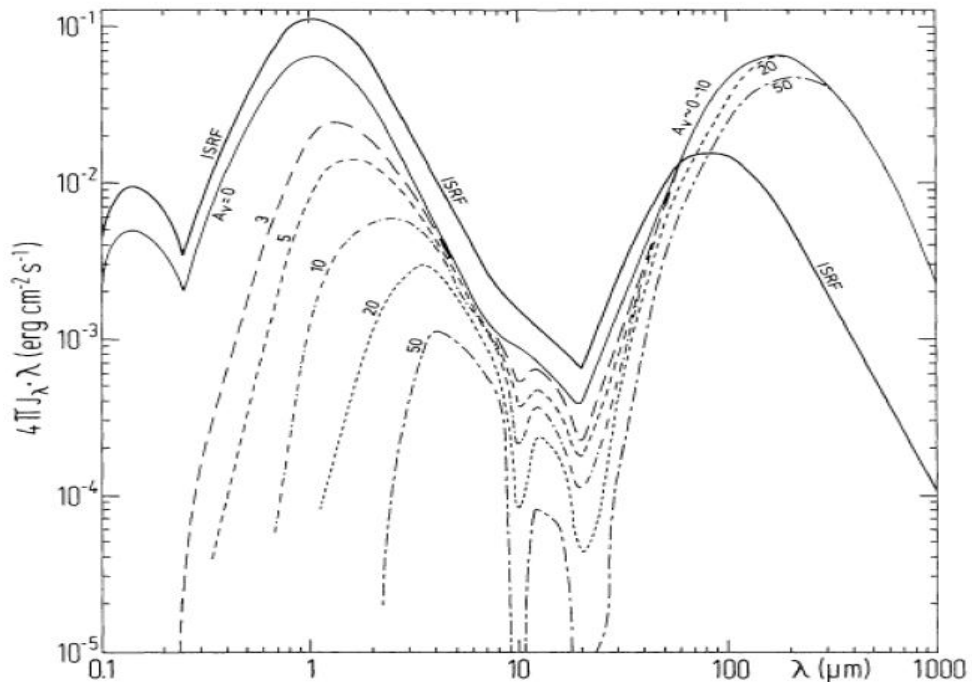


Figure 1.3: The interstellar radiation field (ISRF) inside a giant molecular cloud, located at $D_G = 1.5 \times 10^{17}$ km with A_v values up to 200 [9].

Reddening in this curve can be attributed to:

- (i) Absorption, which is illustrated in the curve in **Figure 1.4** at 217 nm ($\sim 4.6 \mu\text{m}^{-1}$) is associated with the presence of carbon grains. The increasing emission observed in the far-IR is due to down-conversion of absorbed UV in all grain types.
- (ii) Scattering, *cf.* the reddening of the Sunlight at sunset, due to reduction in the intensity of shorter wavelengths in the line-of-sight [10-13].

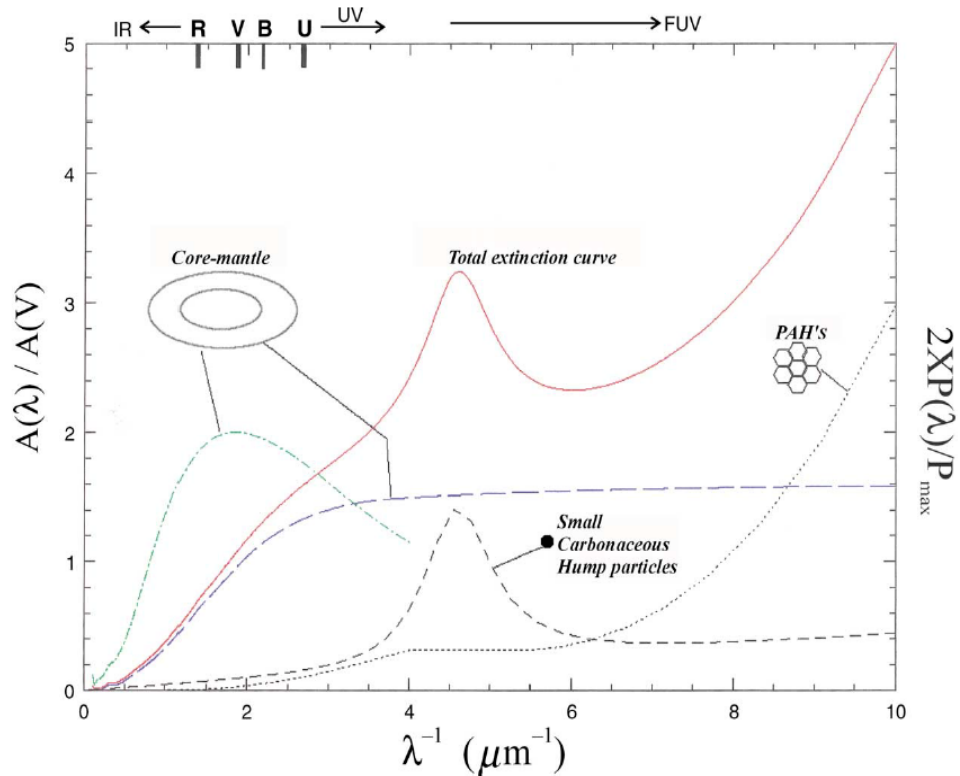


Figure 1.4: The interstellar extinction curve for a diffuse cloud [11].

Reddening can be measured as an excess of colour using the following equation:

$$E_{B-V} = A_B - A_V \quad (1.1)$$

where A_B and A_V are the total extinctions in the astronomical B (blue, 450 nm), and V (visible, 550 nm) bands. B and V can be estimated from **equations (1.2) and (1.3)**:

$$B = B_0 + A_B \quad (1.2)$$

$$V = V_0 + A_V \quad (1.3)$$

where B_0 and V_0 are the intrinsic values for the magnitudes of the star at these wavelengths. The interstellar extinction is commonly described as a total extinction, A_λ/A_V [10-13]:

$$\frac{A_\lambda}{A_V} = \frac{1}{R_V} \frac{A_\lambda - A_V}{A_B - A_V} + 1 \quad (1.4)$$

where A_λ is the extinction due to dust and R_V is the total-to-selective ratio at visual wavelength. A_λ can be calculated from equation (1.5):

$$A_\lambda = 2.5 \log_{10} \left(\frac{F_\lambda^0}{F_\lambda} \right) \quad (1.5)$$

F_λ and F_λ^0 refer to the observed flux and the flux in the absence of extinction, respectively. The total-to-selective ratio, R_V , is defined as:

$$R_V = \frac{A_V}{A_B - A_V} \quad (1.6)$$

Equation (1.5) can therefore be used to estimate how many photons pass through the cloud. For example, at the edge of the clouds where A_V is 0, 100 photons would pass completely through this region of the cloud. However, only one photon of every 100 would pass toward the centre of the cloud, where A_V is 5.

1.1.1 Chemical Composition of Interstellar Matter

The ISM contains about 10 – 15 % of the mass in the Milky Way galaxy and consists of two components: 99% gas and 1% dust. The gas phase is very cold (<100 K) and consists of 93.38% hydrogen (either molecular or atomic), 6.49% helium and small

amounts (0.11%) of oxygen, carbon and nitrogen. The other component provides a solid surface on which surface reactions and energetic processes can occur. Based on the measurements of extinction of the interstellar light as shown in **Figure 1.4**, dust particles are assumed to be non-spherical and about 0.1 – 0.2 μm in size. Dust grains absorb and scatter light most effectively at wavelengths comparable to their size. Therefore, from the absorption and scattering of IR, optical and UV radiation by dust grains, the size of particles can be calculated. The shape of interstellar dust grains is determined from polarisation of the interstellar light, as a differential extinction of starlight associated to the presence of non-spherical grains, aligned to a small degree with respect to the galactic plane due to the magnetic fields [10-13].

The chemical composition of dust grains is not fully known but observations based on spectroscopic investigations (*e.g.* UV and far IR), suggest that the core of these particles consists of graphite (C) and silicates (SiO_2 , FeSiO_3 , Fe_2SiO_4 , MgSiO_3 , and Mg_2SiO_4) with a variety of iron species such as metallic Fe, FeO, and Fe_3O_4 . The outer surface of the dust particles is covered by a solid ice mantle which contains water (H_2O) and carbon monoxide (CO) as main components; and traces of methanol (CH_3OH), carbon dioxide (CO_2), methane (CH_4), formic acid (HCOOH), carbonyl sulphide (OCS), and ammonia (NH_3) [14, 15]. The presence of these mantles has been demonstrated in infrared absorption studies of dense regions of the ISM. For example studies by Gibb *et al.* and Boogert *et al.* (**Figure 1.5**), identified H_2O and CO as the main components of the icy mantles of the dust in sources W33A, HH46, and L1014 between 2.5 – 25 μm [16, 17]. The molecules detected in the interstellar ices toward protostars are shown in **Table 1.1**. The infrared (IR) absorption feature observed at 4.62 μm ($\sim 2164 \text{ cm}^{-1}$) was thought to be due to solid CO [18], but was later attributed to OCN^- [15, 16]. This anion has been produced in the laboratory *via* UV irradiation of ice mixture (H_2O : CO: NH_3) under astrophysically relevant conditions [19, 20]. These experiments reproduced the observed feature and are considered as a first evidence for the presence of the complex ice chemistry in the ISM.

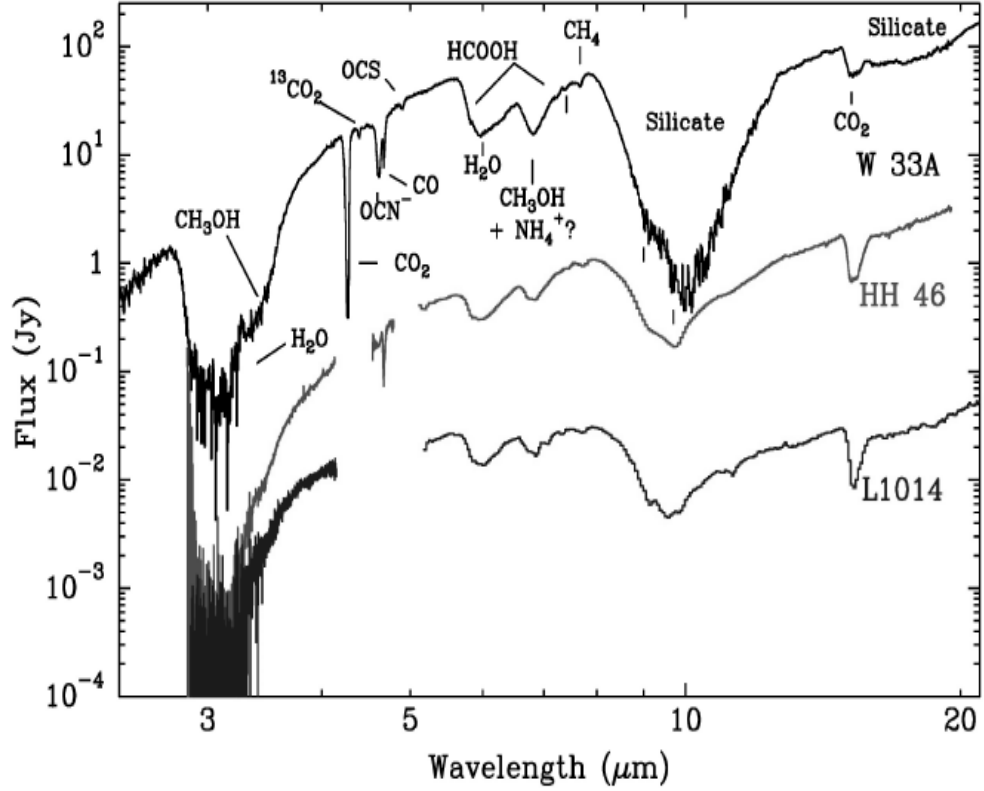


Figure 1.5: The IR spectrum between 2.5 and 25 μm of three objects: top; the Infrared Space Observatory (ISO) toward the deeply embedded massive protostars W33A [16]; middle and bottom; Combined VLT/Keck (3 - 5 μm) and Spitzer (5 - 20 μm) spectra of the solar mass protostar HH 46 and the substellar object L1014 [17].

Table 1.1: The abundance of molecules detected in the interstellar ices towards protostars [15, 16].

Molecule	Abundance % w.r.t. H_2O	Molecule	Abundance % w.r.t. H_2O
H_2O	100 [9]	H_2CO	3-7 [10]
CO	3-50 [9]	C_2H_6	≤ 0.4 [10]
CO_2	7-25 [9]	OCS	0.1 [10]
CH_3OH	2-25 [9]	OCN^-	≤ 1.9 [11]
NH_3	< 10 [9]	NH_4^+	3-17 [12]
CH_4	0.9-1.9 [10]	HCOOH	≤ 1.7 [13]

1.1.2 Formation of Interstellar Ice

As with the formation of snowflakes in Earth's atmosphere, ices in space form when the molecules from the gas phase condense and become ices on dust grains. This occurs at temperatures as low as 10 K and produces thin icy films in the range of 30 - 100 molecular layers [21]. However, ices in the ISM form through two routes; (i) hydrogenation of atoms such as oxygen adsorbed on dust grains to form water ice and (ii) condensation of molecules such as carbon monoxide (CO) and molecular nitrogen (N₂). Variation of temperature within the interstellar clouds (from diffuse to dense) has a large impact on the ices, in particular on their thickness.

Figure 1.6 illustrates ice formation at several values of visual extinction (A_V), as previously described by Öberg [22]. Chemical models of the ISM indicate that, with the exception of molecular hydrogen (H₂), all molecules are removed from the gas phase *via* the freeze-out mechanism onto dust grains within a timescale of $10^9 / n_H$ yr [23, 24]. This timescale is only realistic if there is no desorption processes occurring.

Tielens *et al.* suggested a chemical model of ice formation through gas phase and grain surface reactions [25]. They proposed that the molecules which form ices are produced from atoms accreted to the grain surface. To confirm this model, they assumed that the atoms have desorption energies higher than the energy needed for the atom to hop from one site on the surface to a neighbouring site. The atom scans the grain surface for a certain amount of time, depending on the grain temperature and desorption energy of the atom. During the surface scan, the atom may find a (radical) reaction partner on the surface and react to form a new species.

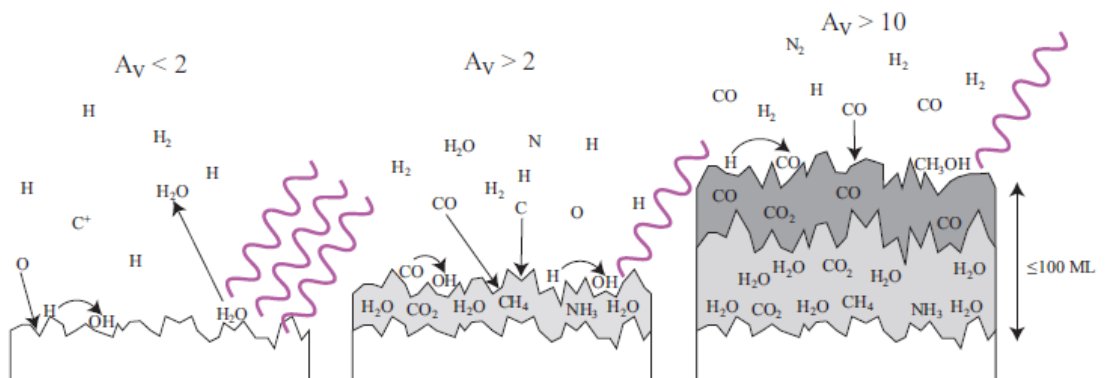


Figure 1.6: Sketch of the proposed mechanism of ice formation in the evolution from a diffuse to a dense cloud [22].

Since hydrogen atoms are considered to be the most mobile species present on the grains, simple H-containing species such as H_2O , CH_4 , and NH_3 can be formed. Indeed, observations towards protostars and dense clouds indicate that ice layers containing H-rich molecules are dominated by H_2O (polar ices). In contrast, carbon monoxide (CO) is produced by gas phase reactions and freezes out only as the top layer of the icy film. By hydrogenation of carbon monoxide (CO), other molecules such as formaldehyde (H_2CO) and methanol (CH_3OH) are eventually formed [26, 27]. Laboratory studies show that more complex ices can form by vacuum ultraviolet (VUV) and proton irradiation, as models of cosmic ray (CR) irradiation of ices which occurs in the ISM.

1.1.3 Cosmic Rays and Radiation Fields in The ISM

The most important role of the interstellar icy grain mantles is to enrich the chemical complexity of the ISM with a wide range of chemical species, from simple molecules such as H_2 , to complex molecules such as amino acids. However, the production of interstellar molecules on and in icy grains depends on the ambient interstellar conditions, particularly the presence of CRs and UV light. This section describes the CRs and the radiation fields, particularly UV photons in the ISM, and their likely impact on the frozen matter and the chemical evolution of space.

1.1.3.1 Cosmic Rays

Production of cosmic rays (CRs) in all galactic environments is thought to be associated with supernovae remnants, an example being the Crab Nebula [28]. These galactic CRs, with energies above 1 GeV, propagate diffusively through the ISM. Observations of CR composition measured at Earth *via* instrumented balloons and satellites shows that CRs consist of 90% protons, 9% alpha particles (two protons and two neutrons, which bound together into helium nuclei), 1% nuclei of heavier elements [29, 30]. The velocity of CRs is typically close to the speed of light and spans a whole range of kinetic energies E . Although the bulk of CRs with $E \leq 0.1$ GeV/nucleon originate from the Sun, the more energetic ones emanate mainly from the ISM [31]. **Figure 1.7** shows the spectrum of CRs which relates the energy with the flux [32-35]. As can be seen from **Figure 1.7**, there are two important points on the spectrum. These points appear with particular slopes; the knee and the ankle

located at 10^{15} eV and 10^{18} eV respectively. These points of interest have fluxes of approximately $1 \text{ particle m}^{-2} \text{ yr}^{-1}$ and $1 \text{ particle km}^{-2} \text{ yr}^{-1}$, respectively [32-35]. CRs play two important roles in star formation processes: firstly, inducing production of UV radiation through collision with H atoms, producing excited atoms which then emit UV photons; secondly, radicals and ionized species are formed. The latter is the most important role of the CRs. In terms of ISM chemistry, as is shown in the reaction scheme below (see **Figure 1.8**), CRs initiate ionization forming reactive species that ultimately lead to the formation of complex molecules [36-38].

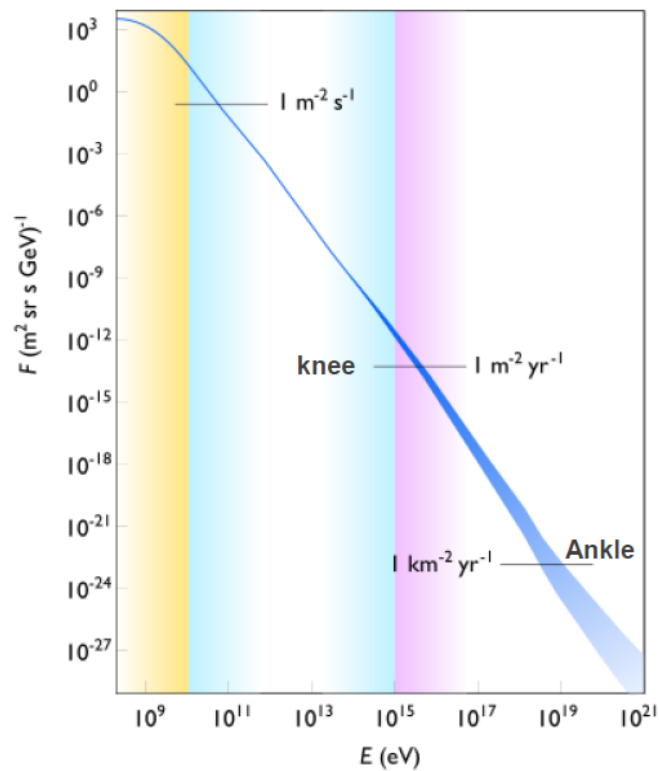


Figure 1.7: The all-particle energy spectrum of cosmic rays [32].

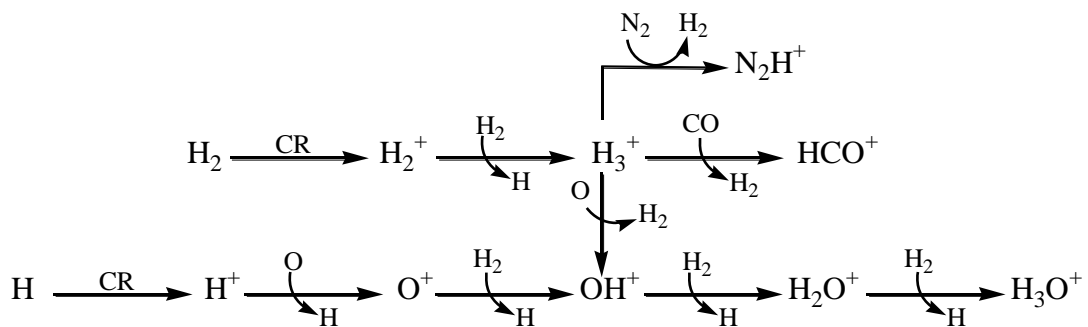


Figure 1.8: Gas phase reaction scheme showing the role of CRs in ionising species in the ISM [36-38].

1.1.3.2 Ultraviolet Radiation

Non-thermal behaviour of gaseous and solid species in the ISM depends on the impact of ultraviolet (UV) photons on these species. There are two possible sources from which UV radiation is produced. The first source is local young stars which provide a wide range of UV photon wavelengths at a typical flux of 10^8 photons $\text{cm}^{-2} \text{s}^{-1}$ at the outer regions of the molecular clouds. These UV photons contribute to the interstellar radiation field (ISRF) [9]. The ISRF measured by Mathis and co-workers is shown in **Figure 1.3**. However, this strong flux of UV photons cannot fully penetrate the interstellar clouds, as a result of the presence of interstellar dust grains. These tiny particles of interstellar dust scatter part of the UV field, resulting in visual extinction (in an experimental study, at $A_v=5$, the ISRF reduced to about 10^4 photons $\text{cm}^{-2} \text{s}^{-1}$) [9, 39]. Additionally, in very dense clouds, ISRF UV photons will be absorbed by the outer regions of the clouds. As a second source of UV photons, CRs penetrate dense clouds and collide with H and H_2 , exciting electrons and ionising the atoms / molecules. UV photons can be produced from the recombination reactions, as shown in **equations (1.7) and (1.8)**:



Typically, CRs can generate a flux of about 10^3 - 10^4 photons $\text{cm}^{-2} \text{s}^{-1}$, in dense clouds over the Lyman – Werner band system (11.2 – 13.6 eV) in VUV [40]. There are a number of interstellar processes induced by UV photons, varying from photolysis of species to photodesorption from icy grain mantles. To date, studies of chemical and physical processes induced by such energetic particles have attracted considerable attention from researchers. However, the chemical and physical evidence on interstellar ices suggests there is undoubtedly a role for UV photons in these processes.

1.1.3.3 Secondary Electrons

When various stellar radiations bombard interstellar ice, they ionise the ices and release a cascade of secondary electrons within the ice. These secondary electrons are generated in four steps:

- 1) Primary electrons are released from the material *via* a coulomb-scattering process between the energetic particles and the target lattice electrons;
- 2) Released primary electrons travel isotropically in a random manner;
- 3) Some of these electrons arrive at the surface and overcome the surface potential barrier and escape.
- 4) Some of those electrons are inelastically scattered in the target lattice from target lattice valence electrons to produce a wide range of low energy secondary electrons.

In fact, the probability of the electrons escaping becomes greater when the inelastic mean free path of the primary electrons is comparable to the size of the dust particles. In the dark regions of the ISM, CRs and X-rays are the only source of ionisation and the production of electrons. CRs with energies of only a few MeV, *ca.* 4 MeV can ionise H and H₂ to produce electrons with energies of 30 eV. These electrons can promote the Lyman-Werner electronic excitation of H₂, resulting in dissociation of the molecule or radiative relaxation back to the electronic ground state [41]. Significantly, electron emission is possible through ions impacting on dust grains. For instance, for energies of around 5 keV, the electron yield from ions impacting on a solid can reach unity, and can produce a few electrons around 1 MeV for He²⁺ ions and 100 keV for H⁺ ions [41]. Both primary and secondary electrons can induce chemical processes through ionisation and electron attachment processes [42, 43].

1.2 Interstellar Molecules

Over 170 molecular species containing from two to thirteen atoms have been detected in the interstellar space (see **Table 1.2**) [44, 45]. This does not include isotopic variants. Most of these molecules have large dipoles, as a result of the bias

toward high sensitivity for such species in rotational spectroscopies (for example radio, μm and mm). IR in contrast is much less sensitive but has the advantage of providing some qualitative characterisation of polyatomic molecules through group frequency analysis in the 2.5 to 25 μm range (see **Figure 1.9**) [11, 46]. Since most of the molecules are found in dense regions of the ISM, a detailed knowledge of the chemistry in these regions is therefore key to interpreting the complex process of star formation and perhaps the origins of life itself. The difficulty is that the chemistry of the ISM is unusual compared with that on Earth.

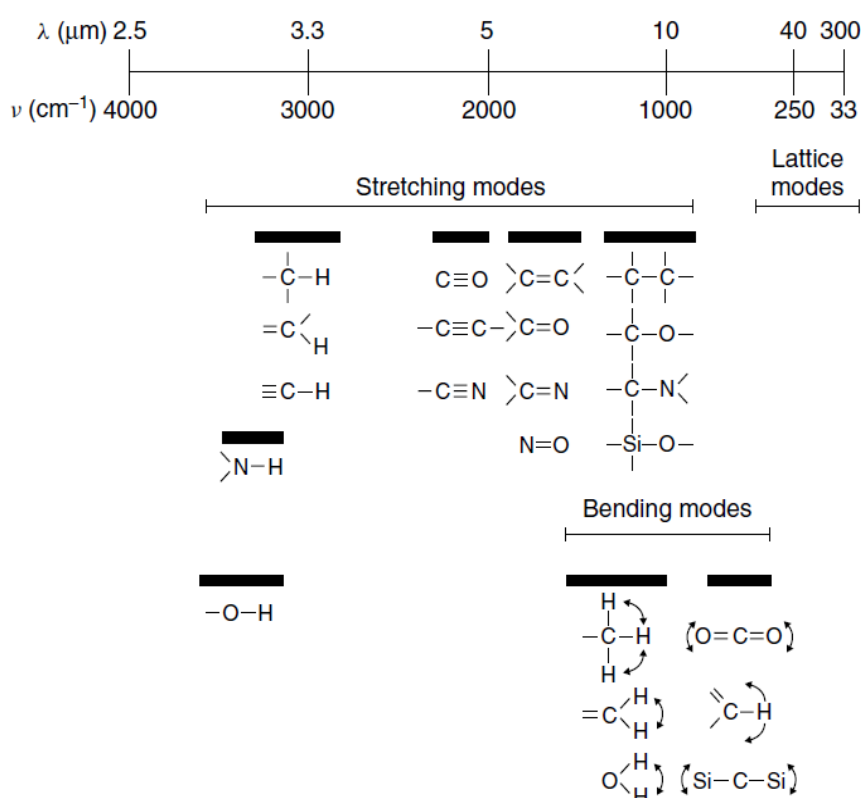


Figure 1.9: The IR vibrational modes of common functional groups in the region 4000-300 cm^{-1} [46].

The chemistry of the ISM is dominated by chemical processes involving ions, *e.g.* H_3^+ (protonated dihydrogen) and HCO^+ (formyl ion) are commonly found in space as a result of gas phase reactions under conditions where the temperature lies between 10 and 50 K and the pressure is as low as 10^{-15} mbar [47]. This is a consequence of the presence of the UV and VUV components of the interstellar radiation field and CRs. Ion-molecule reactions in the gas phase are efficient at the low temperatures

(10 - 50 K), and low pressures of the ISM, and therefore dominate the molecule formation mechanisms.

Table 1.2: List of the observed interstellar and circumstellar molecules [44].

Diatomic	Triatomic	Four atoms	Five atoms	Six atoms	Seven atoms	≥ Eight atoms
H ₂	C ₃	c-C ₃ H*	C ₅	C ₅ H	C ₆ H	CH ₃ C ₃ N
AlF	C ₂ H	l-C ₃ H**	C ₄ H	l-H ₂ C ₄	CH ₂ CHCN	HCOOCH ₃
AlCl	C ₂ O	C ₃ N	C ₄ Si	C ₂ H ₄	CH ₃ C ₂ H	CH ₃ COOH
C ₂	C ₂ S	C ₃ O	l-C ₃ H ₂ **	CH ₃ CN	HC ₅ N	C ₇ H
CH	CH ₂	C ₃ S	c-C ₃ H ₂	CH ₃ NC	HCOCH ₃	H ₂ C ₆
CH ⁺	HCN	C ₂ H ₂	CH ₂ CN	CH ₃ OH	NH ₂ CH ₃	CH ₂ OHCHO
CN	HCO	CH ₂ D ⁺ ?	CH ₄	CH ₃ SH	c-C ₂ H ₄ O	CH ₂ CHCHO
CO	HCO ⁺	HCCN	HC ₃ N	HC ₃ NH ⁺	CH ₂ CHOH	CH ₃ C ₄ H
CO ⁺	HCS ⁺	HCNH ⁺	HC ₂ NC	HC ₂ CHO		CH ₃ CH ₂ CN
CP	HOC ⁺	HNCO	HCOOH	NH ₂ CHO		(CH ₃) ₂ O
CSi	H ₂ O	HNCS	H ₂ CHN	C ₃ N		CH ₃ CH ₂ OH
HCl	H ₂ S	HOCO ⁺	H ₂ C ₂ O	HC ₄ N		HC ₇ N
KCl	HNC	H ₂ CO	H ₂ NCN			C ₈ H
NH	HNO	H ₂ CN	HNC ₃			CH ₃ C ₅ N?
NO	MgCN	H ₂ CS	SiH ₄			(CH ₃) ₂ CO
NS	MgNC	H ₃ O ⁺	H ₂ COH ⁺			NH ₂ CH ₂ COO
NaCl	N ₂ H ⁺	NH ₃				H
OH	N ₂ O	SiC ₃				CH ₃ CH ₂ CHO
PN	NaCN	C ₄				HC ₉ N
SO	OCS					CH ₃ OC ₂ H ₅
SO ⁺	SO ₂					HC ₁₁ N
SiN	c-SiC ₂ *					
SiO	CO ₂					
SiS	NH ₂					
CS	H ₃ ⁺					
HF	SiCN					
SH	AlNC					
FeO ₇	SiNC					

*c- Cyclic molecule, **l- Linear molecule, and (?) Tentative detection.

1.3 Chemistry of the ISM

Due to low densities ($\sim 10^7 \text{ cm}^{-3}$) and low temperatures ($< 100 \text{ K}$) dominating the ISM, most endothermic reactions cannot occur since not enough energy is available. The chemistry of the ISM is restricted to the following processes: (1) exothermic reactions and (2) bimolecular reactions (three-body collisions are unlikely) [48]. For the two types of collisions (*i.e.* two- and three-body), timescales in yr^{-1} can be estimated from the following equations:

$$t_{\text{two-bodycollisions}} = 3 \times 10^2 \text{ molecules cm}^{-3} \text{ yr}^{-1} / n_{\text{H}} \quad (1.9)$$

$$t_{\text{three-bodycollisions}} = 3 \times 10^{23} (\text{molecules cm}^{-3} \text{ yr}^{-1})^2 / n_{\text{H}}^2 \quad (1.10)$$

where n_{H} is the hydrogen density in molecules cm^{-3} . Moreover, exothermic reactions are expected only if they have a relatively high rate constant (k), which results if the activation energy (E_a) of the Arrhenius equation is comparable to the thermal energy ($k_B T$):

$$k = A e^{-E_a/k_B T} \quad (1.11)$$

where A is the pre-exponential factor, E_a is the activation energy in kJ mol^{-1} , k_B is Boltzmann's constant, and T is the temperature in K. Consequently, there are two types of mechanisms that would fit these requirements; gas-phase chemistry and grain surface chemistry.

1.3.1 Gas-phase Chemistry

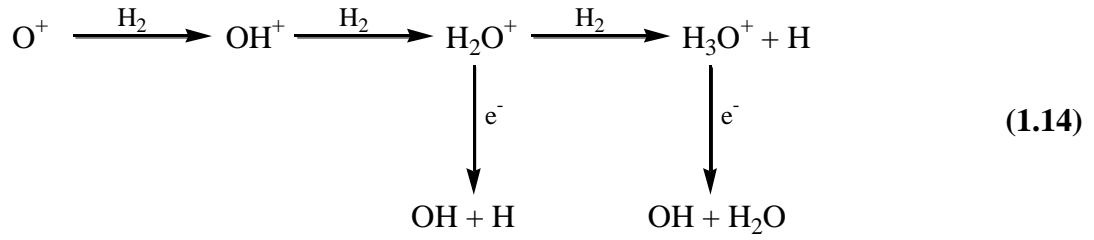
The gas phase reactions in the ISM at low gas densities and low temperatures are triggered by the starlight and CRs and occur as a result of two-body collisions. The exothermic nature of these reactions is responsible for the presence in space of a variety of large molecules, containing up to 12 atoms [49]. **Table 1.3** summarises the basic gas-phase reaction types in the ISM [48, 50].

Table 1.3: The basic gas-phase reaction types of importance in interstellar chemistry [48, 50].

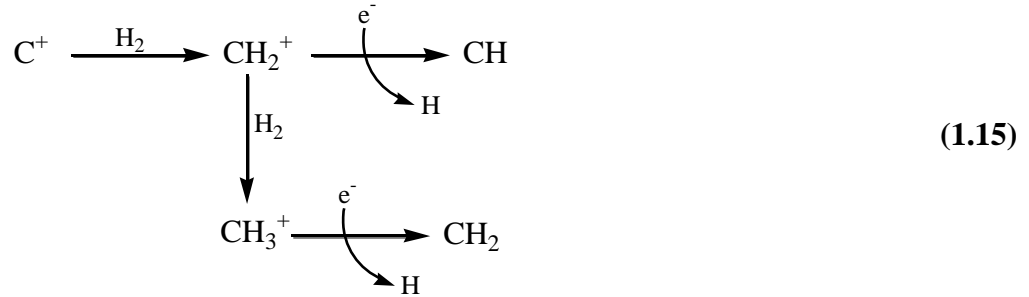
Chemical Reaction Type	Reactions
1- Ion- molecule	
i) Charge transfer	$A^+ + B \rightarrow B^+ + A$
ii) Radiative association	$A^+ + B \rightarrow AB^+ + h\nu$
iii) Atom transfer	$A^+ + BC \rightarrow AB^+ + C$ $AB^+ + C \rightarrow A^+ + BC$
2- Electron recombination	
i) Radiative	$A^+ + e^- \rightarrow A + h\nu$
ii) Dissociative	$AB^+ + e^- \rightarrow A + B$
3- Photochemical	
i) Photodissociation	$AB^+ + h\nu \rightarrow A^+ + B$
ii) Photoionisation	$A + h\nu \rightarrow A^+ + e^-$
4- Neutral-neutral	
i) Atom transfer	$A + BC \rightarrow AB + C$
ii) Radiative association	$A + B \rightarrow AB + h\nu$
iii) Chemionisation	$A + B \rightarrow AB^+ + e^-$
5- Other reactions	
i) Ion-ion neutralisation	$A^+ + B^- \rightarrow AB$
ii) Negative ion-neutral	$A^- + B \rightarrow AB + e^-$ $A^- + BC \rightarrow AB^- + C$

The transparency of the diffuse clouds allows a high flux of the UV radiation which dissociates the molecules inside these clouds. A substantial fraction of the material in diffuse clouds is therefore present in the atomic form. Ionisation of atomic H, the major component of the diffuse medium, by CRs then initiates ion-molecule chemistry. With O atoms, this produces OH and H₂O neutral products:





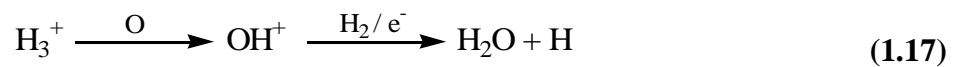
Ionised carbon represents the route to formation of the C-containing molecules in diffuse clouds that are formed *via* radiative association reactions of C^+ with H_2 which results in the formation of CH_2^+ , which then reacts with H_2 to form CH_3^+ . Neutral CH and CH_2 are formed through dissociative recombination reactions with electrons:

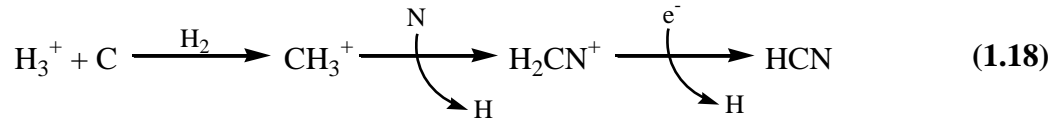


The chemistry of dark clouds is dominated by H_2 molecules, He atoms and dust grains. The latter prevents the interstellar radiation field from penetrating the clouds. Although the UV and VUV flux in the dense clouds is less than in the diffuse clouds, the cold gas chemistry in both regions is similar. The CRs ionise H_2 molecules to form H_3^+ , as in the following reaction:



The H_3^+ produces a number of simple molecules, such as H_2O and HCN, *via* a chain of gas-phase reactions [51]:



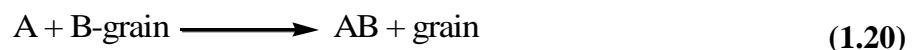


1.3.2 Grain Surface Chemistry

Over the last decade, observations of the chemical composition of the ISM have shown that not only do gas-phase reactions lead to the formation of chemical species, but reactions on grain surfaces also play an important role. The formation of molecular hydrogen is assumed to occur *via* grain surface reactions, as opposed to the gas phase, because H atoms cannot react readily by two-body reaction, as there is no way to remove the excess energy of the nascent H₂ by a third body collision, as shown in **equation (1.19)**:



In principle, electronic vibrational transitions are active in diatomic molecules which consist of two different atoms and thus have a dipole. Thus, only the molecules that have a dipole are able to absorb IR irradiation and emit IR photons. In the case of the molecular hydrogen, recombination of two H atoms in the ground state leads to the formation of H₂. To form a relatively stable product, the H₂ must emit a photon, but that is a forbidden process. The recombination of H atoms could proceed through an allowed transition if one of the H atoms is in the ground state and the other one in the 2p excited state [52], whereas the presence of a solid grain (*i.e.* the third body in the reaction) provides the surface on which the internal energy of the reaction product can be released. Therefore H atoms are adsorbed onto the grain surface and then desorbed to the gas phase in the form of H₂ [53]. The dust grains hence provide a substrate on which the atoms are allowed to react and form new molecules. Once atoms or radicals land on the dust surface, they diffuse and react to form new molecules with other species that are already present on the surface. Thus the grain surface reactions can be thought of as three-body reactions [54]:



An exchange reaction between species A and the adsorbed species B results in the formation of a new molecule, AB, which will either return to the gas phase, *e.g.* as in the case of H₂, or will remain trapped on the grain surface, *e.g.* as in the case of H₂O.

1.4 Review of Experimental and Theoretical Studies of ISM Chemistry

1.4.1 Gas-phase Model

Over 5000 reactions were included in the first model of the gas-phase ISM chemistry [55]. This model considered that the dense clouds mainly consist of molecular hydrogen; hence production of the polyatomic ions occurs rapidly through the exothermic ion-molecule reactions:



Another route that was suggested is that there is an intermediate, which represents the short-lived collision complex, which then radiatively relaxes [56]:



The formation and destruction reactions of hydrogen, oxygen, carbon, and nitrogen containing molecules are contained within the chemical models of the gas-phase. In the recent update of the University of Manchester Institute of Science and Technology (UMIST) astrochemistry network, the number of gas reactions is 6173, involving more than 467 species, 47 of which are new [55]. Although the gas phase model works well with species such as C and N-containing molecules, it is not able to explain the formation of key small molecules, including molecular hydrogen, which suggests that there must be an efficient alternative chemistry to produce the necessary observed concentrations of H₂ and other simple hydrides.

1.4.2 Dust Grain Model

Dust particles play a key role in the production of a variety of the molecules observed in the ISM. The newly formed molecules may return to the gas-phase. In order to understand the physical and chemical processes that lead to formation of molecules on the surface of a dust grain, some surface science fundamentals can be used to describe the formation of molecular species in the ISM. Basically, the interactions of atomic and/or molecular species with the surfaces illustrate the physics and chemistry of species adsorbed on surfaces. These interactions are well described using a Lennard-Jones potential energy diagram (see **Figure 1.10**). This is a one-dimensional potential energy diagram for dissociative adsorption which includes the possibility of precursor-mediated kinetics [57]. Using the adsorption of oxygen on a metal surface as an example, curve (a) shows the interactions of atomic oxygen with the surface, and curve (b) shows the interactions of molecular oxygen with the surface. Curve (b) shows a non-activated process (*i.e.* there is no activation barrier), for which:

$$\Delta_{ads}H(O_2) = -\Delta_{des}H(O_2) \quad (1.24)$$

For the chemisorption process molecular oxygen needs energy to overcome the activation barrier, E_{diss}^a and dissociate. Therefore adsorption can be categorised into two types, activated and non-activated adsorption. Activated adsorption occurs when the curve crossing of (a) and (b) is located above the energy zero line, whereas the non-activated process occurs when the crossing of curves (a) and (b) is located below the energy zero line. Thus it is clear, the position of the curve crossing of (a) and (b) specifies the nature of adsorption.

In molecular clouds, the formation of H_2 and other species such as H_2O , CH_3OH , and CO on dust grain surfaces is an efficient process. The schematic representation below (see **Figure 1.11**) shows the processes by which molecules form in star-forming regions through grain-mediated processes [58]. Adsorption of molecules on dust grain surfaces depends on the nature of binding, where molecules can be either physisorbed (weak bonds) through van der Waals interactions or chemisorbed (strong bonds) through covalent bonds as shown in **Figure 1.11 (a)**.

e.g. in the case of H_2 , but in other cases may be insufficient to promote desorption, *e.g.* H_2O [58].

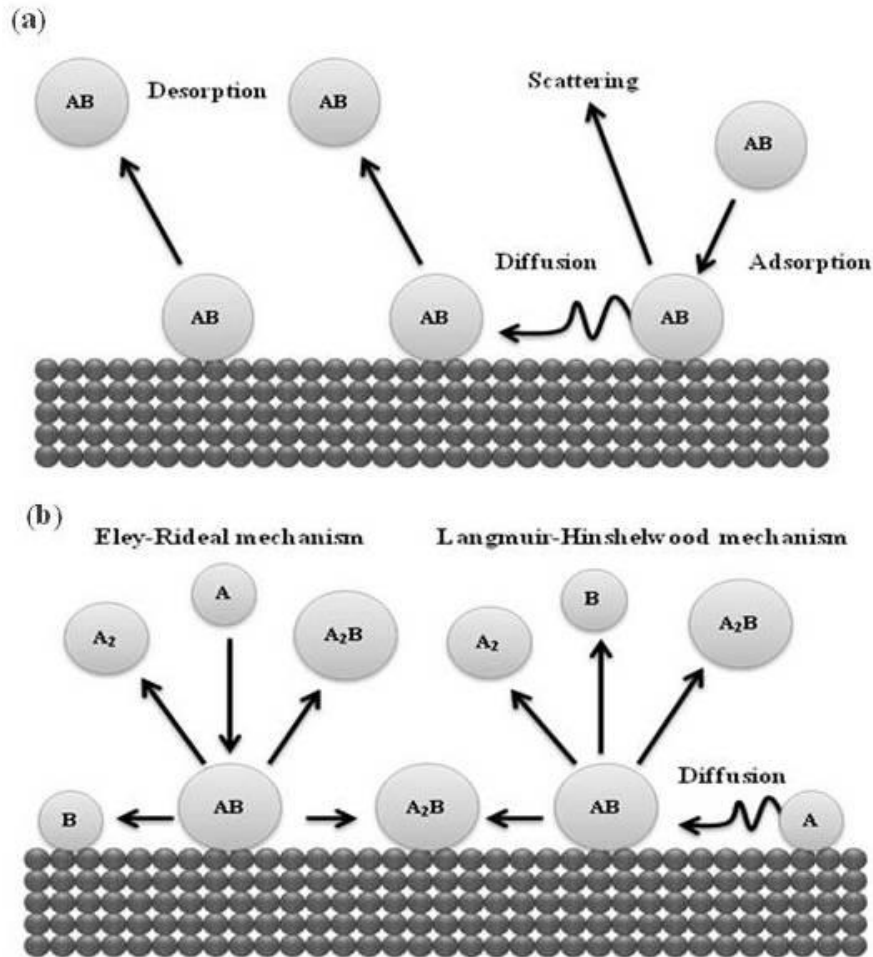


Figure 1.11: The basic (a) chemical and (b) physical processes that occur on dust grains under the astrophysically relevant conditions [58].

1.5 Grain Mimics

In classical surface science, simple molecules such as CO and H_2O have been studied widely on well-defined surfaces such as flat single metal crystals such as Pt(111) [59, 60], Mo(110) [61, 62], Cu(100) [63, 64], Ni(110) [65, 66] and W(111) [67, 68]. As it is difficult to collect real dust grains from space, the composition of dust grains is dependent on the astrophysical environment. To predict the chemical and physical processes that take place on the dust grain surface, it is necessary to mimic these surfaces in the astrochemistry laboratory.

Single metal surfaces have been used as grain mimics. For instance, Al coated by Au has been used as an analogue of the dust grain. Coating the metal surface is used to reduce the background fluorescence caused by metal oxides [69]. However, metals are not good models as there is no evidence for bulk metals in grains, as well as the issues relating to photon- and electron-induced chemistry on metal surfaces.

Metal surfaces coated by silica are used as grain mimics in astrochemistry laboratories [70]. One of the suitable analogues of a dust grain that has been used in astrophysics laboratories is highly-oriented pyrolytic graphite (HOPG). The reason for using grain mimics is to try to reproduce the chemical and physical properties of dust grain surfaces – which are certainly not single metal crystals. The use of silica and graphite as grain mimic surfaces is based on spectral observations of the presence of silicates and graphite within the chemical composition of dust grains [18, 19, 71].

1.6 Thesis Outline

This thesis investigates the interactions of solid acetonitrile (CH_3CN) on silica and H_2O ice surfaces as interstellar dust grain models. Both thermal and non-thermal interactions of CH_3CN adsorbed on the top of silica and on water/silica systems under astrophysically relevant conditions were investigated. The reason for the choice of CH_3CN as a case study in this thesis resides in its observation in the ISM and its role as a potential source of other more complex molecules. The work utilises ultrahigh vacuum (UHV) based surface science methods to understand the behaviour of CH_3CN when it is heated and irradiated with low energy electrons and medium energy protons.

Chapter 2 describes the experimental setup including the dust model preparation and the experimental techniques used, such as temperature-programmed desorption (TPD), reflection-absorption infrared spectroscopy (RAIRS), and electron-promoted desorption (EPD).

As water is the major component in interstellar ice, **Chapter 3** discusses thermal and the non-thermal desorption of water ice. Results obtained from the thermal desorption are discussed and compared with those obtained from previous water TPD

experiments. Simple kinetic simulations were used to model the experimental data. The non-thermal desorption of water ice was investigated by mass spectrometry and RAIRS. Measurements of the total cross-section for desorption confirm that electrons promote desorption of water ice. A simple model of H₂O desorption was built to predict the abundance of water in the dark cloud Barnard 68 (B68). This model includes desorption promoted by electrons, photons from the ISRF, the internal VUV field, and re-adsorption from the gas phase.

Chapter 4 throws light on the surface science of CH₃CN in the interstellar dust models. Experimental results from TPD for different surface exposures of CH₃CN were used to gain comprehensive knowledge of the surface structure of CH₃CN on the silica surface. Both submonolayer and multilayer analyses were performed to confirm the surface structure. Furthermore, kinetic models of desorption were used to estimate desorption energies and pre-exponential factors for CH₃CN. Growth of CH₃CN on the top of silica and water/silica systems was monitored by RAIRS. The binding energies of the CH₃CN/H₂O complex and the orientation of CH₃CN/H₂O were investigated using computational methods. Finally, annealing of solid CH₃CN itself and within a mixture with water was probed by RAIRS, in order to monitor the changes in the surface.

Chapter 5 investigates both low energy electron and proton irradiation of solid CH₃CN. Low energy electron irradiation in the electron energy range between 250 eV and 400 eV was employed in this study. The lack of any chemical products of irradiated solid CH₃CN adsorbed on silica and/or water/silica systems is discussed with a determination of the total cross-sections for C≡N loss. Proton irradiation data provided by INAF Catania shows evidence for chemical products as a result of irradiation of solid CH₃CN with 200 keV H⁺. Both studies are compared in the remainder of this chapter. The rate constant of the physical process (*i.e.* desorption) promoted by electrons, and the rate constant of the chemical process (*i.e.* formation of new molecules) are both calculated from the cross-sections and the fluxes of electrons and protons respectively.

The overall conclusions and the future outlook of work in this thesis are presented in **Chapter 6**.

1.7 References

- [1] D. A. Williams and E. Herbst, *Surf. Sci*, 2002, **500**, 823.
- [2] H. Zinnecker, *IAU Symposium*, 2001, **200**, 1.
- [3] R. J. Trumpler, *Lick Obs. Bull.*, 1930, **420**, 154.
- [4] C. Heiles, *Astrophys. J. Suppl.*, 1967, **15**, 97.
- [5] Hubble Site, *Embryonic Stars Emerge from Interstellar "Eggs"*.
http://hubblesite.org/newscenter/archive/releases/1995/44/image/b/format/web_p rint/ (Accessed 10/06/2009).
- [6] Taken from *The Lagoon Nebula, Explore Astronomy*, The University of Manchester.
<http://www.jb.man.ac.uk/astronomy/nightsky/AList/Sagittarius.html> (Accessed 18/06/2009)
- [7] Taken from *The HH 46/47*
<http://www.nasaimages.org/luna/servlet/detail/nasaNAS~12~12~64191~168594:HH46-47> (Accessed 18/06/2009).
- [8] D. H. Wooden, S. B. Charnley, and P. Ehrenfreund, *Composition and Evolution of Interstellar Clouds: Comets II*, the University of Arizona Press, Tucson, 2005.
- [9] J. S. Mathis, P. G. Mezger, and N. Panagia, *Astron. Astrophys.*, 1983, **128**, 212.
- [10] J. S. Mathis, W. Rumpl, and K. H. Nordsieck, *Astrophys. J.*, 1977, **217**, 425.
- [11] J. M. Greenberg, *Surf. Sci*, 2002, **500**, 793.
- [12] B. T. Draine, *Annu. Rev. Astron. Astrophys.*, 2002, **41**, 1.
- [13] A. Li, *J. Phys.:Conf. Ser.*, 2005, **6**, 229.
- [14] R. I. Kaiser, C. Ochsenfeld, D. Stranges, M. Head-Gordon, and Y.T. Lee, *Farad. Discuss.*, 1998, **109**, 183.
- [15] J. C. Lee and B. Ravel, *Astrophys. J.*, 2005, **622**, 970.

- [16] E. L. Gibb, D. C. B. Whittet, W. A. Schutte, A. C. A. Boogert, J. E. Chiar, P. Ehrenfreund, P. A. Gerakiness, J. V. Keane, A. G. G. M. Tielens, E. F. Van Dishoeck, and O. Kerkhof, *Astrophys. J.*, 2000, **536**, 347.
- [17] A. C. A. Boogert, K. M. Pontoppidan, F. Lahuis, J. K. Jørgensen, J. Augereau, G. A. Blake, T. Y. Brooke, J. Brown, C. P. Dullemond, N. J. Evans, V. Geers, M. R. Hogerheijde, J. Kessler-Silacci, C. Knez, P. Morris, A. Noriega-Crespo, F. L. Schöier, E. F. van Dishoeck, L. E. Allen, P. M. Harvey, D. W. Koerner, L. G. Mundy, P. C. Myers, D. L. Padgett, A. I. Sargent, and K. R. Stapelfeldt, *Astrophys. J. Suppl.*, 2004, **154**, 359.
- [18] B. T. Soifer, R. C. Puetter, R. W. Russell, S. P. Willner, P. M. Harvey, F. C. Gillett, *Astrophys. J.*, 1979, **232**, L53.
- [19] R. J. A. Grim and J. M. Greenberg, *Astrophys. J.*, 1987, **321**, L91.
- [20] F. A. van Broekhuizen, *PhD Thesis*, (Leiden University, Leiden, 2005).
- [21] K. M. Pontoppidan, H. J. Fraser, E. Dartois, W.-F. Thi, E. F. van Dishoeck, A. C. A. Boogert, L. d’Hendecourt, A. G. G. M. Tielens, and S. E. Bisschop, *Astron. Astrophys.*, 2003, **408**, 981.
- [22] K. Öberg, *PhD Thesis*, (Leiden University, Leiden, 2009).
- [23] D. A. Williams and S. D. Taylor, *Quart. J. Roy. Astron. Soc.*, 1996, **37**, 565.
- [24] K. Willacy and T. J. Millar, *Mon. Not. R. Astron. Soc.*, 1998, 298, 562.
- [25] A. G. G. M. Tielens and W. Hagen, *Astron. Astrophys.*, 1982, **114**, 245.
- [26] N. Wanatabe and A. Kouchi, *Astrophys. J.*, 2002, **571**, L173.
- [27] G. W. Fuchs, H. M. Cuppen, S. Ioppolo, C. Romanzin, S. E. Bisschop, S. Andersson, E. F. van Dishoeck, and H. Linnartz, *Astron. Astrophys.*, 2009, **505**, 629.
- [28] F. A. Aharonian, A. G. Akhperjanian, K.-M. Aye, A. R. Bazer-Bachi, M. Beilicke, W. Benbow, D. Berge, P. Berghaus, K. Bernlöhr, O. Bolz, C. Boisson, C. Borgmeier, F. Breitling, A. M. Brown, J. Bussons Gordo, P. M. Chadwick, V. R. Chitnis, L.-M. Chounet, R. Cornils, L. Costamante, B. Degrange, A.

Djannati-Ataï, L. O'C. Drury, T. Ergin, P. Espigat, F. Feinsein, P. Fleury, G. Fontaine, S. Funk, Y. A. Gallant, B. Giebels, S. Gillessen, P. Goret, J. Guy, C. Hadjichristidis, M. Hauser, G. Heinzelmann, G. Henri, G. Hermann, J. A. Hinton, W. Hofmann, M. Holleran, D. Horns, O. C. de Jager, I. Jung, B. Khélifi, Nu. Komin, A. Konopelko, I. J. Latham, R. Le Gallou, M. Lemoine, A. Lemièrre, N. Leroy, T. Lohse, A. Marcowith, C. Masterson, T. J. L. McComb, M. de Naurois, S. J. Nolan, A. Noutsos, K. J. Orford, J. L. Osborne, M. Ouchrif, M. Panter, G. Pelletier, S. Pita, M. Pohl, G. Pühlhofer, M. Punch, B. C. Raubenheimer, M. Raue, J. Raux, S. M. Rayner, I. Redondo, A. Reimer, O. Reimer, J. Ripken, M. Rivoal, L. Rob, L. Rolland, G. Rowell, V. Sahakian, L. Saugé, S. Schlenker, R. Schlickeiser, C. Schuster, U. Schwanke, M. Siewert, H. Sol, R. Steenkamp, C. Stegmann, J.-P. Tavernet, C. G. Théoret, M. Tluczykont, D. J. van der Walt, G. Vasileiadis, P. Vincent, B. Visser, H. J. Völk and S. J. Wagner, *Nature*, 2004, **432**, 75.

- [29] R. D. Blandford and D. Eichler, *Phys. Rep.*, 1987, **154**, 1.
- [30] H. Bloemen, In *Interstellar Processes*, edited by D. J. Hollenbach and H. A. Thronson, Jr., (Reidel, Dordrecht, 1987) p. 143.
- [31] K. M. Ferrière, *Rev. Mod. Phys.*, 2001, **73**, 1030.
- [32] F. McNally, Simulating Light Production in Ice Top, IceCube Website, <http://icecube.wisc.edu/~fmcnally/index.html#Int> (accessed: 06/02/2013).
- [33] W. J. Cronin, T. K. Gaisser and S. P. Swordy, Cosmic Rays at Energy Frontier, *Sci. Am*, 1997, January issue, 44.
- [34] S. P. Swordy, *Space. Sci. Rev*, 2001, **99**, 85.
- [35] T. Stanev, High Energy Cosmic Rays, 2nd edition, (Praxis Publishing Ltd, Chichester, 2010).
- [36] E. Herbst and W. Klemperer, *Astrophys. J.*, 1973, **185**, 505.
- [37] F. C. Fehsenfeld and E. E. Ferguson, *J. Chem. Phys.*, 1972, **56**, 3066.
- [38] E. Herbst, *Chem. Soc. Rev.*, 2001, **30**, 168.

- [39] S. S. Prasad and S. P. Tarafdar, *Astrophys. J.*, 1983, **267**, 603.
- [40] C. J. Shen, J. M. Greenberg, W. A. Schutte, and E. F. van Dishoeck, *Astron. Astrophys.*, 2004, **415**, 203.
- [41] D. M. Suszcynsky, J. E. Borovsky, and C. K. Goertz, *Adv. Spce. Res.*, 1993, **13**, 83.
- [42] C. D. Lane and T. M. Orlando, *Appl. Surf. Sci.*, 2007, **253**, 6646.
- [43] C. R. Arumainayagam, H. Lee, R. B. Nelson, D. R. Haines, and R. P. Gunawardane, *Surf. Sci. Rep.*, 2010, **65**, 1.
- [44] Taken from *The 129 reported interstellar and circumstellar molecules*
<http://www.cv.nrao.edu/~awootten/allmols.html> (Accessed 05/03/2009)
- [45] Taken from *The 151 molecular species detected in space*
<http://astrochemistry.net/> (Accessed 05/03/2009)
- [46] S. A. Sandford, *Meteor. Plan. Sci.*, 1996, **31**, 449.
- [47] E. Herbst, *Chem. Soc. Rev.*, 2001, **30**, 168.
- [48] R. Carbó and A. Ginebreda, *J. Chem. Educ.*, 1985, **62**, 832.
- [49] A. F Jalbout and M. A. H. Shipar, *J. Chem. Sci.*, 2008, **120**, 329.
- [50] A. G. G. M. Tielens. *The Physics and Chemistry of the Interstellar Medium*, (Cambridge University Press, Cambridge, 2005).
- [51] D. Smith, *Phil. Trans. R. Soc. Lond. A.*, 1987, **323**, 269.
- [52] R. J. Gould and E. E. Salpeter, *Astrophys. J.*, 1963, **138**, 393-407.
- [53] S. M. Cazaux, *PhD Thesis*, (University of Groningen, Groningen, 2004).
- [54] D. A. Williams, *J. Phys: Conf. Ser.*, 2005, **6**, 1.
- [55] D. McElroy, C. Walsh, A. J. Markwick, M. A. Cordiner, K. Smith, and T. J. Millar, *Astron. Astrophys.*, 2013, **550**, A36.
- [56] E. Herbst and W. Klemperer. *Astrophys. J.*, 1973, **185**, 505.

- [57] G. Attard and C. Barnes, *Surfaces*, (Oxford University Press, Oxford, 2008).
- [58] H.J. Fraser, and E.F. Van Dishoeck, *Adva. Space. Res.*, 2004, **33**, 14-22.
- [59] H. Ogasawara, B. Brena, D. Nordlund, M. Nyberg, A. Pelmenschikov, L.G.M. Pettersson, and A. Nilsson, *Phys. Rev Lett.*, 2002, **89**, 2761021.
- [60] F. Kitamura, M. Takeda, M. Takahashi, and M. Ito, *Chem. Phys. Lett.*, 1987, **142**, 318.
- [61] H. H. Hwu, J. G. Chen, *Surf. Sci.*, 2003, **536**, 75.
- [62] J. -W. He, W. K. Kuhn and D.W. Goodman, *Surf. Sci.*, 1992, **262**, 351.
- [63] A. Spitzer, A. Ritz, and H. Lüth, *Surf. Sci.*, 1985, **152-153**, 543.
- [64] S. Andersson and J. B. Pendry, *Phys. Rev. Lett.*, 1979, 43, 363.
- [65] G. Benndorf and C. Nöbl, *Surf. Sci.*, 1984, **138**, 292.
- [66] P. R. Mahaffy and M. J. Dignam, *Surf. Sci.*, 1980, **97**, 377.
- [67] H. Chen, D. G. Musaev, and M. C. Lin, *J. Phys. Chem. C.*, 2007, **111**, 17333.
- [68] L. Chen, D. S. Sholl, and J. K. Johnson, *J. Phys. Chem. B.*, 2006, **110**, 1344.
- [69] R. J. A. Grim and J. M. Greenberg, *Astron. Astrophys.*, 1987, **181**, 155.
- [70] J. D. Thrower, M. P. Collings, F. J. M. Rutten and M. R. S. McCoustra, *Mon. Not. R. Astron. Soc.*, 2009, **394**, 1510-1518.
- [71] A. S. Bolina, A. J. Wolff, and W. A. Brown, *J. Phys. Chem. B*, 2005, **109**, 16836.

CHAPTER – 2 Experimental

Contents

2.1 Introduction.....	32
2.2 Experimental.....	36
2.2.1 UHV Chamber (Beam Rig)	36
2.2.1.1 UHV Chamber and Pumping System.....	36
2.2.1.2 Pressure Measurements	39
2.2.1.3 The Molecular Beam Source.....	40
2.2.1.4 Sample Manipulation and Mounting	42
2.2.1.5 Temperature Calibration	44
2.2.2 Experimental Techniques and Instrumentation	46
2.2.2.1 Temperature-programmed Desorption (TPD).....	48
2.2.2.2 Reflection-absorption Infrared Spectroscopy (RAIRS).....	53
2.2.2.3 Electron-stimulated Desorption (ESD).....	59
2.2.3 Sample Preparation	62
2.2.4 Computational Methods	64
2.2.4.1 The Chemical Kinetics Simulator (CKS)	64
2.2.4.2 HyperChem®.....	65
2.2.4.3 SRIM/TRIM	66
2.3 References.....	67

2.1 Introduction

The key requirement for studying the interactions of gaseous materials on solid surfaces through surface science experiments is ultrahigh vacuum (UHV), which is defined as pressure less than 1×10^{-9} torr. Such low pressures ensure not only that a surface will remain clean long enough for the experiments to be carried out, but also that any interference from gas phase scattering during low-energy electron and ion-based experiments will be avoided.

The number of gas molecules impinging on a surface of unit area per second (Z_w) is given by:

$$Z_w = \frac{P}{\sqrt{2\pi m k_B T}} = \frac{P N_A}{\sqrt{2\pi M R T}} \quad (2.1)$$

where P is the pressure, m is the molecular mass in kg, k_B is Boltzmann constant, T is the absolute temperature of the gas in K and N_A is the Avogadro number, M is the molar mass in kg mol⁻¹, and R is the gas constant [1]. Gas pressure is usually defined in units of Pa but in surface science experiments, P is commonly measured in Torr or mbar (1 Torr = 1.3332 mbar = 133.32 Pa). If $P = 4 \times 10^{-4}$ Pa (3×10^{-6} torr) and taking M to be the molar mass of carbon monoxide (CO, 28 g mole⁻¹), and $T = 300$ K, then $Z_w \approx 10^{15}$ molecules cm⁻² s⁻¹. Therefore, if each incident gas molecule sticks on the surface with unit probability, at this pressure, the surface is covered with one monolayer of molecules within a second. It is common in surface science experiments to define the unit of gas exposure as a Langmuir (L) where, 1 L = 10^{-6} Torr s = 1.33×10^{-4} Pa s. Hence, 1 L exposure will cover the surface with a monolayer of adsorbed molecules (a monolayer refers to the density of binding sites on a surface of 10^{15} cm⁻²) assuming unit sticking coefficient. If the UHV conditions are considered, then a solid surface will be entirely covered by an adsorbate layer under a pressure of 1.33×10^{-7} Pa (10^{-9} Torr) within 10^3 s [2]. An additional reduction of pressure to 10^{-10} Torr will raise this time to 10^4 s, such that there is sufficient time to conduct experiments. Various parameters in a vacuum, such as molecular density, n , mean free path, λ , and the time constant to form a monolayer, τ , vary with the pressure:

$$n = \frac{P}{k_B T} \quad (2.2)$$

$$\lambda = \frac{1}{\sqrt{2\pi d^2 n}} \quad (2.3)$$

$$\tau = \frac{n_0}{Z_w} = \frac{n_0 \sqrt{2\pi m k_B T}}{P} \quad (2.4)$$

where d is the diameter of the molecule and the expression πd^2 represents the molecular cross-section n_0 is the number of atoms in a monolayer, and Z_w is the incident flux [3, 4].

Residual gas analysis (RGA) in a vacuum provides a measure of the quality of the vacuum and is conducted by means of a quadrupole mass spectrometer (QMS). This consists of three components: (1) an electron impaction source, which is located on the top of the mass spectrometer; (2) a quadrupole mass filter in the middle consisting of four parallel cylindrical rods to which fixed direct current (DC) and radio frequency (RF) potentials are applied, when the mass spectrometer is operated, and (3) electron multiplier for ion detection at the bottom. Briefly, when the gaseous molecules enter the ion source, they are ionized through impact with electrons emitted from the filament (typically 70 eV electrons are used). Before directing the ions to the detector, they pass through the quadrupole mass filter which selects ions with a particular mass to charge ratio (m/z). Finally, when the ions enter the detector, they strike a metallic cone (Faraday cup) which allows the ion current to be recorded to around the pA-range. Alternatively, a secondary electron multiplier (SEM) or a channeltron multiplier can be used to detect the very low current of ions.

Once high vacuum (HV) has been achieved, by using a combination of rotary and diffusion or turbomolecular pumps, the remaining gas in the UHV chamber is mostly water desorbing from the internal surfaces, rather than N_2 , O_2 or CO_2 from the atmosphere [5].

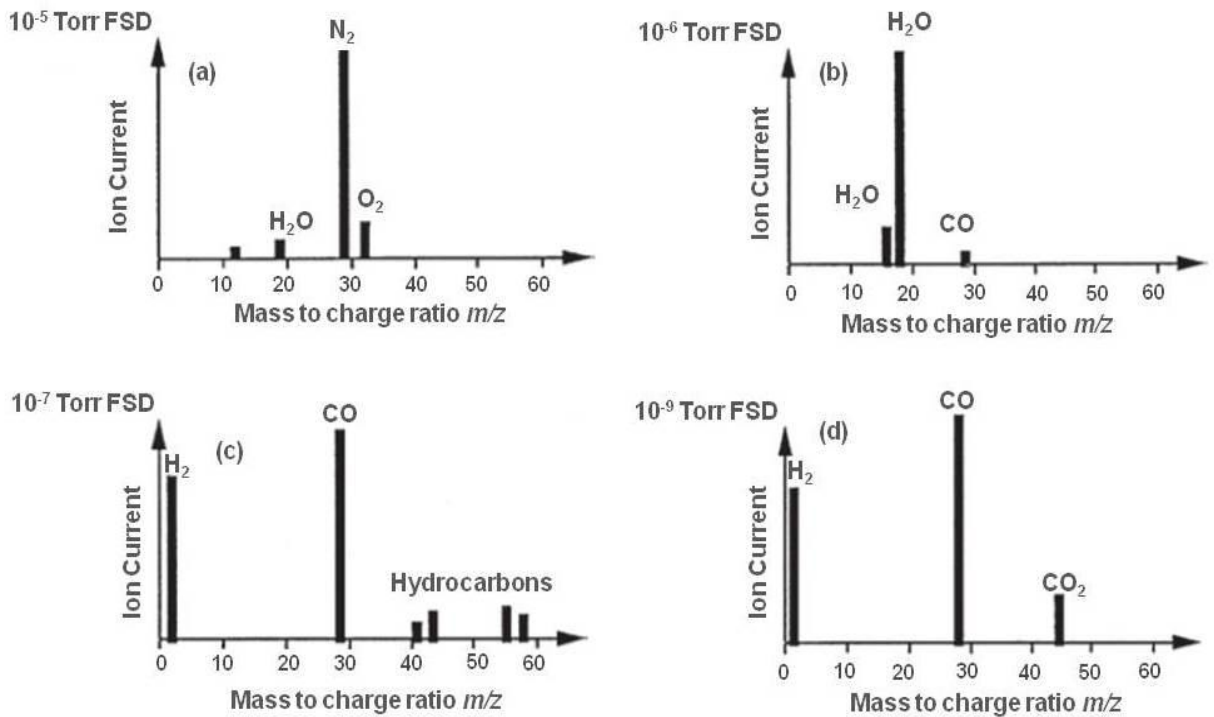


Figure 2.1: Typical mass spectra of the four different stages, a, b, c, and d, from a HV to a UHV system. The ion fragments recorded were positive ions [5].

The vacuum conditions can be described in terms of the gas contents inside the system which can be summarized as:

- a. A high level of mass 32 (O_2) indicates that there is an air leak in the vacuum system (see **Figure 2.1a**).
- b. The presence of a high amount of water (mass 18) in the spectrum shows that the system needs baking (see **Figure 2.1b**).
- c. A high mass of hydrocarbons in the spectrum shows backstreaming of oil vapour from rotary pumps or diffusion pumps; a foreline trap or cold trap should be fitted to prevent this, and should be baked to clean it (see **Figure 2.1c**).
- d. A clean, high vacuum system (see **Figure 2.1d**).

The RGA of the system used in this work shows the chamber components before and after baking. **Figure 2.2a** shows that the major components are H₂O and H₂, which is a clear indication that the system needs to be baked, while **Figure 2.2b** shows that the system is clean for performing the experiments. At this stage, the base pressure of 10⁻¹⁰ Torr is reached in the chamber.

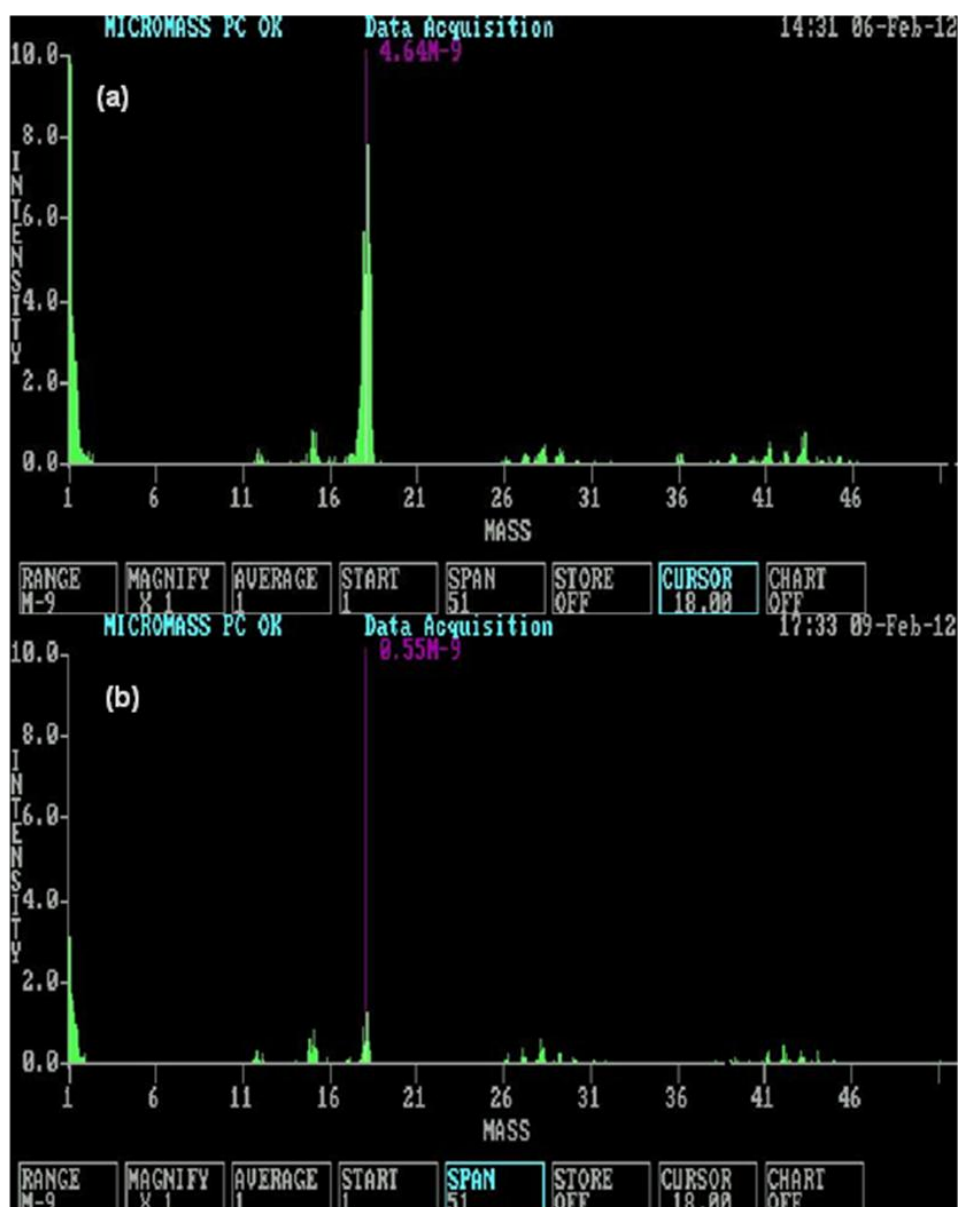


Figure 2.2: Residual gas analysis of the UHV chamber used during this research (a) before and (b) following bakeout at 120 °C for 60 hours. Note that the m/z=3 signal has been cropped from 10.0 counts/s in (ii) to improve clarity. The features labelled in (i) are at m/z=2, 16, 17, 18, 28, and 44 corresponding to H₂, O, OH, H₂O, CO, and CO₂, respectively.

2.2 Experimental

2.2.1 UHV Chamber (Beam Rig)

A detailed description of the UHV Chamber (beam rig) with the system layout can be found in previous PhD theses [6, 7]. Originally, this system was designed to investigate surface processes on metal single crystals, where the surface is exposed to different physical and chemical conditions in order either to modify or to study the chemical and physical behaviour of such surfaces. The system has since been modified to allow its use in solid state and space laboratory astrophysics (see **Figure 2.3**).

2.2.1.1 UHV Chamber and Pumping System

The vacuum chamber is a cylinder with an internal diameter of 40 cm (supplied by Leisk Engineering Ltd.). The chamber and all connected parts are made from stainless steel. Standard conflat flanges are used to attach the demountable parts to the vacuum chamber. These flanges have a knife edge that affords a seal by cutting into an oxygen-free high conductivity (OFHC) copper ring (gasket). The use of copper gaskets instead of rubber permits bakeout at an elevated temperature.

In order to reach the UHV, it is necessary to bake the whole vacuum system. During bakeout, the system is heated to at least 120 °C for 48-60 hours. The heating process accelerates desorption of impurities (mostly H₂O) from the walls of the vacuum chamber. Two types of pumps must be used to achieve UHV conditions: diffusion pumps and mechanical roughing pumps. The diffusion pump is known as one of the oldest and most reliable pumps for generating pressures down to 10⁻¹⁰ torr. In this system, a liquid N₂ trapped, 9" oil diffusion pump (Edwards High Vacuum Ltd, E09.) charged with polyphenyl ether fluid (Santovac 5) is employed. Since the diffusion pump cannot begin its work with full atmospheric pressure inside the chamber, it is backed by a mechanical rotary pump (Edwards High Vacuum Ltd, E2M40) to reduce the pressure to the 10⁻³ torr range. Once UHV is achieved, additional pumping is afforded by a Ti-sublimation pump (Leisk Engineering Ltd.) and an ion pump (Varian VacIon). A schematic representation of the UHV system is shown in **Figure 2.4**.



Figure 2.3: Photograph of the “Beam Rig” experimental setup.

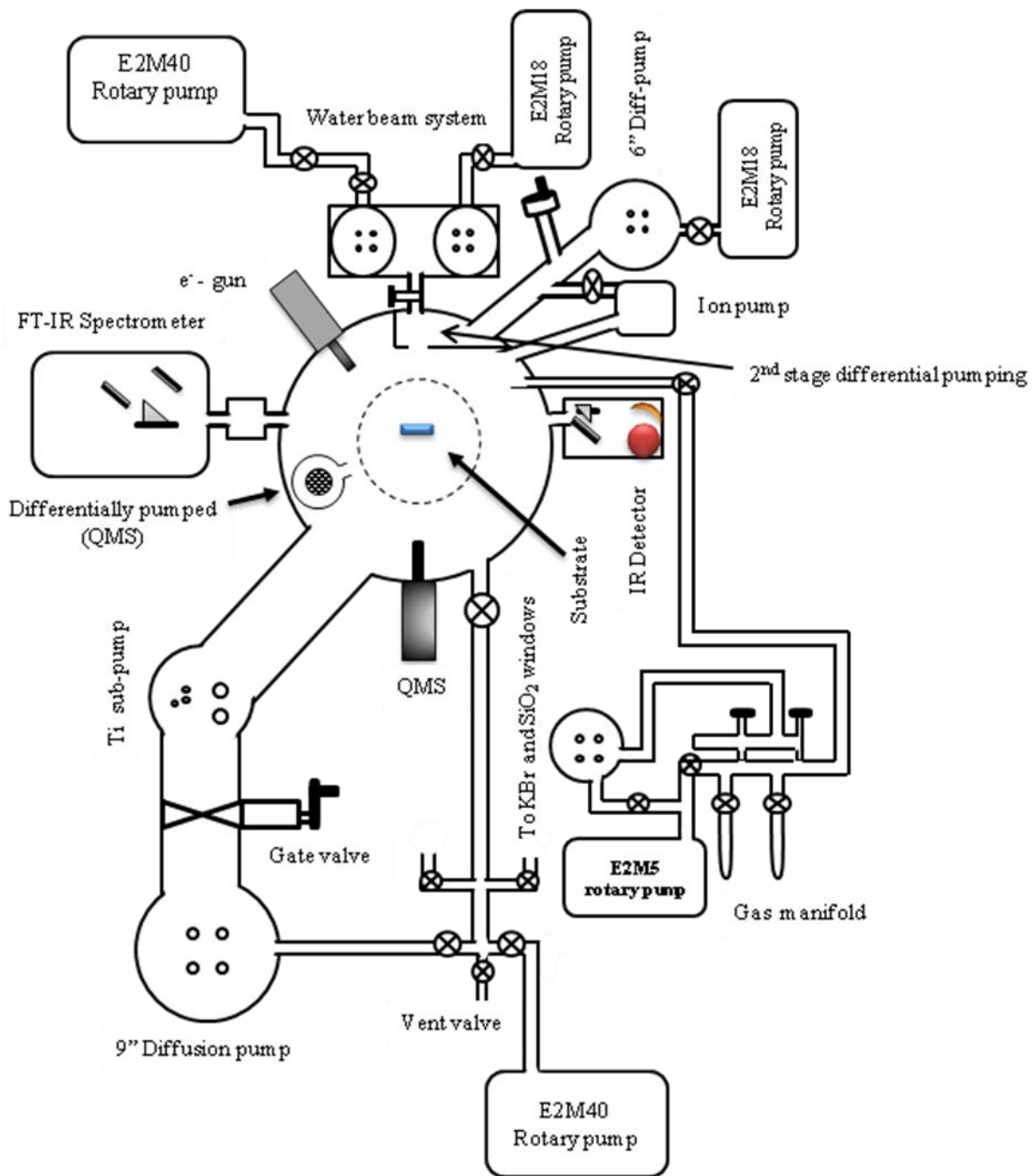


Figure 2.4: Schematic representation of the UHV chamber.

2.2.1.2 Pressure Measurements

In the main UHV chamber, UHV pressures are measured using an uncalibrated twin tungsten filament-Bayard Alpert Gauge (supplied by MDC Vacuum Products, LLC), as shown in **Figure 2.5**. Pirani gauges are used to measure the higher pressures in the backing line. Both pressure gauges are controlled by the main pressure controller box. In the second stage differential pumping section (see **Figure 2.4**), there is a separating stainless steel wall with a variable diameter line-of-sight orifice placed inside the main UHV chamber to accommodate the molecular beam system. This small chamber is pumped by a liquid N₂ trapped, 6" oil diffusion pump (Edwards High Vacuum Ltd, E06), backed by a mechanical rotary pump (Edwards High Vacuum Ltd, E2M18).

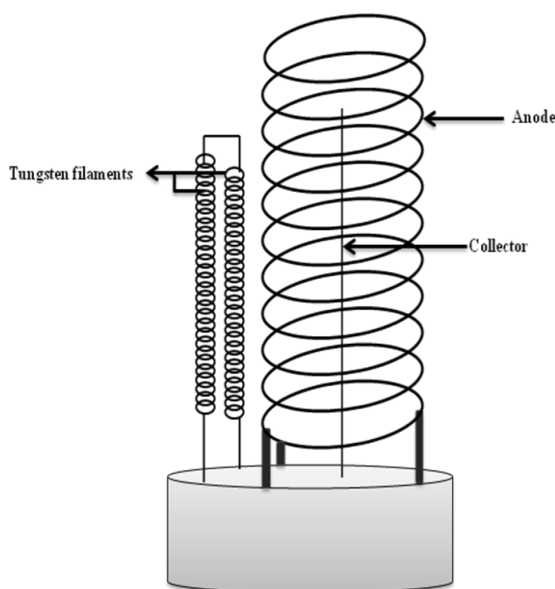


Figure 2.5: Twin tungsten filament-Bayard Alpert gauge (ion gauge).

Although this small chamber does not have a pressure gauge, it is assumed that the pressure is around 1×10^{-9} torr. Under appropriate conditions, after the bakeout procedure, the base pressure in the main UHV chamber is $< 2 \times 10^{-10}$ torr. The pressure during the exposure of the sample to a gas is determined using the ion gauge. This type of gauge emits electrons (with energy of approximately 100 eV) which ionise and/or fragment the surrounding gas-phase molecules. These positively

charged fragments are collected by a grid at negative potential and the ion current collected is used to determine the pressure in the chamber. However, not all species are ionised by electrons with the same efficiency, *i.e.* do not lead to the same number of fragments. The average number of ionic fragments produced by a particular species is given by the “ionisation (or gauge) coefficient”. This coefficient has to be taken into account to avoid any overestimation of the number of molecules present.

2.2.1.3 The Molecular Beam Source

The molecular beam source is the second important part of the UHV system and is used to generate a beam of water vapour which is injected into the main UHV chamber. The molecular beam source is separated from the main chamber with a gate valve (Edwards High Vacuum) and isolated from the bakeout process. The molecular beam assembly itself (see **Figure 2.6**) consists of two chambers: the source chamber and the first differential stage, separated by a 5 mm diameter orifice. This orifice has a mount for the skimmer. In order to align the water beam with the substrate in the main UHV chamber, the orifice can be translated by two linear drivers.

The source chamber was pumped by a 9” oil diffusion pump (Edwards High Vacuum Ltd, E09) charged with silicone fluid (Dow Corning DC-704) and backed by a mechanical rotary pump (Edwards High Vacuum Ltd, E2M40), supported by a mechanical booster (Edwards High Vacuum EH250). The use of a mechanical booster provides efficient pumping during operation of the molecular beam system. For the first differential chamber, a 6” oil diffusion pump (Edwards High Vacuum Ltd, E09) charged with silicone fluid (Dow Corning DC-704) was employed. The 6” diffusion pump is backed by a mechanical rotary pump (Edwards High Vacuum Ltd, E2M18). The pressures in these chambers were measured by Penning gauges (Edwards High Vacuum CP25-K), and the backing pressures are measured by Pirani gauges (Edwards High Vacuum Ltd, PRL10). All pressure gauges are controlled by means of two Edwards High Vacuum Pirani Penning 1005 controllers. Typically, the high vacuum region of the first differential chamber and source chamber reaches a pressure of 10^{-7} mbar.

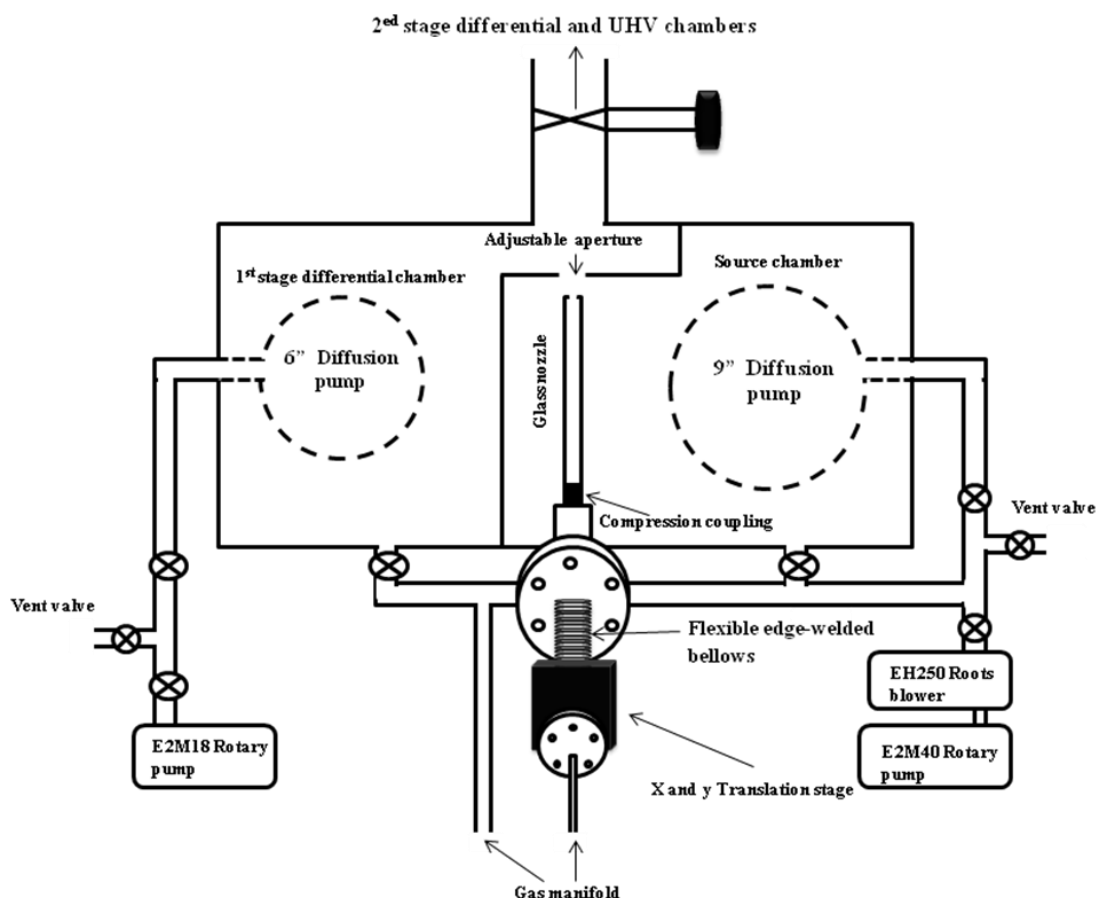


Figure 2.6: Schematic of the molecular beam source in the UHV chamber.

During operation of the molecular beam, the pressure of the source is increased up to 2×10^{-4} mbar, while operating the mechanical booster pump and controlling the beam through the valve of the water source. The beam source itself is a glass nozzle mounted on a xy translation stage which allows alignment of the beam with the other orifices in system. **Figure 2.7** displays a sketch of the glass nozzle, which consists of a 6 mm diameter quartz glass tube with a hole approximately 0.5 mm in diameter. The glass nozzle is fitted with a tungsten coil, which can be resistively heated to a temperature below 700 K. The molecular beam source is equipped with a chopper (Chopper 100, supplied by Human Machine Interface Ltd.) which consists of a rotating circular blade. This can be used to produce pulses of gas at the surface under investigation, but was not employed in this work.

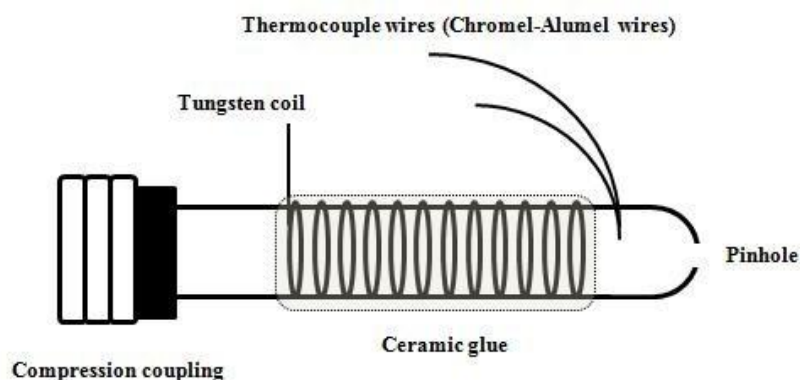


Figure 2.7: Glass nozzle through which the H₂O beam passes.

2.2.1.4 Sample Manipulation and Mounting

The substrate onto which the ices studied are deposited is a polished stainless steel disc (10 mm diameter) coated with a layer of amorphous silica (SiO₂), of about 200 nm SiO₂ thickness is deposited onto the stainless steel surface *via* electron beam evaporation. The use of amorphous silica to mimic the interstellar dust is because there is spectroscopic evidence for silica and silicates as a component in interstellar dust. The choice of thickness of silica to be deposited is to ensure complete coverage of the metallic substrate, hence avoiding problems with processes on or promoted by the metal substrate. The substrate is mounted on the end of a rotatable manipulator (see **Figure 2.8**), which can be moved along the x, y, and z axes, and rotated through 360°. The substrate is heated through Ta-wires that are spot-welded to 0.075 nickel foil, which is wrapped and spot-welded to 2 mm diameter molybdenum rods (see **Figure 2.9**). The presence of a sapphire insulator in the copper assembly holding the molybdenum rods provides electrical insulation, ensuring that the high current (up to 40 A) will pass only through the rods in order to heat the Ta-wires resistively and consequently heat the substrate. The substrate temperature is measured by a K-type thermocouple, in which the wires are composed of chromel and alumel; the chromel wire consists of 90% Ni, 10% Cr, and alumel consists of 95% Ni, 2% Mn, 2% Al, and 1% Si. The temperature is read on a temperature controller (Eurotherm, model 2404).

The upper part of the manipulator contains the re-entrant, which is filled with liquid nitrogen to cool the substrate. The feedthrough for the K-type thermocouple on the

sample is located on the same level as the re-entrant. Two heating power circuit feedthroughs with ceramic insulation are connected to a high current controller in order to heat the substrate.

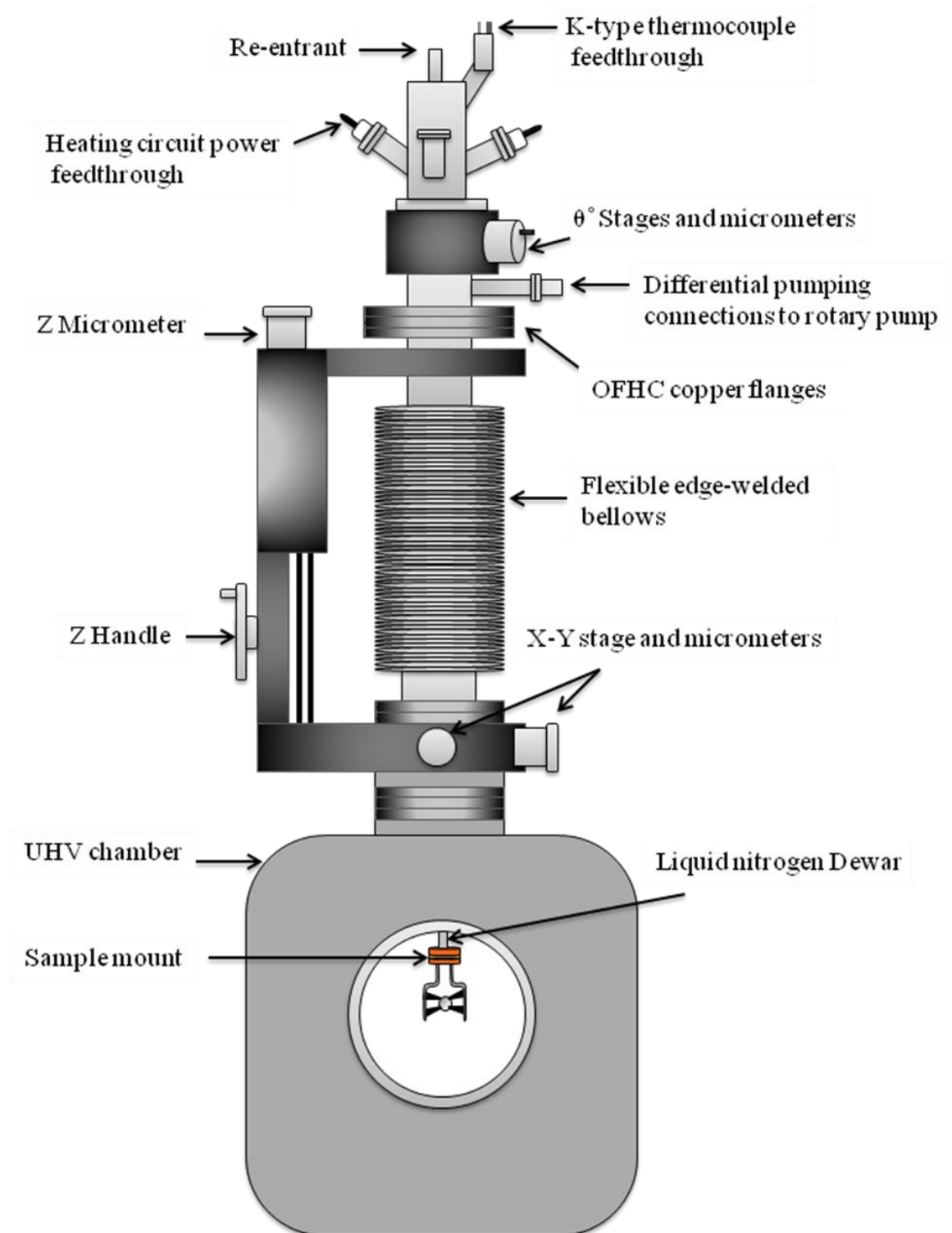


Figure 2.8: Schematic of substrate manipulation and mounting.

Both the thermocouple re-entrant wires and power cables are insulated by glass fibre sleeving and then wrapped around the liquid nitrogen Dewar. The electrical components and the re-entrant are mounted on a differentially pumped rotatable seal, to provide for sample rotation in vacuum.

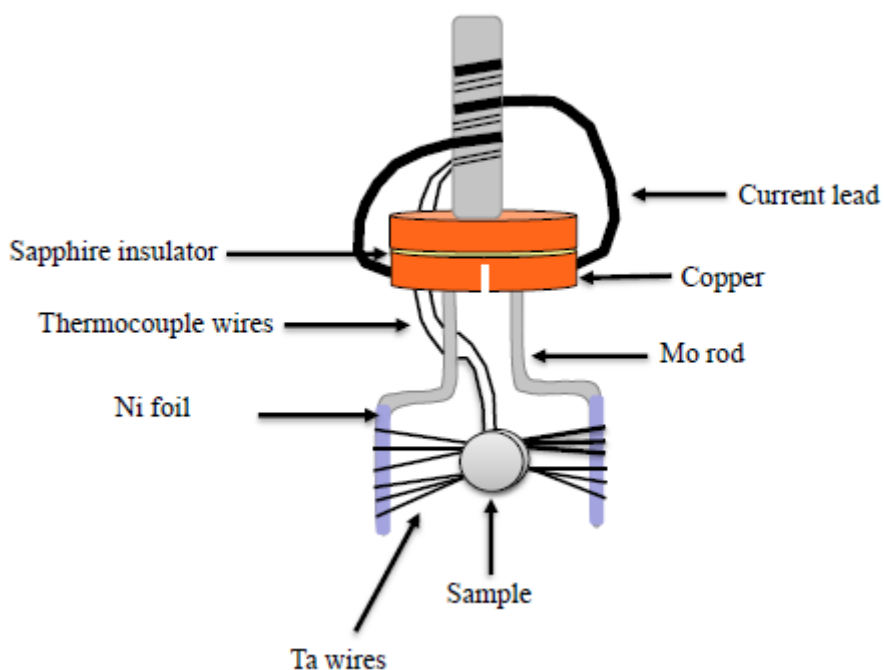


Figure 2.9: Schematic drawing of substrate mounting.

2.2.1.5 Temperature Calibration

The raw TPD data obtained from the QMSTM software lack a temperature reading. However, the QMS software records the voltage of the K-type thermocouple wires as a function of the ion signal for fragments being monitored during TPD experiments. Due to the variation of the electrical resistance between the thick copper wires and the thin tantalum wires, the latter can be heated easily as the current passes through them. The substrate temperature also increases. This heating is performed using a power supply (Farnell Type H60/50), which provides current up to 50 A. The current from the power supply is controlled using a temperature controller (Eurotherm, model 2404). The controller was able to maintain the temperature with set-points down to 123.15 K (-150 °C). This was interfaced to both the power supply and the K-

type thermocouple spot-welded to the edge of the substrate. These arrangements ensured that a reasonable linear heating ramp of 0.1 K s^{-1} could be achieved for TPD experiments. The QMS possesses an auxiliary input channel that can record voltages in the range of 0-10 V.

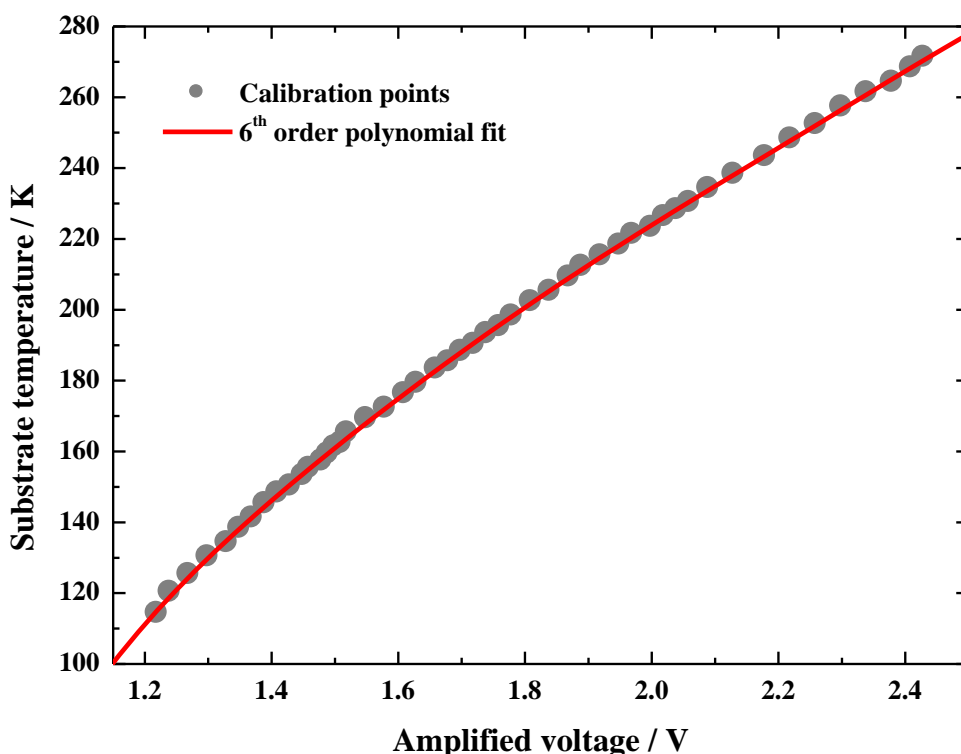


Figure 2.10: Temperature calibration curve for the K-type thermocouple on the beam rig.

An electromotive force (emf) of a few millivolts is generated by a K-type thermocouple with 0 V at 0 °C. This amplifies the raw thermocouple voltage and offsets it sufficiently. In addition, it shows that the region of interest is also within the 0-10 V limits, to be consistent with the QMS. Amplification was achieved using a homemade device which consists of an integrated circuit (Analog Devices AD595) that is offset by +2.5 V *via* a voltage reference integrated circuit (Analog Devices AD680JTZ). Before commencing the calibration procedure, the substrate was cooled down to a base temperature of 114.15 K, using liquid nitrogen. The voltage of the raw thermocouple was then recorded at this base temperature. The voltages measured at the feedthrough are not exact values but have to be corrected with the standard K-type thermocouple chart. The calibration procedure was then performed at a heating

rate of 0.1 K s^{-1} to 271.15 K and the raw thermocouple voltage was also recorded and corrected. The voltage in the QMS was also recorded during the heating. All the data of this calibration, the corrected temperature and the voltage recorded by the QMS software were imported into Origin and fitted with a 6th order polynomial curve, using a nonlinear least-squares fitting routine [8]. **Figure 2.10** shows the calibration curve and the associated polynomial coefficients are listed in **Table 2.1**.

Table 2.1: Coefficients for 6th order polynomial calibration curve of the K-type thermocouple.

Coefficient for polynomial $AV^6 + BV^5 + CV^4 + DV^3 + EV^2 + FV + G$	Coefficient value
A	-71.3 K V^{-6}
B	808.9 K V^{-5}
C	-3785.3 K V^{-4}
D	9377.3 K V^{-3}
E	$-13022.5 \text{ K V}^{-2}$
F	9791.3 K V^{-1}
G	-3040.4 K

2.2.2 Experimental Techniques and Instrumentation

For the laboratory astrochemistry investigations, a number of instruments are attached to the UHV chamber to provide for surface experimental techniques. All experiments are performed in the centre of the main UHV chamber. This chamber is equipped with two leak valves, from which gases are dosed from the gas manifold system into the chamber. **Figure 2.11** shows a schematic representation of the full experimental set up of the UHV chamber. The infrared studies are conducted using the RAIRS technique, in which an external mercury cadmium telluride (MCT) detector is used to detect an IR beam reflected on the substrate. IR windows are used; KBr is purged with dry air (CO_2 free). The fourier transform infrared (FT-IR) spectrometer used is a Nicolet spectrometer (Nexus 870 FT-IR) which has an

external IR beam port on the right side, through which the IR beam is directed to the substrate surface in the main UHV chamber at an angle of 6° to the plane of the surface, using a combination of a plane and a parabolic mirror, and the reflected beam is directed to the optics housing, in which a combination of a plane, a parabolic and an ellipsoidal mirror finally direct the IR beam to the MTC detector.

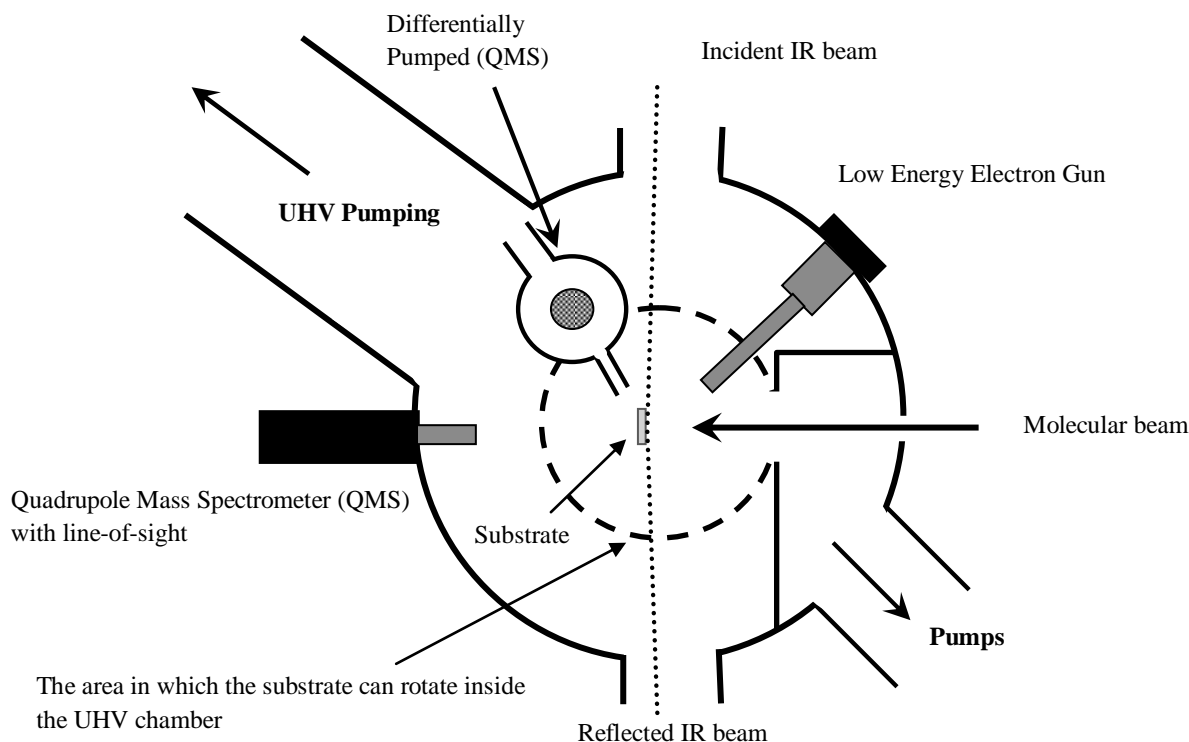


Figure 2.11: Schematic representation of the UHV chamber with the TPD and RAIRS experimental setup. The substrate faces the QMS equipped with line-of-sight, by which the only molecules desorbing from the substrate are recorded.

The main UHV chamber has a QMS (QMS; VG Microtech PC300D), which is placed at the bottom of the chamber and mounted on a rotatable motor within 130° of θ . The mass spectrometer itself is equipped with a cross-beam source that provides line-of-sight of the substrate during the experiments. Changing the substrate position to face the source line-of-sight ensures that only the molecules desorbing from the substrate are measured. The QMS is a modified VG Microtech PC300D and uses a single channel electron multiplier (SEM) detector. An ELG-2 electron gun and its EGPS-1022 power supply (Kimball Physics) are also attached to the UHV chamber.

These are used in electron-stimulated desorption (ESD) experiments, where low energy electrons induce desorption of molecules at astrophysically relevant temperatures.

2.2.2.1 Temperature-programmed Desorption (TPD)

TPD has been increasingly used as a technique to determine both the kinetics and thermodynamics of desorption processes or decomposition reactions of molecules adsorbed on surfaces. The TPD experiments are usually conducted in three steps:

1. Adsorption of one or several gaseous species on the surface at low temperature;
2. Desorption of the adsorbed species by heating the sample in a controlled manner [usually using a linear temperature ramp, β , where the temperature, T , as function of time, t , is given by $T(t) = T_0 + \beta t$, where T_0 is the sample temperature at the beginning of the TPD experiment];
3. Monitoring of the molecules released in the gas phase with a QMS as shown in **Figure 2.12**.

The rate of desorption (r_{des}) of molecules desorbing from the surface is expressed mathematically as:

$$r_{des} = -\frac{d\Theta}{dt} = k_m \Theta^m \quad (2.5)$$

where Θ is the surface coverage, k_m is the rate constant of the desorption reaction, and m is the reaction order. The rate constant can be described with an Arrhenius equation:

$$k_m = \nu \exp\left(\frac{-E_{des}}{RT}\right) \quad (2.6)$$

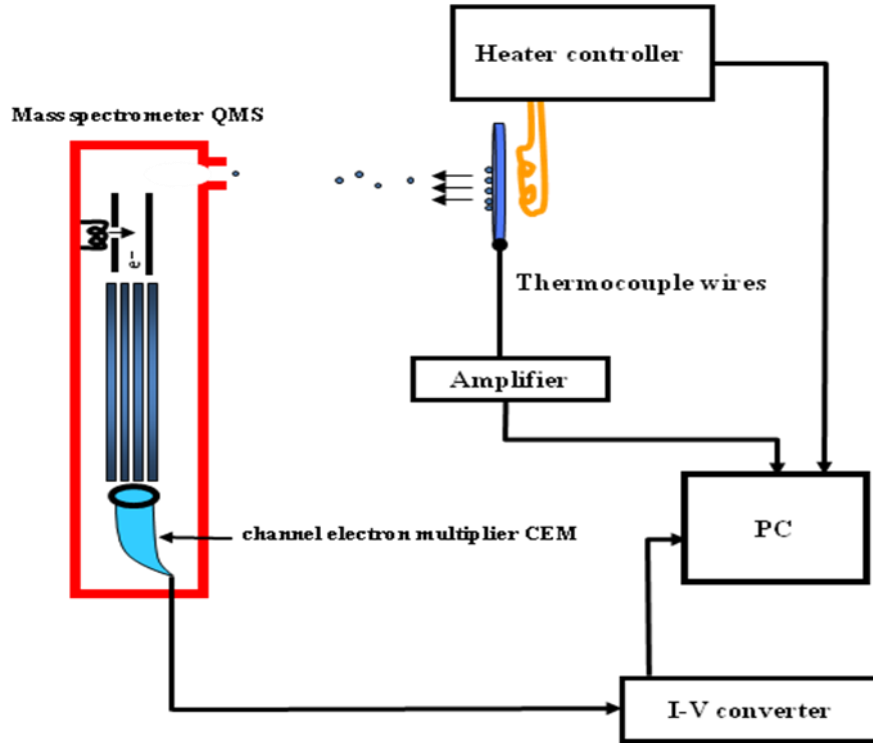


Figure 2.12: Schematic drawing of TPD experimental setup.

where ν is the pre-exponential factor, E_{des} is the desorption energy, R is the gas constant, and T is the absolute temperature. In chemical kinetics, **equation (2.6)** shows that ν and E_{des} cannot be functions of Θ , whereas in surface science, **equation (2.6)** is only applied for zero-order desorption kinetics. The surface binding energy in astrophysics is described as E_{des}/k_B , in units of K [9, 10]. By substituting **equation (2.6)** into **equation (2.5)**, the rate of desorption is given by the Polanyi-Wigner **equation (2.7)**:

$$r_{des} = -\frac{d\Theta}{dt} = \Theta^m \nu \exp\left(\frac{-E_{des}}{RT}\right) \quad (2.7)$$

Assuming that the sample temperature increases linearly:

$$T = T_0 + \beta t, \quad (2.8)$$

one obtains **equation (2.9)**:

$$\frac{d\Theta}{dT} = \frac{1}{\beta} \frac{d\Theta}{dt} = -\frac{k_m \Theta^m}{\beta} \quad (2.9)$$

At $T=T_p$ (maximum desorption peak), then $\frac{d^2\Theta}{dT^2} = 0$. By differentiating **equation (2.9)** with respect to T :

$$\frac{d^2\Theta}{dT^2} = -\frac{1}{\beta} \frac{dk}{dT} \Theta^m - \frac{k_m \Theta^{m-1}}{\beta} \frac{d\Theta}{dT} \quad (2.10)$$

and substituting k_m by **equation (2.10)** at $T=T_p$, then the general equation for any order is:

$$\frac{E_{des}}{RT_p^2} = \frac{\nu}{\beta} m \Theta^{m-1} \exp\left(\frac{-E_{des}}{RT_p}\right) \quad (2.11)$$

The first order desorption ($n=1$) then follows:

$$\frac{E_{des}}{RT_p^2} = \frac{\nu}{\beta} \exp\left(\frac{-E_{des}}{RT_p}\right) \quad (2.12)$$

The above equation implies that T_p is independent of the surface coverage Θ , and if ν is known, it is then possible to calculate E_{des} . If ν/β in **equation (2.12)** is assumed to be between $10^8 - 10^{13} \text{ K}^{-1}$ ($m=1$), then the relationship between desorption energy E_{des} and the temperature of the peak maximum T_p is given by [11]:

$$\frac{E_{des}}{RT_p} = \ln \frac{T_p \nu}{\beta} - 3.64 \quad (2.13)$$

This is the classic Redhead equation. For a first-order desorption reaction, the above equation can be used to determine E_{des} from a single TPD trace, assuming that ν is 10^{13} s^{-1} .

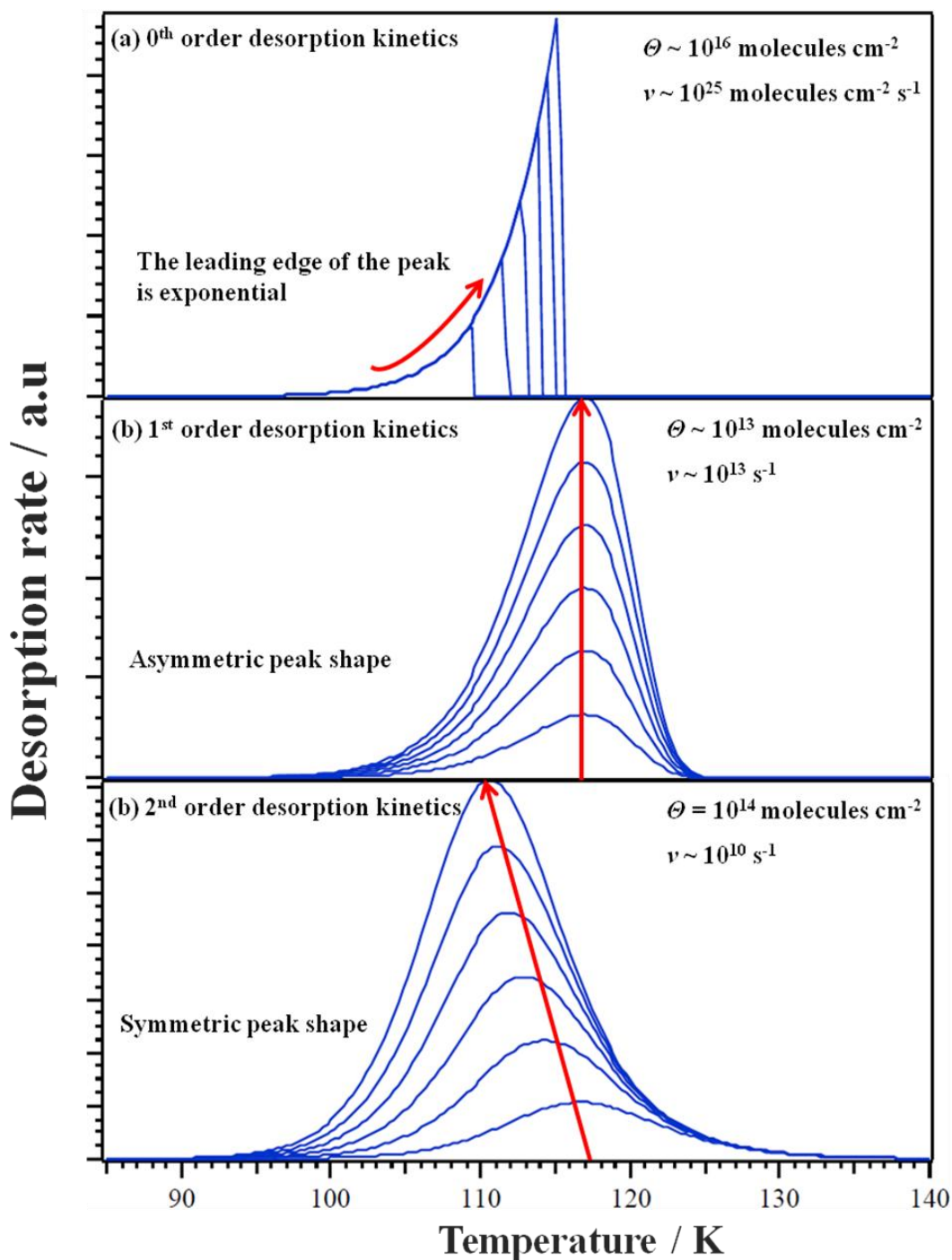


Figure 2.13: The shape of desorption traces for zero, first, and second desorption order [12].

From the analysis of the TPD spectra, the following information can be obtained:

- i) The desorption order: an empirical parameter central to the kinetics of desorption. Zero order desorption kinetics imply that desorption rate is coverage-independent, and all peaks have a common leading edge; this is characteristic of desorption of solids in the multilayer regime. First order desorption is characterised by a desorption rate proportional to the coverage, leading to traces having their maximum of desorption at the same temperature; desorption of sub-monolayer solids usually follows this behaviour. Second order desorption traces exhibit coincident trailing edges and are characteristic of recombinative desorption (see **Figure 2.13**).
- ii) The desorption energy: this parameter describes the adsorbate-surface (in the sub-monolayer regime) or adsorbate-adsorbate (in the multilayer regime) interactions, and can be calculated from **equation (2.12)**.
- iii) The state of adsorbed species can be known from the features of the TPD spectra, where a single peak refers to single adsorbate, whereas mixing different molecules in the bulk of the sample leads to desorption of the adsorbed species from the surface at different temperatures.

For desorption spectra with peaks having a common leading edge, the Habenschaden-Küppers (HK) or leading edge analysis (LEA) allows estimation of coverage- and temperature-dependent activation parameters (*i.e.* E_{des} and ν) [13]. It is argued in this analysis that, at the beginning of desorption, a small amount of species desorbs and so the surface concentration is really constant. According to the logarithmic form of the Polanyi-Wigner **equation (2.7)**, at kinetic order = 0:

$$\ln r_{des} = \ln \left(\frac{d\Theta}{dt} \right) = \ln \nu - \frac{E_{des}}{RT} \quad (2.14)$$

and so an Arrhenius plot of $\ln(d\Theta/dt)$ versus $1/T$ yields a straight line with slope $-E_{des}/R$ and the intercept is $\ln(\nu)$, from which E_{des} and ν are determined respectively. Additionally, computational methods, such as the Chemical Kinetics Simulator

(CKS), allow the use of kinetic modelling of the desorption process, in order to predict both desorption energy (E_{des}) and the pre-exponential factor (ν).

2.2.2.2 Reflection-absorption Infrared Spectroscopy (RAIRS)

Vibrational spectroscopies such as infrared (IR) and Raman spectroscopies are very powerful tools for studying the chemical composition of materials. They provide information on the molecular structure of the molecules resulting from the adsorption of a gas onto a surface. Fundamentally, a molecule with N atoms has $3N$ degrees of freedom for translation, along three axes (x , y , and z), rotations and vibrations. Thus, the molecules in the gas phase are distinguished by their vibrations, which are $3N-5$ for linear molecules or $3N-6$ for non-linear molecules [14]. However, for molecules in the solid phase, translational and rotational degrees of freedom are very weak and then are converted into vibrational degrees of freedom. Therefore, molecules in the solid phase have $3N$ degrees of freedom.

In general, the classical vibrational frequency of a diatomic molecule, the frequency, ν is given by **equation (2.15)**:

$$\nu = \frac{1}{2\pi} \sqrt{\frac{k}{\mu}} \quad (2.15)$$

where k is the chemical bond force constant, in dynes cm^{-1} and μ is the reduced mass [$m_1 m_2 / (m_1 + m_2)$], where m_1 and m_2 are the masses of atom 1 and atom 2 in kg. **Equation (2.15)** can also be used for polyatomic molecules, in the following form:

$$\nu = \frac{1}{2\pi} \sqrt{\frac{k}{m}} \quad (2.16)$$

For a chemical species to be observable in the IR, it needs to undergo a change in dipole moment during the vibrational cycle; homonuclear diatomic molecules are not observable in the IR, with exception of molecules in the solid phase because solid surfaces reduce the symmetry of these molecules and hence, the electron density for these will be smaller, which makes them IR active. However, most other molecules

are IR active. The principle of FT-IR spectroscopy is based on that of the Michelson interferometer shown in **Figure 2.14**. Firstly, the white light from the source is focused by Lens 1 and separated by the beam splitter into reflected and transmitted beams. The reflected light is focused onto the detector, after reflection from the stationary mirror (Mirror 1), whereas the transmitted light is focused by the mobile mirror (Mirror 2) and then split by the beam splitter and focused by Lens 2 onto the detector. The intensity $I(x)$ of both beams depends on the position x of the mobile mirror. Assuming that the incident light is a monochromatic wave, one can express its associated electric field, E :

$$E(x,t) = E_0 \cos(kx - \omega t) \quad (2.17)$$

The electric field reaching the detector is given by:

$$E_D = \frac{1}{2} \{ E_0 \cos(k_0 x - \omega_0 t) + E_0 \cos[k_0(x + 2\Delta x) - \omega_0 t] \} \quad (2.18)$$

where $2\Delta x$ is the difference between two optical paths from the beam splitter. Assuming that $x = 0$ and substituting both of $2\Delta x$ by $2x$ and k_0 by $2\nu_0\pi$, the following equation is obtained:

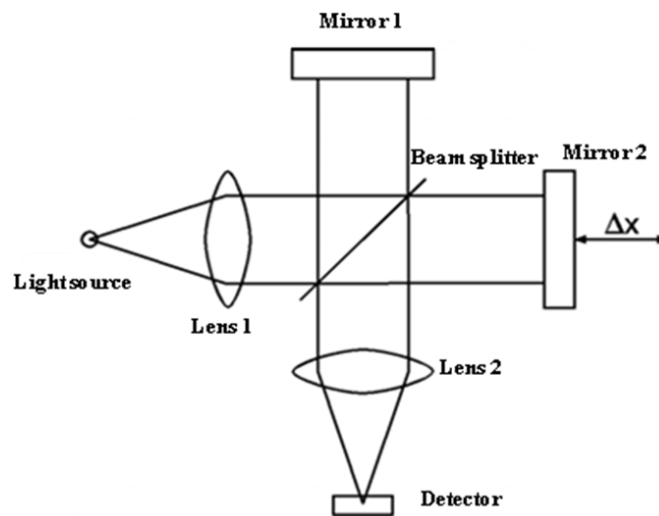


Figure 2.14: The optical path in a Michelson interferometer in the FTIR spectrometer.

$$I(x) = c_0 \varepsilon_0 (E^2) = \frac{c_0 \varepsilon_0}{4} E_0^2 [1 + \cos(4\pi\nu_0 x)] \quad (2.19)$$

This equation can be rewritten using the spectral intensity $I(\nu) = \varepsilon_0 c_0 E_0^2 \delta(\nu - \nu_0)/2$ to yield

$$I(x) = \frac{1}{2} \int_0^\infty I(\nu) [1 + \cos(4\pi\nu x)] d\nu \quad (2.20)$$

From this equation, the basic relationship for FT-IR spectroscopy can be derived:

$$I'(x) = I(x) - \frac{1}{2} \int_0^\infty I(\nu) d\nu = \frac{1}{2} \int_0^\infty I(\nu) \cos(4\pi\nu x) d\nu \quad (2.21)$$

where the interferogram function $I'(x)$ or $I(x)$ provides complete information about the spectrum $I(\nu)$ [15]. FT-IR spectroscopy has two significant advantages:

- i- Recording spectra with higher signal-to-noise as a dispersive instrument in much shorter time (the Jacquinot advantage), the energy throughput in an interferometer can be higher than a dispersive spectrometer, where it is restricted by the slits.
- ii- Recording spectra with higher signal-to-noise ratio for the same measurement time (the Fellgett advantage), and
- iii- Recording spectra with higher accuracy in frequency measurements. This is known as the Connes advantage. This is obtained by comparison with visible laser output, usually from a He-Ne laser.

Investigation of materials using IR spectroscopy is performed *via* two methods or modes; transmission or reflectance mode. In transmission mode; the IR beam transmits through the material to the IR detector. If I_0 represents the intensity of the incident IR beam, and I the intensity after transmitted by the material with c concentration with l path length, then the transmittance (T) is given by **equation (2.22)**:

$$T = \frac{I}{I_0} = \exp(-kcl) \quad (2.22)$$

where k is the absorption coefficient, which is the imaginary part of the refractive index of the medium, n , where

$$\mathbf{n} = n + ik \quad (2.23)$$

and the refractive index $n=n$ in a non-absorbing or dielectric medium. However, **equation (2.22)** shows that the transmittance is inverse exponential in concentration. Therefore, a linear form of **equation (2.22)** can be obtained by taking the logarithm to base 10:

$$\log_{10}\left(\frac{I}{I_0}\right) = -\epsilon cl \quad (2.24)$$

where ϵ is a constant known as the extinction coefficient ($\epsilon=k/\ln 10$). Although transmittance infrared spectroscopy (TIR) provides reliable information concerning the chemical composition of the materials, it has two limitations: (1) there is large bulk absorption, unless the sample is very thin, and (2) there are many samples of interest that are not sufficiently transparent to IR light. In these cases, the reflectance mode is useful and has many applications both in routine and surface research analysis. Reflection and refraction absorption are all related through Maxwell's equations for electromagnetic radiation for interfaces of different n . **Figure 2.15** shows the relationship between reflection and refraction angles, which is given by Snell:

$$\frac{n_2}{n_1} = \frac{\sin \theta_1}{\sin \theta_2} \quad (2.25)$$

where n_1 and n_2 are the refractive indices of the two media forming the interface. From **Figure 2.15**, the plane containing the incident and reflected rays is called the plane of incidence. Two extreme cases of incidence angle can be seen:

- 1- Near normal incidence ($\theta \approx 0^\circ$). This is commonly used for studying very thick films on reflective surfaces (*e.g.* metals) in a double-pass transmission experiment.
- 2- Grazing incidence ($\theta \approx 75 - 85^\circ$). This is most often used for very thin films on reflective surfaces and is known as reflection-absorption infrared spectroscopy (RAIRS).

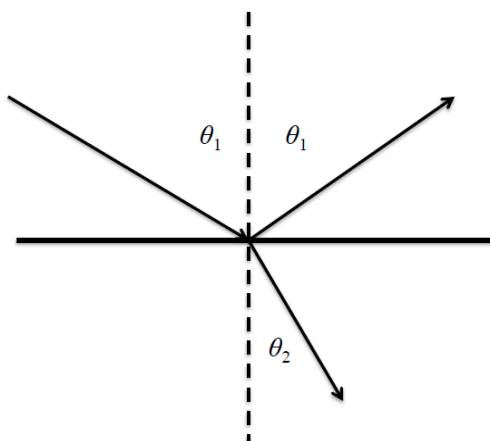


Figure 2.15: The relationship between reflection and refraction.

In reflection-absorption infrared spectroscopy (RAIRS), the IR beam reflects from the front face of a highly reflective surface, such as that of a metal single crystal surface. In principle, a grazing-incidence reflection of the IR light can improve the sensitivity of RAIRS measurements of thin films to sub-monolayer coverages deposited on the metal surface. The intensity of the reflected IR light depends on the orientation of the electric field of the IR radiation ports and of the molecules that lie on the surface. Although the s-polarised IR beam interrogates only the component of the vibrational modes parallel to the surface, it is eliminated by reflection at the grazing incidence. In contrast, the p-polarised IR beam, which interrogates the component of the vibrational modes perpendicular to the surface, is doubled in intensity: see **Figure 2.16**. The selection rules of the reflection of an IR light beam on a metallic surface show that only the vibration modes absorbing radiation polarised perpendicularly to the surface are IR active and allow observation of an absorption band. Consequently, the p-polarised component of the IR radiation is reflected from the surface at high incidence angles, and hence enhances the intensity of the vibrational modes [5, 14-16].

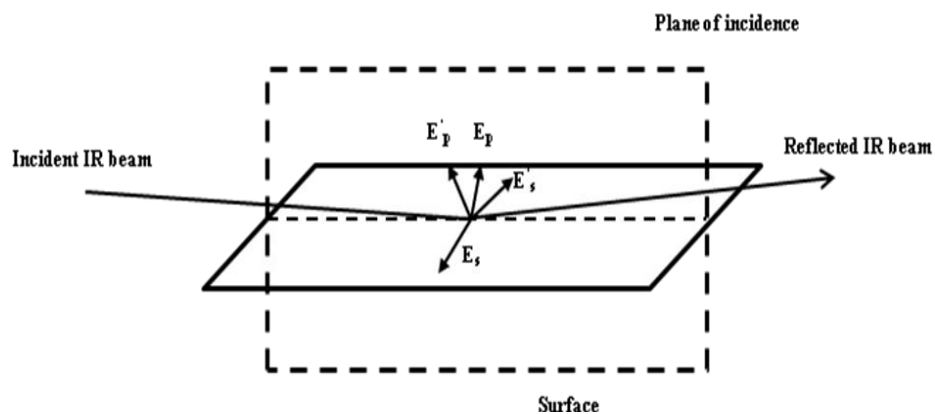


Figure 2.16: Schematic representation of the reflected IR beam with the parallel and perpendicular components of the electric field.

The absorbance (A) of the reflected IR beam can be calculated from the following equation:

$$A = \log_{10} \left(\frac{\Delta R}{R_0} \right) = -\log_{10} \left(\frac{I_S}{I_B} \right) \quad (2.26)$$

where $\log_{10} (\Delta R/R_0)$ is the intensity spectrum on a scale of fractional absorbance, I_S and I_B are the intensities of the reflected IR from the sample and the background spectra, respectively. **Figure 2.17** shows the full arrangement in the RAIRS experiments.

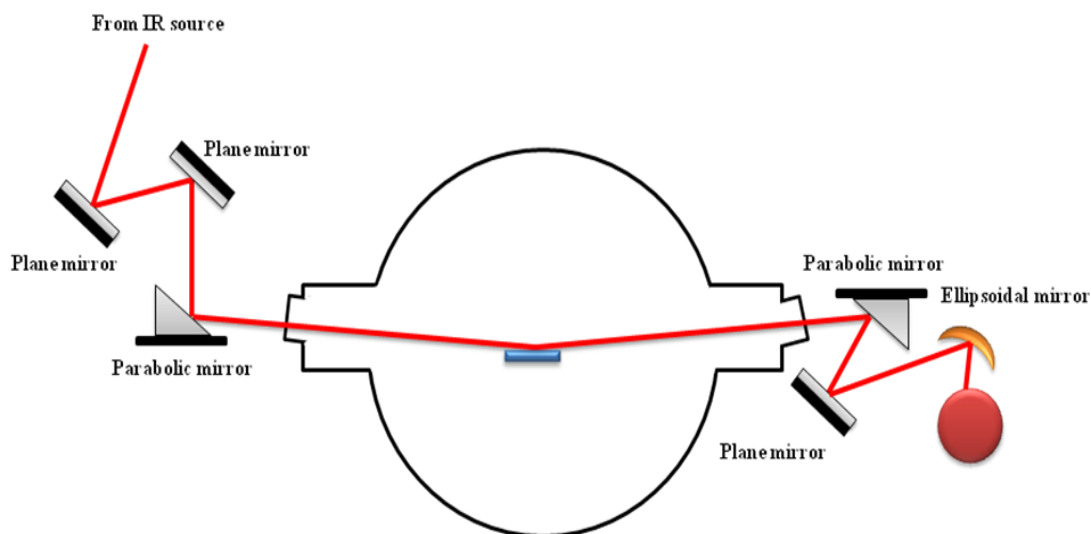


Figure 2.17: Schematic drawing of the UHV chamber with the RAIRS experimental setup of the beam rig.

2.2.2.3 *Electron-stimulated Desorption (ESD)*

This technique is one of the most sensitive used to study desorption processes. It is used to probe a wide range of surface systems and provides a wealth of information, including the nature of intermolecular forces, the bonding geometry and the thermodynamics of the adsorbed species. In the ESD technique, the adsorbed species desorb at low temperatures, using low energy electron collisions (< 500 eV) to excite the adsorbate species. The excited species can be converted to either neutral or positively or negatively charged species. The basis of this technique is that the use of electrons will modify the adsorbed species by breaking the molecular bonds to produce neutral or charged fragments, which can then be monitored by the mass spectrometer after they desorb. This non-thermal desorption process is crucial for understanding the mechanisms and dynamics of electron impact effects on the molecular layers condensed on the surface. A number of mechanisms have been used to describe ESD, but the most well-known is the Menzel-Gomer-Redhead (MGR) model (see **Figure 2.18**).

According to the MGR model, low energy electron impact induces desorption by exciting or ionising the adsorbed species (M-A) from the ground state to some excited state *via* Frank-Condon transitions [17-19]. For relatively stable species, the excited molecules will relax by releasing the excess energy through desorption from the surface. **Figure 2.18** shows the mechanisms by which desorption can occur. In **Figure 2.18a**, relaxation occurs *via* ionic desorption. The ion leaving the surface with the ion energy distribution indicated in **Figure 2.18a**. In **Figure 2.18b**, relaxation to the ground potential energy surface occurs and desorption of neutral species with the kinetic energy distribution results. Therefore, the mechanism by which ESD occurs is non-thermal desorption. However, the MGR model is applicable only to molecules adsorbed on metal surfaces. For non-metal surfaces, for example, the silica overlayers on the metal substrate in this work, simple electronic excitation and dissociative electron attachment are more important.

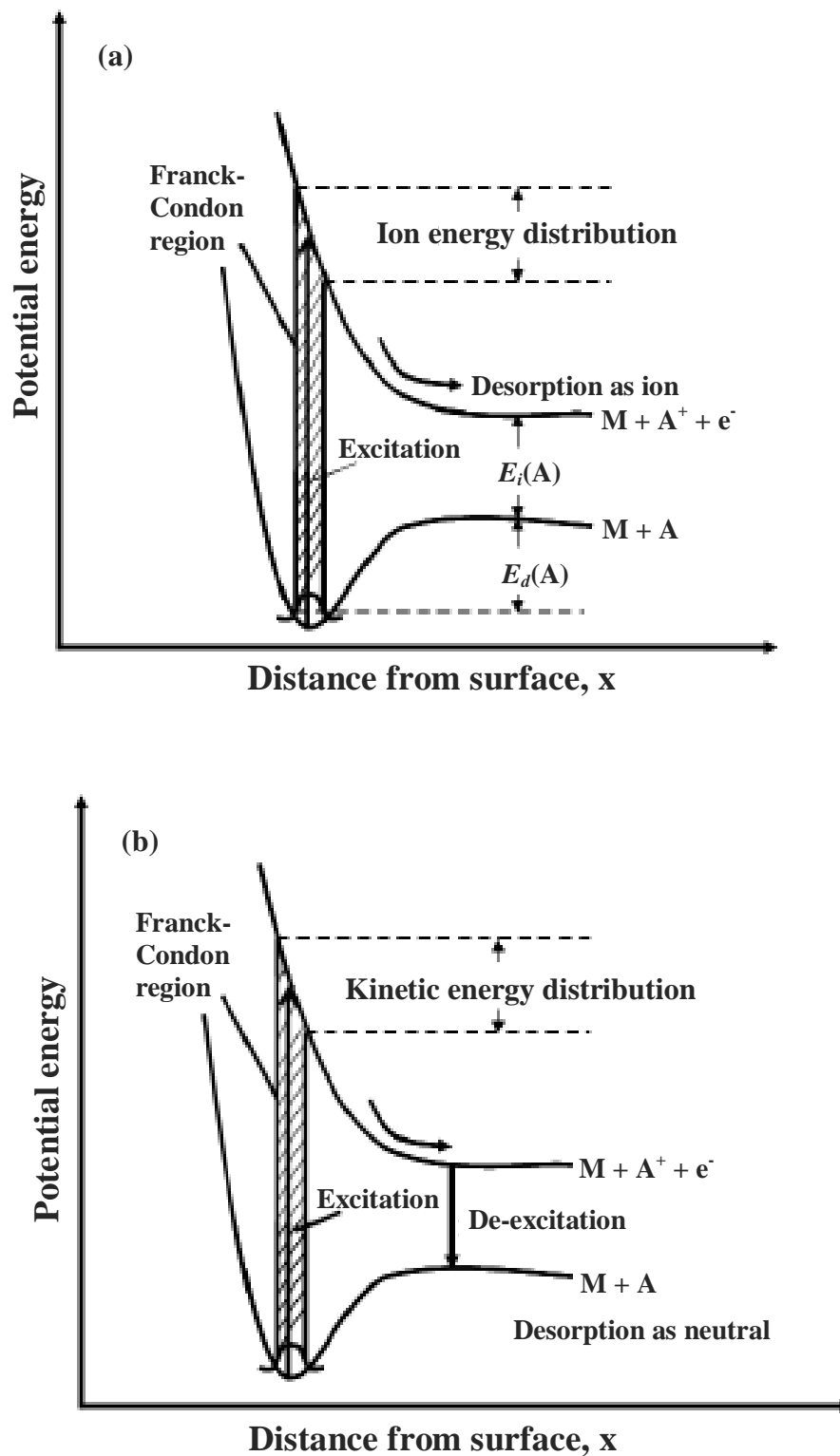


Figure 2.18: Schematic potential curves of the interaction between a surface M and an adsorbed atom A . Possible interaction pathways including: (a) desorption of an ion A^+ from the surface through excitation mechanism, and (b) desorption as neutral *via* de-excitation of species in excited state. [17, 18]. $E_d(A)$ is the binding energy of the atom to the surface, and $E_i(A)$ is the ionisation potential of the atom.

The most important aspect of ESD is the electron desorption cross-section (cross-section is a term describing an effective area for the interaction between two particles, in this case a molecule and an electron) which can be obtained by considering ESD to be a first order desorption process, where the rate of desorption due to electron bombardment of electron flux φ in $\text{cm}^{-2} \text{s}^{-1}$ is

$$-\frac{d\Theta}{dt} = \varphi_{e^-} \sigma_{e^- des} \Theta \quad (2.27)$$

where $\sigma_{e^- des}$ is the total cross-section for the electron-stimulated desorption in cm^2 , and Θ is the surface coverage. Sometimes Θ refers to the surface coverage in a particular binding state, which is affected by electron bombardment. Integrating **equation (2.27)** yields **equation (2.28)**:

$$\frac{\Theta_{s,t}}{\Theta_{s,0}} = \exp \left\{ - \left(\varphi_{e^-} \sigma_{e^- des} t \right) \right\} \quad (2.28)$$

Since ESD is used to model a first order desorption process, then $\varphi_{e^-} \sigma_{e^- des}$ can be substituted by k_{des} , and hence the following equations are obtained:

$$\frac{\Theta_{s,t}}{\Theta_{s,0}} = \exp \left\{ - \left(k_{des} t \right) \right\} \quad (2.29)$$

$$\frac{\Theta_{s,t}}{\Theta_{s,0}} = \exp \left\{ - \left(\frac{t}{\tau} \right) \right\} \quad (2.30)$$

where $\Theta_{s,t}$ is the surface coverage after time t of electron irradiation, $\Theta_{s,0}$ is initial surface coverage, t is the time constant, in s, and τ is the lifetime, in s. By taking a measure of surface concentration (e.g. IR band strengths of the molecule and / or desorption peak areas obtained from the TPD traces) and irradiation time, the lifetime constant, τ , can be calculated and hence the cross-section, using **equation (2.31)** [20]:

$$\sigma_{e^{-}des} = \frac{1}{\varphi_{e^{-}}\tau_{des}} \quad (2.31)$$

The electron flux, $\varphi_{e^{-}}$ is obtained from **equation (2.32)**:

$$\varphi_{e^{-}} = \frac{I}{e} \quad (2.32)$$

where I is the current density of electrons in $C\ cm^{-2}\ s^{-1}$, and e is the electronic charge in C [20].

2.2.3 Sample Preparation

Electron-beam evaporation is used to coat metal surfaces with a new material. It utilises a high vacuum to deposit different thicknesses of elements and compounds on substrates. **Figure 2.19** shows the pumping system of the e-beam system. The main chamber is evacuated by a liquid N_2 trap, a 6" oil diffusion pump (Edwards High Vacuum Ltd, E06) charged with polyphenyl ether fluid (Santovac 5), and connected to a rotary pump (Edwards High Vacuum E2M18). In the main chamber, where the deposition takes place, the solid material, in the form of granules or powder, is placed in a crucible liner and heated by a beam of high energy electrons generated from the filament located above the crucible liner. As a result, the solid material will melt and be evaporated as a consequence of the ionisation created by the electrons.

The total number of atoms or molecules, N , deposited onto a substrate surface can be determined from the following equation:

$$N = \frac{P(T)A}{\pi L^2 \sqrt{2\pi m k_B T}} \quad (2.33)$$

where $P(T)$ is the equilibrium vapour pressure of the deposited material, A is the evaporation area, m is the molecular mass in kg, k_B is Boltzmann's constant, and T is the absolute temperature of the gas in K.

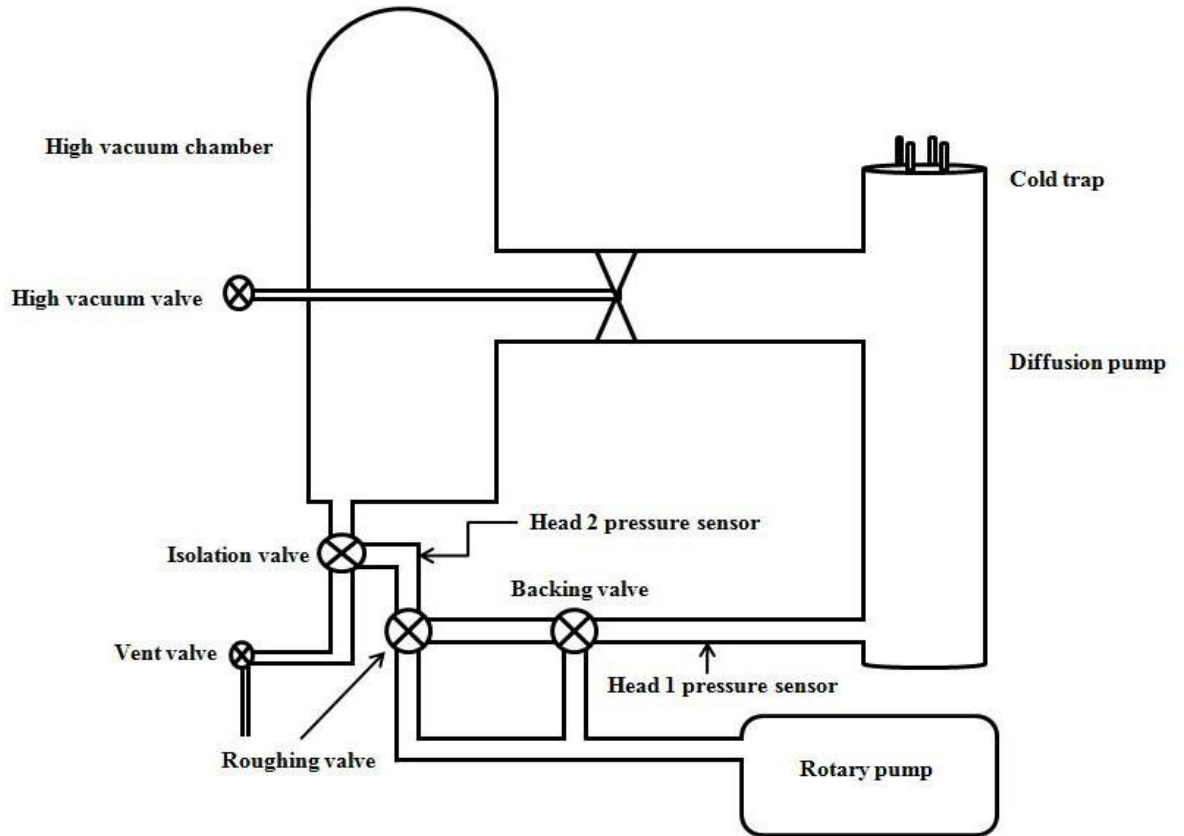


Figure 2.19: Schematic drawing of e-beam evaporation pumping system.

The thickness of the deposited film can be monitored during the deposition by means of a quartz crystal microbalance (QCM). This consists of an AT-cut quartz crystal which vibrates at its fundamental frequency f_0 , which depends on the crystal thickness d_q :

$$f_0 = S / d_q \quad (2.34)$$

where S is a constant equal to 1.67×10^6 Hz mm. The QCM is usually located close to the target surface. During deposition, the mass of the QCM is increased by Δm , whereas the resonant decreases by Δf , as shown in **equation (2.35)**:

$$\Delta f = \frac{Kf_0^2 \Delta m}{\rho_q SA} = \frac{KS \Delta m}{\rho_q d_q^2 A} \quad (2.36)$$

where K is a constant (usually close to unity) which depends on the spatial distribution of the deposited material over the area A of the crystal, and ρ_q is the density of the quartz [21-23].

2.2.4 Computational Methods

2.2.4.1 *The Chemical Kinetics Simulator (CKS)*

The CKS is a package created by IBM Almaden Research Center [24]. It is an easy-to-use code for modelling the kinetics of chemical reactions using stochastic methods. The most important aspects of this software are that CKS does not need other support programs when it is operated and it is fully equipped with a number of tools to help fit models to experimental data. CKS is not limited to simulating homogenous systems, and also works with heterogeneous systems. For example, solid and gas phase interactions can be simulated successfully using CKS. Once the reaction mechanism is inserted with all initial reaction conditions and appropriate rate constants, CKS provides the results in the form of graphs and tables of concentrations *versus* time, temperature, *etc.* In fact, CKS allows the user to perform simulations of chemical reaction models by using algebraic methods, or rate laws, derived from the mechanistic steps describing the reaction, and numerical simulation of a mechanism, using a computer. In algebraic methods, an analysis of the reaction mechanism is undertaken to produce the rate law equation. This can be obtained from coupling the differential equations, assuming the time dependence of each species in the reaction. The final algebraic expression will give a good comparison of the experimental data with the computable or controllable concentrations. However, only the simplest of the mechanisms are likely to have algebraic solutions.

The stochastic method is a reliable way, of simulating complicated chemical reactions, which works with no constraints and provides high accuracy data. **Figure 2.20** shows a diagram of the basic simulation cycle used in the program [24].

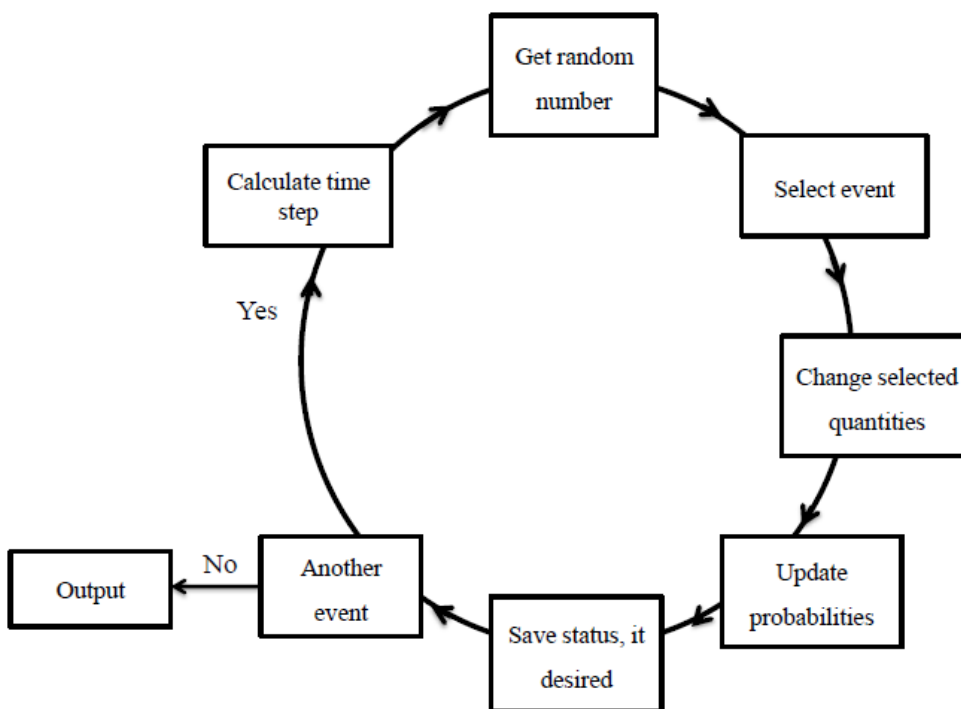


Figure 2.20: The basic simulation cycle used in the program [24].

2.2.4.2 HyperChem®

HyperChem® is a molecular modelling and simulation software package created by Hypercube, Inc. which allows complex chemical calculations to be performed. It combines a number of computational methods such as *ab initio* quantum mechanics, density functional theory (DFT), semi-empirical quantum mechanics, molecular mechanics, and mixed mode calculations (semi-empirical with *ab initio* or with DFT). Systems in this work are designed to use both *ab initio* and semi-empirical methods to estimate binding energies, IR vibrational frequencies, and enthalpies of formation. The *ab initio* package contains a number of electronic structure methods; a) Hartree–Fock methods, b) post-Hartree–Fock methods, and c) multi-reference methods. *Ab initio* quantum mechanics is a powerful computational method for predicting many physical parameters and features of molecules, such as the geometry of a molecule, its binding energy, reaction barrier height, vibrational frequencies, IR and nuclear magnetic resonance (NMR) spectra, reaction rate, and partition function. In general, semi-empirical methods originate from the same concept as *ab initio*

methods. They are based on molecular orbital (MO) theory, but make simplifying assumptions and apply a minimal basis set to describe the valence electron behaviour [25].

2.2.4.3 SRIM/TRIM

Briefly, SRIM/TRIM is a group of programs used to simulate ion bombardment (10 eV – 2 GeV) on solids and gases. The first part of this package is **Stopping and Range of Ions in Matter (SRIM)** code, which simulates the effects of protons when they penetrate matter until they are stopped using a simple quantum mechanical treatment of ion-atom collisions. By using SRIM, the collisions between the incident ion and the atom in the target matter are simulated including the exchange and correlation interaction between electrons in overlapping shells. Thus, electron excitations and plasmons occur during the interactions with the target. Once all the information about the collision event is inserted, the SRIM program will provide data (tables and graphs) of the stopping range of ions within the target.

The other part of this simulation program is **TRansport of Ions in Matter (TRIM)**; it is the most used part in the SRIM/ TRIM simulation. It uses Monte-Carlo simulations to provide data on the energy transferred in every target atom collision. SRIM/TRIM contains a compound library which is easy to re-edit in order to add new compounds. More details are available from the SRIM tutorial and textbook of how to use the simulation tools and theory by which the SRIM/TRIM performs calculations [26]. The limitation of the SRIM/TRIM code in the current study is that it cannot treat electron stopping power.

2.3 References

- [1] G. Attard and C. Barnes, *Surfaces*, (Oxford University Press, Oxford, 2008).
- [2] G. A. Somorjai, *Introduction to Surface Chemistry and Catalysis*, (John Willey & Sons, New York, 1994).
- [3] K. Oura, V. G. Lifshits, A. A. Saranin, A.V. Zotov, and M. Katayama, *Surface Science*, 1st ed, (Springer-Verlag, Berlin, 2003).
- [4] A. Chambers, R. K. Fitch, B. S. Halliday, *Basic Vacuum Technology*, 2nd ed, (IoP, London, 1998).
- [5] J. C. Vickerman and I. S. Gilmore, *Surface Analysis – The Principal Techniques*, 2nd ed, (John Willey & Sons, Chichester, 2009).
- [6] V. Fiorin, *PhD Thesis*, (University of Nottingham, Nottingham, 2001).
- [7] J. Thrower, *PhD Thesis*, (Heriot-Watt University, Edinburgh, 2009).
- [8] H. J. Fraser, M. P. Collings, and M. R. S. McCoustra, *Rev. Sci. Instrum.*, 2002, **73**, 2161.
- [9] D. P. Woodruff and T. A. Delchar, *Modern Techniques of the Surface*, 2nd ed, (Cambridge University Press, Cambridge, 1994).
- [10] H.J. Fraser, and E.F. Van Dishoeck, *Adva. Space. Res.*, 2004, **33**, 14.
- [11] P. A. Redhead, *Vacuum*, 1962, **12**, 203.
- [12] V. L. Frankland, (*PhD Thesis*, (Heriot-Watt University, Edinburgh, 2011).
- [13] E. Habenschaden, and J. Küppers, *Surf. Sci. Lett.*, 1984, **138**, 147.
- [14] Workman, Jr, L. Weyer, *Practical Guide to Interpretive Near-Infrared Spectroscopy*, (CRC Press, Boca Raton, 2008).
- [15] H. Kuzmany, *Solid-State Spectroscopy*, 2nd ed, (Springer-Verlag, Berlin, 2009).
- [16] D. R. Vij, *Handbook of Applied Solid State Spectroscopy*, (Springer, New York, 2006).

- [17] D. Menzel and R. Gomer, *J. Chem. Phys.*, 1964, **41**, 3311.
- [18] D. Menzel and R. Gomer, *J. Chem. Phys.*, 1964, **40**, 1164.
- [19] P. A. Redhead, *Can. J. Phys.*, 1964, **42**, 886-905.
- [20] E. Theodore, E. Madey, and Jr. J. T. Yates, *J. Vac. Sci. Technol.*, 1971, **4**, 525.
- [21] D. A. Buttry and M. D. Ward, *Chem. Rev.*, 1992, **92**, 1355.
- [22] M. Rodahl, F. Höök, A. Krozer, P. Brzezinski and B. Kasemo, *Rev. Sci. Instrum.*, 1995, **66**, 3924.
- [23] K. A. Marx, *Biomacromolecules*, 2003, **4**, 1099.
- [24] CKS 1.0, IBM Almaden Research Center, © IBM Corporation 1995.
- [25] Hyperchem Release 8.0.2, Molecular Modelling System, © 2007, Hypercube Inc.
- [26] J.F. Ziegler, J.P. Biersack, U. Littmark, 2011. The Stopping and Range of Ions in Solids. Pergamon, New York. See also: <http://www.srim.org/>.

CHAPTER – 3 Desorption of ASW Adsorbed on Amorphous SiO₂

Contents

3.1 Introduction.....	70
3.2 Water (H₂O)	70
3.2.1 <i>Phases of H₂O Ice</i>	<i>71</i>
3.2.2 <i>H₂O Isotopologues</i>	<i>72</i>
3.2.3 <i>Formation of Interstellar Water.....</i>	<i>73</i>
3.3 Thermal Desorption of ASW Adsorbed on Amorphous SiO₂	76
3.3.1 <i>Experimental Procedure.....</i>	<i>76</i>
3.3.2 <i>Results and Discussion.....</i>	<i>78</i>
3.4 Non-thermal Desorption of ASW Adsorbed on Amorphous SiO₂	86
3.4.1 <i>Experimental Procedure.....</i>	<i>86</i>
3.4.2 <i>Results and Discussion.....</i>	<i>87</i>
3.5 Modelling of Water Abundance in the Interstellar Clouds	91
3.5.2 <i>Results and Discussion.....</i>	<i>99</i>
3.5.3 <i>Comparison of the model and the observations.....</i>	<i>109</i>
3.6 Conclusion and Astrophysical Implications	111
3.7 References.....	113

3.1 Introduction

This chapter discusses how water (H₂O) molecules interact with amorphous silica. For example, how strongly do they bind to the silica surface? What chemistry or physics occurs when H₂O molecules are heated and/or irradiated with low energy electrons? Such questions are crucially important in explaining the role water plays in the chemical evolution of the interstellar medium (ISM). In order to obtain a more complete understanding of water behaviour, surface science techniques such as temperature-programmed desorption (TPD), electron-promoted desorption (EPD), and reflection-absorption infrared spectroscopy (RAIRS) were used to provide information on the water molecules on silica surfaces. The experimental results obtained were simulated and the resulting parameters built into a ‘Toy’ kinetic model simulating typical interstellar medium (ISM) conditions.

3.2 Water (H₂O)

Water (H₂O), in both the condensed and gas phase, is a key molecule in the Solar System and beyond. It has been detected in both forms in many galactic environments such as planets, comets, and the ISM [1-4]. Observations also show that H₂O is the major interstellar ice component in most lines-of-sight, with a typical abundance of 1×10^{-4} with respect to H [5]. The next most abundant species in interstellar ices are CO, CO₂ and CH₃OH [2, 6]. Water ice plays two crucial roles in interstellar and circumstellar chemistry: firstly, ices act as a reservoir of coolants (*e.g.* CO, CO₂ and CH₃OH) during star formation. Secondly, since the interstellar ices are dominated by water, therefore, water ices are considered as chemical factories where many chemical species are believed to be formed in the icy mantles, including water itself. The formation of H₂O ice in astrophysical environments occurs at low pressure and low temperatures (between 10 and 120 K). It is therefore necessary to reproduce such conditions in the laboratory to produce ice with a structure relevant to astrophysics.

3.2.1 Phases of H₂O Ice

There are four important phases of water ice at low pressure: hexagonal crystalline I_h, cubic crystalline I_c, low density amorphous LDA, and high density amorphous HDA ice (see **Figure 3.1**) [7]. If the bulk density is considered, then HDA has lower density than LDA due to its porosity. Experimentally, LDA ice is formed at temperatures above 120 K by vapour deposition of water onto a cold substrate, whereas the HDA ice is formed by deposition at temperatures below 50 K [8]. Amorphous ices are transformed into cubic crystalline ice at temperatures above 150 K and converted into a stable hexagonal crystalline form at temperatures in the range of 195 – 233 K. In most astrophysical environments this transformation is not possible and H₂O is found as amorphous solid water (ASW), which is a metastable state because of the high activation barrier preventing its transformation into the stable crystalline state [9].

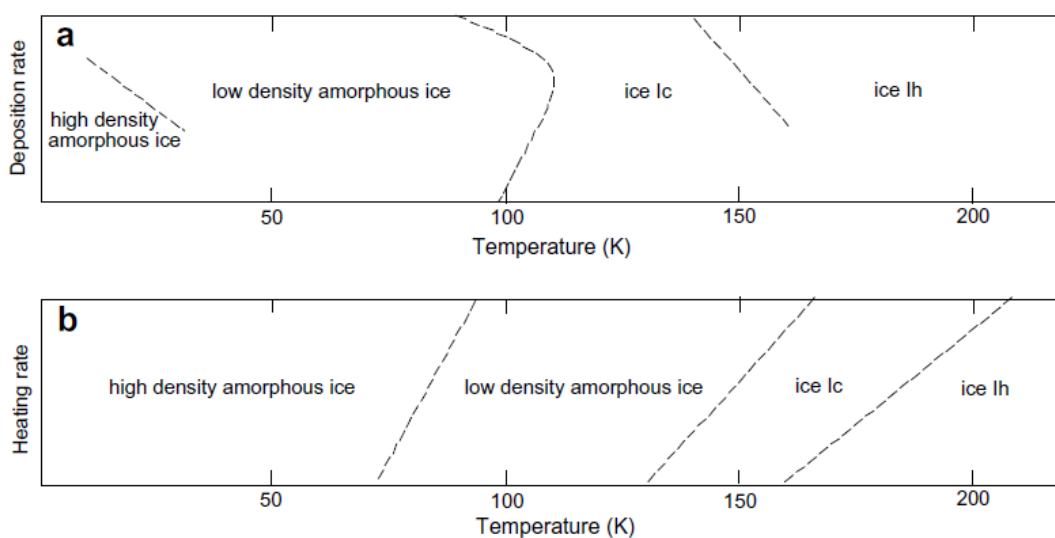


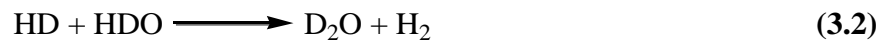
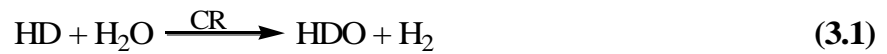
Figure 3.1: Schematic of structural phases of H₂O showing (a) formation of H₂O ice phases *via* vapour deposition and (b) under heating [8].

The phase transition from porous-ASW (p-ASW) or HDA to LDA (compact-ASW or c-ASW) allows the ice to retain or trap molecules with low sublimation temperatures, which are then expelled during crystallisation [8]. This trapping process means that chemical species can be retained in the ice to temperatures higher than might otherwise be expected, thus permitting them to potentially participate in additional

processes. In dense clouds, the chemical bonds of the trapped molecules can be broken by UV photons and CRs. The reactive species thus formed can rearrange to form more complex molecules (*e.g.* formamide from UV irradiation of H₂O, HCN, and NH₃) [10]. This process is thought to be responsible for creating various complex molecules that are unlikely to be formed under the conditions found in dense clouds (*i.e.* low pressures and low temperatures) through both gas-phase and gas-grain (on ices) processes [11, 12].

3.2.2 H₂O Isotopologues

Water is observed in space in several isotopic variants including both heavy hydrogen (*i.e.* deuterium, D) and heavy oxygen. Interestingly, heavy water (HDO, or D₂O) has been observed in space with a variable D/H ratio. The possible reaction pathway for heavy water formation *via* isotopic exchange between H₂O and molecular hydrogen has the classical form of the following reactions [13-15]:



There are three possible environments in space in which the isotopic exchanges can occur. Firstly, in solar nebula, thermal isotopic exchange between H₂ and H-containing molecules may occur. Secondly, in the dense ISM at temperatures as low as 50 K, isotopic exchanges occur between ionized species and molecules. Within this region, dust grains are responsible for significant D enrichment of molecules. Because both D and D₂ are more likely to be incorporated into molecules formed on grains, they are less likely to desorb from cold grains. Thirdly, in hot cores, at temperatures below 200 K, isotopic exchange occurs between radicals (H or D) and neutral molecules [13-15]. Water observations using the Submillimeter Wave Astronomy Satellite (SWAS) have observed H₂¹⁸O [16]. Water vapour emissions containing the heavier oxygen isotope have been detected in the ISM and in planetary environments such as the atmosphere of Mars, Jupiter, and Saturn. Thus,

laboratory studies should consider these species and the processes in which they participate.

3.2.3 Formation of Interstellar Water

The formation of water in space is still a topic of interest for many researchers because of the crucial role water plays in life. Fundamentally, the formation of water in space depends on the physical conditions of the region where the formation takes place: (1) in hot gas environments, (2) in cold gas environments, and (3) on grain surfaces. Firstly, in hot gas ($T > 300$ K), elemental oxygen is predominantly converted into CO, the remainder will react with hydrogen to form water vapour, through a chain of neutral-neutral reactions with molecular hydrogen:



These processes occur during star formation, close to the forming central star (hot cores) or in the interface between the outflows and the surroundings (shocks) [17, 18].

In cold molecular clouds ($T < 300$ K), where UV light from the ISRF cannot penetrate, ion-molecule reactions can drive water formation by dissociative recombination of H_3O^+ with electrons [17, 18]:



Chemical models predict that in a 10^4 yr period the relative abundance of water in such regions will be around $3 \times 10^{-7} / n_{\text{H}_2}$ (see **Figure 3.2**) [16].

However, gas phase H_2O formation is not sufficient to account for the observed abundance of H_2O in the ISM. The reaction pathway for water formation by hydrogenation of oxygen atoms on the cold surface of dust grains is required to account for the difference between observation and gas-phase only simulations *cf.* H_2 as shown in **Figure 3.3**. As can be seen from **Figure 3.3**, most of the oxygen in the gas phase reacts sufficiently with carbon to form carbon monoxide.

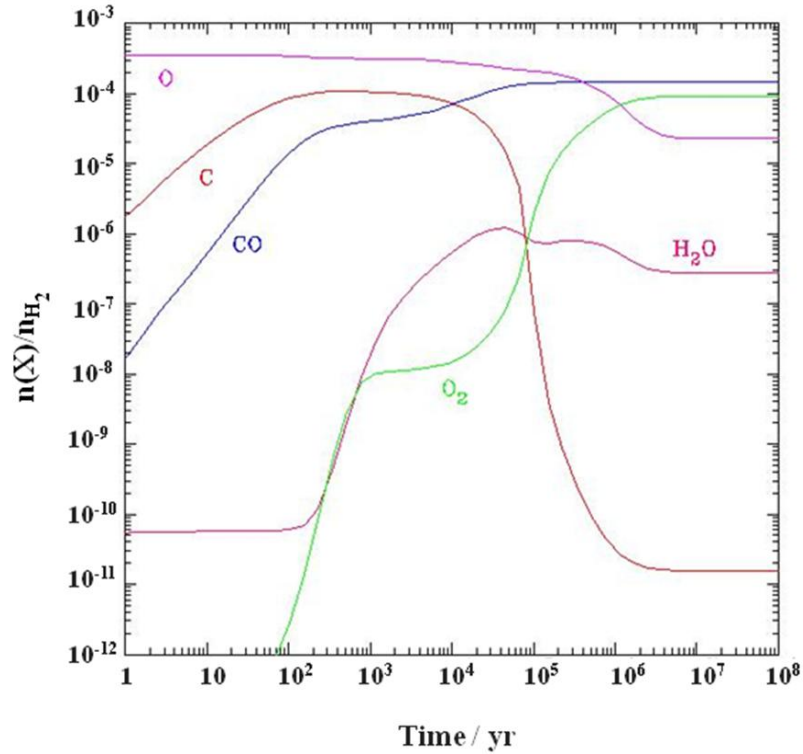


Figure 3.2: Relative abundance of key interstellar species in the gas phase, including H_2O , O_2 , CO , C and O [16].

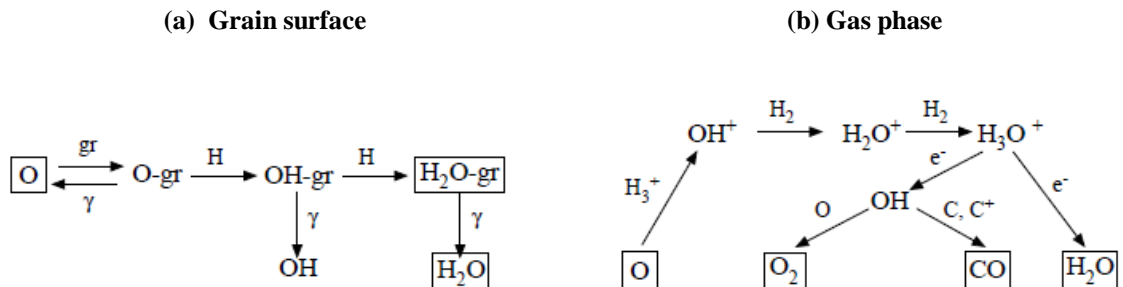
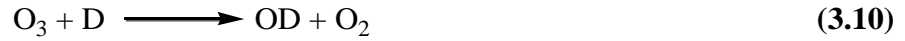


Figure 3.3: Reaction pathways of water: (a) hydrogenation of oxygen atoms is believed to occur on the dust grain surfaces (γ donates a photon or CR), and (b) depletion of the atomic oxygen to form H_2O and CO in the gas phase [19].

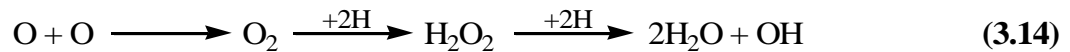
Recent studies of water formation have also demonstrated that water may be formed in dark molecular clouds *via* the hydrogenation of ozone (O_3) on dust grain surfaces. Mokrane *et al.* [13] found that the reaction between O_3 and D occurred on the water ice surface without any activation barrier, resulting in the formation of D_2O , which converts into HDO through isotopic exchange at temperatures above 120 K:



This result supports the chemical model that asserts that O_3 molecules are the precursor of water in dark clouds [13]. According to the models of Cuppen *et al.* [20], water ice formation occurs *via* hydrogenation of oxygen containing species onto dust grain surfaces as shown in **equation (3.13)**:



This reaction dominates in cool diffuse clouds, whereas in cold dense clouds, reactions including ozone (O_3) are a possible route for water formation shown in **equation (3.14)** and **equation (3.15)**:



and,



The water formed on a dust surface will remain as an icy mantle until it desorbs non-thermally, *via* cosmic ray collisions or thermally, when the temperature exceeds roughly 110 K.

It is thought that water ice is the reservoir for a range of volatile molecules that can return to the gas phase through desorption. Thus, desorption of molecules from water ice is controlled by the structure and the behaviour (*i.e.* reactions and desorption) of water itself. Temperature-programmed desorption (TPD) and electron-promoted desorption (EPD) experiments have been carried out, investigating both the thermal and non-thermal desorption processes under the astrophysically relevant conditions. By combining the experimental results in a simple model, the abundance of H₂O in the dense clouds will be simulated later in this chapter.

3.3 Thermal Desorption of ASW Adsorbed on Amorphous SiO₂

3.3.1 *Experimental Procedure*

Figure 3.4 shows an Atomic Force Microscopic (AFM) image of the amorphous silica (SiO₂) used as a model of the interstellar dust (the top image) and a Scanning Electron Microscope (SEM) image of a typical interplanetary dust grain (the lower image). The former provides a good approximation of an interstellar dust grain. Although the interplanetary dust grains appear to have a greater number of deeper pores, it can be seen from **Figure 3.4** that both samples show structure on a similar scale of *ca.* 0.1 μm. This suggests that the sample used in these experiments is a good mimic for the interstellar dust grain, at least in terms of morphology [21, 22].

Before conducting any experiment, the substrate was heated to 200 °C for 10 - 15 minutes to remove any volatile contaminants from the surface. The ASW samples were prepared by condensing water vapour onto the amorphous silica surface held at temperature of 110 K under UHV conditions. This temperature ensures the formation of c-ASW ($T \leq 130$ K). In order to minimize contamination with air, the water was subjected to three freeze-pump-thaw cycles in the gas manifold line, at 1×10^{-7} torr. For more controlled ASW deposition, the water vapour was dosed *via* the molecular beam system. Thus, the pressure in the main chamber during dosing of water remained at 2.0×10^{-10} torr. Dosing H₂O from the molecular beam reduces background H₂O pickup when performing dosing of other gases. The thickness of ASW can be controlled reproducibly by the exposure time, with the water vapour pressure in the source chamber of the molecular beam system stabilised at 2.0×10^{-4}

mbar. Assuming a sticking coefficient to be equal to one, 1 L (1 Langmuir) of water is adsorbed in 14 s.

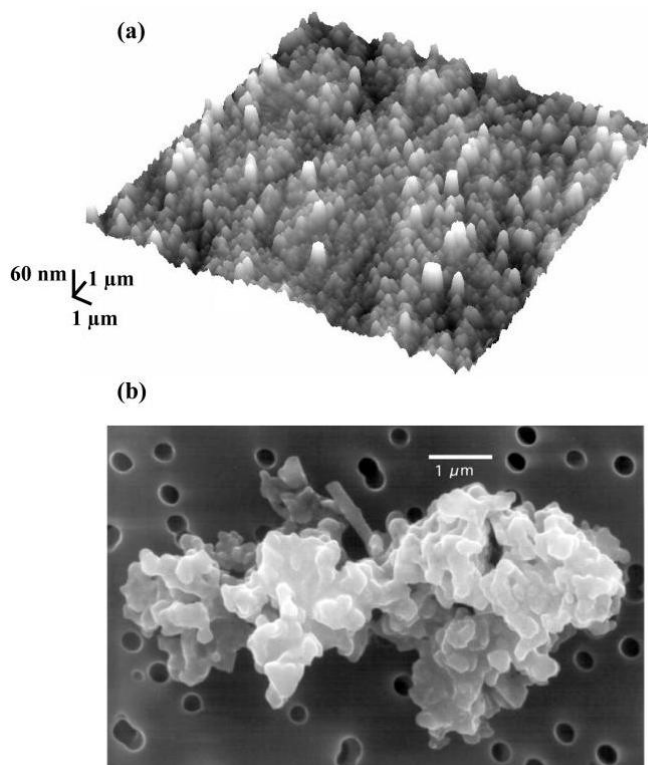


Figure 3.4: An AFM image of the amorphous silica substrate (a) [21], which was used in the experiments, compared with (b), which is an SEM image of an interplanetary dust particle [22].

ASW films formed with H₂O doses ranging from 0.7 L to 350 L were studied. Temperature-programmed desorption (TPD) experiments were performed using a linear temperature ramp of 0.1 K s⁻¹. The desorbing species were monitored using a quadrupole mass spectrometer (VG Quadrupole Micromass PC300D) placed inside the UHV chamber. A full description of the experimental apparatus used in this thesis is given in **Chapter 2**.

3.3.2 Results and Discussion

The raw data for water TPD experiments were recorded using the Micromass™ software and then imported into Origin™ software. The thermocouple voltages were converted into temperature using the temperature function described in **Section 2.2.1.5 in Chapter 2**. TPD curves shown in **Figure 3.5** present the desorption rate as a function of temperature for a range of doses. **Figure 3.5** shows a representative set of TPD traces (recorded on $m/z = 18$ *i.e.* H_2O^+) of water films deposited on the silica surface at 112 K. As can be seen from **Figure 3.5a** and **3.5b**, at low surface coverages (< 1.4 L), a single desorption feature is evident at *ca.* 145 K, with a peak desorption temperature that increases with coverage. This peak also displays coincident leading edges, which is consistent with a zeroth-order desorption process.

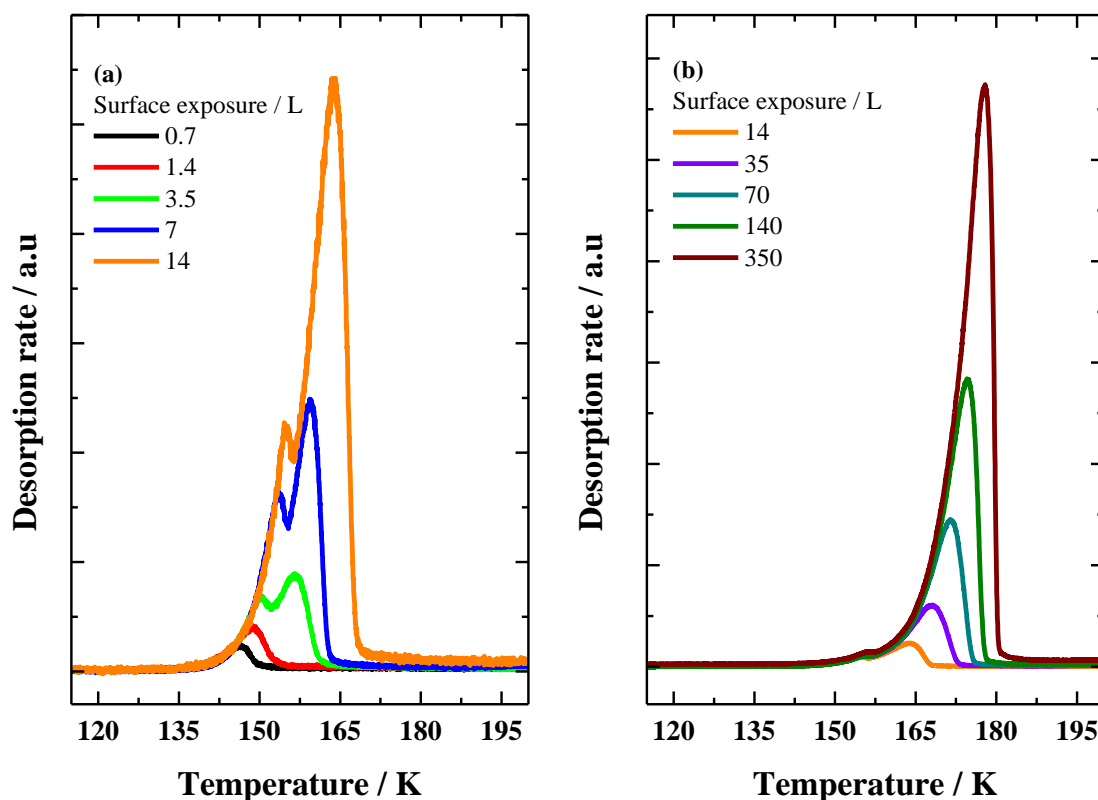
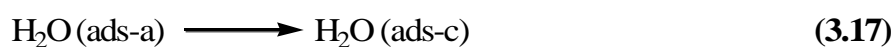


Figure 3.5: TPD traces for H_2O ice films at; (a) low coverages and (b) high coverages, adsorbed on the silica substrate. The exposures are labelled on each curve: (a) 0.7, 1.4, 3.5, and 7 L, and (b) 7, 14, 35, 70, 140, and 350 L. All samples were adsorbed on the silica surface at 112 K. For desorption, a temperature ramp, β , of 0.1 K s^{-1} was used.

For doses of 3.5 L and greater, a second desorption feature appears at higher temperature. This feature continues to grow with increasing coverage. It also shows coincident leading edges and an increasing peak temperature consistent with zeroth-order desorption. Zero-order desorption kinetics are observed for all water exposures suggesting the formation of H₂O islands through a clustering film growth in which H₂O does not wet the silica surface.

The first feature with the low temperature desorption peak is attributed to the desorption of c-ASW, whereas the higher temperature desorption peak is attributed to the desorption of crystalline water ice (I_c). As the temperature increases, the crystallization process competes with the desorption of c-ASW, and then finally water desorbs from the silica surface as I_c. TPD traces for exposures in the range of 3.5 – 14 L of solid H₂O adsorbed on amorphous SiO₂ surface (see **Figure 3.5a**) indicate clearly that the crystallization kinetics are thickness and temperature dependent. Such behaviour of water crystallization was earlier reported by Smith *et al.* [23, 24] and Speedy *et al.* [25]. The rapid decay of the desorption rate, which can be seen clearly at exposures of 7 L and 14 L, also supports the phase transformation of water ice. This is consistent with the studies in the literature of water crystallization kinetics [23]. Conversion to the more stable crystalline phase competes with desorption of amorphous H₂O, such that for higher doses (≥ 14 L), desorption from the crystalline phase dominates the desorption trace. Thus, the competing processes can be represented by:



Moreover, there is no further growth of the amorphous ice peak, which appears as a small “bump” (see **Figure 3.5b**) at exposures above 14 L. This confirms that most of water converted to crystalline phase during the TPD. **Figure 3.5b** also shows that there is no further change in the shape of the leading edge peak with increasing the surface exposure.

The concentration of H₂O on the surface in molecules cm⁻² for each dose was calculated using the following equation:

$$\Theta = \frac{N_A L}{(2\pi MRT)^{1/2}} \quad (3.19)$$

where N_A is the Avogadro number, R is the gas constant, T is the temperature, and M is the molar mass of water (1.802×10^{-3} kg mol⁻¹). The sample dose L ($1\text{L} = 1.0 \times 10^{-6}$ Torr s⁻¹ = 1 monolayer) varies for each dose, according to the data in **Table 3.1**.

Table 3.1: Surface concentrations of H₂O adsorbed on amorphous SiO₂ at 112 K.

Dose / L	Surface concentration (Θ) / molecules cm ⁻²
0.7	3.35×10^{14}
1.4	6.70×10^{14}
3.5	1.67×10^{15}
7	3.35×10^{15}
14	6.70×10^{15}
35	1.67×10^{16}
70	3.35×10^{16}
140	6.70×10^{16}
350	1.67×10^{17}

Figure 3.6 shows that the rate of desorption increases linearly with increasing surface exposure. The relative sticking probability, S/S_0 , for physisorption of water adsorbed on amorphous SiO₂ was determined from **Figure 3.6** by fitting all points as a single straight line with an R² value of 0.996. As expected, this indicates a constant relative sticking probability for water adsorbing on amorphous SiO₂ at 112 K.

The kinetic parameters for a zeroth order desorption can be determined by performing the leading edge analysis (LEA) using **equation (2.14)** [26].

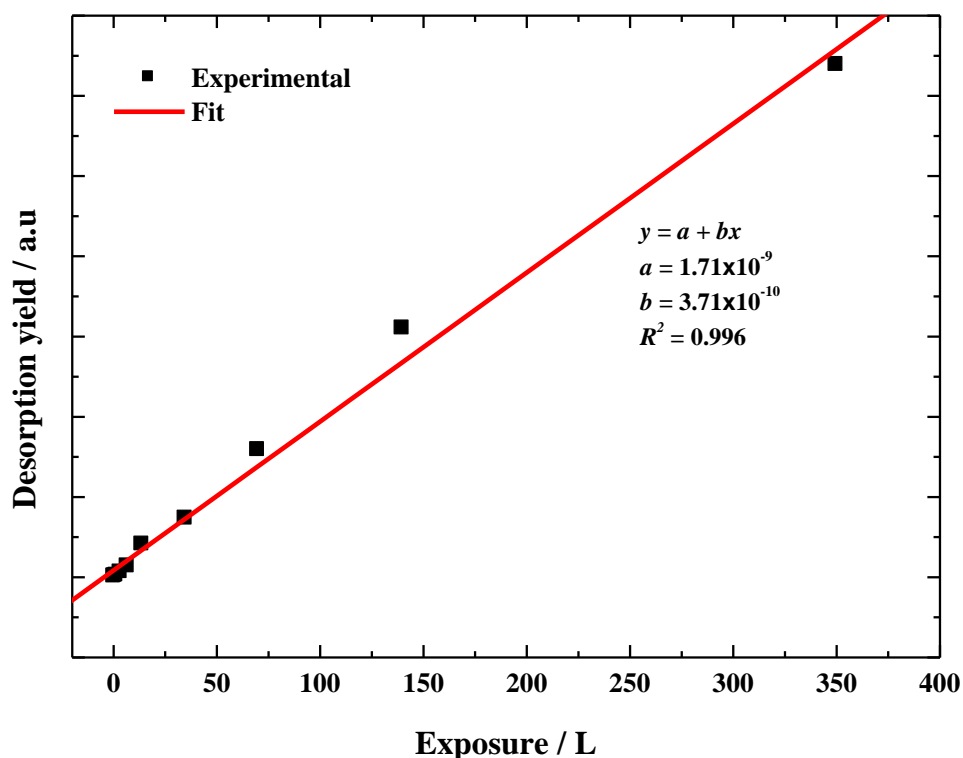


Figure 3.6: The relationship between desorption yield (*i.e.* the integrated peak area) and the surface exposure in Langmuir. This plot indicates that the desorption yield increases linearly as the thickness of the surface film, increases confirming that $S/S_0 = 1$.

By plotting the relationship between $\ln(d\Theta/dt)$ against $1/T$, as shown in **Figure 3.7**, E_{des} in kJ mol^{-1} can be estimated from the slope, and the pre-exponential factor ν from the intercept. The LEA was applied to the desorption peaks for both phases of water (see **Table 3.2**) and revealed desorption energies of 43 ± 4 and 46 ± 3 kJ mol^{-1} for ASW and CSW, respectively. These values are in good agreement with the heats of sublimation reported in the literature (46 kJ mol^{-1} for ASW and 48 kJ mol^{-1} for CSW) [23, 27-31]. The errors for E_{des} obtained from the logarithmic fitting of the leading edge, were used to estimate the final errors for each individual value of E_{des} , as shown in **Table 3.2**. The average value of the E_{des} was also calculated and listed in **Table 3.2**. The desorption energies are in good agreement with those of Brown and co-workers who investigated H_2O TPD from highly oriented pyrolytic graphite (HOPG) [32].

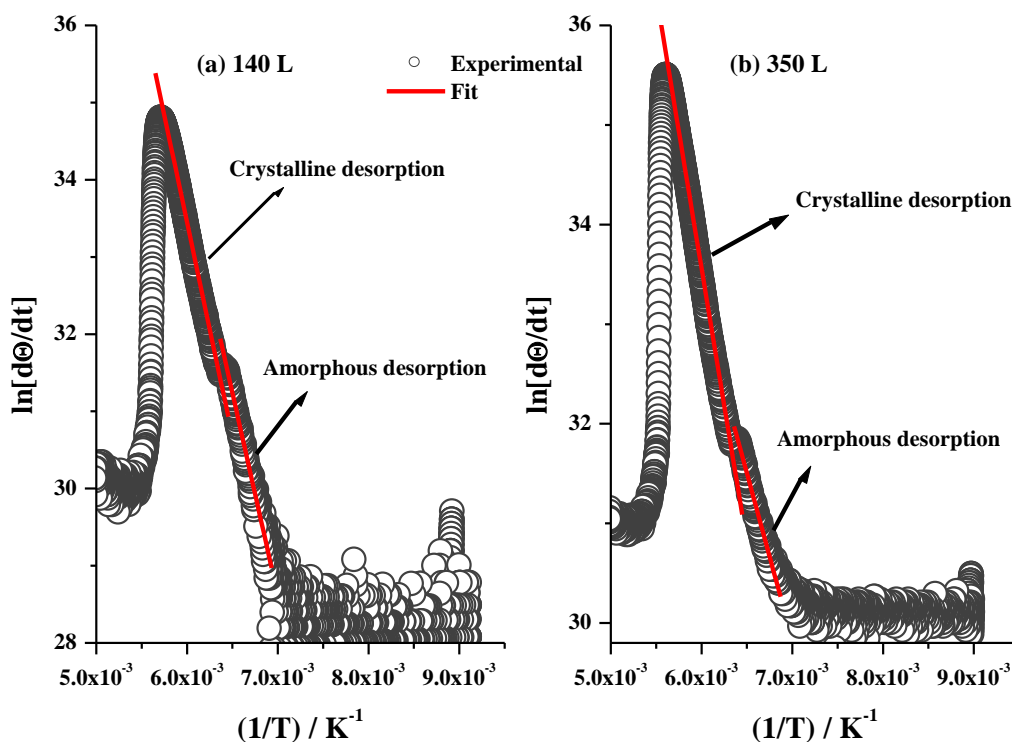


Figure 3.7: Leading edge analysis of desorption of (a) 140 and (b) 350 L H₂O from the surface of amorphous silica.

Table 3.2: Calculated desorption energies by the Arrhenius expression. CSW only presents above 1.4 L exposure.

Exposure / L	ASW	CSW
	$E_{des} / \text{kJ mol}^{-1}$	$E_{des} / \text{kJ mol}^{-1}$
0.7	40±3	-
1.4	35±2	-
3.5	45±1	28±1
7	51±1	37±3
14	44±2	33±1
35	44±2	40±1
70	43±1	45±1
140	43±4	46±1
350	29±2	46±1
Limit	43±4	46±3

The value of E_{des} changes significantly within the range 3.5 L – 14 L. This behaviour of water may result from the roughness of the silica surface, which means that a fractional order desorption is observed until a complete film is formed on the rough surface.

In the limit of high pumping speed during performing TPD experiments, the change in partial pressure is given by [33],

$$\Delta P = \frac{RTA_s}{S} \left(-\frac{d\Theta}{dt} \right) \quad (3.20)$$

where A_s is the surface area of the substrate, in cm^2 , and S is the pumping speed in molecules $\text{cm}^{-2} \text{s}^{-1}$. By substituting **equation (3.20)** into **equation (2.14)** and taking the natural logarithms the following expression is obtained:

$$\ln(\Delta P) = \ln\left(\frac{RTA_s}{S} v\right) - \left(\frac{E_{des}}{RT}\right) \quad (3.21)$$

Making the definition $RTA_s / S = \alpha$, then,

$$\ln(\Delta P) = \ln(\alpha v) - \left(\frac{E_{des}}{RT}\right) \quad (3.22)$$

Thus, the pre-exponential from the LEA extrapolation includes a factor of α , reflecting the pumping speed (uncertain), which varies during the experiments, and the surface area, which is unknown due to the roughness of the silica surface. Therefore, the LEA cannot be used to measure the pre-exponential factor for the desorption process. However, the LEA provides reliable value of the desorption energy. Therefore, an alternative analysis can be carried out using kinetic modelling which permits evaluation of E_{des} and v .

Kinetic modelling was performed using the Chemical Kinetic Simulator (CKS) package [34] in order to determine v . Zero-order desorption kinetics were assumed

for the bulk ice desorption. A simple reaction scheme was constructed to describe the water desorption from the surface (see **Figure 3.8**).

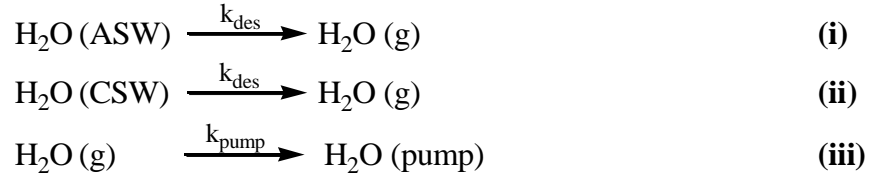


Figure 3.8: The reaction scheme of the CKS model for water desorption.

where (ASW), (CSW), and (pumped) denote respectively amorphous solid water, crystalline solid water and gas phase water being pumped out of the UHV chamber. Fitting the experimental data through CKS depends on the inputs (*i.e.* surface concentration, and estimates of E_{des} , and ν). The concentration of ASW is equivalent to the concentration of water molecules (θ) adsorbed on the surface (see **Table 3.1**). Following the studies of Smith *et al.* on TPD of water from a metal surface, the binding energy for water molecules to a water-ice multilayer was assumed to correspond to the latent heat of sublimation of water ice [23]. This is also consistent with the E_{des} obtained from the LEA. Kinetic simulations were run where E_{des} and ν are systematically varied to match the experimental results. **Figure 3.8** shows a comparison between the experimental and simulated TPD traces for water. The experimental data are best simulated with a ν value of 1.0×10^{28} molecules $\text{cm}^{-2} \text{s}^{-1}$ and E_{des} of 42.1 kJ mol^{-1} (5069.5K).

Figure 3.8a shows the fit of the experimental data, in which the transformation from amorphous to crystalline ice took place. **Table 3.3** shows the whole range of E_{des} and ν obtained from the CKS calculations. As can be seen, the value of E_{des} for CSW (*ca.* 49.3 kJ mol^{-1}) is in good agreement with the reported value for the latent heat of water ice, which is approximately 50.6 kJ mol^{-1} [29].

Unfortunately, there are some difficulties in simulating the low exposure data. This may be a consequence of more complex kinetics including, for example, fractional order desorption. Analysis of such data may require a more sophisticated model and was therefore not possible.

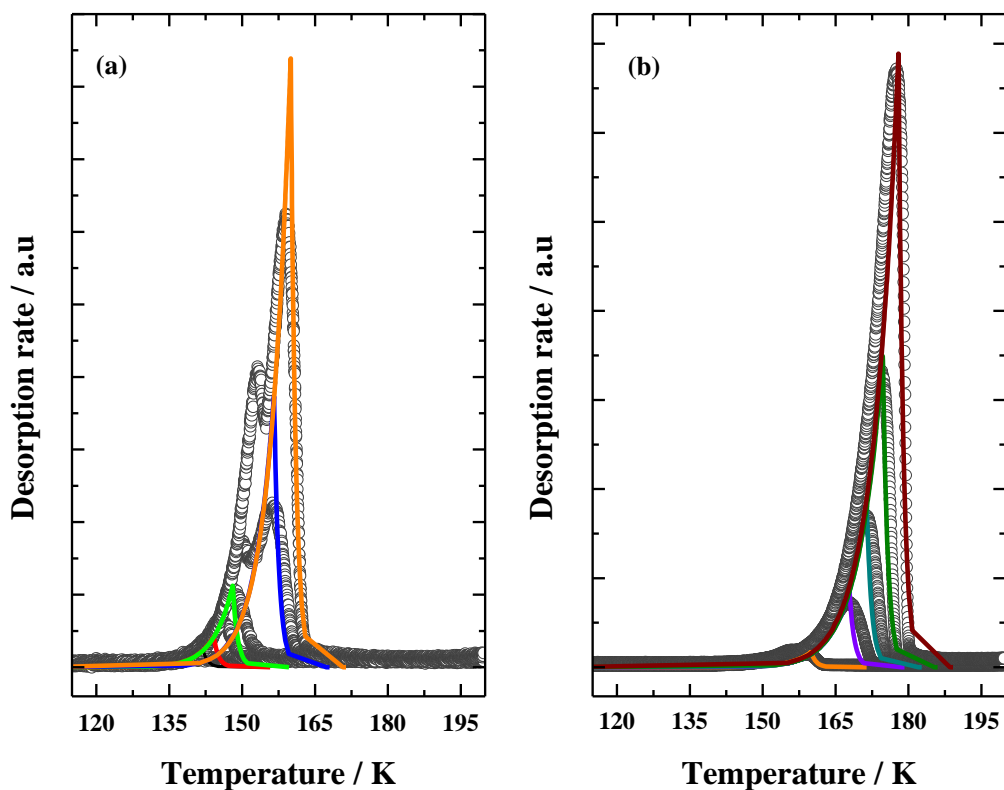


Figure 3.8: TPD traces for water layer desorption. (a) Low surface exposures: 0.35, 0.7, 1.4, 3.5, and 7 L, and (b) High surface exposures: 7, 14, 35, 70, 140, and 350 L. The coloured lines refer to the simulation and the dotted refer to the experimental. All samples were adsorbed on the silica surface at 112 K. For desorption $\beta = 0.1 \text{ K s}^{-1}$.

Table 3.3: Kinetic parameters used in the two population CKS model.

$\text{H}_2\text{O (c-SAW)} \rightarrow \text{H}_2\text{O (g)}$		$\text{H}_2\text{O (CAW)} \rightarrow \text{H}_2\text{O (g)}$		$\text{H}_2\text{O (g)} \rightarrow \text{H}_2\text{O (pump)}$
$E_{des} /$ kJ mol^{-1}	$\nu /$ $\text{molecules cm}^{-2} \text{s}^{-1}$	$E_{des} /$ kJ mol^{-1}	$\nu /$ $\text{molecules cm}^{-2} \text{s}^{-1}$	$k /$ $\text{molecules cm}^{-2} \text{s}^{-1}$
42.1 ± 1	$1.0 \pm 1 \times 10^{28}$	49.3 ± 2	$1.0 \pm 1 \times 10^{30}$	0.1 ± 1

3.4 Non-thermal Desorption of ASW Adsorbed on Amorphous SiO₂

3.4.1 Experimental Procedure

Electron-promoted desorption experiments were performed under UHV and low temperature conditions with a constant H₂O exposure of 14 L. Electron irradiation was performed using an ELG-2 electron gun and its EGPS-1022 power supply (Kimball Physics) attached to the UHV chamber. The ELG-2 electron gun has a unipotential refractory cathode which is able to produce a beam with a small energy spread of typically 0.5 eV. The sample was irradiated with electron energies in the range of 200-300 eV within irradiation intervals of 0, 50, 100, 200, 500, 1000, 2000, and 5000 s. During EPD experiments, irradiation and RAIR scans needed to be obtained without moving the sample, so the electron beam was incident at a much larger angle to the surface normal. The electron beam was rastered across the entire surface with a frequency of 2 s over a surface area of approximately 0.75 cm². **Figure 3.9** shows the scan generator “sawtooth” waveform, which is used synchronously by the scan coils for the electron beam during the electron irradiation experiments.

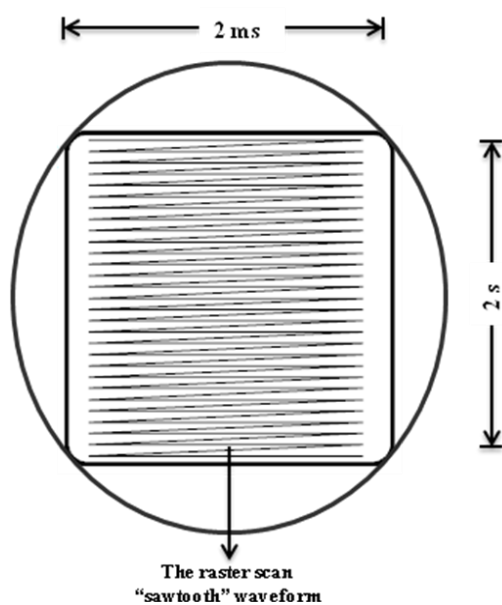


Figure 3.9: Sketch showing the Scan generator “sawtooth” waveform used to scan 0.75 cm² of the substrate.

Surface changes such as desorption and/or chemical reactions were monitored using RAIRS. The substrate was positioned at an angle of 107.5° in the UHV chamber, allowing both the electron beam and the IR beam to be incident on the surface simultaneously. In this geometry, the angle of incidence for the electrons on the surface is 45° . RAIR spectra were obtained by the co-addition of 1024 scans with a resolution of 2 cm^{-1} . The spectra were collected prior to and following irradiation.

3.4.2 Results and Discussion

The electron-promoted desorption of water was investigated using RAIRS to monitor the loss of H_2O from the amorphous silica. The use of this technique allows the determination of the total loss of H_2O from the surface as well as the observation of any structural changes that may occur during electron irradiation, such as crystallisation or amorphisation. In these experiments, approximately 14 L of H_2O adsorbed on the silica surface and subsequently irradiated with electrons. **Figure 3.10** shows the RAIR spectra of the OH-stretching bands prior to and following irradiation of 14 L H_2O adsorbed on the silica surface. The sharp features appearing above 3600 cm^{-1} are due to gas phase H_2O and result from fluctuations in the concentration of gas phase H_2O in the IR beam path external to the UHV chamber. There is no spectroscopic evidence of new product features during irradiation of water ice. It can be also seen from **Figure 3.10** that there is a significant decrease in the intensity of the OH-stretching band as the irradiation time increases from 0 to 5000 s. The data was analysed using simple first order kinetics [35-37], using **equation (2.27)**. If the ice is optically thin, the integrated area of the OH stretch band can be taken as being proportional to Θ , as plotted *versus* the irradiation time, in **Figure 3.11**. By fitting the decay as shown in **Figure 3.11** using non-linear relationship using **equation (2.30)**, the lifetime, τ_{des} can be obtained. The total cross-section for the loss of H_2O , σ_{e-des} can then be calculated according to **equation (2.31)**. Knowledge of the flux of electrons is necessary in order to quantify the H_2O loss. This was calculated during the experiments by combining the electron current and the electronic charge through **equation (2.32)**.

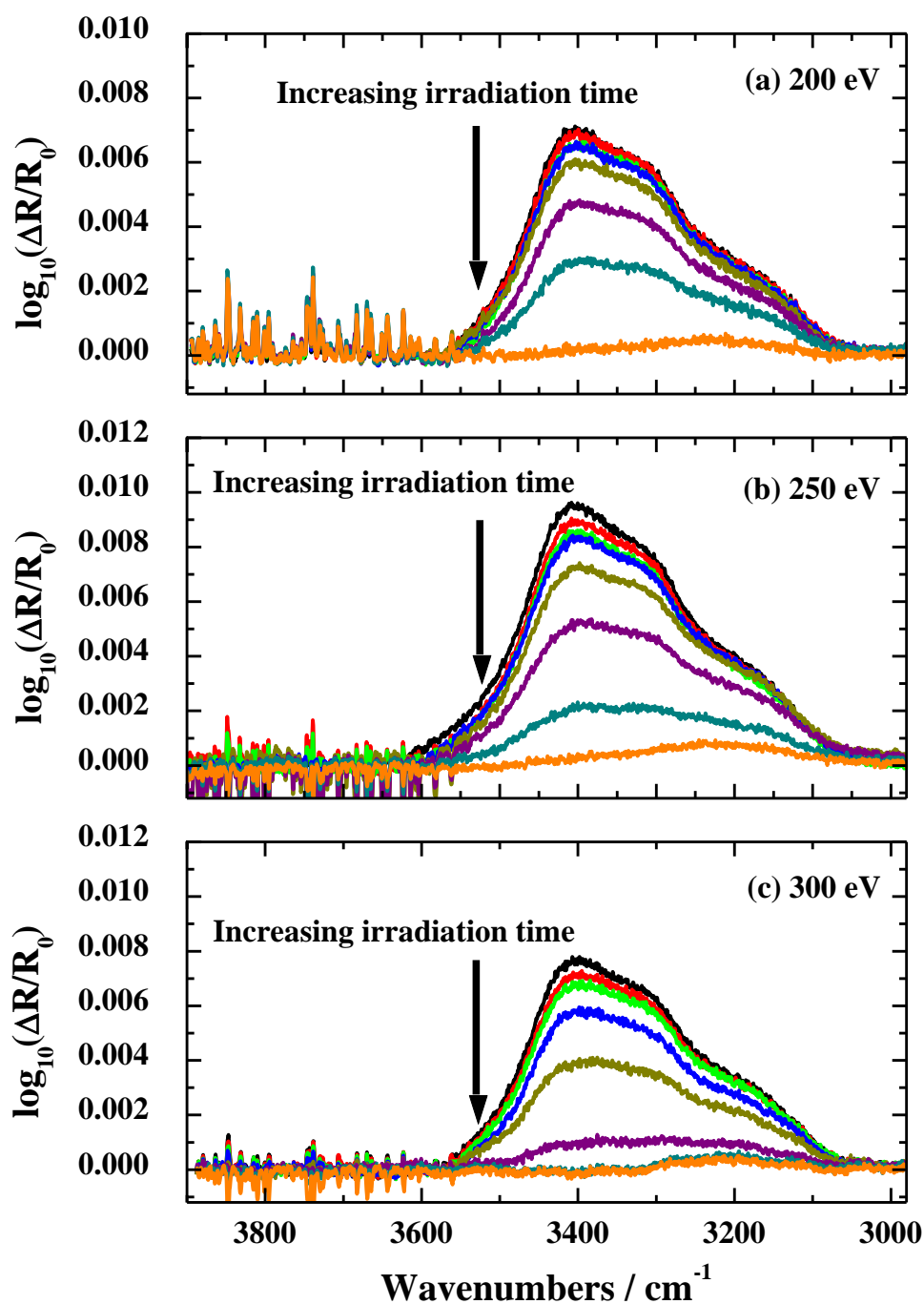


Figure 3.10: OH stretching band for 14 L H₂O adsorbed on amorphous SiO₂, as a function of irradiation time. The electron energies were; (a) 200 eV, (b) 250 eV, and (c) 300 eV. Spectra are shown as difference with respect to the bare silica surface for irradiation times 0 (black), 50 (red), 100 (green), 200 (blue), 500 (dark yellow), 1000 (purple), 2000 (dark cyan), and 5000 s (orange).

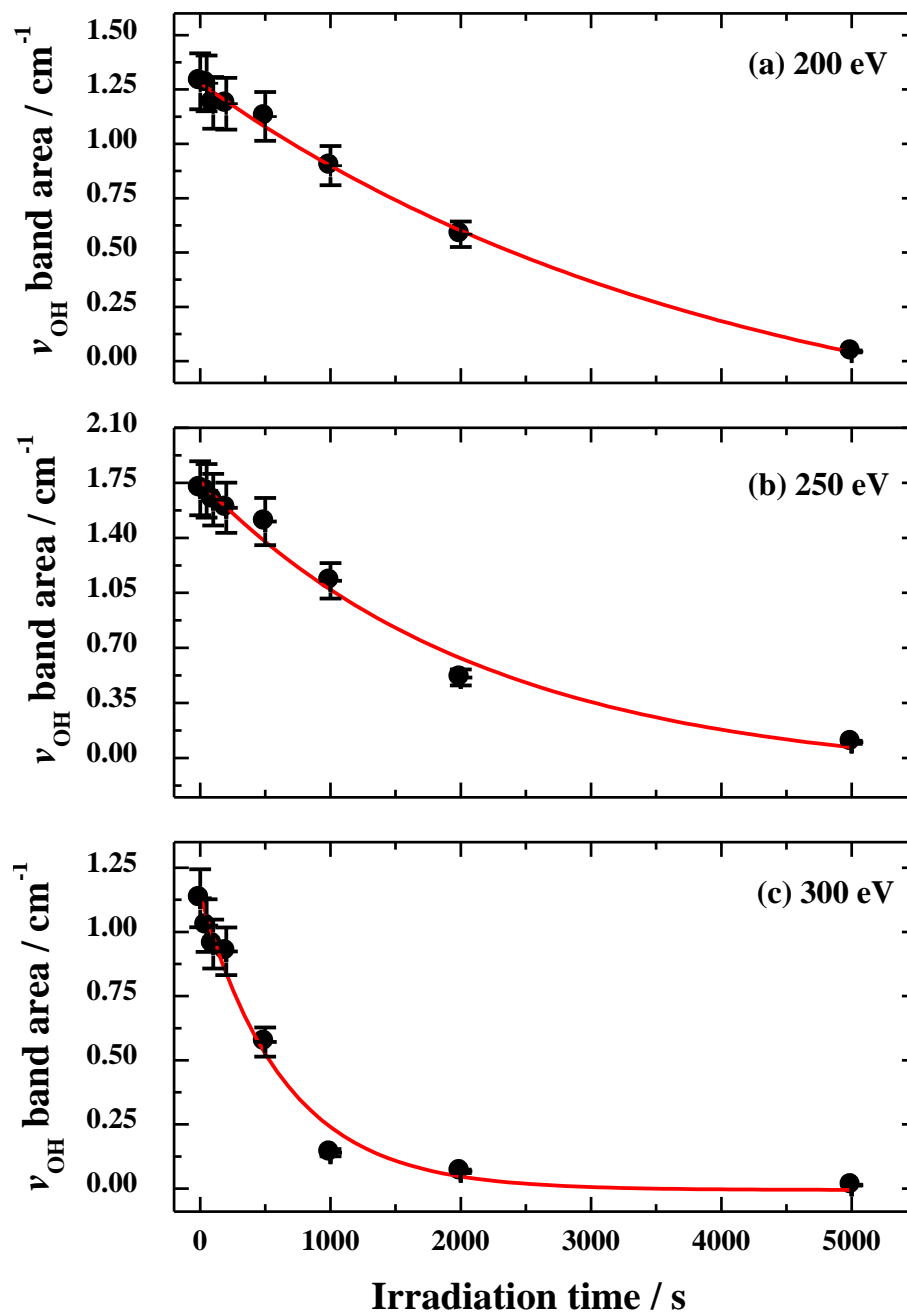


Figure 3.11: OH band decay as a function of irradiation time (solid circles), along with the fitted exponential decay function (solid line). Electron energies are: (a) 200 eV, (b) 250 eV, and (c) 300 eV. Error bars on the dots represent the standard deviation in several measurements.

The electron current reading is recorded during the experiments and the final electron current error calculated for the employed energies (*i.e.* 200 eV, 250 eV, and 300 eV). This error was combined with the standard error of the electron charge, resulting in the electron flux error. To estimate the cross-section error, the error on the decay constant is considered along with the error on the electron flux. The resulting relative error can then be multiplied by the cross-section to produce the final error.

Table 3.5 shows the calculated cross-sections of H₂O loss with the corresponding electron flux. These results suggest that the EPD cross-sections of H₂O increase monotonically with increasing electron energies. Indeed, there is a general tendency that the EPD cross-section of water ice increases with increasing the energy from 100 to 400 [38-41].

Table 3.5: The calculated total cross-section of H₂O loss, observed through RAIRS. The origin of error estimates is given in the text.

Electron energy / eV	Electron flux / electron cm ⁻² s ⁻¹	Electron-cross section / cm ²
200	1.4(±0.1)×10 ¹²	1.6(±0.1)×10 ⁻¹⁶
250	1.7(±0.1)×10 ¹²	3.2(±0.4)×10 ⁻¹⁶
300	1.6(±0.1)×10 ¹²	5.2(±0.6)×10 ⁻¹⁶

Interactions between water molecules and electrons result in the formation of neutral water molecules and / or H and OH radicals:



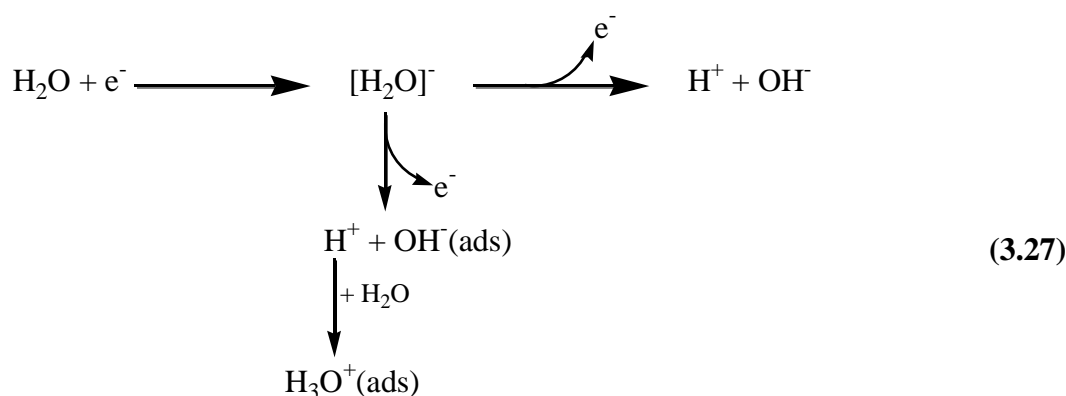
The interaction between electrons and water ice can also produce electronically excited water molecules (H₂O^{*}), which may subsequently dissociate, as in the following equations:



It is more likely that dissociation of water molecules proceeds *via* a transient negative ion resonance over a short timescale:



In addition, transient negative ions can directly produce either ions or radicals, as in the following equations:



The total desorption cross-sections in this work are in the range of 10^{-16} cm^2 , which is consistent with those reported in the literature [38-42]. As water does not possess a resonance in this range of energy (200 eV – 350 eV), there is no significant change in the cross section. As reported by Laffon *et al.*, the only core excitation of solid water can be seen at 535 eV. This belongs to the transition to the $4a_1$ state associated with the oxygen atom and lies outside the experimental energy range [43].

3.5 Modelling of Water Abundance in the Interstellar Clouds

It has been realised that CR and UV-driven chemistry, surface chemistry, freeze-out and desorption are key processes occurring in the ISM. The latter two processes are of particular importance in controlling the molecular abundance in interstellar dense clouds. At temperatures as low as 10 K, atoms and/or molecules adsorb onto the surface of dust grains (with sticking probability of unity), forming icy mantles. At the same time, processing by interstellar radiation (*e.g.* CRs, UV photons, and secondary electrons) causes adsorbed molecules to desorb from the surface of the icy grains, returning them to the gas phase. These processes control the abundance of molecules

in both the solid and gas phases within the interstellar clouds. The Bok globule, Barnard 68 (B68), is a molecular cloud which attracts significant attention because it is a nearby, relatively isolated, and morphologically simple molecular cloud with distinct boundaries. It has a diameter of 3.86×10^{15} km [44], and a central temperature of 7 K [44, 45]. It is located toward the southern constellation Ophiuchus within the Milky Way galaxy, at a distance of 500 light-years ($\sim 8.95 \times 10^{13}$ km). The gas and dust in the cloud block visible light, as observed through telescopes (see **Figure 3.12**). The IR light is not scattered by the dust grains and therefore the black hole becomes visible. As reported by Caselli *et al.*, the gas phase H₂O relative abundance is less than 1.3×10^{-9} with respect to the hydrogen density, and the upper limit of H₂O gas phase column density is less than 2.5×10^{13} molecules cm⁻³ [46].

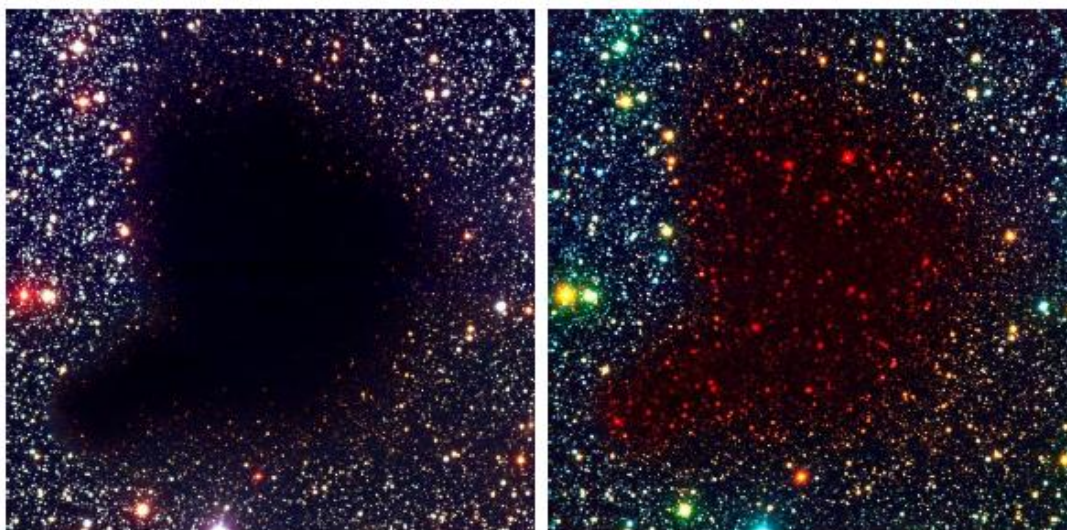


Figure 3.12: Visible and near-infrared images of Barnard 68 (B68). At visible wavelengths (left) the cloud is a dark “hole”, due to shielding by small interstellar dust particles and gas, while at near-infrared wavelengths (right) the cloud is transparent and the stars located behind the cloud clearly appear in the image [45].

The focus of this section is to model the abundance of H₂O in the dense region of the cloud using a simple kinetic model: a so-called ‘Toy’ model. This model combines thermal and non-thermal desorption of solid H₂O and adsorption (freeze-out) of H₂O molecules from the gas phase. The following reaction scheme (**Figure 3.13**) is proposed to demonstrate the processes by which water desorbs from the dust grain surfaces:

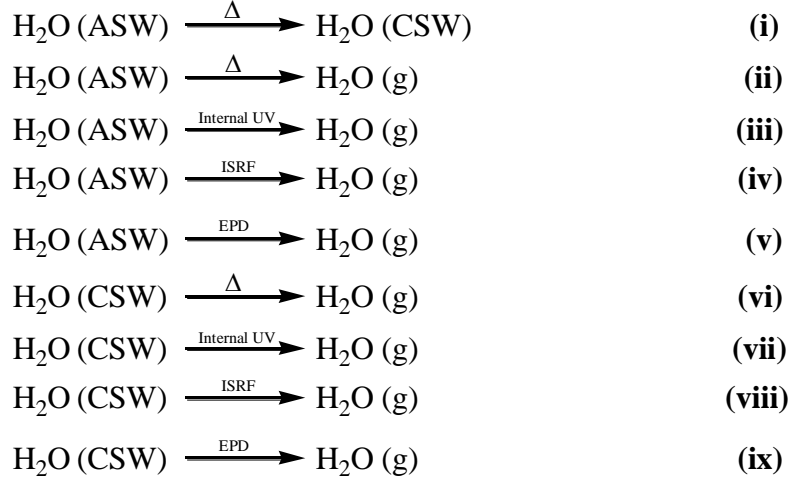


Figure 3.13: The thermal and non-thermal desorption mechanisms for H₂O, where (ASW), (CSW), and (g) represent the physical state of H₂O as amorphous solid water, crystalline solid water, or gas phase water, respectively. The driving force for the process represented for each reaction step is mentioned above the arrow, where Δ , internal UV, ISRF, and EPD denote thermal processes, CR induced photon promoted processes, processes promoted by photons from the interstellar radiation field, and electron promoted processes respectively.

Table 3.6: Calculated parameters used to estimate the first order rate constants for the non-thermal desorption of H₂O [21].

Process	Relevant flux / cm ⁻² s ⁻¹		Cross-section / cm ²	k / s^{-1}
EPD H ₂ O (e ⁻)	90 electrons		3.2×10^{-16}	2.9×10^{-14}
PSD H ₂ O (VUV _{Internal})	5.0×10^3 photons		4.0×10^{-21}	2×10^{-17}
PSD H ₂ O (UV _{ISRF})	$A_v=0$	1×10^8 photons	1×10^{-19}	1×10^{-11}
	$A_v=2$	1×10^6 photons		1×10^{-13}
	$A_v=4$	1×10^4 photons		1×10^{-15}
	$A_v=6$	1 photon		1×10^{-19}

If non-thermal desorption in the ISM is a first order desorption process, the cross-section of desorption (σ) can be used to determine the first order rate constant (k) by considering the flux (ϕ) of CRs or photons promoting desorption (see **equation (3.22)**). **Table 3.6** shows the calculated fluxes, cross-sections and corresponding first order rate constants for the non-thermal desorption of H₂O, based on the work

reported by Baragiola [47, 48], Thrower [21], and in this thesis. The calculated k values were used to perform astrophysical stimulations at a fixed temperature of 10 K, and at a heating rate of 1 K / 1000 yr. Below, is a detailed discussion of how the parameters listed in **Table 3.7** were obtained.

The main impact of CRs on ices is to generate a cascade of secondary electrons. The simulation flux is approximated as the flux of secondary electrons generated by the passage of 1 MeV protons (H^+) through 100 nm of H_2O ice. The flux of cosmic ray protons, as shown in **Figure 3.14** [49], is fairly constant over the range of 1 to nearly 100 MeV. However, for H^+ with energy over 100 MeV, the flux falls away. Mennella and co-workers in their study of the ion irradiation impact on ices assumed that 1 MeV CRs have a flux of around $1 \text{ cm}^{-2} \text{ s}^{-1}$ [50]. The electronic stopping power, S_{power} , of ions in ice can be estimated using the SRIM code [51]. For collisions of a 1 MeV H^+ with liquid H_2O , S_{power} has a value of $19.22 \text{ keV } \mu\text{m}^{-1}$. The yield of secondary electrons η in μm^{-1} can be calculated thus:

$$\eta = \frac{S_{power}}{W} \quad (3.28)$$

where W is the typical energy deposited per ionization event. This value is usually around 2-3 times larger than the ionization potential (IP) of the molecule being ionized [52]. For ASW, the IP is 11 eV [53], and so W is 22 eV. Thus, for a 1 MeV proton, the yield of secondary electrons (η) is estimated to be $900 \mu\text{m}^{-1}$. This value corresponds to a secondary electron flux (φ_{e^-}) of $90 \text{ electrons cm}^{-2} \text{ s}^{-1}$ in a 100 nm film. The fractional H_2O ionisation cross-section *versus* secondary electron energy is reported in **Figure 3.15** [54]. Taking the integral of this curve indicates that secondary electrons with energies in the range employed in this work form a significant fraction of the yield. In addition, previous studies of EPD on H_2O have shown that the total inelastic cross-section for H_2O ice does not fall significantly below 100 eV as a result of low energy excitations [55]. Thus, the flux of electrons used in this model can be considered a good approximation for investigating the impact of electrons and CRs on H_2O ice. The cross-section obtained from the experimental data for electron irradiation of H_2O at 250 eV is $3.2 \times 10^{-16} \text{ cm}^2$. This

yields a first-order rate constant for EPD, taking into account the electron flux of $2.9 \times 10^{-14} \text{ s}^{-1}$.

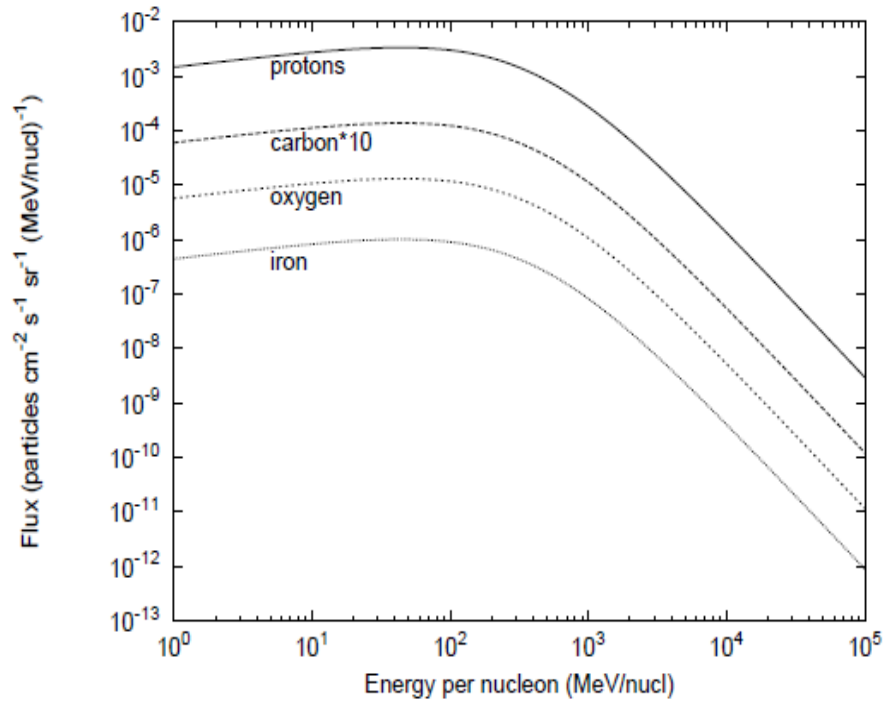


Figure 3.14: Differential cosmic ray flux of protons, carbon, oxygen and iron in the energy range from 1 MeV to 10^5 MeV [49].

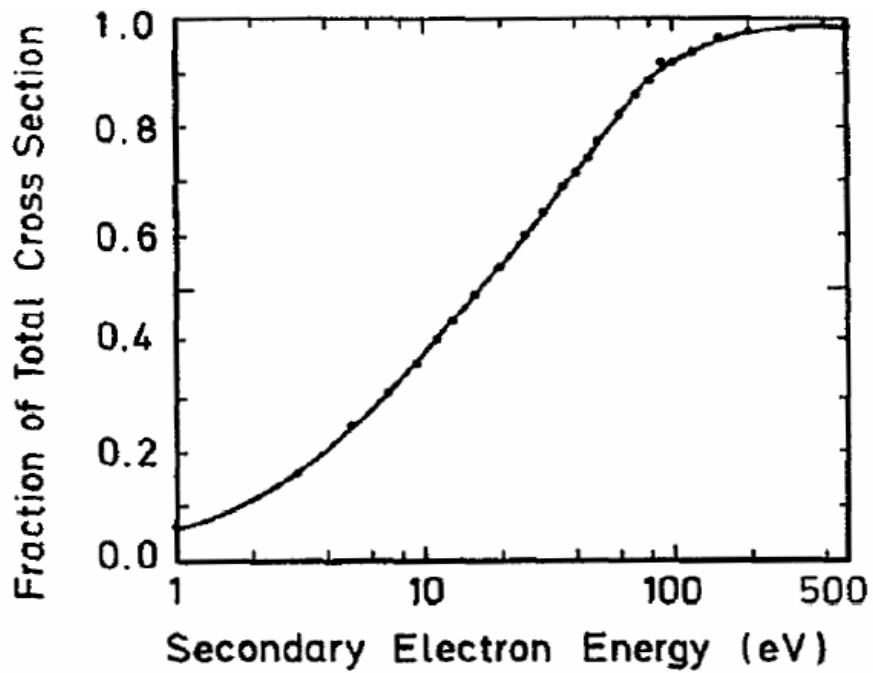


Figure 3.15: Calculated fraction of the total ionization cross-section for H_2O as a function of secondary electrons [54].

There are two contributions to the interstellar photon flux to which ices are exposed. The first is the contribution of the interstellar radiation field (ISRF). The intensity of the ISRF is a function of the visual extinction, A_v , and is therefore greater in the outer, more translucent, regions of the cloud. It is also very dependent on the wavelength. The flux of long wavelength (*ca.* 200 – 250 nm) UV photons produced by the ISRF corresponding to each value of A_v was estimated based upon the work of Mathis *et al.* [56]. H₂O has a low absorption cross-section for photons over much of the wavelength range of the ISRF. However, it has been shown that indirect adsorbate-mediated photodesorption of H₂O can occur whereby other species present in the ice absorb photons and transfer energy to neighbouring H₂O, promoting desorption [57]. Here, the cross-section of 1×10^{-19} cm² was measured for benzene at 250 nm, reflecting the work of Thrower [21]. The rate constant for PSD at $A_v = 0$, where the photon flux taken into account is 1×10^{-11} s⁻¹. However, as shown in **Table 3.6**, the value of the rate constant varies significantly with the amount of the photon flux, which differs for every A_v value.

The second contribution to photodesorption is made by the internal VUV field in the cloud, *i.e.* the flux of VUV photons produced by CR-induced fluorescence of H₂ ($\phi_{VUV} = 5 \times 10^3$ cm⁻² s⁻¹) [49, 58]. To first approximation, the internal VUV field is independent of A_v and therefore constant throughout the cloud. The production of VUV photons at A_v values of 2 and 4 is dominated by H₂ fluorescence, through the Lyman and Werner series, which is well represented by the output of a hydrogen discharge lamp as shown in **Figure 3.16** [59, 60]. Therefore, H₂O desorption rates from experimental studies employing such lamps can be applied directly. The quantum yield for photon-induced desorption of H₂O within the wavelength range of the UV internal field is 10^{-3} [59]. This is combined with the UV photon absorption cross-section at 121 nm of 4×10^{-18} cm² to give a desorption cross-section of 4×10^{-21} cm² [20, 61]. Therefore, the rate constant for PSD, taking into account the photon flux, is 2×10^{-17} s⁻¹.

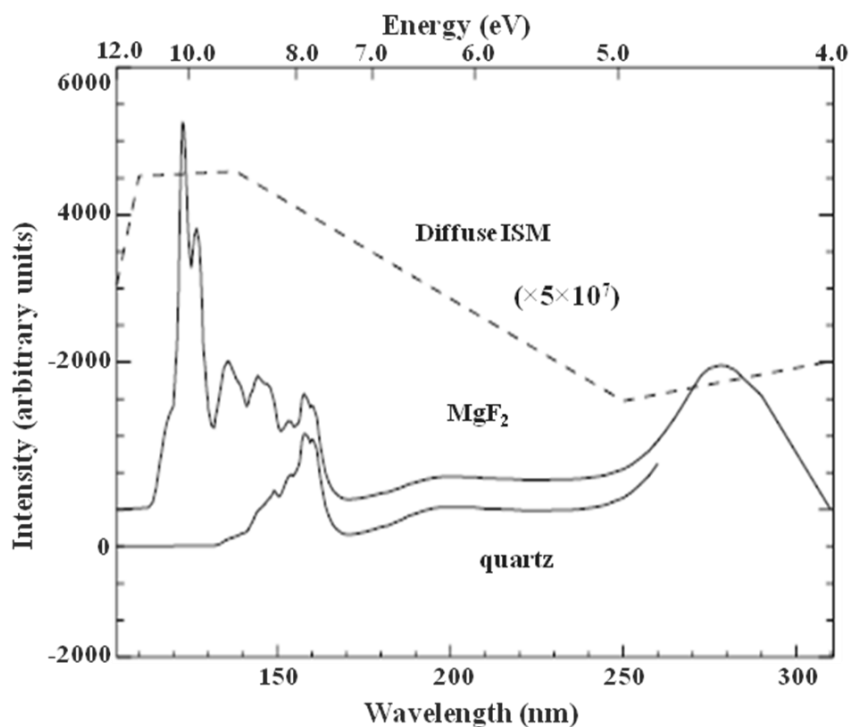


Figure 3.16: The UV internal: comparison between the observations (the upper dashed line) with the microwave stimulated hydrogen flow discharge lamp for a MgF_2 window (top line) and a quartz window (bottom line) [60].

As shown in **Figure 3.13**, the thermal desorption is included in the current model. The parameters used such as the desorption energy and the pre-exponential factor were obtained from the experimental data on desorption H_2O from amorphous SiO_2 . These parameters were taken as averages from the previous work of Collings *et al.* [62, 63] as shown in **Table 3.6**.

Table 3.6: Kinetic parameters based on CKS model [62, 63], used in the thermal desorption of H_2O .

Surface concentration molecules cm^{-2}	$\text{H}_2\text{O}(\text{ASW}) \rightarrow \text{H}_2\text{O}(\text{CSW})$		$\text{H}_2\text{O}(\text{ASW}) \rightarrow \text{H}_2\text{O}(\text{g})$		$\text{H}_2\text{O}(\text{CSW}) \rightarrow \text{H}_2\text{O}(\text{g})$	
	ν molecules $\text{cm}^{-2} \text{s}^{-1}$	E kJ mol^{-1}	ν molecules $\text{cm}^{-2} \text{s}^{-1}$	E kJ mol^{-1}	ν molecules $\text{cm}^{-2} \text{s}^{-1}$	E kJ mol^{-1}
3×10^{17}	1×10^{28}	37	1.5×10^{30}	46.6	1.5×10^{30}	47

These data have been used in the previous model of Throner [21], in an effort to model the possible routes for H₂O ice desorption with a surface concentration of 3.4×10^{17} molecules cm⁻², corresponding to 10² molecular layers adsorbed on the substrate surface. At low temperatures, in the region of 10 K, it is believed that most of the species in the gas phase are depleted within 10⁶ years by freeze-out onto the grain surfaces. This means the additional step shown in (x) has to be added to complete the reaction scheme shown in **Figure 3.13**:



This reaction is assumed to occur isothermally in the molecular cloud Barnard 68. Therefore, to produce a possible model of H₂O re-adsorption, it is necessary to consider the surface area of the dust grains per unit volume, a , in cm² cm⁻³, the hydrogen density, n_{H_2} , and the H₂O abundance in Barnard 68. The surface area of dust particles with dimensions of 10⁻⁵ cm has been previously estimated by Roberts *et al.* to be $2.4 \times 10^{-22} n_{\text{H}}$ [64]. Thus, the surface area of dust grains per unit volume in Barnard 68 ($n_{\text{H}} = 10^5$ cm³ [44, 45, 64]) is 2.4×10^{-17} cm² cm⁻³. The rate of H₂O adsorption on grains can be determined from **equation (3.29)**:

$$r_{ads} = \frac{P}{(2\pi k_B T m)^{1/2}} \quad (\text{3.29})$$

where P is the pressure, m is the molecular mass in kg, k_B is Boltzmann constant and T is the absolute temperature of the gas in K. From the ideal gas law (*i.e.* $P = mRT/MV$), **equation (3.30)** can be rewritten as the following:

$$r_{ads} = 3637 \left(\frac{T}{M} \right)^{\frac{1}{2}} N_v \quad (\text{3.30})$$

The molar mass, M , of H₂O is 18.0153 g mol⁻¹. The gas phase density of H₂O with respect to the adsorbing surface area, N_v , in molecules cm⁻², can be calculated from the volumetric gas phase concentration of H₂O, V , in molecules cm⁻³, and the surface

area of the dust grain, a , in $\text{cm}^2 \text{cm}^{-3}$. Therefore, the rate of re-adsorption for H_2O in Barnard 68 can be expressed as shown in **equation (3.31)**:

$$r_{ads} = 2.06 \times 10^{-14} T^{\frac{1}{2}} V \quad (3.31)$$

The rate constant for re-adsorption is 2.06×10^{-14} molecules $\text{cm}^{-2} \text{s}^{-1}$. Finally, it is important to consider the concentration of H_2O being adsorbed onto the dust grain surfaces. The abundance of H_2O (2.2×10^{-4} [5]) relative to the density of H atoms n_H in Barnard 68 has been used to calculate the concentration of the H_2O adsorbed onto the grain surface area per unit volume, a , to give an approximate concentration of 1×10^{18} molecules cm^{-2} .

3.5.2 Results and Discussion

Figure 3.17 shows the simulated adsorption and desorption traces for H_2O molecules in Barnard 68 under isothermal conditions ($T = 10 \text{ K}$) for $A_v = 0$ and $A_v = 6$ respectively. **Figure 3.17a** assumes that all H_2O is initially adsorbed onto dust grains with surface concentration of $\sim 10^{18}$ molecules cm^{-2} towards the edge of the cloud (*i.e.* $A_v = 0$). It can be seen that there is a significant increase in the concentration of H_2O molecules in the gas phase, reaching, with time, an equilibrium with volumetric concentration greater than 23 molecules cm^{-3} . It is also shown in **Figure 3.17a** that not all of the ice desorbs and there is a residual amount of H_2O molecules remaining on the dust surface, which, at equilibrium, is $\sim 10^{15}$ molecules cm^{-2} . This concentration of ice is too low to be observed. The equilibrium between the phases occurs after a few 10^4 years.

If all the H_2O starts in the gas phase, as shown in **Figure 3.17b**, there is a fraction of H_2O molecules adsorbed onto the dust surfaces. This results in the formation of an ice layer containing $\sim 10^{15}$ molecules cm^{-2} . It can be seen from **Figure 3.17b** that there is no significant change and the fractional concentration of water is constant. This might be due to the ambient conditions caused by the ISRF at the edge of Barnard 68. This indicates that even in situations where $A_v = 0$, ice films can remain

on grains for chemically significant timescales. The situation at the core of Barnard 68 (*i.e.* $A_v = 6$) is shown in **Figure 3.17c** and **Figure 3.17d**.

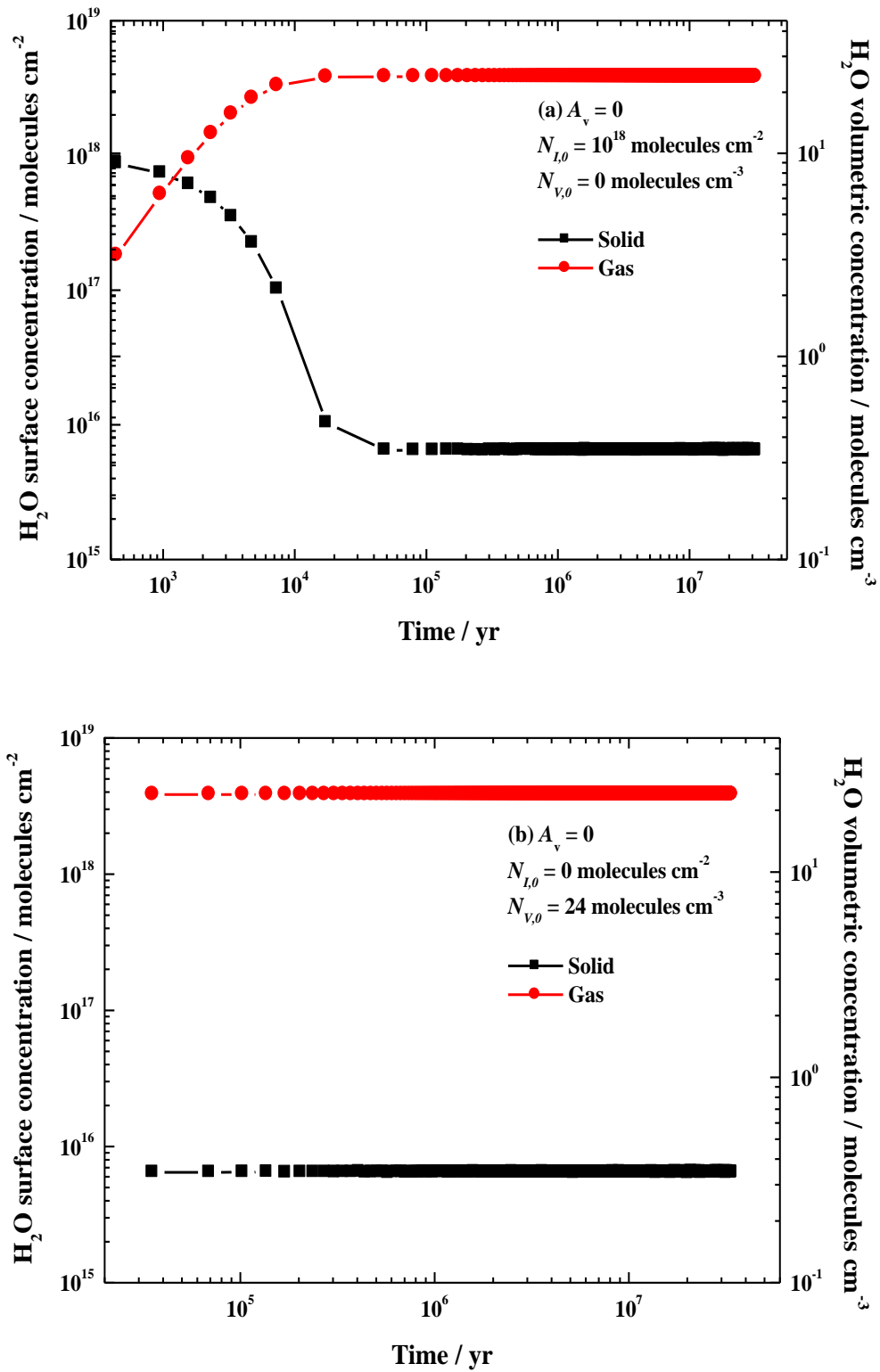


Figure 3.17: Continued on the following page.

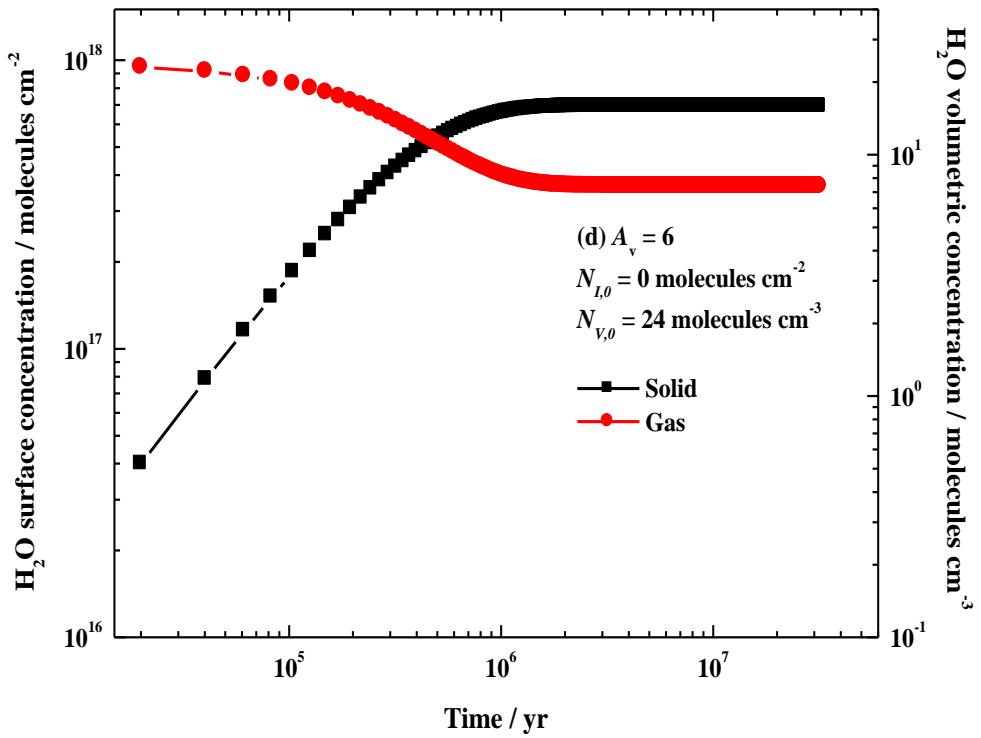
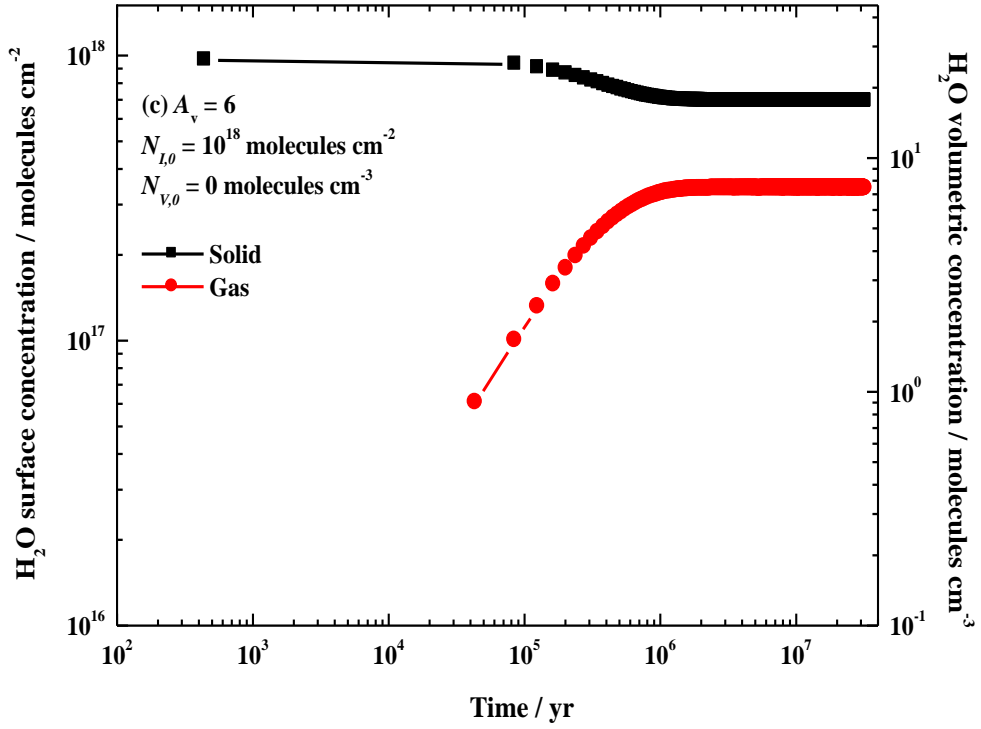


Figure 3.17: Traces showing H_2O re-adsorption at $T = 10$ K, where; (a) $A_v = 0$ (all H_2O in ice), (b) $A_v = 0$ (all H_2O in gas phase), (c) $A_v = 6$ (all H_2O in ice), and (d) $A_v = 6$ (all H_2O in gas phase). The initial concentration of H_2O as an ice is 1×10^{18} molecules cm^{-2} and as gas is 24 molecules cm^{-3} . Lines are to guide the reader's eye.

Assuming that all H₂O molecules are initially adsorbed on the surface of dust grains, with an initial concentration of $\sim 10^{18}$ molecules cm⁻², **Figure 3.17c** shows that the equilibrium of water (gas and solid phase) is reached after 10⁶ years. The increase of the H₂O gas phase (~ 7 molecules cm⁻³) is due to non-thermal desorption induced by secondary electrons and the internal VUV field, as reported in the previous model of Throner [21]. If all the H₂O was initially in the gas phase at the centre of the cloud ($A_v = 6$), as shown in **Figure 3.17d**, the model shows significant re-adsorption forming approximately 7×10^{17} molecules cm⁻² of water ice. This is predicted to occur over 10⁶ years (**Figure 3.17d**).

Figure 3.18 shows a comparison of H₂O concentration in Barnard 68 at different regions, in which $A_v = 0$, $A_v = 2$, $A_v = 4$, and $A_v = 6$. For **Figures 3.18a** and **3.18b**, where the concentrations of H₂O ice in molecules cm⁻² and the temperature is approximately 10 K, the initial concentration of H₂O ice is assumed to be 10^{18} molecules cm⁻² as shown in **Figure 3.18a**, whereas in **Figure 3.18b**, it is assumed that there is no H₂O ice adsorbed onto the surface (*i.e.* all the H₂O is in the gas phase). Significantly, the concentration of H₂O ice decreases at the edge of the cloud ($A_v = 0$) faster than in the other regions within the cloud. Moreover, the H₂O ice concentration reaches equilibrium at $A_v = 0$ within 5×10^4 yr, which is earlier than the other locations ($A_v = 2$, $A_v = 4$, and $A_v = 6$), as shown in **Figure 3.18a**.

It can clearly be seen from **Figure 3.18b** that the increase of H₂O ice concentration at $A_v = 2$ reaches equilibrium with a surface concentration of approximately 3×10^{17} molecules cm⁻² after $\sim 10^6$ yr. A significant increase in the concentration of H₂O ice, up to 8×10^{17} molecules cm⁻², can be seen more clearly toward the centre of the cloud (*i.e.* $A_v = 4$ and $A_v = 6$). In this region, the equilibrium was achieved after 2×10^6 yr. At the edge of the cloud equilibrium was reached earlier than in other regions within the clouds with a fairly constant concentration of water ice of 6×10^{15} molecule cm⁻². For **Figures 3.18c** and **3.18d**, where the concentrations of H₂O in molecules cm⁻³ and the temperature is approximately 10 K, the initial concentration of H₂O is assumed to be 24 molecule cm⁻³ as shown in **Figure 3.18d**, whereas in **Figure 3.18c**, it is assumed that there is no H₂O in the gas phase (*i.e.* all the H₂O is adsorbed on the dust

grain surfaces). The concentration of H_2O in the gas phase increases, as shown in **Figure 3.18c**, due to the desorption of H_2O ice.

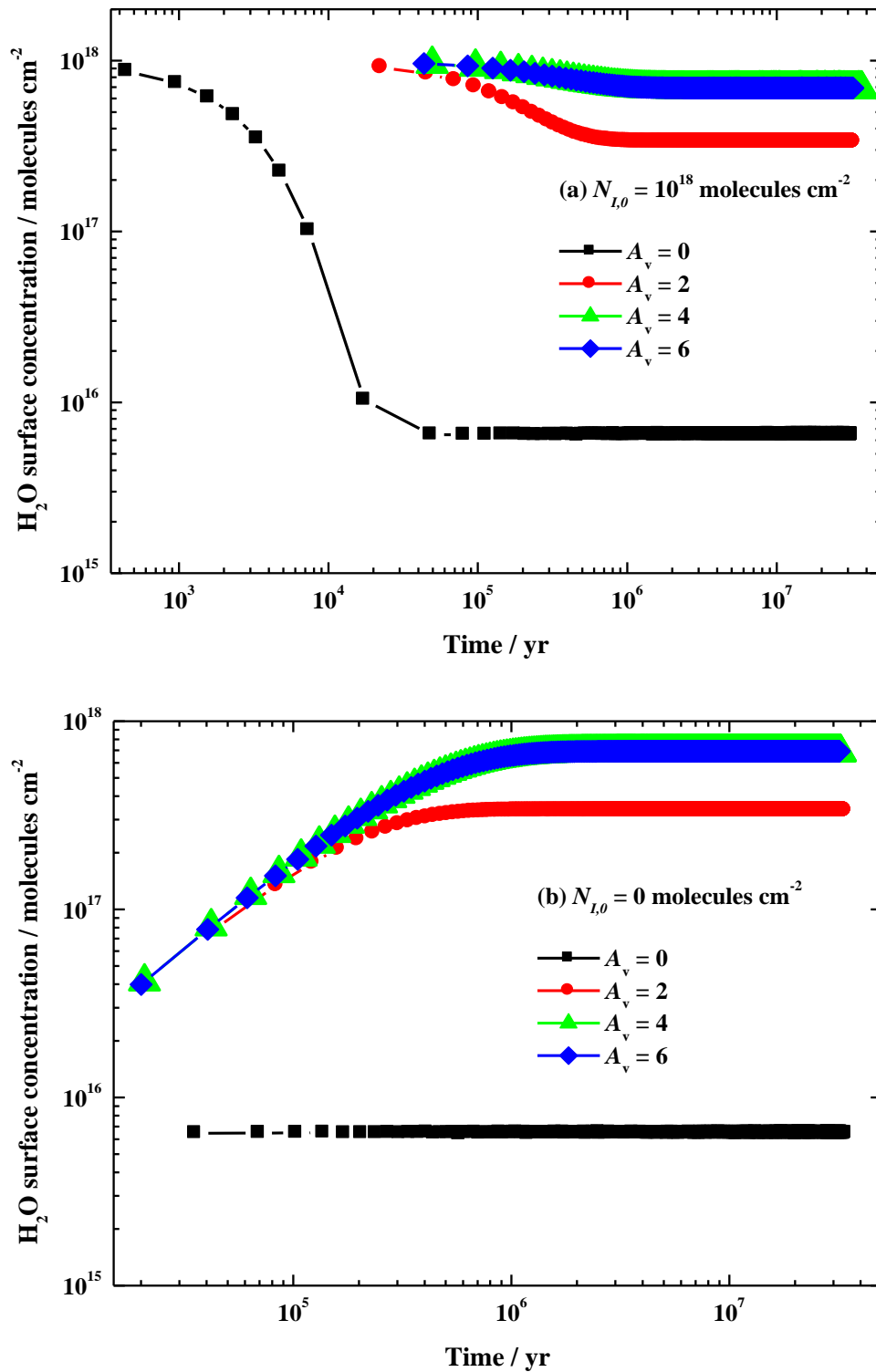


Figure 3.18: Continued on the following page.

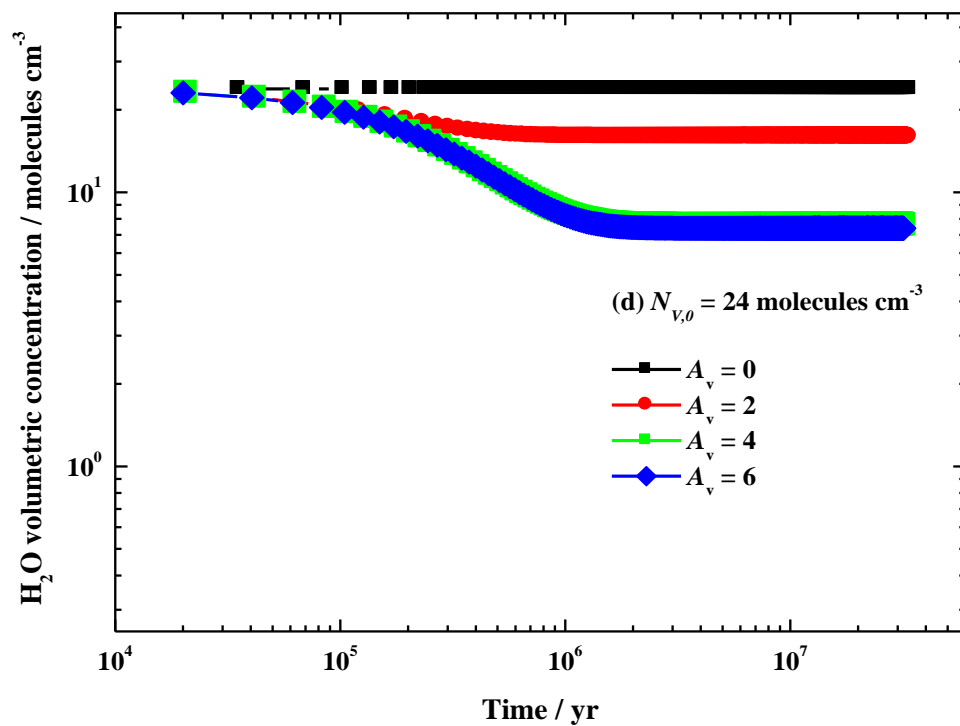
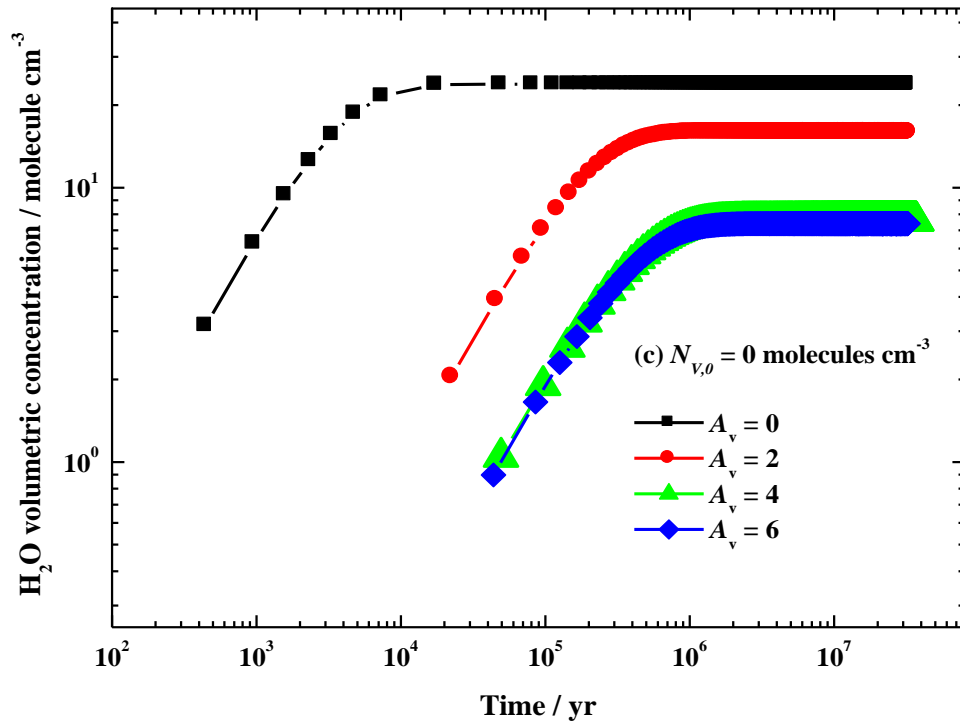


Figure 3.18: Traces showing comparison of water re-adsorption at $T = 10$ K and different values of A_v (0, 2, 4, and 6), where: (a) surface concentration of H_2O at $N_{l,0} = 1 \times 10^{18}$ molecules cm^{-2} , (b) surface concentration of H_2O at $N_{l,0} = 0$, (c) gas phase concentration of H_2O at $N_{v,0} = 0$, and (d) gas phase concentration of H_2O at $N_{v,0} = 24$ molecules cm^{-3} . Lines are to guide the reader's eye.

This starts at early times at the edge of the cloud and reaches equilibrium after a few 10^4 yr with a concentration of 22 molecules cm^{-3} . Further from the edge, towards the centre of the cloud, the concentration of gas starts to rise within 10^4 yr and continues to increase between 8×10^5 yr and 3×10^6 yr with concentrations of 17 molecules cm^{-3} for $A_v = 2$, and 7 molecules cm^{-3} for both $A_v = 4$ and 6.

With an initial gas phase concentration of 24 molecules cm^{-3} (**Figure 3.18d**), the model shows that the H_2O gas phase concentration stabilises at the edge, whereas there is a decrease in the concentration of H_2O in the cloud at $A_v = 2$, $A_v = 4$, and $A_v = 6$. At $A_v = 2$, the gas phase concentration of H_2O dropped to 18 molecules cm^{-3} at equilibrium, which occurs within 10^6 yr. This decrease is more significant at $A_v = 4$ and $A_v = 6$, where the gas phase concentration of H_2O decreased to around 8 molecules cm^{-3} and equilibrium achieved after 2×10^6 yr.

The typical timescale for the adsorption, t_{ads} , of any species can be calculated if the species are assumed to not desorb [65]. Assuming sticking probability (S) of H_2O to be equal to one and considering both the age of the molecular cloud (3×10^9 yr) and the density of H atoms (n_H), the timescale of adsorption is given by **equation (3.32)**:

$$t_{ads} = \frac{3 \times 10^9 \text{ yr}}{S(n_H / \text{cm}^{-3})} \quad (3.32)$$

Consequently, if $n_H = 1 \times 10^5 \text{ cm}^{-3}$ for B68, the ice would be expected to form within a timescale of around 3×10^4 yr. However, the simulations discussed above, which include non-thermal desorption, give a value of 1×10^6 yr for completion of the adsorption. This result is consistent with the adsorption lifetime calculations; assuming that the adsorption is a first order reaction then t_{ads} in units of s can be obtained from **equation (3.33)**:

$$t_{ads} = \frac{1}{k_{ads}} \quad (3.33)$$

This gives around 4.85×10^{13} s, corresponding to 1.50×10^6 yr, which is consistent with the timescale in this model.

In order to investigate the contribution of the thermal processing in this model, the temperature profile has to be included in this simulation. If the molecular cloud Barnard 68 is considered as a low mass star formation region, then the following equation derived by Awad *et al.* [66], can be used to determine the heating rate within each location of the cloud:

$$T_d(t, d) = 10 + 0.1927(t)^{0.5339} \times (d/R)^{-0.5} \text{ K} \quad (3.34)$$

where $T_d(t, d)$ is the temperature profile of gas and dust within the object, t is the evolutionary age of the collapsing object, d is the distance from the centre and R is the radius. According to **equation (3.34)**, it was assumed that the temperature evolves in both time and space. Therefore, **equation (3.34)** is valid for the current work. The values of d in astronomical units (AU) are known from the literature [42] and are presented in **Table 3.8**.

Table 3.8: The values of d corresponding to their A_v values.

A_v	d / AU
0	18343
2	12540
4	11030
6	9550

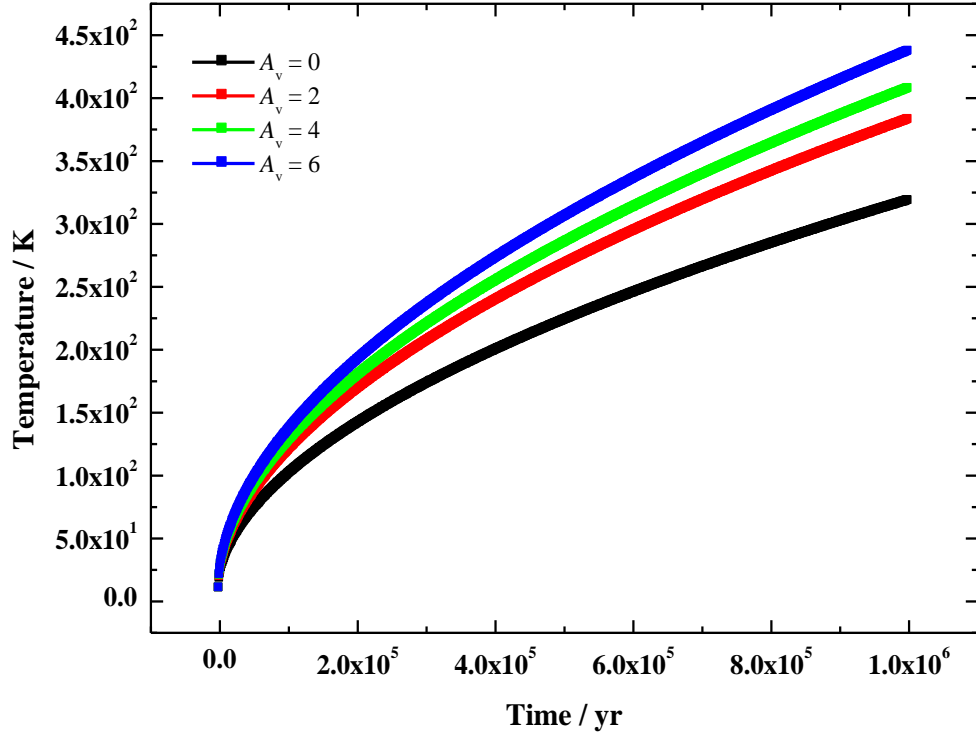


Figure 3.19: Calculated temperature profiles through the molecular cloud Barnard 68. Coloured solid lines represent; $A_v = 0$, $A_v = 2$, $A_v = 4$, and $A_v = 6$.

Figure 3.19 shows the heating rate for each A_v value corresponding to a timescale of 10^6 yr. This was obtained by simulating real values of temperature *versus* time trend. It takes approximately about 2×10^5 yr to reach 200 K, which corresponds to a heating rate of 1 K / 1000 yr.

The temperature profile has to be considered for each A_v value in this model, in an effort to compare the re-adsorption and desorption under thermal conditions. Corresponding H_2O concentrations for the simulations, including the thermal desorption, with the temperature profiles for each value of A_v are shown in **Figure 3.20**. As shown in **Figure 3.20a**, that the concentration of H_2O in the gas phase increases dramatically and achieves equilibrium within $10^4 - 10^5$ yr. This model shows also that the thermal desorption occurs faster than the re-adsorption (see **Figure 3.20b**).

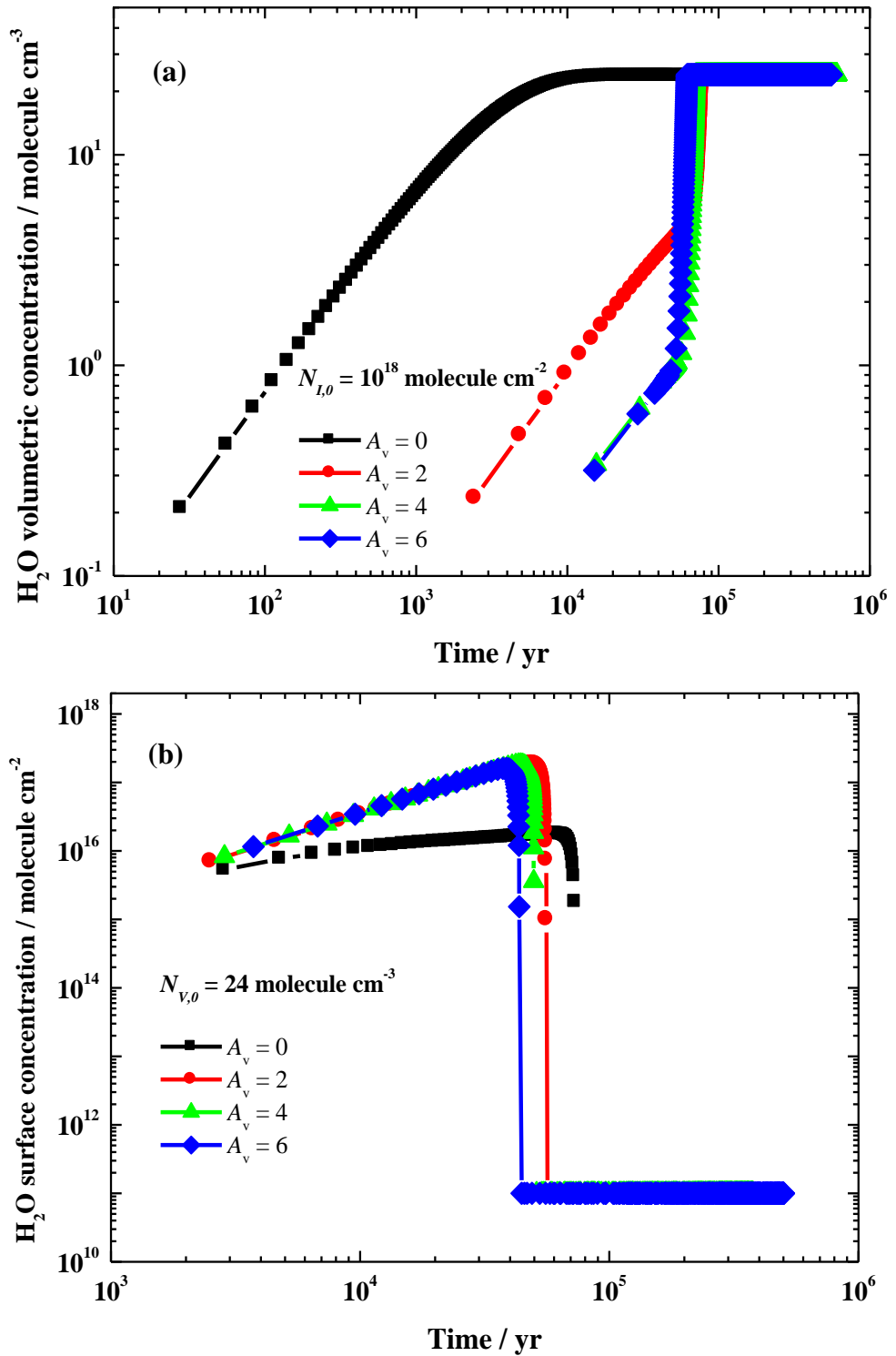


Figure 3.20: Traces showing the concentration of H₂O in the gas phase as a result of thermal processing with a heating rate of 1 K /1000 yr for $A_v = 0$, $A_v = 2$, $A_v = 4$, and $A_v = 6$, where (a) surface concentration of H₂O at $N_{L,0} = 1 \times 10^{18}$ molecules cm⁻², and (b) gas phase concentration of H₂O at $N_{V,0} = 24$ molecules cm⁻³. Lines are to guide the reader's eye.

3.5.3 Comparison of the model and the observations

The results obtained from this model were compared with the observations of Caselli and co-workers [46]. It can be seen clearly that there is a significant discrepancy between this model and the observations. At the edge of the cloud, in which $A_v = 0$, the ice abundance is about 7.7×10^{-6} , whereas, at $A_v = 6$ (towards the centre of B68) the gas phase abundance is 2.4×10^{-5} which indicates that most of water exists in the gas phase. Caselli and co-workers report that the abundance of ice is 1×10^{-4} with respect to H_2 , which is reasonable, but set an upper limit of 1.3×10^{-9} of the gas phase H_2O abundance in the centre. However, the current model gives a value more than 10^4 orders of magnitude larger than the observations. Furthermore, the gas phase abundance should reach an upper limit of about 1×10^{-7} , for $A_v \sim 2$. This suggests the presence of other processes, in addition to adsorption on grains, by which water is removed from the gas phase. Gas phase water can be rapidly dissociated into fragments upon collisions with photons, electrons, and H^+ ions. **Figure 3.21** shows the main possible routes for gas phase water dissociation. From the cross-sections of the mechanisms shown in **Figure 3.21**, along with the calculated photon and electron fluxes, the rate constants for H_2O destruction were obtained from experimental studies [67-69], as shown in **Table 3.8**.

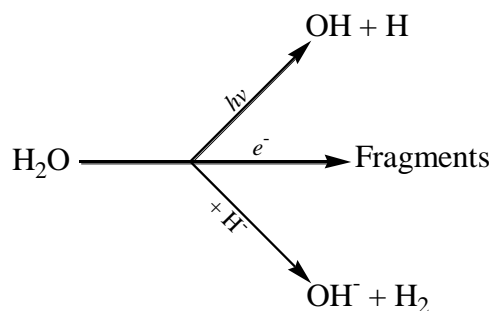


Figure 3.21: Destruction mechanisms of gas phase H_2O .

The initial values to calculate the rate constants were previously estimated. The flux of UV photons in the cloud, which is around $5 \times 10^3 \text{ cm}^{-2} \text{ s}^{-1}$, is produced by CR-induced fluorescence of H_2 [49, 58]. The cross-section of H_2O photodissociation at Lyman α wavelength is $1.2 \times 10^{-17} \text{ cm}^2$ [67]. Taking the VUV flux as before gives the rate constant for the H_2O photodissociation as $6 \times 10^{-14} \text{ s}^{-1}$. The second route suggests that H_2O molecules in the gas phase are destroyed through collisions with electrons.

Electrons in the interstellar space constitute a small percentage of the interstellar radiation.

Table 3.8: Fluxes, cross-sections and corresponding rate constants for the destruction of the H₂O gas phase.

Mechanism	Relevant flux / cm ⁻² s ⁻¹	Cross-section / cm ²	k / s ⁻¹
VUV Photon	5×10^3	1.2×10^{-17}	6×10^{-14}
e ⁻	1.7×10^{-6}	1×10^{-16}	1.7×10^{-22}

The average energy of electrons in the interstellar medium is around 100 MeV [68], which corresponds to a velocity of 1.7×10^4 cm s⁻¹. For electrons with total density of 0.03 cm⁻³ [69], the flux of electrons is *ca.* 1.7×10^{-6} cm⁻² s⁻¹. The cross-section for electron induced dissociation on gas phase H₂O at energy of 1 keV is at 1×10^{-16} cm². Thus, the rate constant of the H₂O destruction is 1.7×10^{-22} s⁻¹.

The destruction of gas phase water through collision with hydrogen anions has been measured to occur with a rate coefficient of 4.8×10^{-9} cm³ s⁻¹ [70]. Ross *et al.* report that the hydrogen anion density in the transition zone of planetary nebulae is in the range from 1×10^{-5} cm⁻³ to 1×10^{-4} cm⁻³ [71]. Therefore, the rate constant is greater than 4.8×10^{-14} s⁻¹. As there is no evidence of the presence of hydrogen anions in the molecular cloud B68, it is likely that the rate constant for this pathway would be much less than 10^{-14} s⁻¹ in pseudo first-order conditions.

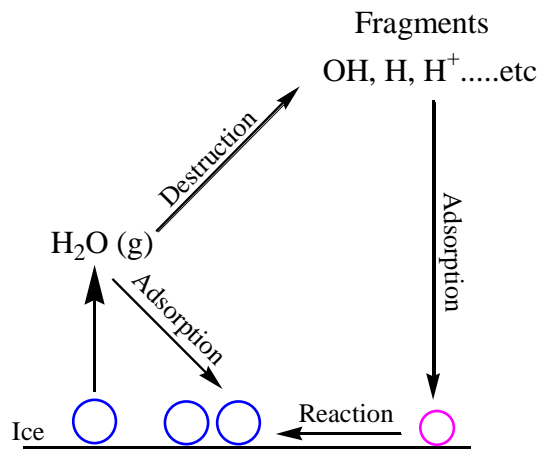


Figure 3.22: Illustration of the proposed mechanism of H₂O cycle in the interstellar medium.

It is clear from **Table 3.8** that VUV photodissociation dominates the H₂O destruction pathways in dense environments. Indeed, it is probably sufficient to account for the discrepancy between this work (*i.e.* the ‘Toy’ model) and observations. A more complete model should incorporate the processes illustrated by the cycle in **Figure 3.22** and reconsider the adsorption of H₂O fragments, from which fast surface recombination can occur.

3.6 Conclusion and Astrophysical Implications

The thermal desorption of water ice from amorphous silica has been studied in the surface astrochemistry laboratory under conditions close to those dominant in the ISM. The results obtained from TPD measurements for water film exposures ranging from 0.7 to 350 L show that the desorption of water ice from an amorphous silica surface follows zeroth-order kinetics. This also provides important information relevant to the ice morphology. The zeroth-order desorption kinetics from sub-monolayer exposures suggests an island growth mechanism. The formation of islands shows that water does not wet the silica. The evidence for transformation of an amorphous phase into crystalline phase appears in the observation of two desorption peaks for water films, in particular at exposures of 3.5, 7 L and above. These TPD results are in agreement with previous studies, in that desorption of water ice from graphite has desorption energies in the range between 39 kJ mol⁻¹ and 42 kJ mol⁻¹. The desorption at high temperatures (~ 180 K), for surface exposures greater than 35 L, demonstrates the strength of H₂O-H₂O interactions *via* H-bonding, resulting in clustering and islanding.

Measurements of EPD show that water films desorb under electron bombardment. Cross-sections are in the range of $1.6 \pm 0.1 \times 10^{-16} - 5.2 \pm 0.6 \times 10^{-16} \text{ cm}^2$ (250 - 350 eV), which are large compared to photon interaction cross-sections which are $10^2 - 10^3$ times smaller. This means electron-promoted desorption initiated by CR irradiation could be important in astrophysical environments dominated by CRs.

The concentration of H₂O molecules in both solid and gas phases within interstellar molecular clouds was studied using a ‘Toy’ Model, using the molecular cloud Barnard 68 as a case study. These simulations combine kinetic parameters for regions of the cloud for which observations exist. The results of ‘Toy’ kinetics

model demonstrate that most H₂O molecules are in ice films in the cloud core. However, non-thermal desorption ensures a small equilibrium gas phase concentrations of H₂O can be produced at ice concentrations of 8×10^{17} molecules cm⁻²; this equilibrium can occur within 10⁶ yr. This model also shows that the re-adsorption is more significant toward the centre of the cloud ($A_v = 2$, $A_v = 4$, and $A_v = 6$) where the non-thermal processes are dominant. This model showed a significant discrepancy compared with the observations, which is likely to be the result of a rapid dissociation of gas phase water by VUV photons.

3.7 References

- [1] A. H. Delsemme, *J. Phys. Chem.*, 1983, **87**, 4214.
- [2] E. L. Gibb, D. C. B. Whittet, W. A. Schutte, A. C. A. Boogert, J. E. Chiar, P. Ehrenfreund, P. A. Gerakiness, J. V. Keane, A. G. G. M. Tielens, E. F. Van Dishoeck, and O. Kerkhof, *Astrophys. J.*, 2000, **536**, 347.
- [3] J. Klinger, *J. Phys. Chem.*, 1983, **87**, 4209.
- [4] A. C. A. Boogert, P. Ehrenfreund, *Astrophysics of Dust: ASP Conference Series*, 2004, 309, 547
- [5] E. A. Bergin, S. Maret, F. F. S. Van der Tak, J. Alves, S. M. Carmody, and C. J. Lada, *Astrophys. J.*, 2006, **645**, 369.
- [6] K. M. Pontoppidan, C. P. Dullemond, E. F. van Dishoeck, G. A. Blake, A. C. A. Boogert, N. J. Evans, J. E. Kessler-Silacci, and F. Lahuis, *Astrophys. J.*, 2005, **622**, 463.
- [7] N. Watanabe and A. Kouchi, *Prog. Surf. Sci.*, 2008, **83**, 439.
- [8] P. G. Debenedetti, *J. Phys.: Condens. Matter*, 2003, **15**, R1669.
- [9] M. T. Capria, *Earth Moon Planets*, 2002, **89**, 161.
- [10] R. Saladino, C. Crestini, S. Pino, G. Costanzo, and E. Di Mauro, *Phys. Life Rev.*, 2012, **9**, 84.
- [11] P. Jenniskens and D. F. Blake, *Science*, 1994, **265**, 753.
- [12] L. J. Allamandola, M. P. Bernstein, S. A. Sandford, and R. L. Walker, *Space. Sci. Rev.*, 1999, **90**, 219.
- [13] H. M. Butner, S. B. Charnley, C. Ceccarelli, S. D. Rodgers, J. R. Pardo, B. Parise, J. Cernicharo, and G. R. Davis, *Astrophys. J.*, 2007, **659**, L137.
- [14] H. Mokrane, H. Chaabouni, M. Accolla, E. Congiu, F. Dulieu¹, M. Chehrouri, and J. L. Lemaire, *Astrophys. J.*, 2009, **705**, L195.

- [15] A. Ratajczak, E. Quirico, A. Faure, B. Schmitt, and C. Ceccarelli, *Astron. Astrophys.*, 2009, **496**, L21.
- [16] The Submillimeter Wave Astronomy Satellite (SWAS): Observing the Chemical Evolution of Molecular Clouds, <http://www.cfa.harvard.edu/swas/science2.html> (accessed on 12/11/2012)
- [17] D. A. Neufeld, S. Lepp, G. J. Melnick, *Astrophys. J. Suppl.*, 1995, **100**, 132.
- [18] M. Elitzur and T. de Jong, *Astron. Astrophys.*, 1978, **67**, 323.
- [19] G. J. Melnick and E. A. Bergin, *Adva. Space. Res.*, 2005, **36**, 1027.
- [20] H. M. Cuppen and E. Herbst, *Astrophys. J.*, 2007, **668**, 294.
- [21] J. D. Thrower, *PhD Thesis*, (Heriot-Watt University, Edinburgh, 2009).
- [22] IDP image obtained from Wikipedia with permission from E. K. Jessberger. http://en.wikipedia.org/wiki/File:Porous_chondriteIDP.jpg (accessed on 12/01/2013).
- [23] R. S. Smith, C. Huang, E. K. L. Wong, and B. D. Kay, *Surf. Sci.*, 1996, **367**, L13.
- [24] R.S. Smith, C. Huang, E. K. L. Wong, and B. D. Kay, *Phys. Rev. Lett.*, 1997, **79**, 909.
- [25] R. J. Speedy, P. G. Debenedetti, R. S. Smith, C. Huang, and B. D. Kay, *J. Chem. Phys.*, 1996, **105**, 240.
- [26] E. Habenschaden and J. Küppers, *Surf. Sci. Lett.*, 1984, **138**, L147.
- [27] P. A. Thiel and T. E. Madey, *Surf. Sci. Rep.*, 1987, **7**, 211.
- [28] D. R. Haynes, N. J. Tro, and S. M. George, *J. Phys. Chem.*, 1992, **96**, 8502.
- [29] D. M. Murphy and T. Koop, *Quart. J. Roy. Meteor. Soc.*, 2005, **131**, 1539.
- [30] S. Kaya, J. Weissenrieder, D. Stacchiola, S. Shaikhutdinov, and H.-J. Freund, *J. Phys. Chem. C*, 2007, **111**, 759.
- [31] R. Feistel and W. Wagner, *Geochim. Cosmochim. Ac.*, 2007, **71**, 36.

- [32] A. S. Bolina, A. J. Wolff, and W. A. Brown, *J. Phys. Chem. B.*, 2005, **109**, 16836.
- [33] M. R. S. McCoustra, *Lecture Notes on Surface Science*, Heriot-Watt University, Fall 2010.
- [34] CKS 1.0, IBM Almaden Research Center, © IBM Corporation 1995.
- [35] H. Cottin, M. H. Moore, and Y. Bénilen, *Astrophys. J.*, 2003, **590**, 874.
- [36] P. A. Gerakines, W. A. Schutte, and P. Ehrenfreund, *Astron. Astrophys.*, 1996, **312**, 289.
- [37] P. Ehrenfreund, M. P. Bernstein, J. P. Dworkin, S. A. Sandford, and L. J. Allamandola, *Astrophys. J.*, 2001, **550**, L95.
- [38] G. A. Kimmel, T. M. Orlando, P. Cloutier, and L. Sanche, *J. Phys. Chem. B.*, 1997, **101**, 6301.
- [39] N. Timneanu, C. Caleman, J. Hajdu, and D. van der Spoel, *Chem. Phys.*, 2004, **299**, 277.
- [40] N. S. Faradzhev, K. L. Kostov, P. Feulner, T. E. Madey, and D. Menzel, *Chem. Phys. Lett.*, 2005, **415**, 165.
- [41] E. Alizadeh and L. Sanche, *Chem. Rev.*, 2012, **112**, 5578.
- [42] Y. Itikawa and N. Mason, *J. Phys. Chem. Ref. Data*, 2005, **34**, 1.
- [43] C. Laffon, S. Lacombe, F. Bournel and Ph. Parent, *J. Chem. Phys.*, 2006, **125**, 204714.
- [44] D. Hollenbach, M. J. Kaufman, E. A. Bergin, and G. J. Melnick, *J. Astrophys.*, 2009, **690**, 1497.
- [45] J. F. Alves, C. J. Lada, and E. A. Lada, *Nature*, 2001, **409**, 159.
- [46] P. Caselli, E. Keto, L. Pagani, Y. Aikawa, U. A. Yıldız, F. F. S. van der Tak, M. Tafalla, E. A. Bergin, B. Nisini, C. Codella, E. F. van Dishoeck, R. Bachiller, A. Baudry, M. Benedettini, A. O. Benz, P. Bjerkeli, G. A. Blake, S. Bontemps, J. Braine, S. Bruderer, J. Cernicharo, F. Daniel, A. M. di Giorgio, C. Dominik, S.

- D. Doty, P. Encrenaz, M. Fich, A. Fuente, T. Gaier, T. Giannini, J. R. Goicoechea, Th. de Graauw, F. Helmich, G. J. Herczeg, F. Herpin, M. R. Hogerheijde, B. Jackson, T. Jacq, H. Javadi, D. Johnstone, J. K. Jørgensen, D. Kester, L. E. Kristensen, W. Laauwen, B. Larsson, D. Lis, R. Liseau, W. Luinge, M. Marseille, C. McCoey, A. Megej, G. Melnick, D. Neufeld, M. Olberg, B. Parise, J. C. Pearson, R. Plume, C. Risacher, J. Santiago-García, P. Saraceno, R. Shipman, P. Siegel, T. A. van Kempen, R. Visser, S. F. Wampfler, and F. Wyrowski, *Astron. Astrophys.*, 2010, **521**, L29.
- [47] M. S. Westley, R. A. Baragiola, R. E. Johnson, and G. A. Baratta, *Planet. Space Sci.*, 1995, **43**, 1311.
- [48] M. S. Westley, R. A. Baragiola, R. E. Johnson, and G. A. Baratta, *Nature*, 1995, **373**, 405.
- [49] C. J. Shen, J. M. Greenberg, W. A. Schutte, and E. F. van Dishoeck, *Astron. Astrophys.*, 2004, **415**, 203.
- [50] V. Mennella, G. A. Baratta, A. Esposito, G. Ferini, and Y. J. Pendleton, *Astrophys. J.*, 2003, **587**, 727.
- [51] J. F. Ziegler, J. P. Biersack, and M. D. Ziegler, *The Stopping and Range of Ions in Solids*, (Pergamon Press, New York, 2008), see also <http://www.srim.org/>.
- [52] W. F. Schmidt and E. Illenberger, *Nukleonika*, 2003, **48**, 75.
- [53] M. Vinodkumar, K. N. Joshipura, C. G. Limbachiya, and B. K. Antony, *Nucl. Instrum. Methods Phys. Res. B*, 2003, **212**, 63.
- [54] K. A. Long and H. G. Paretzke, *J. Chem. Phys.*, 1991, **95**, 1049.
- [55] M. Dingfelder, A. Travia, R. A. McLawhorn, J. L. Shinpaugh, and L. H. Toburen, *Radiat. Phys. Chem.*, 2008, **77**, 1213.
- [56] J. S. Mathis, P. G. Mezger, and N. Panagia, *Astron. Astrophys.*, 1983, **128**, 212.
- [57] J. D. Thrower, A. G. M. Abdulgalil, M. P. Collings, M. R. S. McCoustra, D. J. Bruke, W. A. Brown, A. Dawes, P. J. Holtom, P. Kendall, N. J. Mason, F. Jamme, H. J. Fraser, and F. J. M. Rutten, *J. Vac. Sci. Technol. A*, 2010, **28**, 799.

- [58] S. S. Prasad and S. P. Tarafdar, *Astrophys. J.*, 1983, **267**, 603.
- [59] K. I. Oberg, H. Linnartz, R. Visser, and E. F. van Dishoeck, *Astrophys. J.*, 2009, **693**, 1209.
- [60] G. M. Munoz Caro and W. A. Schutte, *Astron. Astrophys.*, 2003, **412**, 121.
- [61] N. J. Mason, A. Dawes, P. D. Holtom, R. J. Mukerji, M. P. Davis, B. Sivaraman, R. I. Kaiser, S. V. Hoffmann, and D. A. Shaw, *Faraday. Discuss.*, 2006, **133**, 311.
- [62] M. P. Collings, J. W. Dever, H. J. Fraser, and M. R. S. McCoustra, *Astrophys. Space Sci.*, 2003, **285**, 633.
- [63] H. J. Fraser, M. P. Collings, M. R. S. McCoustra, and D. A. Williams, *Mon. Not. R. Astron. Soc.*, 2001, **327**, 1165.
- [64] J. F. Roberts, J. M. C. Rawlings, S. Viti and D. A. Williams, *Mon. Not. R. Astron. Soc.*, 2007, **382**, 733.
- [65] D. A. Williams and S. D. Taylor, *Quart. J. Roy. Astron. Soc.*, 1996, **37**, 565.
- [66] Z. Awad, S. Viti, M. P. Collings, D. A. Williams, *Mon. Not. R. Astron. Soc.*, 2010, **407**, 2511.
- [67] E. F. van Dishoeck, B. Jonkheida and M. C. van Hemertb, *Faraday Discuss.*, 2006, **133**, 231.
- [68] M. Padovani, D. Galli, and A.E. Glassgold, *Astron. Astrophys.*, 2009, **501**, 619.
- [69] J. Lequeux, *The Interstellar Medium*, (Springer-Verlag, Berlin, 2005).
- [70] O. Martinez Jr., Z. Yang, N. J. Demarais, T. P. Snow, and V. M. Bierbaum, *Astrophys. J.*, 2010, **720**, 173.
- [71] T. Ross, E. J. Baker, T. P. Snow, J. D. Destree, B. L. Rachford, *Astrophys. J.*, 2008, **684**, 358.

CHAPTER – 4 Surface Science of Acetonitrile on Model Grain

Surfaces

Contents

4.1 Introduction.....	119
4.2 Acetonitrile (CH₃CN).....	119
4.3 Experimental Procedure	123
4.4 Results and Discussion	124
4.4.1 TPD of CH ₃ CN.....	124
4.4.1.1 CH ₃ CN Adsorbed on Amorphous SiO ₂	124
4.4.1.1.1 Sub-monolayer and Monolayer Analysis	125
4.4.1.1.2 Multilayer Analysis.....	128
4.4.1.2 TPD of CH ₃ CN Adsorbed on ASW.....	133
4.4.2 RAIRS of CH ₃ CN.....	133
4.4.2.1 CH ₃ CN Adsorbed on Amorphous SiO ₂	133
4.4.2.2 CH ₃ CN Adsorbed on ASW	139
4.4.2.3 Annealed CH ₃ CN / ASW	147
4.5 Conclusions.....	150
4.6 References.....	153

4.1 Introduction

This chapter investigates the chemistry of acetonitrile (CH_3CN) under astrophysically relevant conditions. CH_3CN is one of the key molecules in the interstellar medium (ISM), given its availability (*i.e.* detection and abundance), reactivity and also its relationship with the interstellar icy environment, as a potential precursor of amino acids. The following chapter focuses on the structure and spectroscopy of solid CH_3CN adsorbed on an amorphous silica film and on water ice. TPD studies on both substrates allow us to interrogate the growth morphology of CH_3CN thin films and to some extent the nature of interactions at the $\text{CH}_3\text{CN}/\text{H}_2\text{O}$ and $\text{CH}_3\text{CN}/\text{SiO}_2$ interfaces. RAIRS probes these interactions more directly.

4.2 Acetonitrile (CH_3CN)

Nitrogen-bearing species, in particular nitriles, represent a large class of interstellar molecules; they range from small molecules with three atoms such as XCN ($\text{X}=\text{H}$, R , OH , or O-R) to larger molecules with thirteen atoms such as HC_{10}CN [1]. It is also likely that nitrile structures are included in heteroatomic polycyclic aromatic hydrocarbons (PANHs). **Table 4.1** shows the nitrile molecules observed in Titan's atmosphere, cometary comae, and in the ISM [2]. In the latter, CN-bearing species in the gas phase such as HCN , CH_3CN , CH_2CHCN , $\text{CH}_3\text{CH}_2\text{CN}$ were detected through their rotational spectra at radio frequencies [3]. The abundance of these molecules in cold clouds is as low as $1 \times 10^{-4} \text{ cm}^{-3}$ but this value increases by a factor of 10 in hot cores where the warm up of grain surfaces may play a crucial role in the enrichment of the gas *via* desorption [4, 5]. Infrared spectral investigations toward dust-embedded protostars have shown a characteristic feature at $4.62 \mu\text{m}$ (2165 cm^{-1}) for XCN molecules. However, this feature was not detected in the lines of sight towards quiescent molecular clouds or diffuse regions of the interstellar medium [6]. This suggests that XCN might be a product of gas-grain reactions in star forming regions. On the other hand, whether this feature can account for all CN-bearing species or only for some of them is still debated. Since the majority of nitrile CN stretching frequencies are located between $4.50 - 4.57 \mu\text{m}$ ($2225\text{-}2190 \text{ cm}^{-1}$), the feature at $4.62 \mu\text{m}$ appears to be related to the $-\text{O}-\text{C}\equiv\text{N}$ group. Laboratory investigations on

molecules containing this group (in its ionic and/or radical form) are consistent with the value obtained from the astronomical observations [7-11].

Table 4.1: CN-bearing molecules observed in three different galactic environments [2].

Molecule	Titan's Atmosphere	Comets	ISM
Acetonitrile (CH ₃ CN)	✓	✓	✓
Propionitrile (CH ₃ CH ₂ CN)	-	-	✓
Isobutyronitrile ((CH ₃) ₂ CHCN)	-	-	-
Trimethylacetone ((CH ₃) ₃ CCN)	-	-	-
Acrylonitrile (CH ₂ CHCN)	-	-	✓
Cyanoacetylene (HCCCN)	✓	✓	✓
Cyanogen (C ₂ N ₂)	✓	-	-

These findings confirm that most of the nitriles observed in the ISM exist in the gas phase, and it is also likely that there may be unidentified nitriles, which remain undetected using current techniques.

Acetonitrile (CH₃CN) is a simple organic molecule that contains the nitrile group. CH₃CN (see **Table 4.1**) is observed in various environments in outer space, such as a cold molecular cloud (L134N), protostellar ices (NGC7538:IRS9), protostellar hot core gas (Sgr B2 (N)) and in a cometary coma (Hale-Bopp) [12]. **Table 4.2** shows the gas phase concentration of CH₃CN in planetary, cometary, and interstellar environments [13, 14].

Table 4.2: Gas phase concentration of CH₃CN in space.

Environment	Concentration / molecule cm ⁻³
Titan's atmosphere	1×10 ⁻⁵ [15]
Cometary Comae (Hale-Bopp)	(1.2-5.3)×10 ⁻⁶ [16]
Cold molecular clouds (L134N)	<2×10 ⁻³⁰ [17]
Hot cores Sgr B ₂ (N)	1.3×10 ⁻¹² [18]

There are four pathways likely to be the main routes to CH₃CN formation:

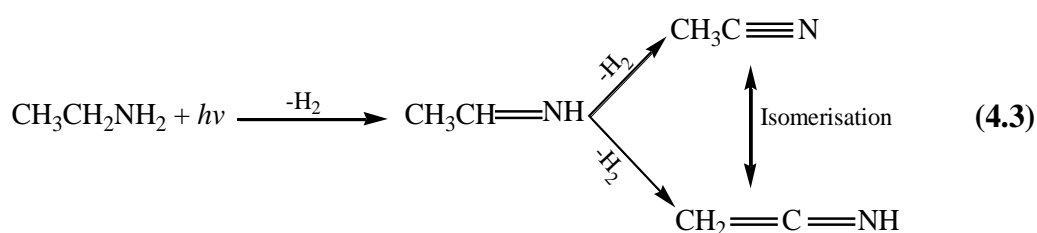
- i. Photolysis of acetamide (CH₃C(O)NH₂) in hot cores results in the production of CH₃CN and H₂O through **reaction (4.1)** [19, 20]:



- ii. Recombination of CN with CH₃ radicals on grain surfaces. It is likely that most of the gas-phase CH₃CN is supplied by desorption from ices after **reaction (4.2)** [21]:



- iii. CH₃CN is also formed on the grain surface at early times during star formation, by the hydrogenation of C₂N [21].
- iv. The existence of acetonitrile and amino acetonitrile in hot cores suggests new pathways to forming both molecules; laboratory studies show that irradiation of ethylene amine with photons results in CH₃CN and CH₂CHNH (amino acetonitrile) *via* dehydrogenation, **reaction (4.3)** [22].



Small molecules with a CN group (*e.g.* CH₃CN) are known to condense easily with several solid surfaces. The chemistry of solid CH₃CN has been given considerable attention because of the role CH₃CN plays in the formation of complex molecules such as amino acids. In the early Solar System, amino acids that may have formed would not have been capable of surviving in the strong UV field of the young star. In contrast, nitriles, with their high photostability, are likely to survive, reach the planetary surface and undergo hydrolysis to form their corresponding acids. For instance, acetonitrile (CH₃CN) and aminoacetonitrile (H₂NCH₂CN) are destroyed by photons approximately 5-10 times more slowly than acetic acid (CH₃COOH) and glycine (H₂NCH₂COOH) [23].

From the prebiotic chemistry point of view, a number of larger molecules such as cyanohydrins and aminonitriles are likely to form on meteoritic bodies *via* Strecker synthesis. This assumes that the reactions between an aldehyde (RCHO), ammonia (NH₃), and hydrogen cyanide (HCN) in water would result in the formation of amino acids, as shown in the following reaction, starting from formaldehyde (H₂CO) to eventually produce glycine (H₂NCH₂COOH) [24, 25]:

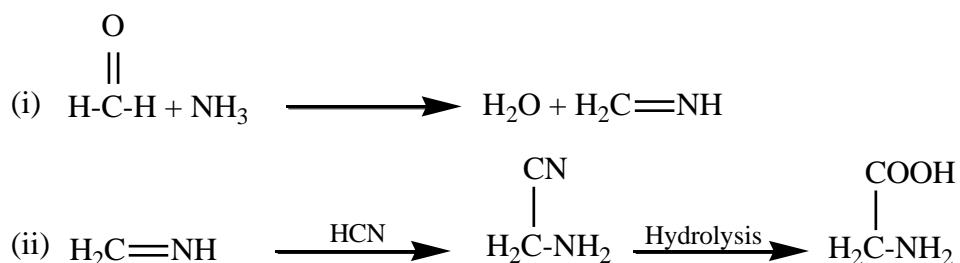


Figure 4.1: Schematic reactions of Strecker synthesis.

Amino acid analogues such as iminodicarboxylic acids (α -amino acids) were detected recently in the Murchison meteorite. Such molecules are important in answering some of the questions on the origin of life. The observation of those molecules suggests that Strecker reactions are likely to play a crucial role in forming extraterrestrial amino acids. However, there is a controversy surrounding the Strecker synthesis, given the recent detection of derivatives of amino acids in the Murchison meteorite. These are much more enriched in deuterium than the

corresponding hydrogenic acids [26-28]. Thus, this observation is inconsistent with Strecker reaction products [29]. Undoubtedly, there are many questions remaining in relation to potential mechanisms for forming amino acids.

Due to its CN reactive group, CH₃CN is considered as an important starting compound in chemical reactions leading to the formation of complex species observed in the ISM. In addition, CH₃CN was very probably delivered onto the Earth through an early bombardment by comets or asteroids, where it was involved in prebiotic chemistry resulting in the production of amino acids [30]. CH₃CN is therefore a good candidate for tracing the origin of complex species. The interactions of CH₃CN with a variety of solid surfaces have also been investigated and well characterized [31-35]. An additional insight into the surface chemistry of solid CH₃CN *via* spectroscopic and kinetic investigations would provide more information of how such a molecule may interact with amorphous SiO₂ and H₂O/SiO₂ surfaces.

4.3 Experimental Procedure

All experiments in this chapter were carried out in the UHV chamber described in **Chapter 2**. The substrate was cleaned before dosing by heating to 475 K for 5-10 minutes. Deposition of water and acetonitrile onto the cool surface of the substrate was performed typically at 108 K through separate dosing lines; water was dosed from a molecular beam system, whereas acetonitrile (99.9% supplied by Fisher Scientific) was deposited from a gas manifold line. Both ultrapure water from the beam source and acetonitrile were further purified by several freeze-pump-thaw cycles in order to remove dissolved gases. For TPD, a sequence of different CH₃CN layers was deposited on the bare silica surface as follows: 0.1, 0.2, 0.5, 1, 2, 5, 10, 20, 50, 100, 200 and 500 L (1 L = 1 × 10⁻⁶ Torr s). The TPD experiments were carried out with a linear heating ramp of 0.09 K s⁻¹, using a suitable power supply (Farnell Type H60/50) and temperature controller (Eurotherm 2404). The desorbed species were observed using a quadrupole mass spectrometer (VG Quadrupole Micromass PC300D) facing the substrate. For RAIRS, layers of acetonitrile (0.1, 0.2, 0.5, 1, 2, 5, 10, 20, 50, 100, 200, and 500 L) were deposited on the bare silica surface and on 14 L compact Amorphous Solid Water (c-ASW). c-ASW is produced after deposition of gas-phase water onto the cold surface of the substrate between approximately 70 and

130 K [36]. RAIR spectra were recorded before (*i.e.* the background spectrum) and after deposition of the samples by means of a Nicolet spectrometer (Nexus 870 FT-IR). Spectra were acquired by the co-addition of 1024 scans with a resolution of 2 cm^{-1} .

4.4 Results and Discussion

4.4.1 TPD of CH_3CN

4.4.1.1 CH_3CN Adsorbed on Amorphous SiO_2

Pressure measurements are made using an uncorrected ion gauge. However, real pressures can be estimated using relative ionisation coefficients. These are approximately 1 for H_2O and 2 for CH_3CN [37]. Therefore, the real exposures to H_2O are not changed by the consideration of the ionisation coefficient, whereas the real exposures to CH_3CN are divided by 2. The exposures were then corrected as 0.05, 0.1, 0.25, 0.5, 1.0, 2.5, 5.0, 10, 25, 50, 100, and 250 L. In order to calculate the thickness of the resulting CH_3CN films, the concentration of molecules adsorbed, Θ_{ads} , on the surface should be estimated. Θ_{ads} can be obtained from the following expression:

$$\Theta_{ads} = \frac{Pt}{\sqrt{2\pi mk_B T}} \quad (4.4)$$

In order to calculate the thickness of CH_3CN layers adsorbed on silica surface, the exposure unit (*i.e.* Torr s) should be converted into SI units, which are Pa s. The temperature T is assumed to be room temperature, 298 K, and k_B is Boltzmann's constant. For CH_3CN , the molecular mass is 6.816×10^{-26} kg. The sticking probability is assumed to be equal to one at the experimental temperature, and therefore all molecules stick onto the surface. The concentrations of CH_3CN adsorbed on the silica surface are presented in **Table 4.3**. To calculate the CH_3CN thickness, the density, ρ , of CH_3CN will be used in these calculations. It is known from the literature that amorphous solid CH_3CN has a structure close to that of liquid CH_3CN , and thus the mass density of solid CH_3CN was assumed to be similar to the pure CH_3CN in liquid phase (0.785 g cm^{-3}) [38]. This corresponds to a molecular density

of 1.15×10^{22} molecules cm^{-3} . From the surface concentrations and this density, the thicknesses of the layers are estimated and listed in **Table 4.3**.

Table 4.3: Surface concentrations of CH_3CN and estimated thicknesses.

Exposure / L	Surface concentration / molecules cm^{-2}	Thickness / nm
1.0	3.16×10^{14}	0.275
2.5	7.89×10^{14}	0.686
5.0	1.58×10^{15}	1.37
10	3.16×10^{15}	2.75
25	7.89×10^{15}	6.86
50	1.58×10^{16}	13.7
100	3.16×10^{16}	27.5
250	7.89×10^{16}	68.6

4.4.1.1.1 *Sub-monolayer and Monolayer Analysis*

Figure 4.2a shows the TPD traces of low coverages (0.05 – 1 L) of CH_3CN desorbing from silica. The traces exhibit trailing edges, which is usually characteristic of second order desorption following recombination reactions. However, CH_3CN molecules initially dosed are not expected to decompose on the silica surface and the apparent second order desorption does not follow recombinative desorption. Alternatively, previous studies by Thrower have shown that this behaviour is due to the silica surface, which presents various binding sites with different binding energies [39]. The adsorbed CH_3CN molecules in the sub-monolayer in interaction with silica experience various binding environments, and have different binding energies. The CH_3CN molecules are mobile on the silica surface at the deposition temperature, and therefore the molecules deposited first can probe the surface and find the more strongly binding sites; therefore, the lowest coverages are more strongly bonded and desorb at higher temperature, around 160-180 K.

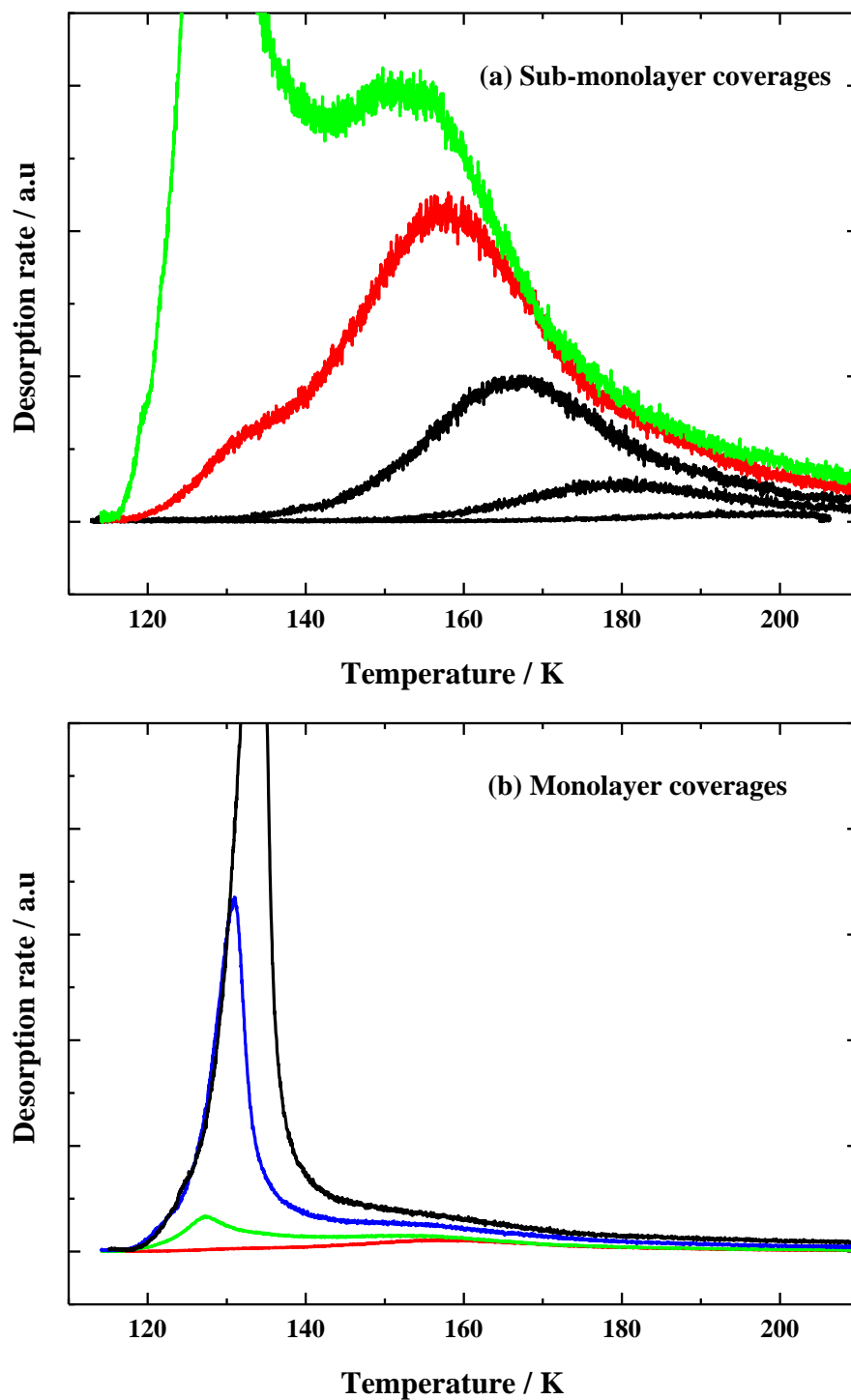


Figure 4.2: TPD traces for CH_3CN films deposited at 110 K. Film thicknesses are labelled: (a) The sub-monolayer coverages (0.05, 0.1, 0.25, 0.5 and 1.0 L) and the first-order desorption regime, (b) the CH_3CN coverages (0.5, 1.0, 2.5 and 5.0 L) of CH_3CN vapour at which the regime follows fractional order desorption kinetic, $\beta = 0.09 \text{ K s}^{-1}$. The red and green traces in (a) and (b) correspond to 0.5 and 1.0 L, respectively.

Increasing the coverage on the surface leads CH₃CN to adsorb at less strongly bonded sites, eventually leading to the apparent second order behaviour observed in **Figure 4.2a**, which is assigned in this work to be a pseudo-first order adsorption of sub-monolayer CH₃CN on silica. The physical behaviour of CH₃CN at such exposures is acetonitrilephilic, *i.e.* CH₃CN binds stronger to the surface than to other CH₃CN molecules. Furthermore, broadening to high temperatures is consistent with either intermolecular repulsion, such as desorption of halides from single metal surfaces (*e.g.* desorption of HCl and HBr from Ge (100)) [40], or multiple binding sites. The heterogeneity of the sample suggests the latter in this case. The silica surface is saturated at an exposure > 0.5 L with no evidence of dissociative adsorption on silica.

In order to determine the coverage-dependent binding energy, E_{des} , for the sub-monolayer coverages, direct inversion of the Polanyi-Wigner equation was used. This is based on the modified equation by Zubkov and co-workers [41], which is adapted as a method for analysing desorption of low coverages from porous surfaces, such as desorption of low surface coverages of C₆H₆ and O₂ from a silica surface [39, 42]. The Polanyi-Wigner equation was thus rearranged to give the desorption energy:

$$E_{des} = -RT \ln \left[\frac{d\Theta_s/dt}{\nu \Theta_s} \right] \quad (4.5)$$

where E_{des} is the desorption energy in kJ mol⁻¹, ν is the pre-exponential factor for desorption in s⁻¹, Θ_s is the surface concentration in molecules cm⁻² and T is temperature in K. The value of ν is assumed to be 10¹³ s⁻¹, which is typical for first-order desorption [43]. The value of $d\Theta_s/dt$ in molecules cm⁻² s⁻¹ is obtained by integrating the area of the CH₃CN peak in the original TPD spectrum against time, t . This is performed for each data point and then inverted to yield Θ_s . However, this type of analysis is invalid for multilayers, as it assumes a value of ν typical of first-order desorption. We acknowledge Dr. François Dulieu and Dr. Emanuele Congiu from l'Observatoire de Paris et l'Université for their contributions to the TPD analysis of CH₃CN. **Figure 4.3** shows the binding energies at low surface exposure ($\Theta_s = 1.0$ corresponds to a surface concentration of 2×10^{14} molecules cm⁻²). As can be seen, the binding energy falls from 50 kJ mol⁻¹ at low coverage to 35 kJ mol⁻¹ as

the surface concentration increases [44]. Following the CH₃CN sub-monolayer coverage, the monolayer is complete at an exposure of 0.5 L on the SiO₂ surface, under the experimental conditions. This is in good agreement with previous studies of C₆H₆ TPD on silica [39]. As the CH₃CN monolayer completes at coverages in the range of 0.25, 0.5, and 1.0 L, the binding strength of CH₃CN to the surface is lower than that in the sub-monolayer regime (see **Figure 4.2b**). The desorption system then follows fractional-order desorption kinetics.

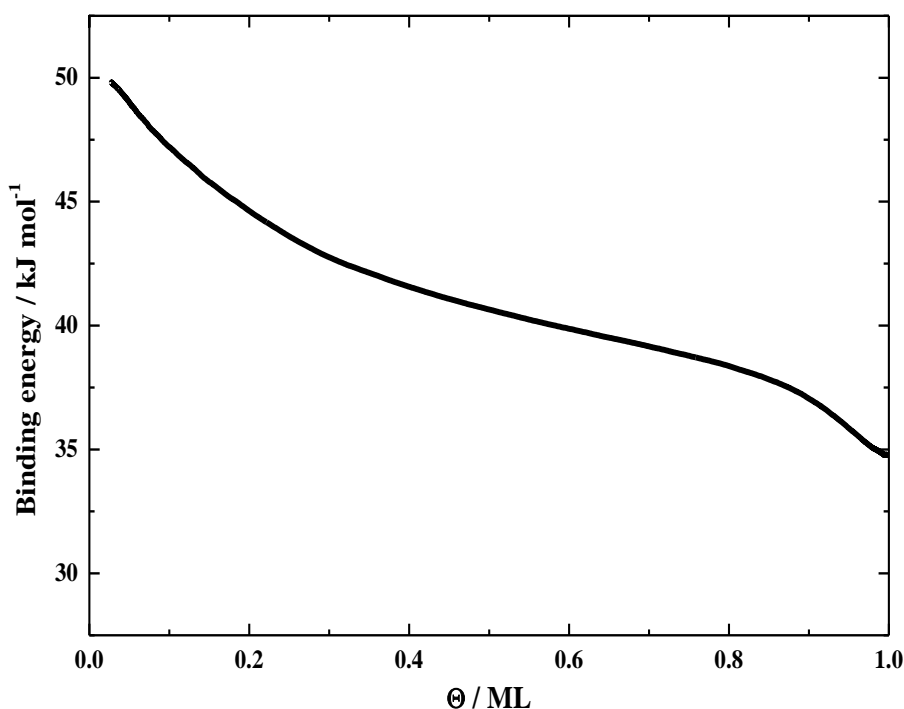


Figure 4.3: $E_{des}(\theta)$ for sub-monolayer coverages of CH₃CN adsorbed on amorphous SiO₂ through inversion of the Polanyi-Wigner equation – saturation of the first layer at $\theta = 1$ corresponds to surface concentration of 2.0×10^{14} molecules cm⁻².

4.4.1.1.2 Multilayer Analysis

For higher surface coverages of CH₃CN (2.5- 250 L), the CH₃CN TPD peak shifts to higher temperatures with increasing coverage. The coincidence of the leading edges for the 2.5 – 250 L TPD traces (see **Figure 4.4**) indicates that desorption occurs from the multilayer and follows zero-order kinetics, *i.e.* the rate of desorption increases exponentially with the temperature, but does not depend on the initial surface coverage. Desorption orders are described in detail in **Section 2.2.2** from **Chapter 2**.

CH₃CN seems to bind slightly more weakly to the surface at high exposures than at low exposures. CH₃CN is thought of as being acetonitrilephobic [44].

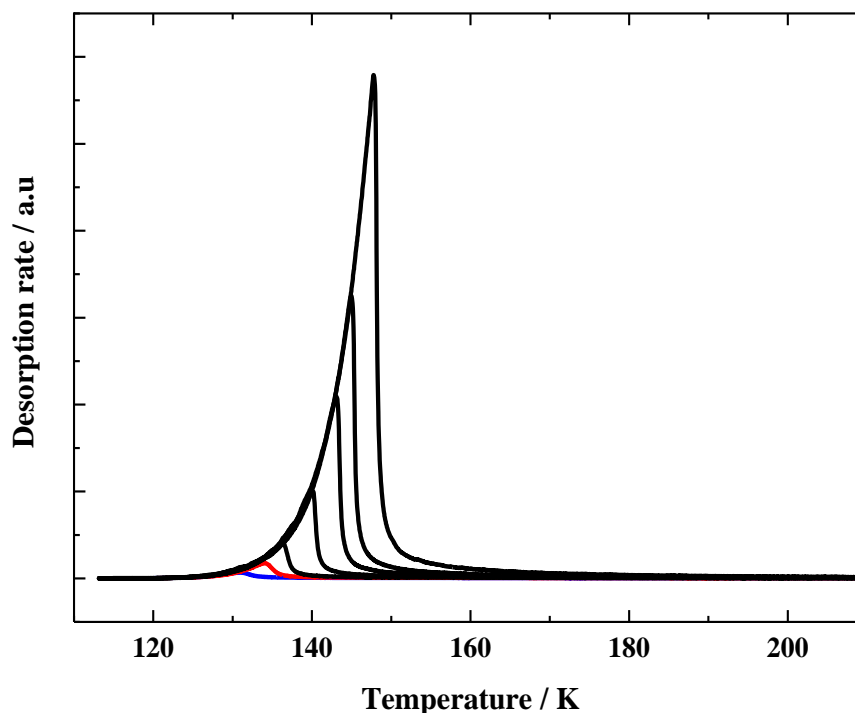


Figure 4.4: TPD traces for thick CH₃CN films deposited at 110 K, surface coverage (Θ_{total}) = 7.89×10^{24} molecules cm⁻², and $\beta = 0.09$ K s⁻¹. Blue and red lines represent the limits of submonolayer and fractional order desorption regimes.

The interactions of the CH₃CN molecules with the SiO₂ surface or with each other would be better described if their binding energy was known. This energy (*i.e.* the desorption energy E_{des}) can be estimated using leading edge analysis. Assuming that desorption of CH₃CN from the silica surface follows a zeroth-order desorption process, and then from the Arrhenius equation (see **equation (2.14)**) using the leading edge analysis (LEA). Both E_{des} and ν were calculated from the slope and the intercept of the plot between $\ln(d\Theta/dt)$ as a function of $1/T$ (see **Figure 4.5**). The values calculated are presented in **Table 4.4**. The errors shown in **Table 4.4** are again obtained from the LEA fit, using the same method as reported in **Section 3.3.2** of **Chapter 3**.

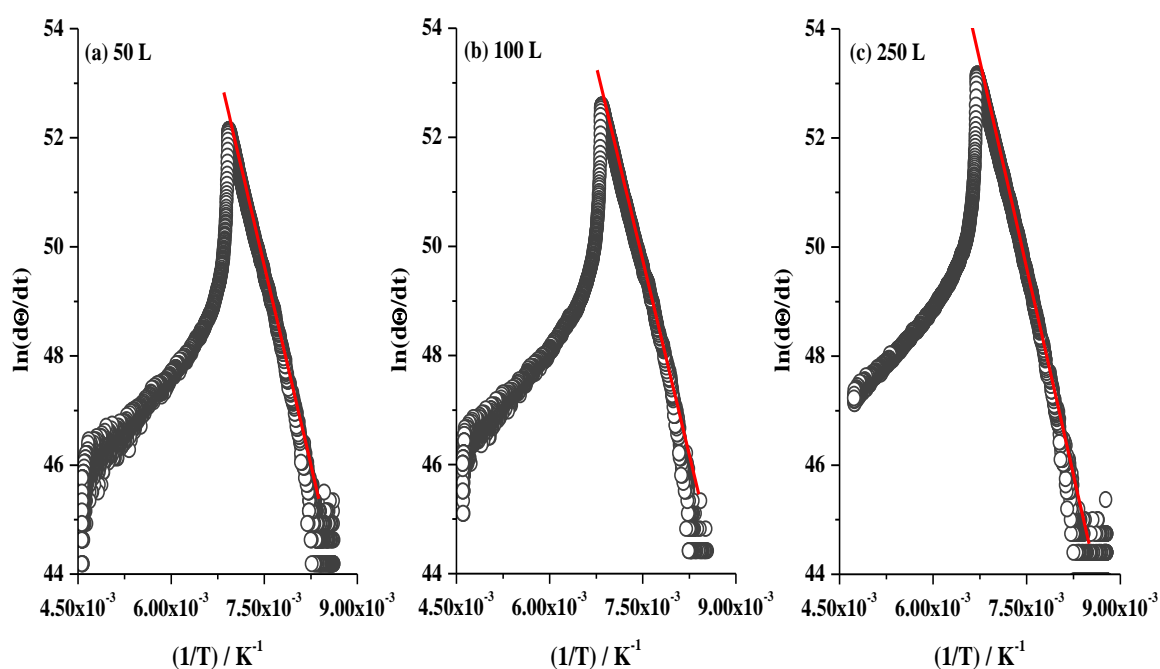


Figure 4.5: Arrhenius plots for the desorption of (a) 50, (b) 100 and (c) 250 L of CH_3CN from amorphous SiO_2 . The abscissa is reciprocal temperature in units of K^{-1} .

Table 4.4: Calculated E_{des} from LEA of H_2O TPD on SiO_2 surface.

Exposure / L	Desorption energy (E_{des}) / kJ mol^{-1}
1.0	40 ± 2
2.5	42.5 ± 1
5	43.6 ± 1
10	39.6 ± 1
25	37.2 ± 1
50	38.4 ± 1
100	37.4 ± 1
250	39.5 ± 1
Limit	38.6 ± 2

As previously explained in **section 3.3.2** of **Chapter 3**, the LEA is used only to obtain the desorption energy, E_{des} . Chemical Kinetics Simulator (CKS) therefore was used to obtain the pre-exponential factor, ν , [45]. In order to model the kinetics of this process, a simple reaction scheme is suggested:



$$\frac{d[\text{CH}_3\text{CN(s)}]}{dt} = -k_{des} \quad (4.7)$$



$$\frac{d[\text{CH}_3\text{CN(g)}]}{dt} = k_{pump}[\text{CH}_3\text{CN(g)}] \quad (4.9)$$

where $\text{CH}_3\text{CN (s)}$, $\text{CH}_3\text{CN (g)}$ and $\text{CH}_3\text{CN (pumped)}$ are acetonitrile in the solid phase, gas phase and the acetonitrile pumped out of the UHV chamber, respectively. The surface concentration of CH_3CN in molecules cm^{-2} is equivalent to the number of molecules desorbed from the surface, and k_{pump} is the pumping coefficient of CH_3CN out of the system. The concentration of molecules to be used in this model was calculated for each exposure from the relationship:

$$Z_w = \frac{PN_A}{(2\pi MRT)^{1/2}} \quad (4.10)$$

where P is the pressure, N_A is Avogadro's constant, T is the absolute temperature of the gas in K, M is the molar mass in kg mol^{-1} , and R is the gas constant. All CH_3CN molecules are assumed to stick on the surface. The following values have been used; an initial CH_3CN surface density of 7.89×10^{16} molecules cm^{-2} for the largest exposure (250 L), an initial temperature of 108 K, a linear temperature ramp and the pumping rate are assumed to be 0.09 K s^{-1} and $0.3 \text{ cm}^2 \text{ mol}^{-1} \text{ s}^{-1}$ respectively.

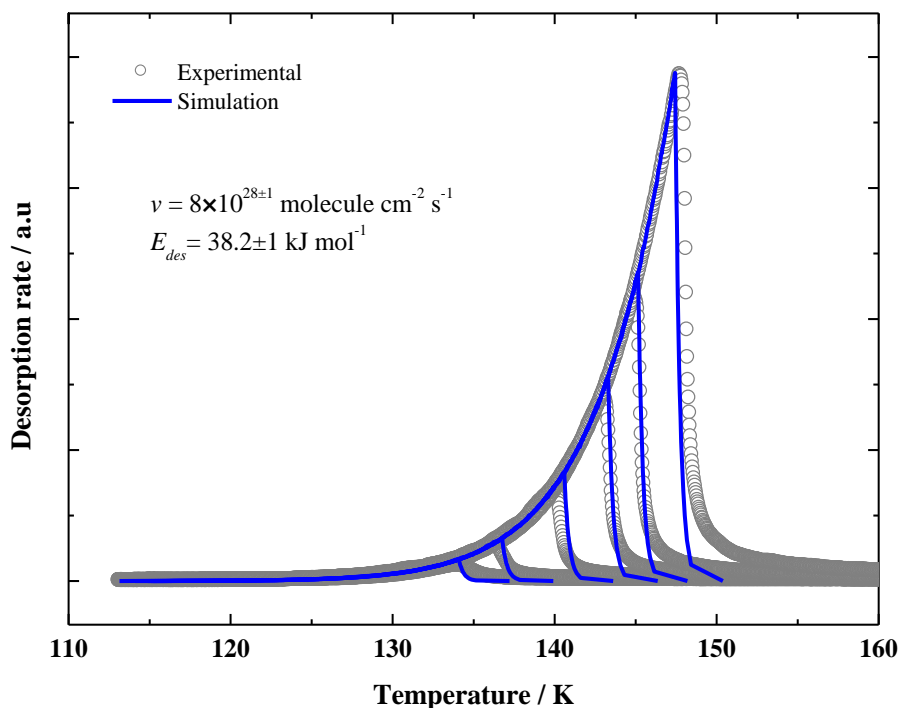


Figure 4.6: TPD traces for thick CH₃CN films deposited at 110 K. Traces labelled: Grey circles are the experimental TPD traces, and the blue lines represent the CKS model of the experiment.

The experimental TPD traces were then modelled using a simple stochastic integration package [46]. The only unknown values were E_{des} and ν , which were varied to obtain the best fit to the experimental data. **Figure 4.6** shows the fits of the experimental TPD traces for the CH₃CN multilayers desorbing from bare silica, with a value of ν of $8 \times 10^{28 \pm 1}$ molecules $\text{cm}^{-2} \text{s}^{-1}$ and E_{des} of 38.7 ± 1 kJ mol^{-1} , at a pumping rate of 0.3 ± 1 molecules $\text{cm}^{-2} \text{s}^{-1}$.

It can be seen clearly that the reproduction of the high temperature tails, which arise from desorption of the sub-monolayer cannot be obtained accurately in the simulations, due to desorption from the amorphous structure of the silica surface.

The qualitative analysis of the CH₃CN TPD traces can be summarised in the following findings:

- i- Sub-monolayer TPD analysis indicates that at the experimental temperature, CH₃CN molecules seem to be free to diffuse over the surface of silica and sample

the most thermodynamically favoured sites. Therefore, CH₃CN molecules tend to require high energy to leave the surface ($E_{des} > 40 \text{ kJ mol}^{-1}$). This is consistent with literature studies of TPD for CH₃CN on metal surfaces [35].

- ii- Zero-order desorption is established for multilayer CH₃CN desorption from the amorphous silica surface.
- iii- The CH₃CN multilayer analysis was provided on the basis of the results obtained from CKS. The desorption energy here is smaller than for the sub-monolayer systems ($E_{des} < 40 \text{ kJ mol}^{-1}$). Generally, these results are in good agreement with reported values for the sublimation energy of nitriles, which lie in the 36 - 42 kJ mol⁻¹ range [47].

4.4.1.2 TPD of CH₃CN Adsorbed on ASW

These experiments would have provided more information about the surface science of CH₃CN. However, as a result of technical issues requiring external repairs for the QMS, the TPD of CH₃CN on ASW has not been performed.

4.4.2 RAIRS of CH₃CN

4.4.2.1 CH₃CN Adsorbed on Amorphous SiO₂

Figure 4.7 shows the RAIR spectrum of a CH₃CN multilayer (250 L) adsorbed on a bare silica surface at 113 K. The assignments of the infrared absorption bands of acetonitrile and of the silica substrate are made on the basis of laboratory investigations of the solid phase under conditions relevant to the outer planetary systems [48] (see **Table 4.5**). The results are in good agreement with the literature studies [48]. The strongest peak, close to 1260 cm⁻¹, is attributed to the longitudinal optical (LO) mode of silica. The peak at 1100 cm⁻¹ is caused by the transverse optical (TO) mode, which is in agreement with previous studies, where it is observed as a weak band [49, 50]. The elimination of degeneracy between LO-TO phonons at the Brillouin zone centre is known as LO-TO splitting. This phenomenon depends on the optical constants (n and k) of the material and, in turn, on the dielectric function ($\epsilon = \epsilon' + i\epsilon''$), where $\epsilon' = n^2 - k^2$ and $\epsilon'' = 2nk$. Experimentally, the constants n and k for

pure CH₃CN at 20, 35, 50, 75, 95, and 110 K have been calculated and are available on the Cosmic Ice Laboratory's Website [51]. Thus, it is possible to calculate the dielectric function for solid CH₃CN and then the wavenumbers of the LO and TO modes from the zero and pole (singularity) of the dielectric function for a system with no damping. The remaining peaks on the RAIR spectrum shown in **Figure 4.7** belong to solid phase CH₃CN; those below 1050 cm⁻¹ are due to the asymmetrical CH-bend, and a combination of the symmetrical and asymmetrical CH-bend. The strong band at 2250 cm⁻¹ is assigned to the C≡N stretch, which is consistent with the literature (2251 cm⁻¹) [48]. The other strong bands at 2935 and 3000 cm⁻¹ are due to the symmetrical CH-stretch and asymmetrical CH-stretch, respectively. For high exposures of CH₃CN grown on a silica surface, the same IR bands have been observed, with only slight shifts in frequency compared to those recorded for CH₃CN in astrophysically relevant conditions. The only difference was the appearance of a small peak at around 2291 cm⁻¹, which is due to miscancellation of CO₂ from the purge gas.

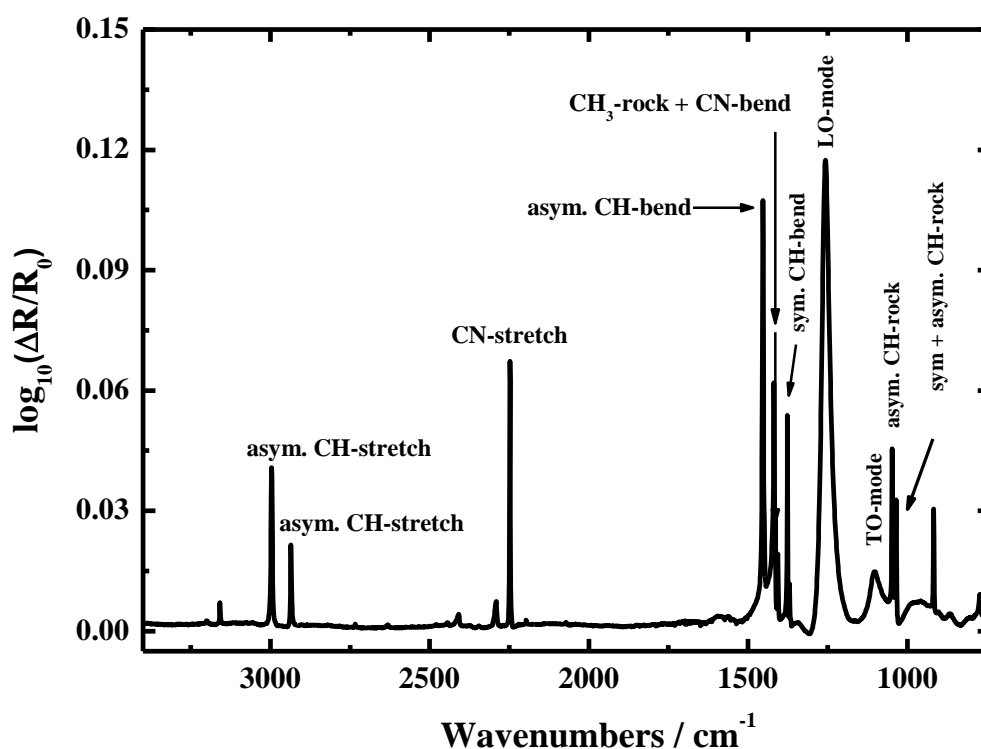


Figure 4.7: Full range RAIR spectrum of a 250 L CH₃CN ice deposited on bare silica. CH₃CN vibration modes are assigned along with those belonging to amorphous SiO₂.

Table 4.5: IR assignments in cm^{-1} of the CH_3CN multilayer adsorbed on amorphous silica at 113 K. RAIR spectra in this work were recorded at 2 cm^{-1} and the literature work was recorded at 1 cm^{-1} resolution.

Mode	Assignment	IR Frequencies / cm^{-1}	
		This work	Literature [48]
$\nu_2 + \nu_4$	sym. CN str. + sym. CC str	3158	3162
ν_5	asym. CH str.	2996	3000
ν_1	sym. CH str.	2935	2939
$\nu_3 + \nu_7$	sym. CH_3 def. + asym. CH_3 rock.	2410	2412
$\nu_3 + \nu_4$	sym. CH_3 def. + sym. CC str.	2291	2296
ν_2	sym. CN str.	2250	2251
$\nu_7 + \nu_8$	asym. CH_3 rock. + asym. CCN bend.	1451	1451
ν_6	asym. CH_3 def.	1418	1416
ν_6	asym. CH_3 def.	1414	1408
ν_6	asym. CH_3 def.	1406	1408
ν_3	sym. CH_3 def.	1375	1372
ν_3	sym. CH_3 def.	1369	1368
-	silica LO ^a mode	1260	-
-	silica TO ^b mode	1102	-
ν_7	asym. CH_3 rock.	1047	1049
ν_7	asym. CH_3 rock.	1038	1040
ν_7	asym. CH_3 rock.	1034	1036
ν_4	sym. CC str.	917	918
$2\nu_8$	asym. CCN bend.	772	774

^a Longitudinal optical mode of silica from the underlying substrate.

^b Transverse optical mode of silica from the underlying substrate.

The peaks in the region between 1350 cm^{-1} and 1520 cm^{-1} are assigned to the asymmetrical CH_3 rock + asymmetrical CCN bend ($\nu_7 + \nu_8$) combination band at 1451 cm^{-1} , and the two vibrational modes of the CH_3 group at 1418 cm^{-1} and 1416 cm^{-1} . There is no evidence for a significant shift in any of the IR features of solid CH_3CN . In comparison with the transmittance IR spectrum of solid CH_3CN reported in the previous study, the main difference has been with respect to the intensity of IR

bands. The strongest band observed in the RAIR spectrum is the band at 2250 cm^{-1} , whereas in the transmittance it is at 1400 cm^{-1} [44]. The reason for this difference is because of the differences in the optics of reflection-absorption *versus* transmission.

Figure 4.8 shows RAIR spectra of thin films of CH_3CN on bare silica with exposures of 0.05, 0.1, 0.25, 0.5, 1.0, and 2.5 L. It can be seen that the lowest exposure at which the CH_3CN is observed is 0.25 L. This exposure produces somewhat less than one monolayer on the silica surface. The completion of the monolayer can be seen at the coverage of 0.5 L. These results are consistent with the TPD results presented in **section 4.4.1**, where the monolayer exposure was found to occur at around 0.5 – 1.0 L. **Table 4.6** shows the IR assignments of CH_3CN exposures from 1 L to 2.5 L. It can be seen from **Table 4.6** that there is no significant shift in the $\text{C}\equiv\text{N}$ stretching band when going from monolayer (2248 cm^{-1}) to multilayer (2250 cm^{-1}). Although the IR spectrometer and the optics housing are purged with dried air, there is spectroscopic evidence for the presence of water vapour, and sharp bands appear in the $1800\text{-}1380\text{ cm}^{-1}$ region and above 3300 cm^{-1} . Interaction of solid CH_3CN at the surface is likely to be with a silanol group, in particular with the OH group. The structure of silanol is shown below (**Figure 4.9**). The silica LO-TO modes increase significantly with increasing CH_3CN exposure, due to Fresnel effects. The intensity of the CN-stretch mode of CH_3CN increases as the surface coverage increases. The absence of most of the CH_3CN features for coverages below 1 L can be attributed to the sensitivity of the IR detector.

Table 4.6: IR assignments of the CH_3CN monolayer adsorbed on amorphous silica at 113 K.

Mode	Assignment	IR Frequencies / cm^{-1}
ν_5	asym. CH str.	2996
ν_1	sym. CH str.	2935
ν_2	sym. CN str.	2248
-	silica LO mode	1260
ν_7	asym. CH_3 rock.	1049
ν_2	OH bending of H_2O	1380
ν_2	OH bending of H_2O	1800

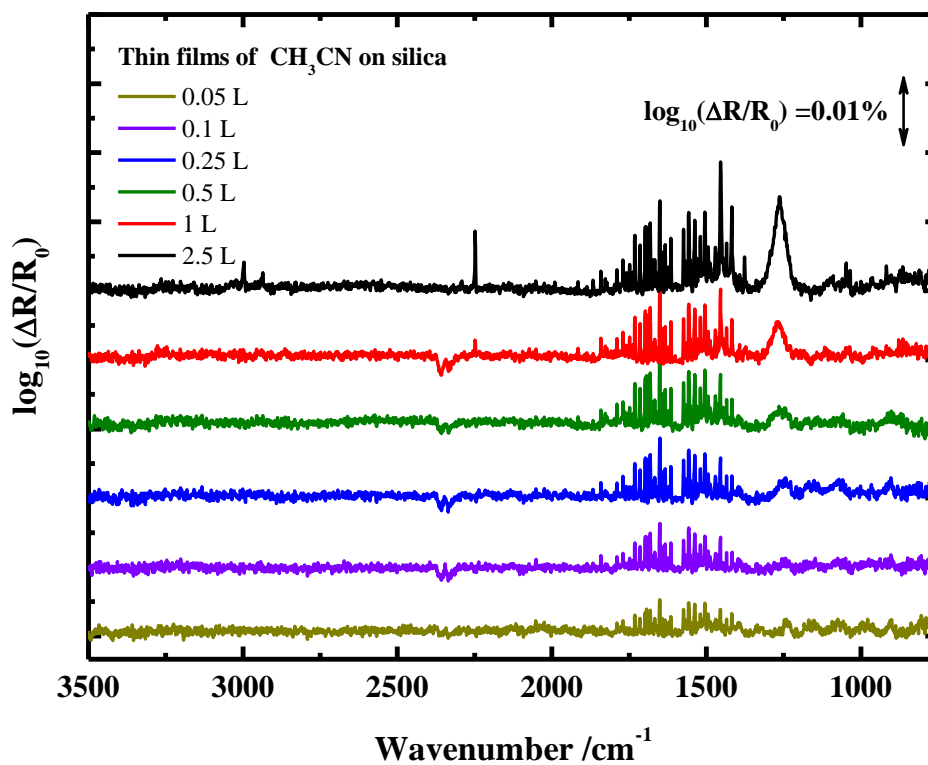


Figure 4.8: RAIR spectra of solid CH₃CN deposited on bare silica: coloured lines represent the 0.05, 0.1, 0.25, 0.5, 1.0, and 2.5 L exposures.

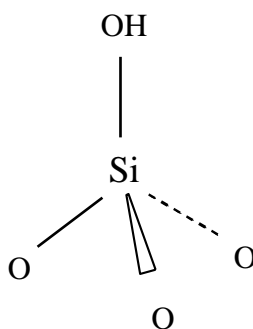


Figure 4.9: The structure of the silanol group at the silica surface.

Most of the IR features of solid CH₃CN appear clearly at high surface exposures within the range of 5, 10, 25, 50, 100, 250 L (see **Figure 4.10**). This range of thicknesses represents the multilayer coverage described in thermal desorption of CH₃CN from a bare silica surface (see **section 4.4.1**).

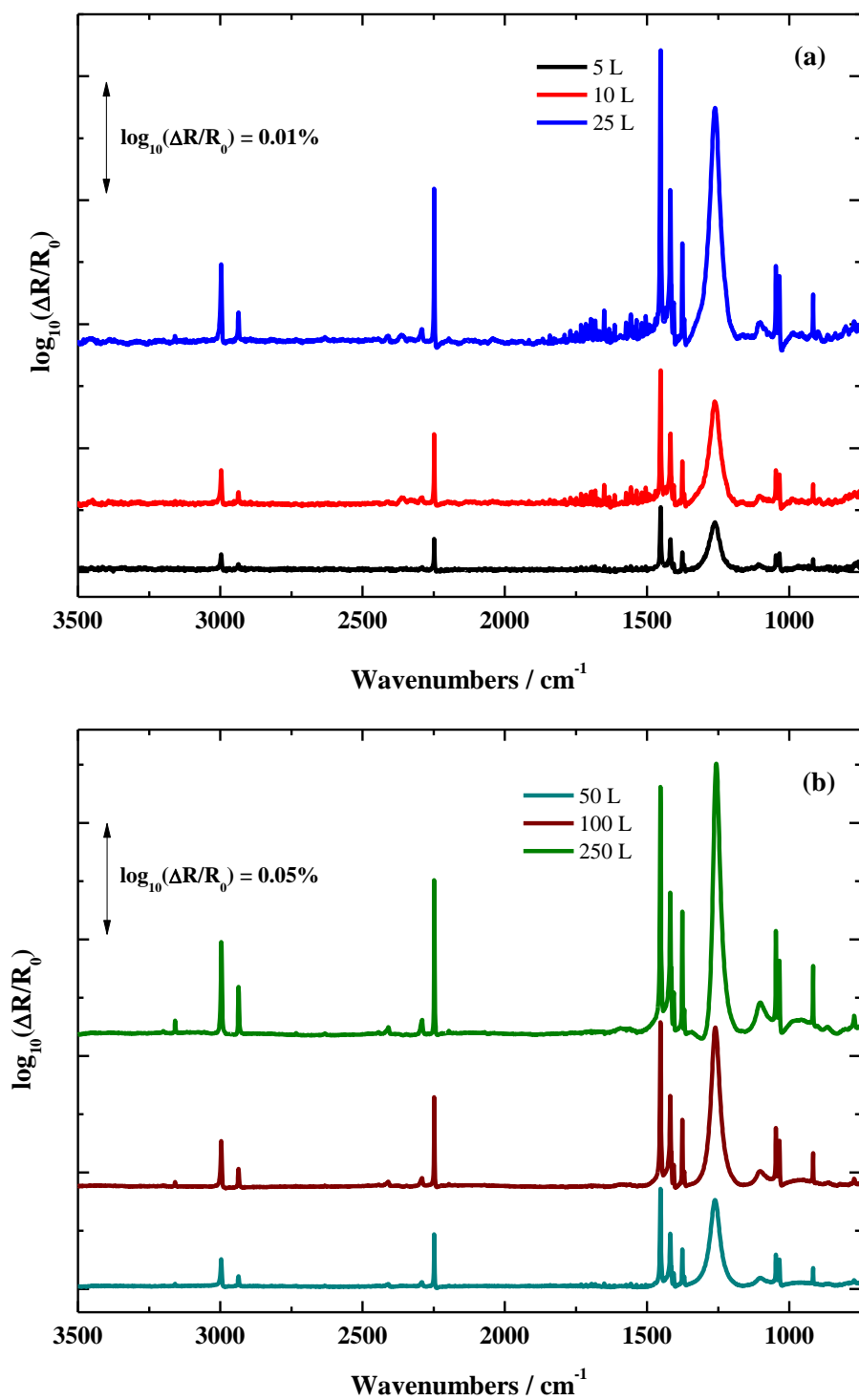


Figure 4.10: RAIR spectra of thick films of solid CH_3CN deposited on bare silica: coloured lines represent (a) 5.0, 10, and 25 L, (b) 50, 100, and 250 L.

4.4.2.2 CH₃CN Adsorbed on ASW

In order to examine the interactions between CH₃CN and an ASW film, various CH₃CN thicknesses were deposited on a thin film of amorphous water of 14 L. The RAIR spectrum of a thin CH₃CN film (~2.5 L) adsorbed on H₂O ice (14 L) shows a more intense C≡N stretch band, compared to that obtained on the bare silica surface (see **Figure 4.11**). This result might be attributed to the hydrogen bonding between the nitrogen atom of CH₃CN and hydrogen from a dangling OH group of the ice surface, as has been suggested by Schaff *et al.* [34]. The increase of the intensity of the C≡N stretch band on water ice is likely to be due to transfer of some of the electron density from N to form C≡N···H-O, which is consistent with the investigations of Schaff *et al.* and Bahr *et al.* [34, 35].

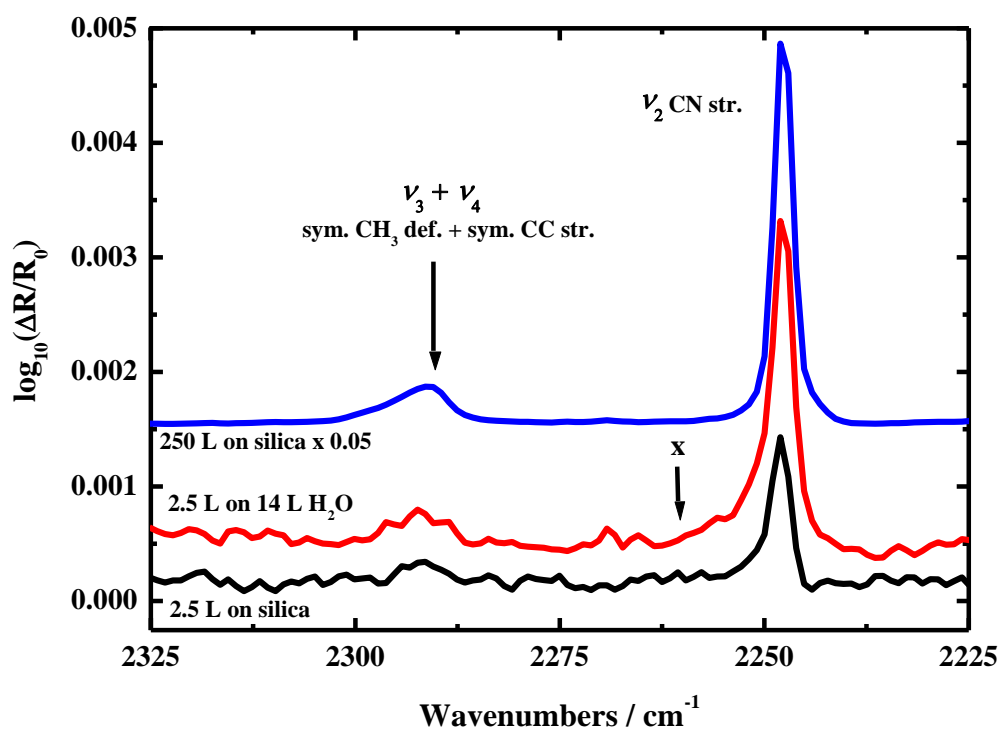


Figure 4.11: RAIRS of CH₃CN in the C≡N stretch region of 250 L and CH₃CN on bare silica and 2.5 L CH₃CN on H₂O and silica.

Given the roughness of the silica surface, the given exposure of H₂O is unlikely to cover the entire surface of silica. Therefore, optical effects can play a crucial role for these spectra. Two of the IR spectra presented in **Figure 4.11** show the same IR

features for a thin CH₃CN layer on a bare silica surface (black line) and on a thin layer of water ice (red line), According to the studies of Schaff *et al.* and Bahr *et al.*, there should be an IR feature of CH₃CN within the monolayer range. This feature was recorded at 2265 cm⁻¹ and appears to be evidence of H-bonding [34, 35]. The IR spectrum represented by the red line (marked with X) shows a significant result, in which there is no appearance of the peak at 2265 cm⁻¹ (see **Figure 4.11**).

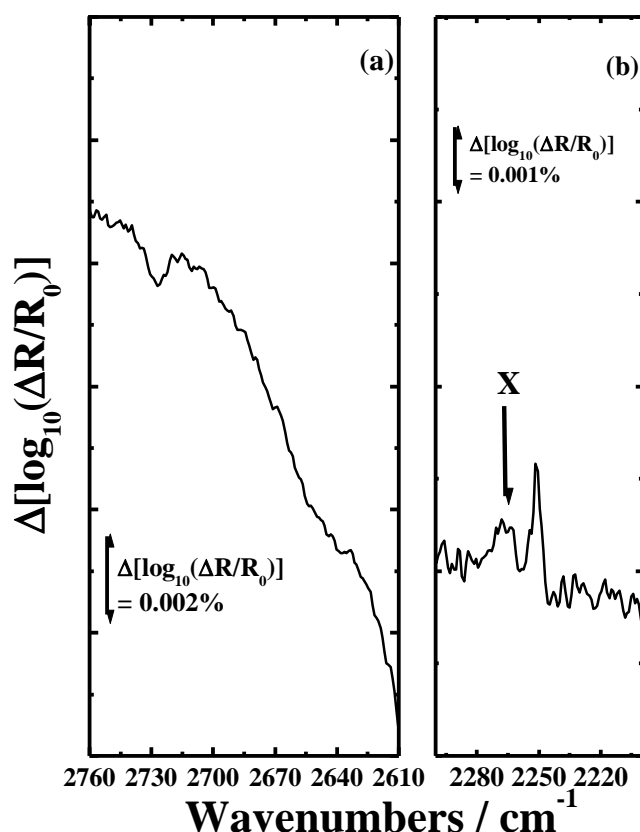


Figure 4.12: RAIR spectra of 5 L CH₃CN adsorbed on 100 L of D₂O. The left panel (a) is the RAIR spectrum of OD dangling bands, and the right panel (b) is the RAIR spectrum of the C≡N band.

More investigations were performed on ultrathin layers of CH₃CN (~ 5 L) adsorbed on a thick film of D₂O (100 L). **Figure 4.12** shows the RAIR spectra from these investigations. As can be seen from **Figure 4.12a**, a band is observed at 2727 cm⁻¹. This is assigned to the stretching mode of the dangling-OD band of solid D₂O, consistent with other infrared experiments on D₂O films adsorbed on metal surfaces

[52-54]. Two C≡N stretch bands are observed at 2252 and 2267 cm⁻¹ on D₂O (see **Figure 4.12b**), for solid CH₃CN. The latter saturates at an exposure of 5 L, while the 2252 cm⁻¹ band grows as the thicker films of CH₃CN are grown. This is consistent with the work of Schaff *et al.* and Bahr *et al.* [34, 35], which report the observation of the two features in the C≡N stretch region for solid CH₃CN on ASW: one at 2252 cm⁻¹, for CH₃CN in the bulk CH₃CN solid, and the second at 2267 cm⁻¹, for CH₃CN adsorbed at the ASW surface.

Figures 4.13 and **4.14** show the RAIR spectra of thin and thick films of CH₃CN adsorbed on the 14 L H₂O film investigated in this study. The broad peak located between 3600 cm⁻¹ and 3100 cm⁻¹ is attributed to the OH-stretch of the H₂O ice film. The small peak at 2350 cm⁻¹ is attributed to CO₂, which might be present in the path of the IR beam. There is no significant shift in either the CN-stretch or of other bands' frequencies, suggesting a weak interaction between CH₃CN and the ice surface. In contrast with this study, Schaff *et al.* observed the CN-stretch at low surface exposure [34]. Bahr *et al.* found that N-atoms form two different bonds with H₂O hydrogen atoms, π- and σ- types, respectively [35]. The absence of π-type CH₃CN-H₂O bonding at low surface exposures makes it difficult to decide the orientation of CH₃CN on H₂O surface. CH₃CN molecules also interact *via* dipolar interactions with each other, which explain the strength of the CN-stretch intensity at 2250 cm⁻¹, with increasing CH₃CN exposures.

Ab initio calculations were performed to calculate both the binding energy and the vibrational frequencies at different geometrical positions of CH₃CN with respect to H₂O. HyperChem 8.0 was employed using the modest level of basis set (6-31G*), Restricted Hartree-Fock (RHF) calculations, a convergence limit of 1×10⁻⁸ and an iteration limit of 200. To optimize the complex geometry, the Polak-Ribiere method was employed as the minimization algorithm [55]. Finally, vibrational spectra of the complex 1 (see **Table 4.7**) and the molecular products (CH₃CN and H₂O) were calculated using the in-built tools in HyperChem. The binding energy obtained from these calculations refers to the attraction between an electron in an atomic orbital and the nucleus of the same atom.

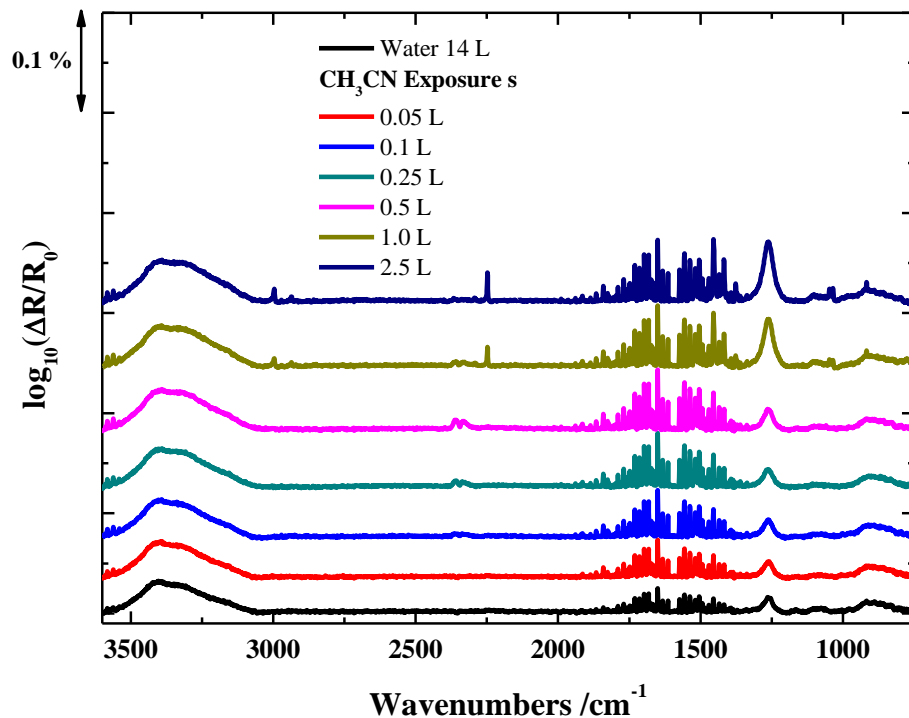


Figure 4.13: RAIR spectra of solid CH₃CN deposited on thin films of water ice: coloured lines represent the 0.05, 0.1, 0.25, 0.5, 1.0, and 2.5 L exposures.

Binding energies of CH₃CN-H₂O complexes can be calculated with the following expression:

$$E_{binding} = E_{complex} - (E_{CH_3CN} + E_{H_2O}) \quad (4.11)$$

where $E_{binding}$ is the binding energy of the CH₃CN complex in kJ mol⁻¹, $E_{complex}$, E_{CH_3CN} and E_{H_2O} are the total energies of the complex, CH₃CN, and H₂O respectively. E_{CH_3CN} and E_{H_2O} are -346375.7 kJ mol⁻¹ and -199566.2 kJ mol⁻¹ respectively. Once $E_{complex}$ was obtained from *ab initio* calculations, **equation (4.11)** was used to calculate the binding energy between CH₃CN and H₂O ($E_{binding}$) for each complex.

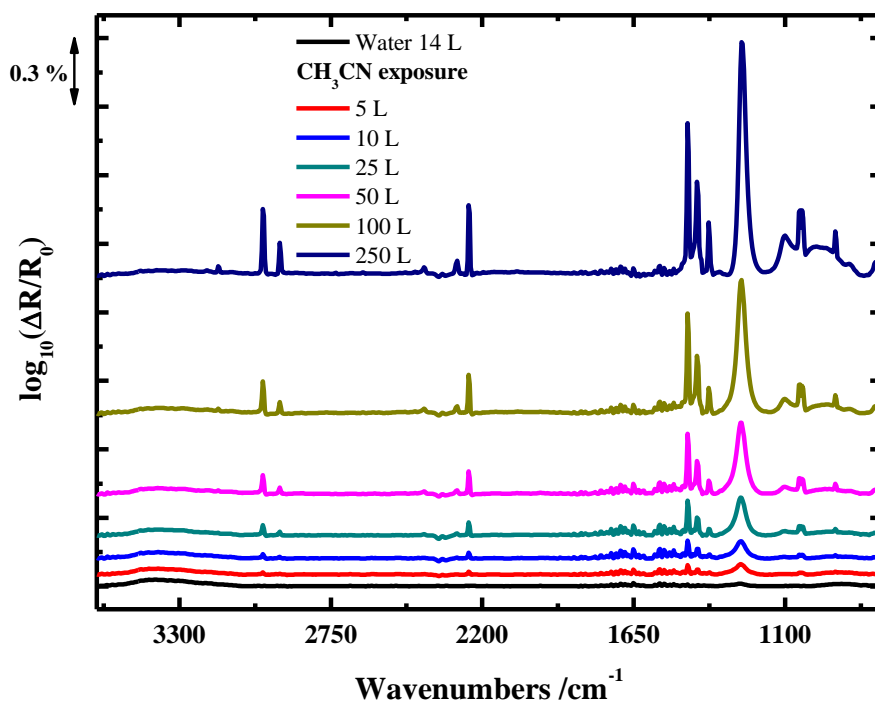
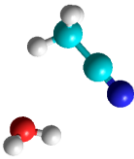
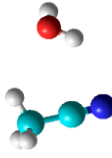
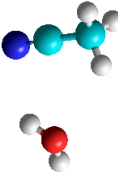
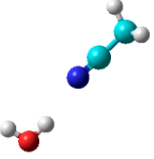
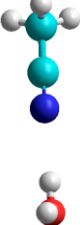


Figure 4.14: RAIR spectra of thick films of solid CH₃CN deposited on thin films of water ice: coloured lines represent the 5.0, 10, 25, 50, 100, and 250 L coverages.

Table 4.7 shows the binding energies for the favourable geometries of CH₃CN with H₂O. The distances between N and H from H₂O are also included in **Table 4.7**. These results represent minima on the potential energy surface (PES) of the complex. Calculated complex binding energies, $E_{binding}$, are negative values, indicating the exothermic nature of the interaction between CH₃CN and H₂O, where the complex was predicted to be bound and stable. In general, the calculated binding energy for CH₃CN-H₂O complexes is in the range of -18 kJ mol^{-1} , which is consistent with a hydrogen bond [56]. There are two different geometrical positions; (a) for the complexes 1, 2 and 3 with binding energy $-18.2 \text{ kJ mol}^{-1}$, (b) complexes 4, 5 and 6 with binding energy $-18.4 \text{ kJ mol}^{-1}$. The *ab initio* calculations also provide information about the distance between the nitrogen of CH₃CN and the hydrogen of the water molecule. In the current calculations, there are two categories of geometrical positions: complexes (1, 2 and 3), with the geometrical position of (a), the N-H bond distance is 2.6 \AA , which is consistent with the hydrogen bond, for donor-acceptor distances of $2.5 - 3.2 \text{ \AA}$. This is regarded as “moderate, mostly electrostatic”. Complexes (4, 5 and 6) with the geometrical position of (b), the N-H

bond distance is 2.2 Å, which is in the range of the hydrogen bond, with distances of 2.2 – 2.5 Å. This is known as “strong, mostly covalent” [56]. These calculations are also in good agreement with the work of Duvernay *et al.*, in which the N-H complex bond length was 2.07 Å and the binding energy was around 15 kJ mol⁻¹ [57].

Table 4.7: RHF/6-31G⁺ structural calculations of H₂O-CH₃CN complexes (binding energies in kJ mol⁻¹ and bond length in Å).

Complex	Molecular structures	Binding energy / kJ mol ⁻¹	N-H bond complex length / Å
1		-18.2	2.6
2		-18.2	2.6
3		-18.2	2.6
4		-18.4	2.2
5		-18.4	2.2
6		-18.4	2.2

To aid understanding of the structure presented in **Table 4.7**, simple structures are assumed, to present how CH₃CN molecules orient on the H₂O ice surface (see **Figure 4.16**). The three molecular structures (1, 2 and 3) with the geometrical position (a) suggest weak binding between one of the H atoms of CH₃CN and the O atom of H₂O. These have a three-fold symmetry, assuming rotation about the C-C axis in CH₃CN. The other structures (4, 5 and 6) represent minima as the H₂O rotates about the OH...NCC axis (see **Figure 4.16b**). As the N-H bond distance is consistent with strong H-bonding, the geometrical position (b) is linear and more stable than that of (a).

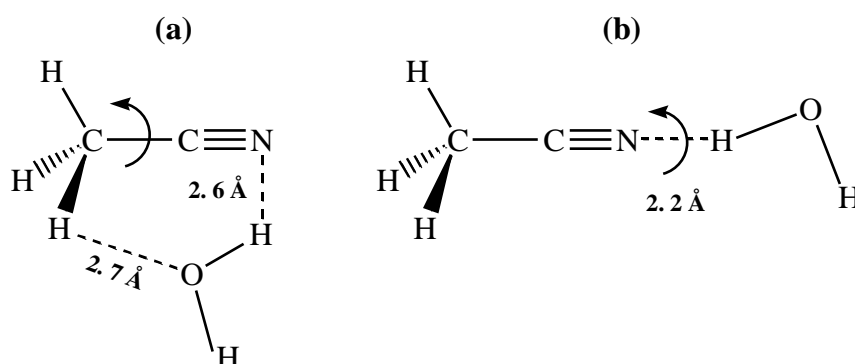


Figure 4.16: The structures of the proposed H-bonding in CH₃CN-H₂O complexes.

More information about the structure of isolated complexes formed in the matrix was obtained from the calculations of the vibrational frequencies for complexes 1, 2, 3, 4, 5, and 6. The IR frequencies obtained from these calculations assume gas phase molecules, where the surface interactions are not taken into account. They are also different from the IR frequencies obtained in gas phase experiments. However, this analysis provides insight as to where these frequencies may lie. The IR frequencies of the complexes were compared to those of an isolated CH₃CN molecule by calculating the frequency shifts of vibrational modes from the difference, $\Delta\nu$:

$$\Delta\nu = \nu(\text{complex}) - \nu(\text{CH}_3\text{CN}) \quad (4.12)$$

Table 4.8: The IR frequencies of the CH₃CN-H₂O complexes 1-6 and the isolated CH₃CN molecule, the frequencies obtained from the calculations described in the text.

	Mode	Assignment	Complexes frequencies / cm ⁻¹	Isolated CH ₃ CN frequencies / cm ⁻¹	$\Delta\nu$ / cm ⁻¹
Complex 1	v ₅	asym. CH str.	3314	3317	-3
	v ₁	sym. CH str.	3236	3235	+1
	v ₂	sym. CN str.	2612	2626	-14
	v ₇	asym. CH ₃ rock.	1178	1174	+4
Complex 2	v ₅	asym. CH str.	3316	3317	-1
	v ₁	sym. CH str.	3237	3235	+2
	v ₂	sym. CN str.	2613	2626	-13
	v ₇	asym. CH ₃ rock.	1177	1174	+3
Complex 3	v ₅	asym. CH str.	3314	3317	-3
	v ₁	sym. CH str.	3237	3235	+2
	v ₂	sym. CN str.	2613	2626	-13
	v ₇	asym. CH ₃ rock.	1178	1174	+4
Complex 4	v ₅	asym. CH str.	3320	3317	+3
	v ₁	sym. CH str.	3239	3235	+4
	v ₂	sym. CN str.	2626	2626	0
	v ₇	asym. CH ₃ rock.	1173	1174	-1
Complex 5	v ₅	asym. CH str.	3320	3317	+3
	v ₁	sym. CH str.	3238	3235	+3
	v ₂	sym. CN str.	2626	2626	0
	v ₇	asym. CH ₃ rock.	1174	1174	0
Complex 6	v ₅	asym. CH str.	3319	3317	+2
	v ₁	sym. CH str.	3237	3235	+2
	v ₂	sym. CN str.	2627	2626	+1
	v ₇	asym. CH ₃ rock.	1174	1174	0

The computational IR frequencies of the complexes and the isolated CH₃CN molecules are shown in **Table 4.8**. According to the calculations, both geometrical positions, **(a)** and **(b)**, seem to exist as a mixture. The $\Delta\nu$ calculations are very small for complexes 4, 5 and 6, compared with those for complexes 1, 2 and 3, as the IR frequencies for complexes 4, 5 and 6 are consistent with those for the isolated CH₃CN molecule. This indicates that complexes (4, 5 and 6) with the geometrical position of **(b)** are more stable and likely to be the dominant within the CH₃CN/H₂O

system. As shown in **Table 4.9**, the $\Delta\nu$ calculations for the experimental results show that the differences between the CH₃CN/H₂O and isolated CH₃CN (i.e. monolayer coverage) are smaller than 5 cm⁻¹ for the ν CN stretching mode, which is reasonable. Moreover, the value of $\Delta\nu$ obtained from experiment for the ν CN stretching mode is much closer to the computational calculations for the geometrical position (**b**) for complexes 4, 5 and 6. Furthermore, based on the work reported by Ahn [58], Bahr [35], and in this thesis (CH₃CN / D₂O system), the 2252 and 2267 cm⁻¹ bands appearing near monolayer completion are due to the formation of σ - and π - type CH₃CN-H₂O bond, respectively.

Table 4.9: The experimental IR frequencies of the CH₃CN-H₂O complex and the isolated CH₃CN.

Mode	Assignment	Experimental complex frequencies /cm ⁻¹	Experimental isolated CH ₃ CN frequencies / cm ⁻¹	$\Delta\nu$ / cm ⁻¹
ν_5	asym. CH str.	2993	2996	-3
ν_1	sym. CH str.	2932	2935	-3
ν_2	sym. CN str.	2251	2248	+3
ν_7	asym. CH ₃ rock.	1043	1049	-6

4.4.2.3 Annealed CH₃CN / ASW

In order to investigate the structural change and identify any molecular interactions that can occur between CH₃CN and H₂O ices, annealing experiments were performed using RAIRS. **Figure 4.17** shows RAIR spectra of CH₃CN ices, annealed stepwise to 183 K. In the first part (see **Figure 4.17a**), 50 L CH₃CN were deposited on bare silica at 113 K. It was then heated up to 118 K for 30 s and then cooled down to the base temperature (113 K). RAIR spectra were recorded before and after the heating. This procedure was repeated after heating to 123, 133, 148, 163, and 183 K. This range of temperature is enough to explore any changes that may occur in particular transformations from amorphous to crystalline ices. Such behaviour occurs for water ice between 140 and 160 K. As seen in **Figure 4.17a**, there is no change in the RAIR spectra upon heating from 118 to 133 K. A slight decrease in the intensity of the IR peaks can be observed as the temperature increases to 148 K. The complete

desorption of CH₃CN from the silica surface is clearly seen above 183 K and the silica LO mode has disappeared as well. The same results were obtained for 50 L CH₃CN on 14 L H₂O ices (see **Figure 4.17b**), decreasing the intensity of the IR peak at a temperature of 148 K.

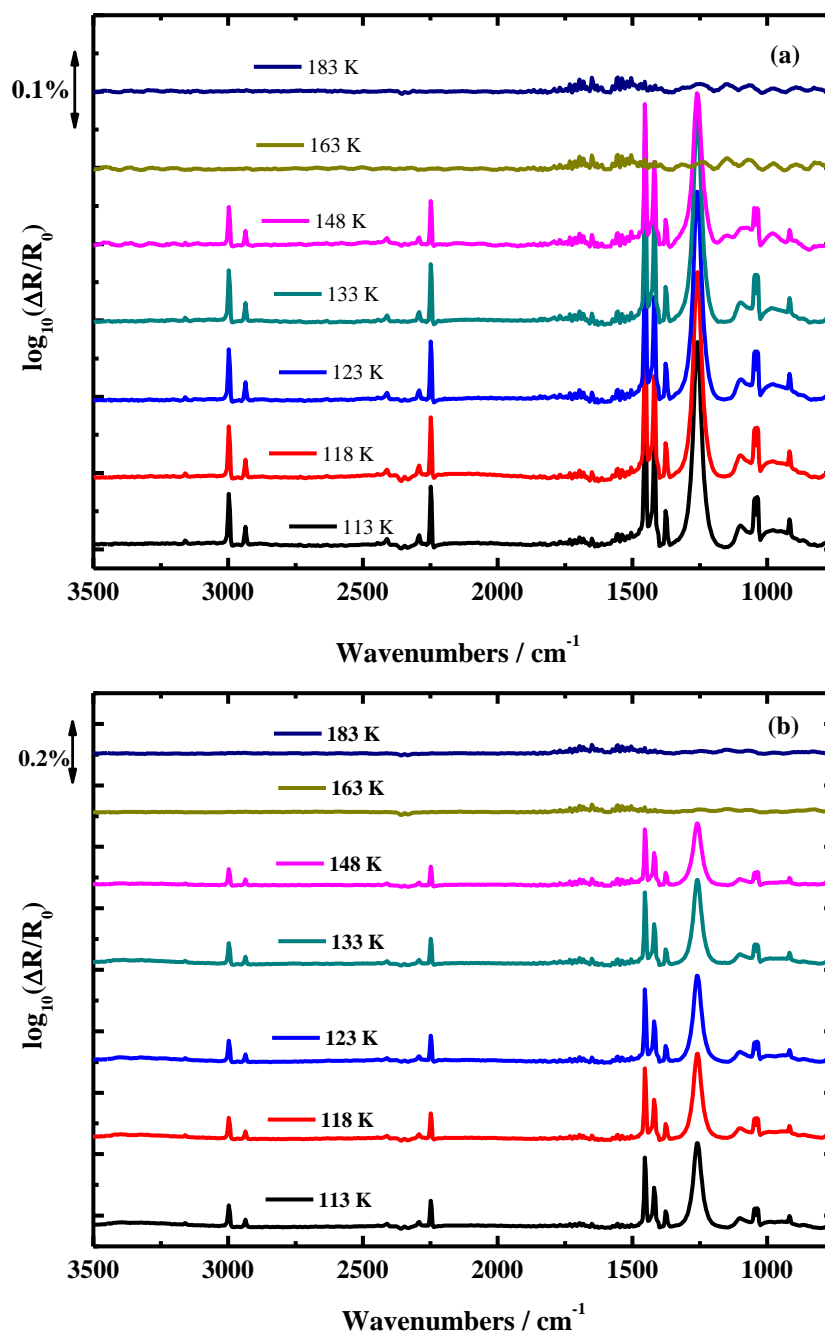


Figure 4.17: RAIR spectra of annealing ices at different temperatures (118, 123, 133, 148, 163, and 183 K): (a) 50 L of CH₃CN on bare silica, and (b) 50 L CH₃CN on 14 L H₂O.

At 163 K the surface appears free of adsorbates. The CH₃CN film is probably crystalline. This is in good agreement with the data obtained at Catania, in which CH₃CN ice was deposited at base temperature of 15 K and heated within the range of 110 K to 140 K[44]. On the other hand, a mixture of H₂O and CH₃CN (H₂O:CH₃CN = 2:1) shows a significant change after annealing at 148 K (see **Figure 4.18**). It can be seen from **Figure 4.18** that almost all of the acetonitrile peaks have disappeared, implying complete desorption of CH₃CN from the mixture of H₂O:CH₃CN ices. However, within the region of the OH-stretching band (3600 - 3100 cm⁻¹), heating from 113 K to 148 K causes a marked change in the shape of the OH-stretching band of H₂O ice, accompanied by a shift of around 30 cm⁻¹ and also sharpening around 3228 cm⁻¹.

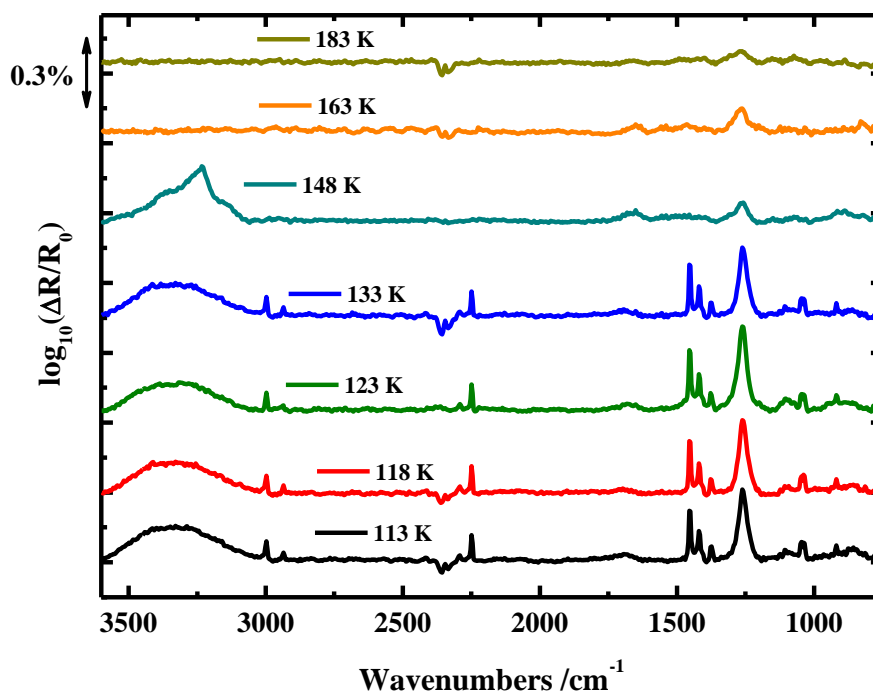


Figure 4.18: RAIR spectra of annealing H₂O:CH₃CN mixture (2:1) on bare silica

This may indicate that the H₂O ice collapses upon heating and forms a crystalline structure [58, 59]. The acetonitrile molecules desorb at a slightly lower temperature than water and leave the system, as they are not re-adsorbed onto the crystalline ice surface. It is likely that a similar crystallisation process takes place in the layered system. The amount of water is too small to observe in these experiments. A recent paper reports CH₃CN spectra [44].

Figure 4.19 shows that during the annealing there is a series of changes in the IR bands, in particular at the 3250 cm^{-1} region, for CH_3 stretching-bands and the CN-stretching band at 2251 cm^{-1} [44]. Heating from 15 K to 110 K caused clear changes, reflecting phase transformation of CH_3CN ice. This could be the same for the $\text{H}_2\text{O}:\text{CH}_3\text{CN}$ ices, warming up the ices results in desorption of CH_3CN and crystallisation of H_2O ice.

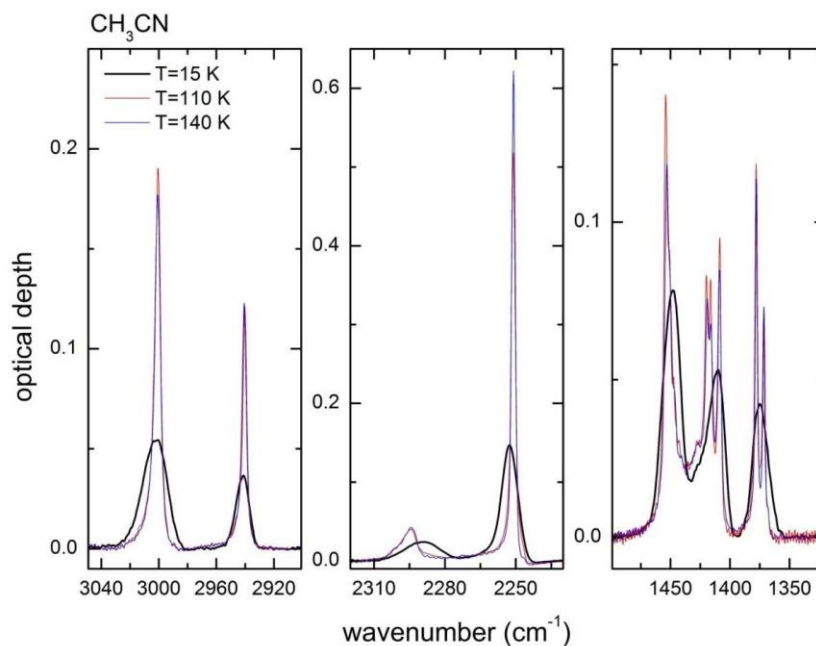


Figure 4.19: TIR spectra of 500 nm CH_3CN , deposited at 15 K and then heated to 110 K and 140 K [44].

4.5 Conclusions

TPD analysis of solid CH_3CN desorbing from amorphous silica surfaces, under astrophysically relevant conditions, revealed that the surface structure of solid CH_3CN during direct heating depends significantly on the thickness of the film adsorbed on the surface. The use of amorphous silica provided a surface on which the molecules can diffuse. Sub-monolayer growth is favoured at a low surface coverage of 0.25 L with E_{des} of $> 40\text{ kJ mol}^{-1}$. Desorption of solid CH_3CN at such surface coverage follows first-order desorption kinetics. Therefore, CH_3CN in a sub-monolayer coverage results in acetonitrilephilic surface behaviour (*i.e.* CH_3CN molecules bind more strongly to the surface than to each other). On the other hand,

RAIRS analysis found difficulties in observing the sub-monolayer, because of the roughness of the mimic surface used in this study. The second type of surface structure is the monolayer with fractional order desorption kinetics. The completion of the monolayer started from 0.5 L, with E_{des} that is slightly smaller than the sub-monolayer. Due to the amorphous nature of the silica surface, simulations were unable to reproduce the high temperature tails in the TPD traces. The formation steps of the monolayer were revealed in the RAIR spectra, where the starting point in forming the monolayer is observed at exposures greater than 0.5 L. The last structure was clearly seen at the saturation level starting from 10 L, where CH₃CN molecules bind to each other in the multilayer. In this range of surface coverages (*i.e.* 10 – 250 L), desorption follows zero-order regime kinetics, as expected for a multilayer desorption. From the results obtained from CKS, it is concluded that the desorption energy and the pre-exponential factor are 38.2 ± 1 kJ mol⁻¹ and $8 \times 10^{28 \pm 1}$ molecules cm⁻² s⁻¹ respectively.

A wide range of surface coverages was investigated using RAIRS at an astrophysically relevant temperature. The RAIR spectrum of CH₃CN multilayers adsorbed on silica is consistent with the literature spectra. The intensity of the IR bands increases with increasing the exposure of CH₃CN. The IR frequencies at low coverages are in good agreement with those for bulk material. Therefore, there is no evidence for a specific chemical bonding between acetonitrile and the silica. CH₃CN on amorphous water ice showed an increase in the intensity of the CN-stretch mode, without shifting, even at low coverage of CH₃CN. This was due to the formation of hydrogen bonding C≡N···H-O. Computational studies revealed that CH₃CN molecules are oriented randomly on water ice. Moreover, calculated binding energies of CH₃CN-H₂O complexes suggest physisorption rather than chemisorption is taking place between acetonitrile and water. RAIR spectra of annealed CH₃CN:H₂O mixtures show evidence for a crystallisation of the water ice, whereas acetonitrile desorbed. In contrast, no similar features could be observed when heating CH₃CN on silica or on H₂O ice. CH₃CN ice is likely to be a crystalline structure, compared to data reported in previous work [44].

The surface structure of CH₃CN adsorbed on a film of H₂O is illustrated in **Figure 4.20**. This is compared with the C₆H₆ structure which has previously been investigated at the same experimental conditions. The results obtained by RAIRS and

TPD suggest that CH_3CN wets a silica surface, as shown in **Figure 4.20a**, for monolayer coverages, whereas C_6H_6 does not wet silica [39]. This is due to H-bonding forming in the case of the CH_3CN and the fact that there is a balance of forces in the case of the C_6H_6 . At high surface exposure, as shown in **Figure 4.20b**, layers of CH_3CN films are built, forming clusters and islands on the H_2O surface, while for C_6H_6 , isolated islands were formed on the H_2O ice surface.

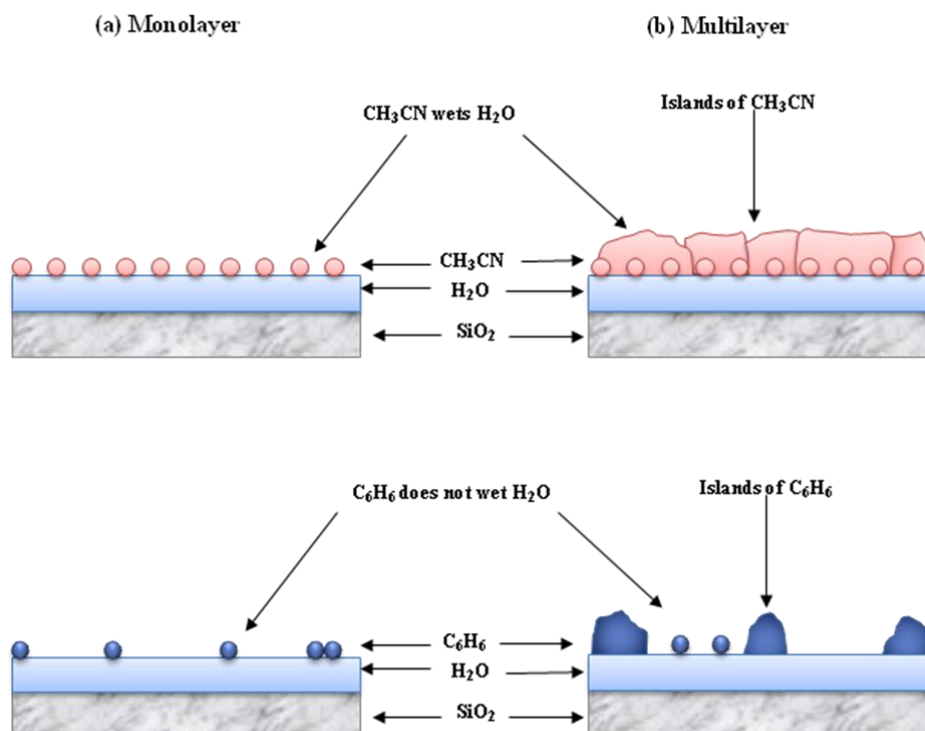


Figure 4.20: Cartoon illustrating the surface morphology of the layered CH_3CN ice system in comparison with C_6H_6 ice system. Both adsorbed on an amorphous SiO_2 surface.

4.6 References

- [1] M. B. Bell, P. A. Feldman, S. Kwok, and H. E. Matthews, *Nature*, 1982, **295**, 389.
- [2] R.L. Hudson and M.H. Moore, *Icarus*, 2004, **172**, 466.
- [3] L. E. Snyder, *Biosphere*, 1997, **27**, 115.
- [4] G. A. Blake, E. C. Sutton, C. R. Masson, and T. G. Phillips, *Astrophys. J.*, 1987, **315**, 621.
- [5] E. F. van Dishoeck and G. A. Blake, *Ann. Rev. Astron. Astrophys.*, 1998, **36**, 317.
- [6] E. L. Gibb, D. C. B. Whittet, W. A. Schutte, A. C. A. Boogert, J. E. Chiar, P. Ehrenfreund, P. A. Gerakiness, J. V. Keane, A. G. G. M. Tielens, E. F. Van Dishoeck, and O. Kerkhof, *Astrophys. J.*, 2000, **536**, 347.
- [7] Y. J. Pendleton and A. G. G. M. Tielens, A. T. Tokunaga, and M. P. Bernstein, *Astrophys. J.*, 1999, **513**, 294.
- [8] R. J. A. Grim and J. M. Greenberg, *Astrophys. J.*, 1987, **321**, L91.
- [9] W. A. Schutte and J. M. Greenberg, *Astron. Astrophys.*, 1997, **317**, L43.
- [10] K. Demyk, E. Dartois, L. d'Hendecourt, M. Jourdain de Muizon, A. M. Heras, and M. Breitfellner, *Astron. Astrophys.*, 1998, **339**, 553.
- [11] M. E. Palumbo, G. Strazzulla, Y. J. Pendleton, and A. G. G. M. Tielens, *Astrophys. J.*, 2000, **534**, 801.
- [12] S. B. Charnley, S. D. R., Y. J. Kuan, and H. C. Huang, *Adv. Space Res.*, 2002, **30**, 1419.
- [13] K. Beatty, C. C. Petersen, and A. Chaikin, *The New Solar System*, 4th ed, (Cambridge University Press, Cambridge, 1999).
- [14] S. B. Charnley, S. D. Rodgers, Y.-J. Kuan, and H. -C. Huang, *Adv. Space Res.*, 2002, **30**, 1419.
- [15] V. Vuitton, R. V. Yelle, and V. G. Anicich, *Astrophys. J.*, **647**, 2006, L175.

- [16] A. J. Remijan, S. N. Milam, M. Womack, A. J. Apponi, L. M. Ziurys, S. Wyckoff, M. F. A'Hearn, I. de Pater, J. R. Forster, D. N. Friedel, P. Palmer, L. E. Snyder, J. M. Veal, L. M. Woodney, and M. C. H. Wright, *Astrophys. J.*, 2008, **689**, 613.
- [17] M. Ohishi, W. M. Irvine, and N. Kaifu, *Astrochemistry of Cosmic Phenomena*, Proceedings IAU Symposium, 1992, **150**, 171.
- [18] R. T. Garrod, S. L. W. Weaver, and E. Herbst, *Astrophys. J.*, **682**, 2008, 283.
- [19] B. C. Spall and E. W. R. Steacie, *Proc. R. Soc. London, Ser. A.*, 1957, **239**, 1.
- [20] F. Duvernay, P. Chatron-Michaud, F. Borget, D. M. Birney, and T. Chiavassa, *Phys. Chem. Chem. Phys.*, 2007, **9**, 1099.
- [21] R. T. Garrod, S. L. Widicus Weaver, and E. Herbst, *Astrophys. J.*, 2008, **682**, 283.
- [22] G. Danger, J.-B. Bossa, P. deMarcellus, F. Borget, F. Duvernay, P. Theulé, T. Chiavassa, and L. d'Hendecourt, *Astron. Astrophys.*, 2011, **525**, 1.
- [23] M. P. Bernstein, S. F. M. Ashbourn, S. A. Sandford, and L. J. Allamandola, *Astrophys. J.*, 2004, **601**, 365.
- [24] D. M. Koch, C. Toubin, G. H. Peslherbe, and J. T. Hynes, *J. Phys. Chem. C.*, 2008, **112**, 2972.
- [25] J. E. Elsila, J. P. Dworkin, M. P. Bernstein, M. P. Martin, and S. A. Sandford, *Astrophys. J.*, 2007, **660**, 911.
- [26] N. R. Lerner and G. W. Cooper, *Geochim. Cosmochim. Acta*, 2005, **69**, 2901.
- [27] J. R. Cronin and S. Pizzarello, *Science*, 1997, **295**, 951.
- [28] S. Pizzarello and G. W. Cooper, *Meteor. Planet. Sci.*, 2001, **36**, 897.
- [29] N. R. Lerner, *Geochim. Cosmochim. Acta*, 1997, **61**, 4885.
- [30] J. Oro, *Nature*, 1961, **190**, 389.
- [31] B. A. Sexton, N. R. Avery, *Surf. Sci.*, 1983, **129**, 21.
- [32] C. Shannon, A. Champion, *Surf. Sci.*, 1990, **227**, 219.

- [33] E. L. Meijer, R. A. van Santen, A. P. J. Jansen, *J. Phys. Chem.*, 1996, **100**, 9282.
- [34] J. E. Schaff, and J. T. Roberts, *Langmuir*, 1999, **15**, 7232.
- [35] S. Bahr and V. Kempster, *J. Chem. Phys.*, 2009, **130**, 214509.
- [36] P. G. Debenedetti, *J. Phys.: Condens. Matter*, 2003, **15**, R1669.
- [37] J. E. Bartmess and R. M. Georgiadis, *Vacuum*, 1983, **33**, 149.
- [38] D. R. Lide, W. M. “Mickey” Haynes, *CRC Handbook of Chemistry and Physics*, 90th ed, (CRC Press, Boca Raton, 2010).
- [39] J. D. Thrower, *PhD Thesis*, (Heriot-Watt University, Edinburgh, 2009).
- [40] M. P. D’Evelyn, Y. L. Yang, and S. M. Cohen, *J. Chem. Phys.*, 1994, **101**, 2463.
- [41] T. Zubkov, R. s. Smith, T. R. Engstrom, and B. D. Kay, *J. Chem. Phys.*, 2007, **127**, 184707.
- [42] V. L. Frankland, *PhD Thesis*, (Heriot-Watt University, Edinburgh, 2011).
- [43] G. Attard and C. Barnes, *Surfaces*, (Oxford University Press, Oxford, 2008).
- [44] A. G. M. Abdulgalil, D. Marchione, J. D. Thrower, M. P. Collings, and M. R. S. McCoustra, F. Islam and M .E. Palumbo, *Phil. Trans. R. Soc. A*, 2013, **371**, 20110586.
- [45] CKS 1.0, IBM Almaden Research Center, © IBM Corporation 1995.
- [46] F.A. Houle, W.D. Hinsberg, *Surf Sci*, 1995, **338**, 329.
- [47] J. S. Chickos, W. E. Acree, *J. Phys. Chem. Ref. Data*, 2002, **31**, 537.
- [48] N. Russo, and R. Khanna, *Icarus*, 1996, **123**, 366-395.
- [49] G. Herzberg, *Infrared and Raman Spectra of Polyatomic Molecules*, 1st ed., (Van Nostrand Reinhold Company Inc., New York, 1945).
- [50] N. Nagai, *Ana. Sci.*, 2001, **17**, 671.
- [51] <http://science.gsfc.nasa.gov/691/cosmicice>.

- [52] I. Engquist, I. Lundström, B. Liedberg, A. N. Parikh, and D. L. Allara, *J. Chem. Phys.*, 1997, **106**, 3038.
- [53] A. B. Horn, M. A. Chesters, M. R. S. McCoustra, and J. R. Sodeau, *J. Chem. Soc. Faraday Trans.*, 1992, **88**, 1077.
- [54] B. Rowland, N. S. Kadagathur, J. P. Devlin, V. Buch, T. Feldman, and M. J. Wojcik, *J. Chem. Phys.*, 1995, **102**, 8328.
- [55] Hyperchem Release 8.0.2, Molecular Modelling System, © 2007, Hypercube Inc.
- [56] G. A. Jeffrey, *An introduction to hydrogen bonding*, (Oxford University Press, 1997).
- [57] F. Duvernay, P. Chatron-Michaud, F. Borget, D. M. Birney, and T. Chiavassaa, *Phys. Chem. Chem. Phys.*, 2007, **9**, 1099.
- [58] D.-S. Ahn and S. Lee, *Bull. Korean Chem. Soc.*, 2007, **28**, 725.

CHAPTER – 5 Low Energy Electron Promoted Desorption of CH₃CN

Contents

5.1	Introduction.....	158
5.2	Chemistry of Acetonitrile.....	158
5.3	Experimental Procedure	160
5.3.1	<i>Electron Irradiation Experiments</i>	<i>160</i>
5.3.2	<i>Proton Irradiation Experiments.....</i>	<i>161</i>
5.4	Results and Discussion	163
5.4.1	<i>Low Energy Electron Processing of CH₃CN.....</i>	<i>163</i>
5.4.1.1	<i>Irradiated CH₃CN Adsorbed on ASW.....</i>	<i>163</i>
5.4.1.2	<i>Irradiated CH₃CN Adsorbed on Amorphous SiO₂</i>	<i>172</i>
5.4.1.3	<i>Interactions of Solid CH₃CN with Low Energy Electrons</i>	<i>178</i>
5.4.2	<i>Proton Processing of CH₃CN</i>	<i>183</i>
5.4.3	<i>Impact of Electron and Proton Irradiation on Solid CH₃CN.....</i>	<i>190</i>
5.5	Conclusions and Astrophysical Implications	193
5.6	References.....	196

5.1 Introduction

This chapter discusses the results obtained from the interaction of low energy electrons and medium energy protons with CH₃CN ices. The interaction of electrons (250 – 400 eV) with CH₃CN adsorbed on H₂O and on silica is investigated using Reflection-absorption Infrared Spectroscopy (RAIRS). Transmission Infrared Spectroscopy (TIRS) is used to probe the interaction of protons (200 keV) in thick films on a transmitting substrate. The loss of CH₃CN under irradiation with electrons and protons, due to both desorption and chemical transformation, is measured and compared, with the aim of understanding the relative contributions of secondary electron-promoted processes *versus* ion-promoted processes in relation to energetic processing of molecular ices in astrophysical environments. The low energy (250 - 400 eV) electrons that have been employed are typical of the secondary electrons that might be generated by passage of these protons, and therefore of CRs, through molecular solids.

5.2 Chemistry of Acetonitrile

In the interstellar space, almost all molecules are subjected to a strong interstellar radiation field, which leads to energetic processing resulting in production of more complex molecules, including CN-bonded molecules. As reviewed in **Section 4.2** in **Chapter 4**, nitriles exist in the interstellar space and are considered to be crucial in astrobiology because they are the putative intermediates from which important prebiotic organic acids (*e.g.* amino acids) are proposed to form. Due to the photostability of nitriles, they are able to survive the strong UV field present in the interstellar space and are therefore able to engage in further chemistry [1]. They can be hydrolysed to form amino acids or polymerise to produce tholins [2]. Understanding the nitrile chemistry promoted by proton and VUV irradiation, as well as thermal effects, is key for the interpretation of astrophysical and astrochemical observations. For example, CH₃CN, CH₃NC, C₂H₅CN, and C₂H₃CN have been observed in Titan's atmosphere [3, 4] and it is suggested that complex CN-containing species may derive from ion–molecule reactions involving these small nitriles.

Nitriles are also important atmospheric molecules in Earth's atmosphere. It has been reported that CH_3CN is a useful gaseous tracer of biomass burning, since simultaneous CO and acetonitrile measurements may be used to estimate the ratio of biomass burning to fossil fuel combustion, which is a key issue for current global warming studies [5].

In astrophysics and astrochemistry, CH_3CN is a molecule of interest because it is a potential source of amino acids, through irradiation with energetic particles. One of the most interesting questions concerns the pathways by which CH_3CN may be desorbed and/or dissociated to other species through interactions with photons [6-10], protons [10, 11], electrons [12-14] and surfaces [15-17]. Previous studies have shown that CH_3CN is destroyed by both UV photons with a flux of 2×10^{14} photons $\text{cm}^{-2} \text{ s}^{-1}$ and protons with a flux of 4×10^{12} protons $\text{cm}^{-2} \text{ s}^{-1}$, at temperatures of 12 K and 24 K respectively. In both situations, molecules such as hydrogen cyanide (HCN), methane (CH_4), methyl isocyanide (CH_3NC), and ketenimine ($\text{H}_2\text{C}=\text{C}=\text{NH}$) were detected [9]. In the case of electrons, the interactions are dominated by dissociative electron attachment (DEA). Sailer *et al.* irradiated gaseous samples of CH_3CN with low energy electrons, in the range of 10 eV at 293 K. They observed five anionic products; (CH_2CN^- , CHCN^- , CCN^- , CN^- , and CH_3^-) and the maximum value of the production cross-section was determined for the CH_2CN^- to be 4×10^{-19} cm^2 . This behaviour of CH_3CN when irradiated by such low energy electrons is explained by the accommodation of an additional electron into an orbital with π_{CN}^* character [12]. In contrast, recent studies by Baas *et al.* on electron irradiation of solid CH_3CN at 30 K resulted in a neutral product (C_2H_6) and four anionic products (H^- , CH_2^- , CH_3^- , and CN^-). These were observed as products of the electron irradiation at energies of 0-20 eV of solid CH_3CN at 30 K [14]. They attributed these to the presence of several negative ion resonances in the 6 to 14 eV energy ranges [14].

The work presented in this chapter reports collaborative investigations made as part of the activities of the European network LASSIE, Laboratory Astrochemical Surface Science In Europe, on the surface and solid state astrochemistry of thin and ultrathin films of CH_3CN , grown under conditions that mimic those of astrophysical environments.

5.3 Experimental Procedure

5.3.1 Electron Irradiation Experiments

The electron irradiation experiments described in this chapter were performed in the UHV chamber described in **Chapter 2**. Deionized water (H_2O , Fluka), isotopically labelled water (D_2O and H_2^{18}O , Aldrich), and CH_3CN (99.9%, Fisher Scientific) were purified using a freeze–pump–thaw procedure under vacuum. Exposures are reported in units of Langmuir ($1 \text{ L} = 1 \times 10^{-6} \text{ Torr s}$). Adsorbate films were subjected to irradiation by a low energy electron beam produced using an ELG-2 electron gun and its EGPS-1022 power supply (Kimball Physics, Inc.). The ELG-2 electron gun with a unipotential refractory cathode is able to produce an electron beam with an energy spread of 0.5 eV. Electron currents were measured with the sample grounded through a picoammeter. The beam of electrons was rastered with a frequency of 0.5 Hz over a surface area of approximately 0.75 cm^2 using a TV raster, as shown in **Figure 3.9 (Chapter 3)**.

The substrate was irradiated with electrons in the 250 to 400 eV energy range, at an incident angle of 45° . No significant differences in the beam current were observed between measurements made during the irradiation of the SiO_2 surface and the uncoated rear surface of the stainless steel disc. Continuous beam irradiation with a beam current in the 100 – 200 nA range, corresponding to electron fluxes of $(1.2 - 1.4) \times 10^{12} \text{ electrons cm}^{-2} \text{ s}^{-1}$, was used throughout, with no evidence for charging effects on the substrate.

Changes in the adsorbate films were monitored using a FTIR spectrometer (Nicolet 8070) in a RAIRS configuration. Spectra were recorded with the coaddition of 1024 scans at a resolution of 2 cm^{-1} . The interactions of low energy electrons with the condensed films were investigated by monitoring the decrease of the νCN peak intensity in the IR spectra as a function of electron irradiation time. From these measurements, the total electron-promoted desorption cross section is determined. Since the chemical identity of the desorbed species cannot be determined by RAIRS, this cross section includes all processes that lead to the loss of CH_3CN molecules from the surface.

The deposition of H₂O, its isotopic variants and CH₃CN, electron irradiation, and RAIRS were all performed at 110 K. The possible interaction routes between electrons and the CH₃CN/H₂O system were studied and enthalpies of reaction, $\Delta_r H$, determined through computational chemistry, using the HyperChem Package [18].

5.3.2 Proton Irradiation Experiments

These experiments were carried out by Palumbo and Islam at Osservatorio Astrofisico di Catania [19]. The apparatus used in the ion irradiation experiments has been described elsewhere [20-22]. In brief, most experiments were performed in a high vacuum chamber with base pressure of about 10^{-7} mbar. A needle valve is used to allow pure CH₃CN to be deposited onto a crystalline silicon substrate placed in thermal contact with a rotatable cold finger, the temperature of which can be varied within the 10 – 300 K range. Under such pressure conditions, it is likely that O-containing molecules, in particular H₂O, may deposit on the substrate. Some samples were therefore grown with the CH₃CN capped with two layers of argon each of approximately 130 nm thickness [23, 24]. The gas inlet is not directed towards the substrate; thus a “background deposition” is obtained. The thickness of the films was monitored during deposition, using a He-Ne laser with absolute accuracy of 5% [25, 26].

Adsorbate films were irradiated by a beam of protons produced by an electrostatic 200 kV ion implanter (Danfysik) with magnetic mass separation. The proton beams were scanned electrostatically to ensure a uniform fluence on the target. Typical fluxes were 1×10^{12} protons $\text{cm}^{-2} \text{s}^{-1}$. The icy samples discussed in this work were irradiated with 200 keV protons at 15 K and 77 K. The size of the spot produced by the proton beam is larger than the area probed by the IR beam. To avoid the microscopic heating of the sample, current densities should range from 100 nA cm^{-2} up to a few $\mu\text{A} \text{cm}^{-2}$. Interactions on the surface were monitored by a Bruker Equinox 55 FTIR spectrometer, which operates at a resolution of 1 cm^{-1} or 2 cm^{-1} in transmission mode. For the IR beam and the proton beam, the incident angle is 45° (the two beams are mutually perpendicular). This arrangement allows the transmittance spectra to be easily obtained *in situ*, without reorienting the sample.

There is a rotatable polarizer placed in the path of the infrared beam in front of the detector. This permits recording the IR spectra in two types; parallel (p-polarization) and perpendicular (s-polarization) to the plane of incidence. It has been shown [26, 27] that when the band profiles recorded in p- and s-polarization are similar, the transitions are weak and the features seen in the transmission spectra directly reflect the variation of the absorption coefficient of the solid sample. This circumstance was observed for the profile of all the CH₃CN bands and the bands present in the spectra after proton irradiation. For the quantitative analysis of these bands, p-polarised spectra were considered, since the signal-to-noise ratio is higher for this polarization. The surface concentration (*i.e.*, column density) Θ in molecules cm⁻² of the new products was calculated using the following equation (then corrected for 45° incidence):

$$\Theta = \frac{\int \tau(\nu) d\nu}{A} \quad (5.1)$$

where $\int \tau(\nu) d\nu$ in cm⁻¹ is the band area (on an optical depth scale) calculated after subtraction of the underlying continuum and A is the band strength in cm molecule⁻¹. The uncertainties in the A values are about 20-30 % [28]. In addition, A values could depend on the temperature [29], the substrate [30] and on the mixture [31]. A simplified expression for **equation (5.1)** is Beer-Lambert law:

$$\Theta = \frac{I(\nu)}{A} \quad (5.2)$$

where $I(\nu)$ is the intensity of the band. The penetration depth of impinging protons is larger than the thickness of the sample, as confirmed using the SRIM code [32].

5.4 Results and Discussion

5.4.1 Low Energy Electron Processing of CH₃CN

5.4.1.1 Irradiated CH₃CN Adsorbed on ASW

The environment in which solids are adsorbed is a key factor that must be considered during irradiation with energetic particles such as UV photons, protons, electrons, *etc.* Solid CH₃CN films with low exposures ranging from 7.5 to 25 L were deposited on 200 L of H₂O condensed on a silica surface at 110 K. The deposition is followed by irradiation with electrons at an energy of 300 eV for 5000 s. **Figure 5.1** shows the behaviour of the C≡N stretching band of solid CH₃CN at 2251 cm⁻¹ during electron irradiation. The spectra are represented as difference spectra of irradiated ice samples with respect to the unirradiated sample. The increasing loss of the C≡N peak intensity demonstrates that removal of CH₃CN from the IR observed region is caused by physical and/or chemical processes promoted by the bombardment by electrons. Since the loss increases with increasing irradiation time, a desorption process is likely to have taken place. However, a new feature appears as a shoulder of the C≡N stretching peak at 2248 cm⁻¹ (denoted “Feature A” on **Figure 5.1a, b, and c**), whose intensity increases with irradiation time.

The position of this feature raises the question as to whether it results from a chemical or a physical transformation. To investigate the possible chemical origin of Feature A, reactions between CH₃CN and H₂O were studied experimentally and theoretically. Solid CH₃CN adsorbed on top of water isotopomers (*i.e.* D₂O and H₂¹⁸O) films was irradiated with electrons, to determine the origin of Feature A observed at 2248 cm⁻¹ in the CH₃CN / H₂O experiments. These experiments did not show evidence for any new spectral features belonging to isotopically labelled products.

Figure 5.2 shows the RAIR spectra of 5 L CH₃CN adsorbed on a 100 L exposure of D₂O condensed on bare silica before and after irradiation with electrons at energy of 300 eV.

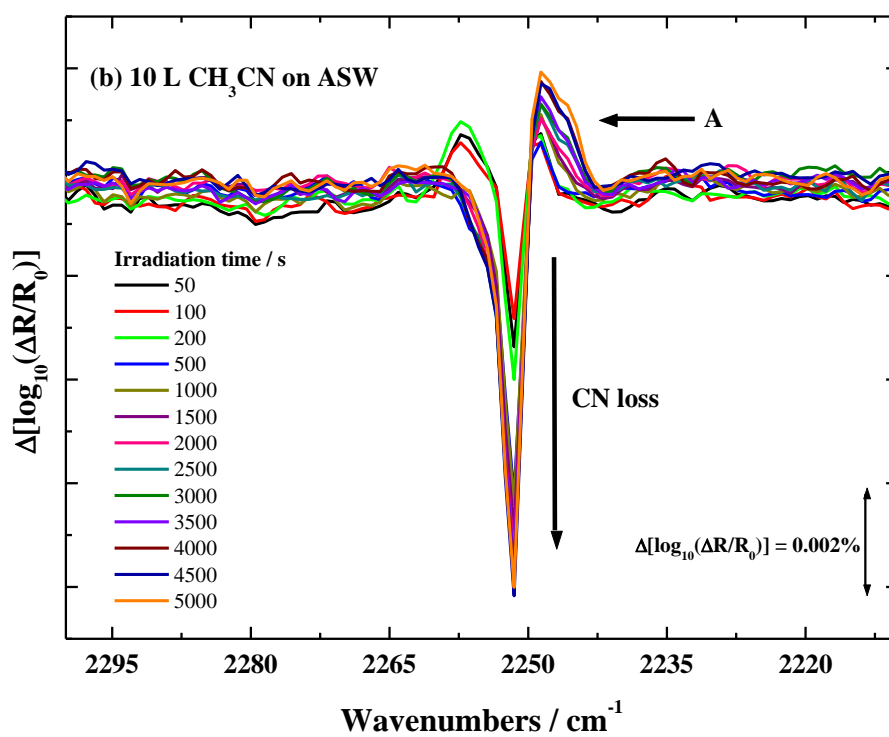
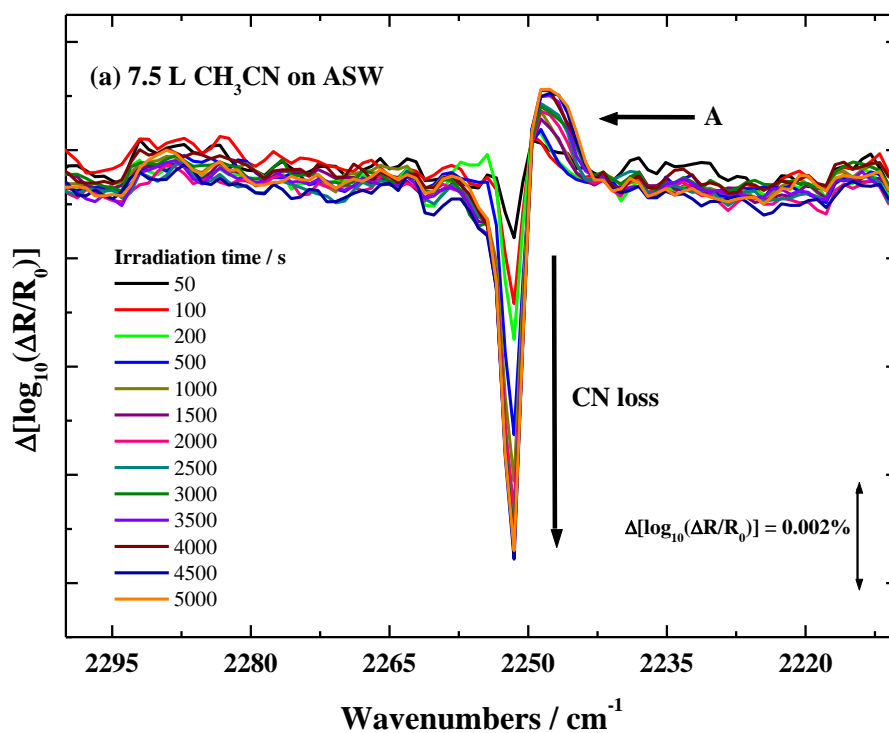


Figure 5.1: Continued on the following page.

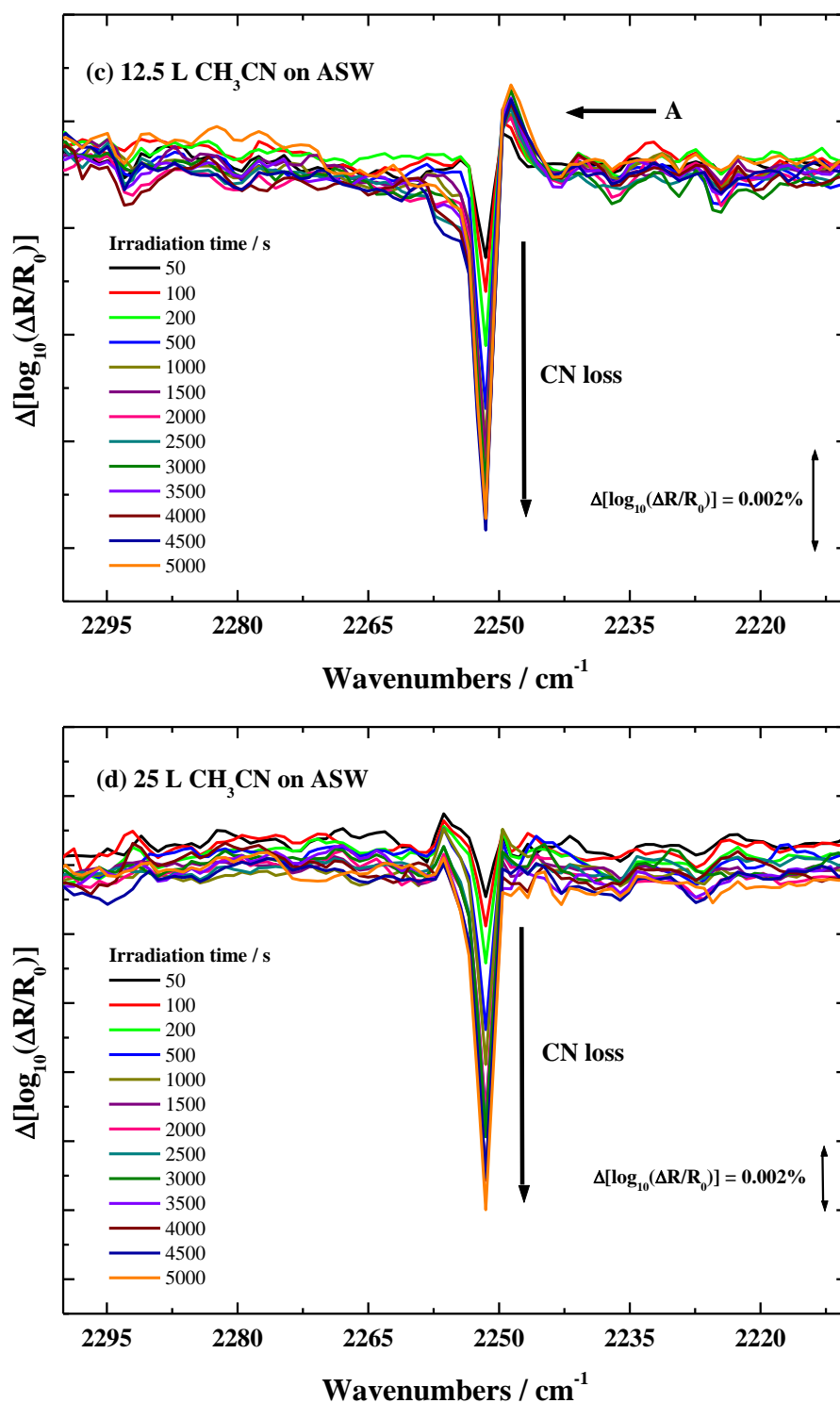


Figure 5.1: RAIR difference spectra of C≡N bands for irradiated solid CH₃CN/ 100 L H₂O system with electrons at energy of 300 eV and temperature of 110 L, where CH₃CN thickness is varied to be (a) 7.5 L, (b) 10 L, (c) 12.5 L and (d) 25 L. Black and coloured lines represent the ices during the irradiation with electrons, respectively. The spectra are offset for clarity.

As can be seen from **Figure 5.2a**, a band is observed at 2727 cm^{-1} . This is assigned to the stretching mode of the dangling-OD band of solid D_2O , consistent with other infrared experiments on D_2O films adsorbed on metal surfaces [33-35]. Two $\text{C}\equiv\text{N}$ stretch bands are observed at 2252 and 2267 cm^{-1} on D_2O (see **Figure 5.2b**) for solid CH_3CN . The latter saturates at an exposure of 5 L, while the 2252 cm^{-1} band grows as the thicker films of CH_3CN are grown. This is consistent with the work of Schaff *et al.* and Bahr *et al.* [15, 17], who report the observation of these two features in the $\text{C}\equiv\text{N}$ stretch region for solid CH_3CN on ASW: one at 2252 cm^{-1} , for CH_3CN adsorbed at the ASW surface, and the second at 2267 cm^{-1} , for CH_3CN in the bulk CH_3CN solid.

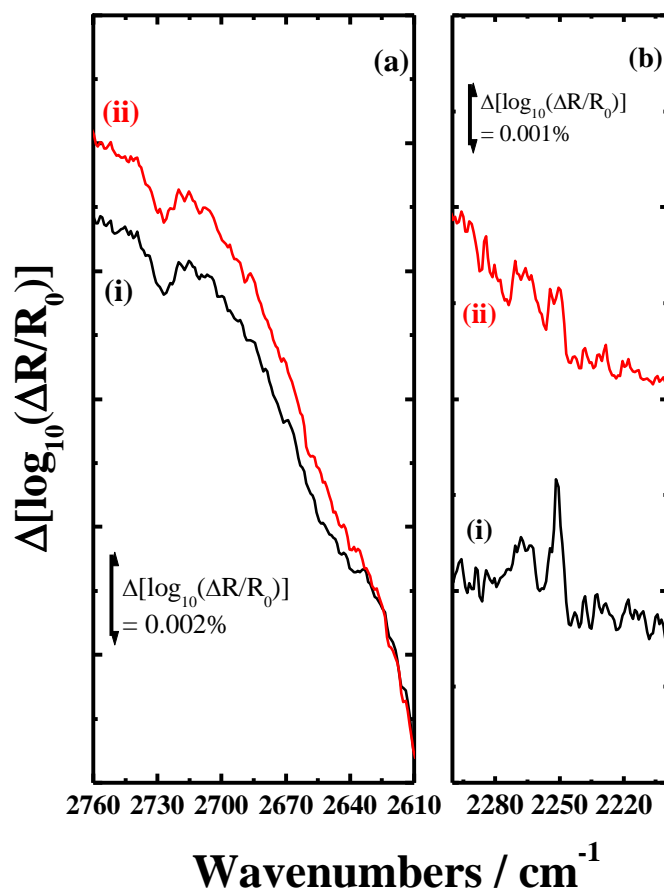


Figure 5.2: RAIR spectra of 5 L CH_3CN adsorbed on a thick film of D_2O : (i) before irradiation, and (ii) after the irradiation. The left panel (a) is the RAIR spectrum of OD dangling bands, and the right panel (b) is the RAIR spectrum of the $\text{C}\equiv\text{N}$ band.

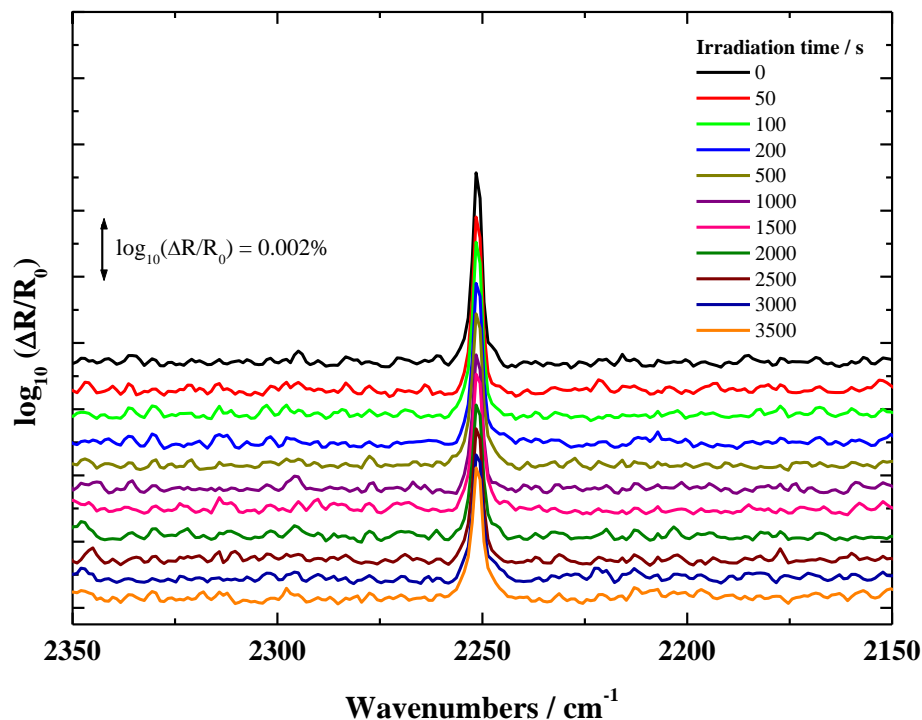


Figure 5.3: RAIR spectra of C≡N bands for 10 L CH₃CN adsorbed on 200 L of amorphous solid H₂¹⁸O system. Black and coloured lines represent the ices prior to and following irradiation with 300 eV electrons at a temperature of 110 K. The spectra are offset for clarity.

The C≡N stretch of solid CH₃CN adsorbed on H₂¹⁸O is shown in **Figure 5.3**. As we can see, simple loss of the C≡N stretch band is observed, consistent with the removal of CH₃CN from the observation region. There is no evidence for any other spectral features in this region, or indeed across the entire spectra.

A simple scheme of the possible reaction products of electron irradiation is presented in **Figure 5.4**. Computational chemistry gives an opportunity to explore the thermodynamics of these processes. Calculation of the enthalpy of formation ($\Delta_f H$) for each of the listed species then allows the enthalpy of reaction ($\Delta_r H$) to be calculated, as illustrated in **Figure 5.4**. These calculations provide the $\Delta_f H$ values for all molecules, which might not be available in the literature. The calculations were performed using HyperChem version 8.0.2 [18]. Semi-empirical calculations were carried out using the AM1 method, with a convergence limit of 1×10^{-8} and an

iteration limit of 200. A geometry optimisation with the Polak-Ribiere algorithm was employed.

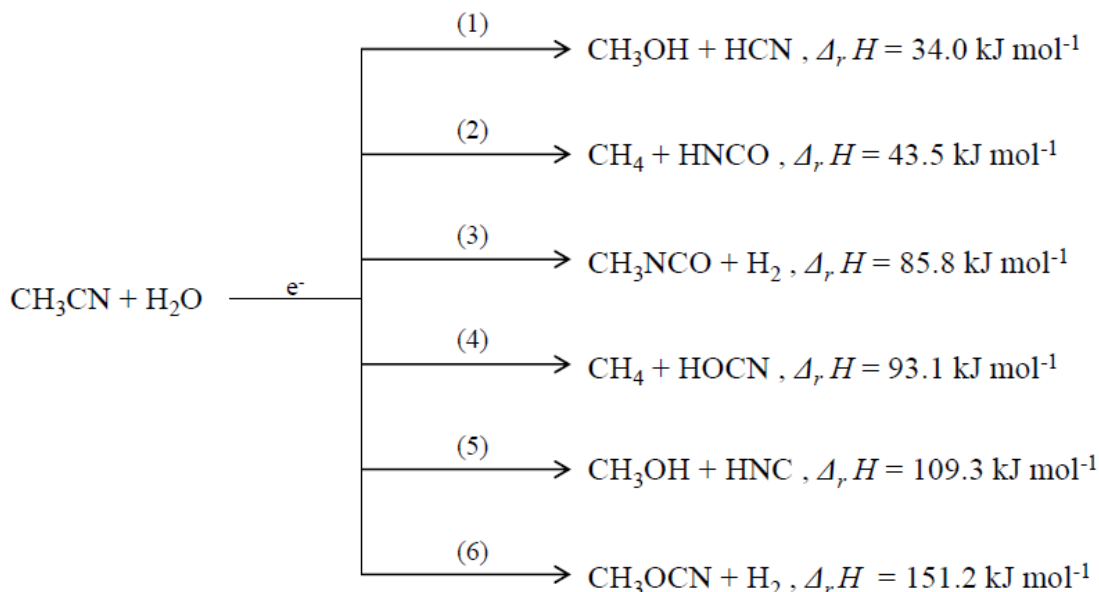


Figure 5.4: Possible reaction channels and products of the electron-promoted CH₃CN + H₂O reaction with their calculated enthalpy of reaction ($\Delta_r H$).

As can be seen from **Figure 5.4**, all pathways are endothermic. Therefore, thermodynamically, reaction pathways with the smallest enthalpy of reaction are likely to be favoured. The products with the lowest enthalpy of reaction are methanol (CH₃OH) with hydrogen cyanide (HCN) [pathway (1), 34.0 kJ mol⁻¹]. For reaction (1), there is no IR evidence for either the C-O stretching band located at 1033 cm⁻¹ in CH₃OH, or the C≡N stretch at 2096 cm⁻¹ in HCN [36]. Therefore, reaction (1) cannot be responsible for the appearance of Feature A.

The second lowest enthalpy of reaction is estimated for the products from reaction (2). The IR frequencies of CH₄ at 3020 cm⁻¹ and 1306 cm⁻¹ for CH₃ stretch and CH₃ deformation bands are not seen in these experiments [37]. Moreover, CH₄ is unlikely to be observed in these experiments, due to evaporation at 110 K. Solid HCNO shows strong IR bands at 3373, 3233, 2251, and 858 cm⁻¹, but only the band at 2251 cm⁻¹ is used to identify the NCO antisymmetric stretch vibration. The NCO antisymmetric stretch itself has two components in two environments: the HNCO and H₂O environments. In the HNCO environment, NCO is observed at 2234 cm⁻¹, while NCO in an H₂O environment is observed at

2260 cm^{-1} [38-40]. Neither feature is observed in this work. Thus, these products are not formed and reaction (2) does not occur.

Methyl isocyanate CH_3NCO in reaction (3) has two distinct features, at 2288 cm^{-1} and 1448 cm^{-1} , associated with $\text{N}=\text{C}=\text{O}$ stretching bands [41]. These IR features are not seen in this work and therefore, reaction (3) is not considered for Feature A.

The only detectable IR feature of the product HOCN from reaction (4), the $\text{C}\equiv\text{N}$ stretching band at 2286 cm^{-1} [42, 43], is not observed. The OCN bending band at 460 cm^{-1} [43] cannot be seen by the IR detector used in this work, due to the limits imposed by the IR detection window of 4000 - 650 cm^{-1} . Therefore, reaction (4) cannot be considered to be the origin of Feature A.

The products in reaction (5) have a high enthalpy of reaction, and there is no IR evidence of the $\text{N}=\text{C}$ stretching band at 2023 cm^{-1} to identify hydrogen isocyanide (HNC) [44-46].

In the last reaction, (6), methyl cyanate CH_3OCN has a feature of the $\text{C}=\text{N}$ stretching band at 2231 cm^{-1} [47], which is not observed in these experiments. Moreover, CH_3OCN is an unstable molecule and isomerises rapidly to produce CH_3NCO [48, 49]. Thus, reaction (6) is not occurring.

Since the proposed chemical processes are not able to explain the presence of Feature A, a physical process should be considered to explain the observations. **Figure 5.5** shows the difference spectra between unirradiated and irradiated CH_3CN of the 7.5, 10, 12.5, and 25 L exposures on the top of 200 L ASW. The intensity of Feature A increases with increasing the surface exposure from 7.5 L to 10 L, then starts decreasing above 10 L until it disappears at 25 L. From preliminary TPD data, CH_3CN at surface exposures 1 L and 5 L was suggested to form a monolayer of CH_3CN , which strongly binds to the ASW surface, as shown in **Figure 4.20a**. In contrast, CH_3CN at surface exposures between 7.5 L and 25 L was suggested to form isolated islands on the surface (see **Figure 4.20b**). The islands grow as the CH_3CN exposure is increased, until the surface is completely covered by 25 L. Some observations relevant to the irradiation of ices from the literature then provide a reasonable explanation of the origin of Feature A.

Irradiation of ASW with low energy electrons produces a population of 10 - 12 eV excitations, which diffuse rapidly through the ASW to the interfaces [50, 51]. Such electronic excitations can result in desorption of the molecules bonded to the ASW surface *via* hydrogen bonding. This was discussed in detail by Thrower and co-workers in investigations of electron-promoted desorption of benzene (C_6H_6) from ASW [52, 53].

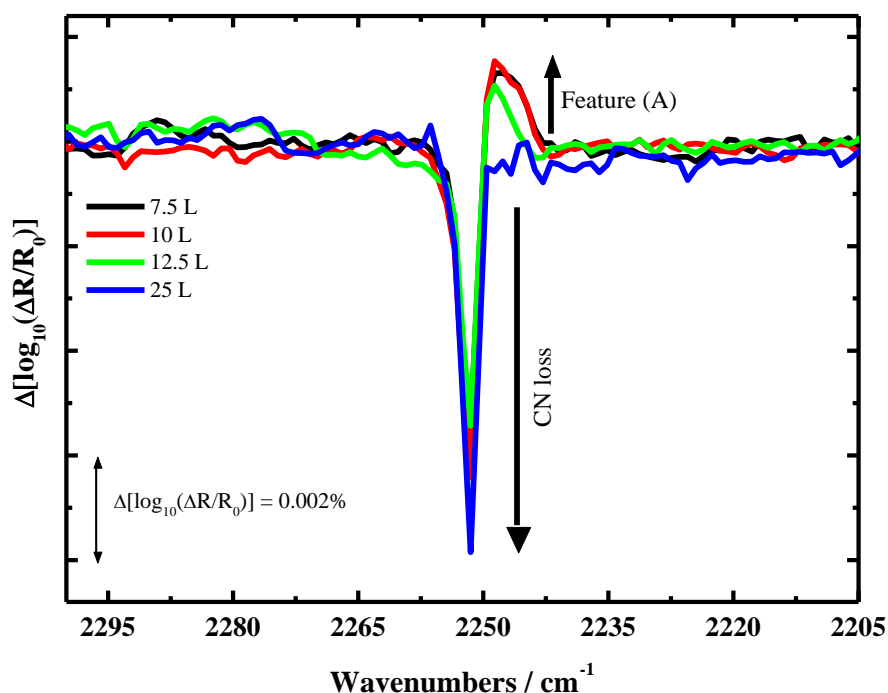


Figure 5.5: RAIR difference spectra of irradiated solid CH_3CN with 300 eV electrons for 5000 s at 110 K: coloured lines represent the different surface exposures of CH_3CN on 200 L H_2O .

Figure 5.6 shows the variation of the $C\equiv N$ stretching band intensity *versus* irradiation time. There is tentative evidence for a fast, electron-promoted desorption component in this work, *cf.* C_6H_6 [52, 53]. However, the present RAIRS experiments lack the ability to fully record such a fast component whilst irradiation is being carried out. The cross-section of total desorption, including the slow and fast components for bulk CH_3CN , are reported in **Section 5.4.1.2**. According to Thrower and co-workers [52, 53], desorption-promoted by electron irradiation of intra-island adsorbate molecules can induce molecules to diffuse

between the islands, and hence rapidly refill the intra-island. Similarly, such refilling can occur for the $\text{CH}_3\text{CN-H}_2\text{O}$ system. This was seen after irradiation of a 10 L exposure of CH_3CN on 100 L of D_2O , where the hydrogen-bonded feature consistent with the interfacial CH_3CN is retained as the bulk $\text{C}\equiv\text{N}$ stretch feature is lost (see **Figure 5.2**).

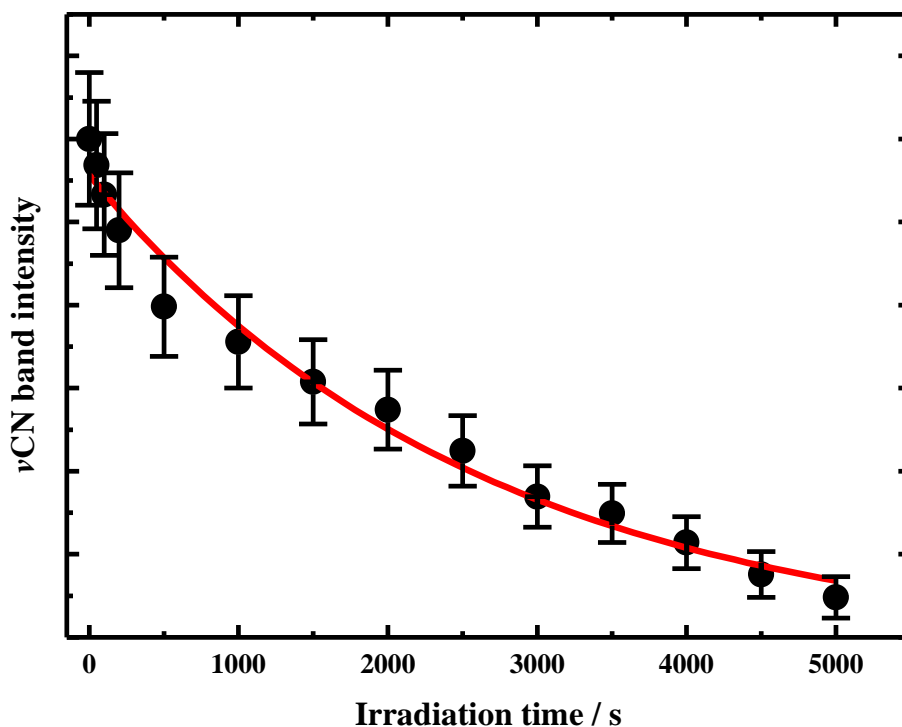


Figure 5.6: The $\text{C}\equiv\text{N}$ band intensity as a function of irradiation time (solid circles). The solid red line is an exponential to guide the eye and emphasize the desorption at short times. Error bars on the dots represent the standard deviation in several measurements.

However, the question of the mechanism of excitation relaxation as energy is discharged at the ASW interface to an island remains. Throrer and co-workers suggest that such relaxation may promote diffusion in a “hot atom”-like manner [52, 53]. This mechanism is supported by this work, as broadening of the solid $\text{C}\equiv\text{N}$ stretching feature could be associated with an amorphisation process disrupting the crystalline order of the CH_3CN films consequent to excitation relaxation at the ASW- CH_3CN island interface [54]. Such a crystalline-to-amorphous transition has been previously reported for H_2O ice irradiated with protons [55, 56].

5.4.1.2 Irradiated CH₃CN Adsorbed on Amorphous SiO₂

A 200 L exposure of CH₃CN was irradiated with electrons of energy ranging from 250 to 400 eV at 110 K. The thickness of CH₃CN equivalent to 200 L (the ionisation efficiency of CH₃CN is 2) is approximately 28 nm (thickness calculations are described in **Chapter 4**). **Figure 5.7** shows RAIR spectra of ultrathin CH₃CN films prior to and following irradiation with electrons, and focuses on the C≡N stretching band. The intensity of the C≡N stretching band decreases with increasing irradiation time. As previously shown, no IR bands belonging to new chemical species are observed in the IR spectra. Only desorption of CH₃CN during irradiation with electrons can account for the intensity decrease of the C≡N stretching band. This decrease of the IR band intensity with increasing irradiation time can be used to determine the rate of the desorption process, with **equation (2.27)** in **Chapter 2**. Analysis of electron-promoted processing is based on the concept that is previously described in **Chapter 2**. Thus, electron irradiation data in this chapter were analysed as in **Chapter 3**. By fitting the non-linear relationship (see **equation (2.30)**, **Chapter 2**) between the intensity of the C≡N stretching bands and irradiation time, the lifetime, τ , was calculated.

Figure 5.8 shows the effect of irradiation time on the IR intensities of the C≡N stretching band, and presents the decay curves which are used to calculate the desorption cross-section using the lifetime, τ , of the exponential decay curve *via* **equation (2.30)**. Finally, the total cross-section of the C≡N loss was calculated from **equation (2.31)**. As the area of the substrate exposed to the IR beam is larger than the electron irradiated region, there will always be a contribution of unirradiated CH₃CN to the spectra, and the C≡N stretch intensities will not decay to zero, as shown in **Figure 5.9**. The values of the EPD cross-section of solid CH₃CN are displayed in **Table 5.1**; these values are plotted *versus* the electron energy in **Figure 5.9**. As can be seen, the cross-section increases from $1.4 \times 10^{-15} \text{ cm}^2$ at 250 eV to $3.2 \times 10^{-15} \text{ cm}^2$ at 300 eV, and then decreases to $0.8 \times 10^{-15} \text{ cm}^2$ at 350 - 400 eV. The increase at 300 eV can be explained by the presence of the $C 1s \rightarrow \pi^*$ excitation in solid CH₃CN between 270 and 300 eV, which has been reported in previous studies of CH₃CN irradiated with both electrons and photons [57, 58].

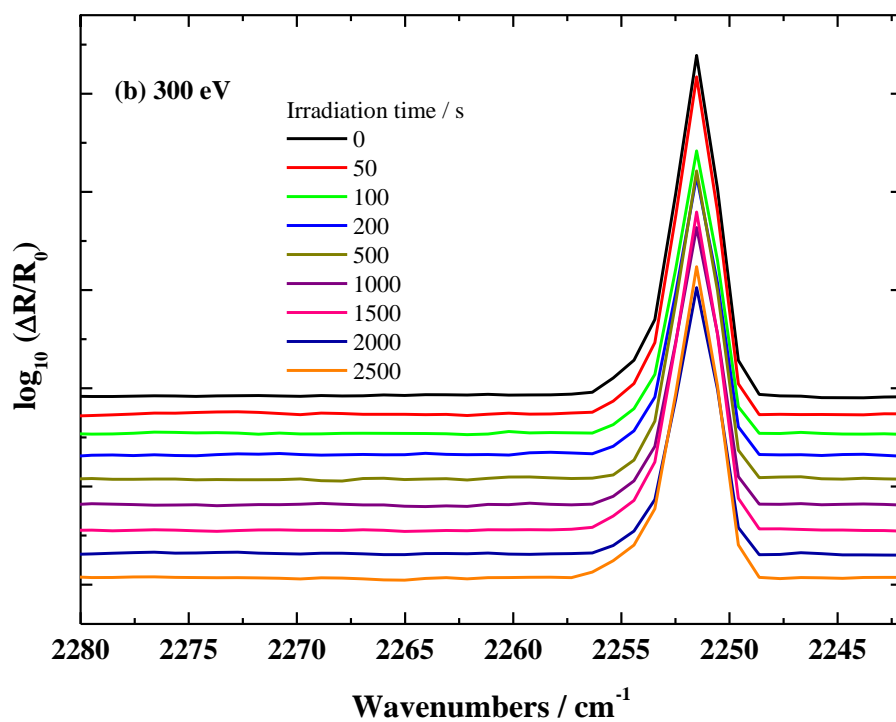
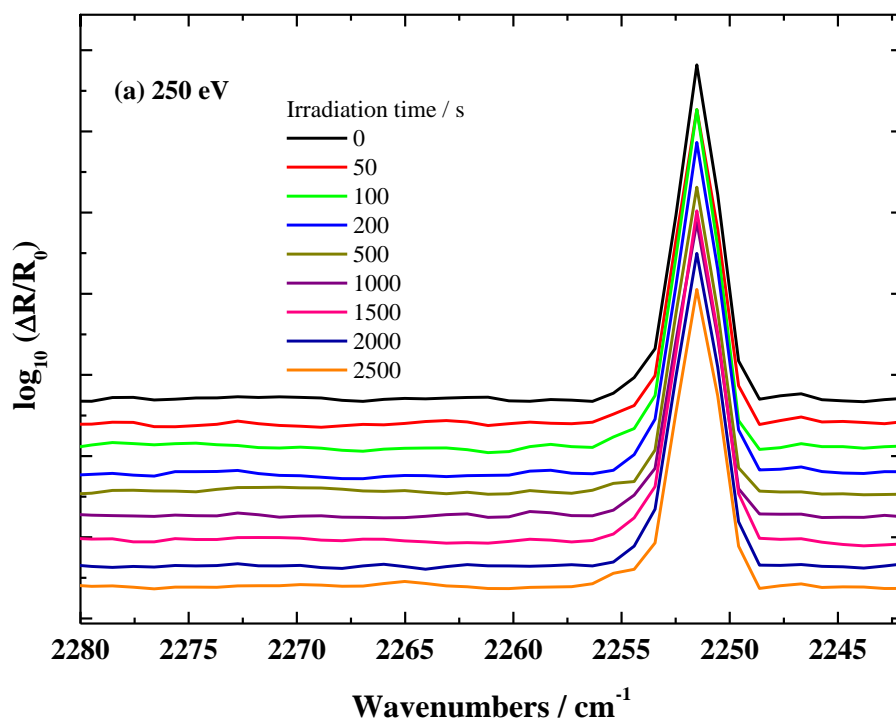


Figure 5.7: Continued on the following page.

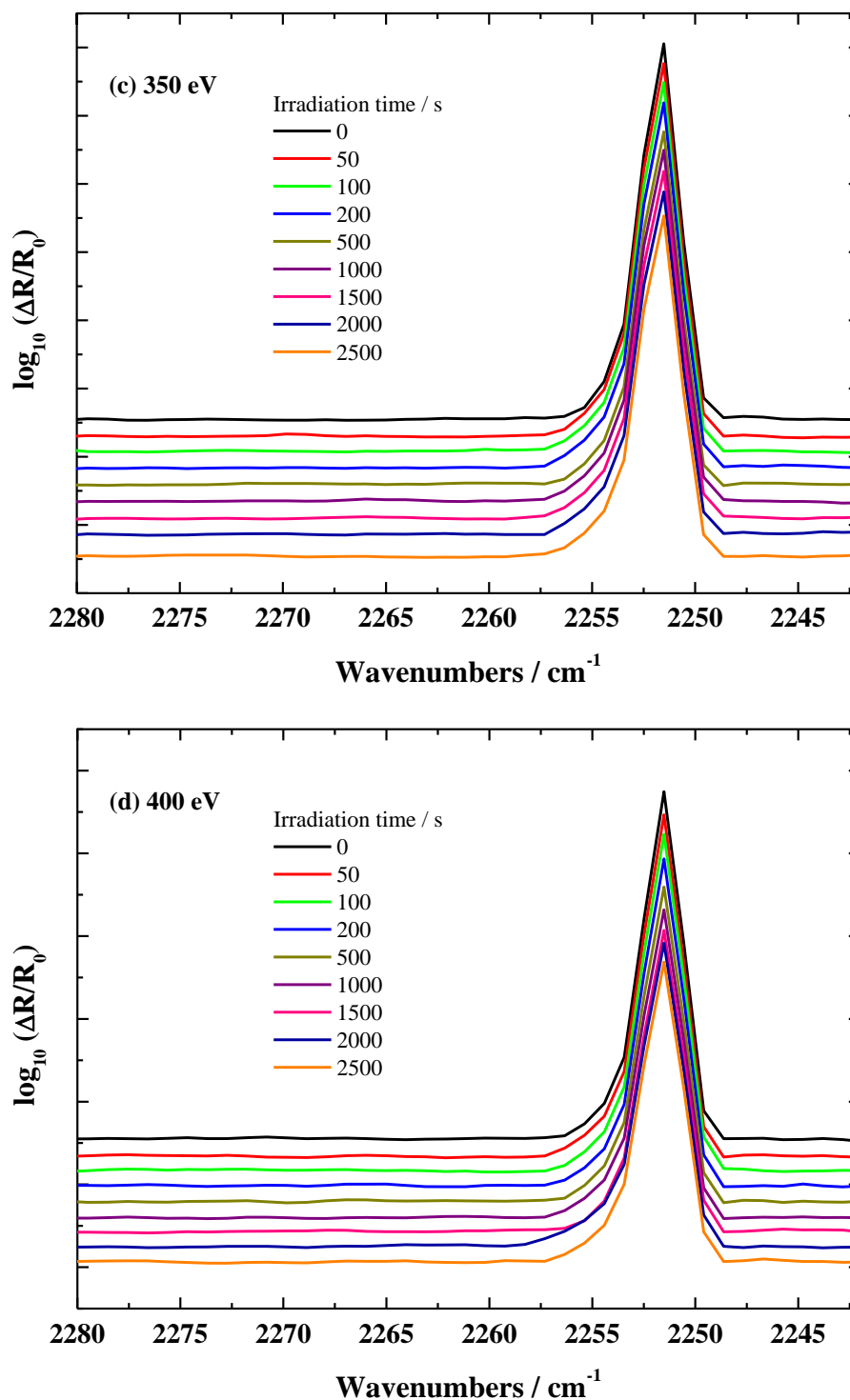


Figure 5.7: RAIR spectra of $\text{C}\equiv\text{N}$ bands for irradiated solid CH_3CN with low energy electrons at surface thicknesses of 200 L and a temperature of 110 L, where the energy varied to (a) 250, (b) 300, (c) 350, and (d) 400 eV. Black and coloured lines represent the spectra of solid CH_3CN ices prior to and following irradiation with electrons.

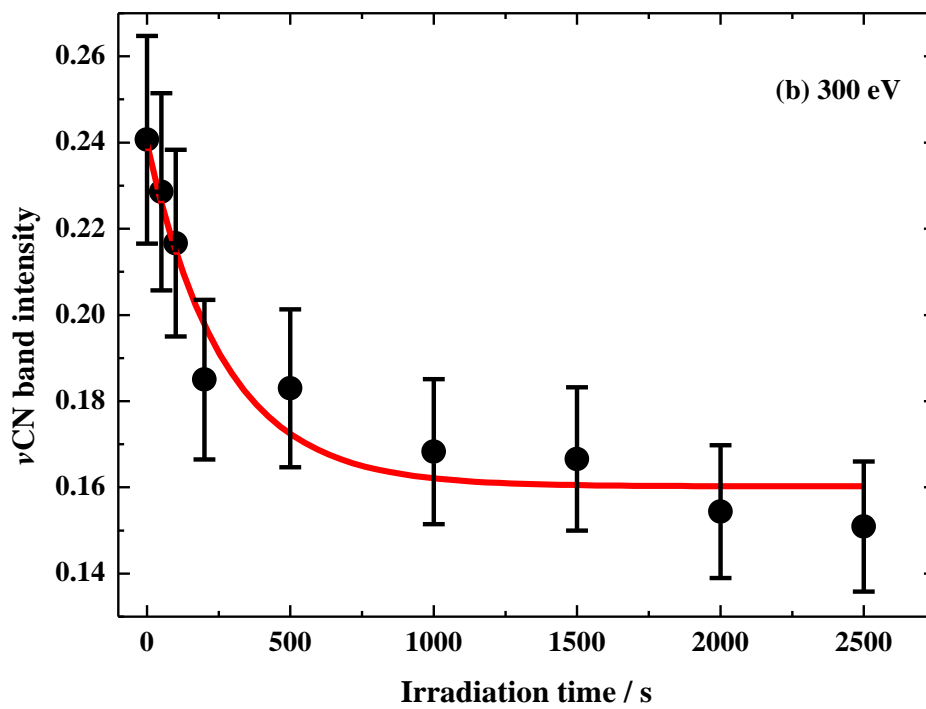
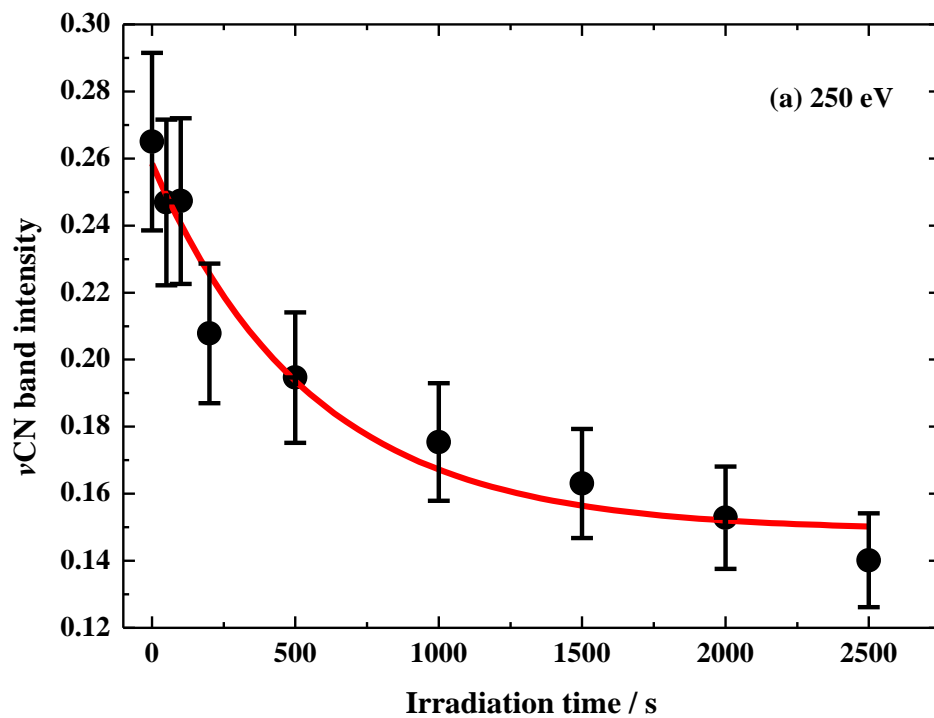


Figure 5.8: Continued on the following page.

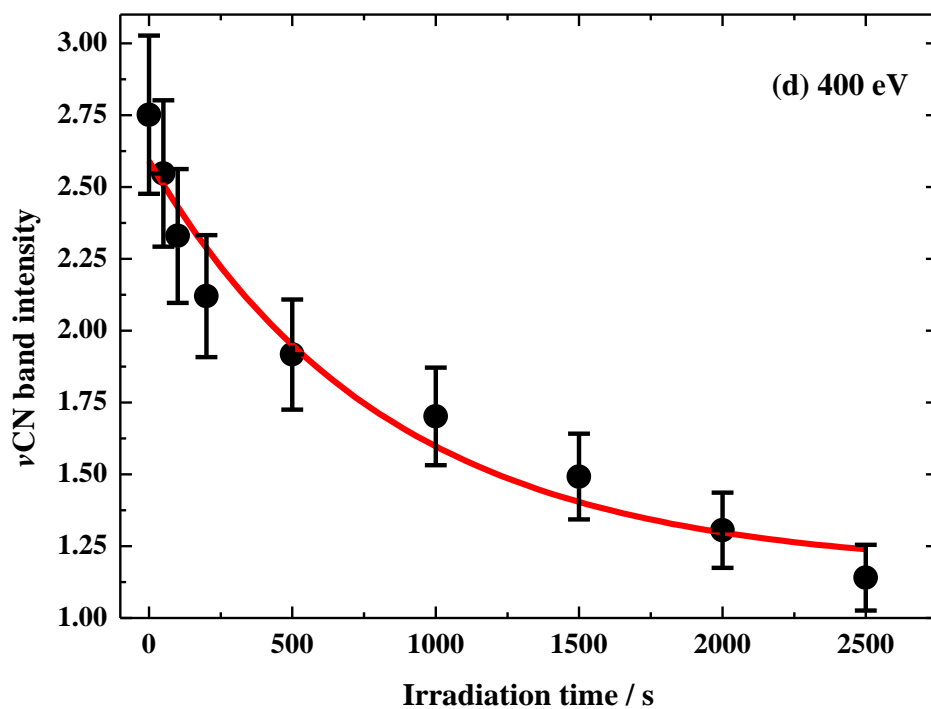
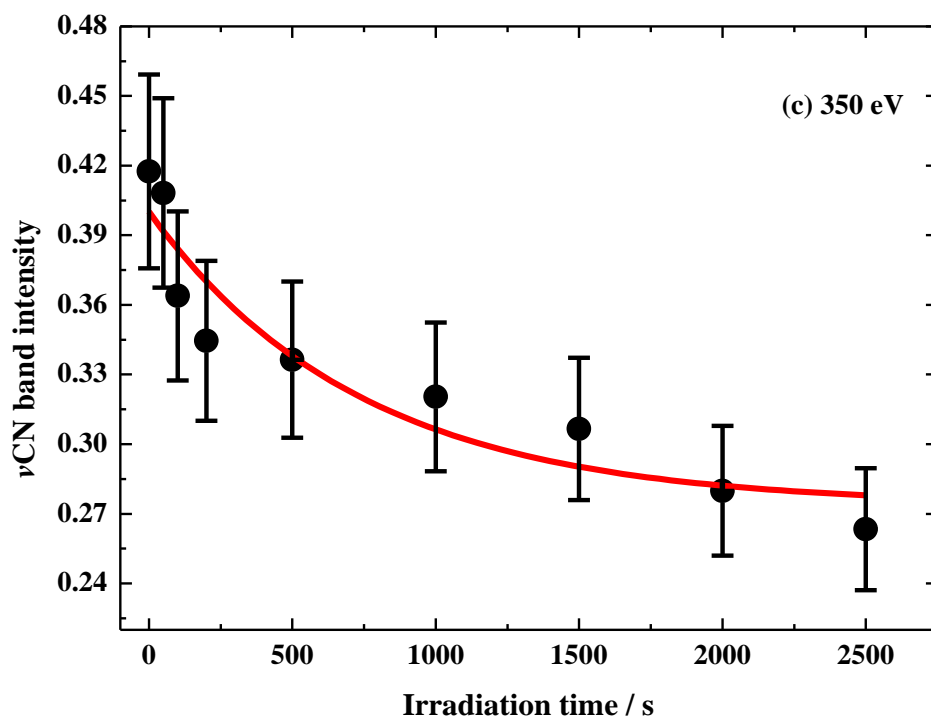


Figure 5.8: Fitted exponential decays for the decay of the C \equiv N stretching bands of CH₃CN adsorbed on ASW as a function of irradiation time at (a) 250, (b) 300, (c) 350 and (d) 400 eV. The thickness of CH₃CN was 28 nm. Error bars on the dots represent the standard deviation in several measurements.

Given the sensitivity of RAIRS to strong IR absorption features such as those containing the $C\equiv N$ moiety, It is possible to use a limiting estimate of electron-promoted reaction product concentration of less than 1% of a monolayer to estimate the cross-section for electron-promoted chemistry in the CH_3CN films to be around 10^{-19} cm^2 [59]. In contrast, these experiments give a cross-section for loss larger by the factor of 75 than this cross-section for electron-promoted chemistry. Therefore, the electrons are more likely than chemistry to promote loss, in this work. The errors shown in **Table 5.1** are again obtained from the errors of non-linear fit and the electron flux error, using the same method as reported in **Section 3.4.2** of **Chapter 3**.

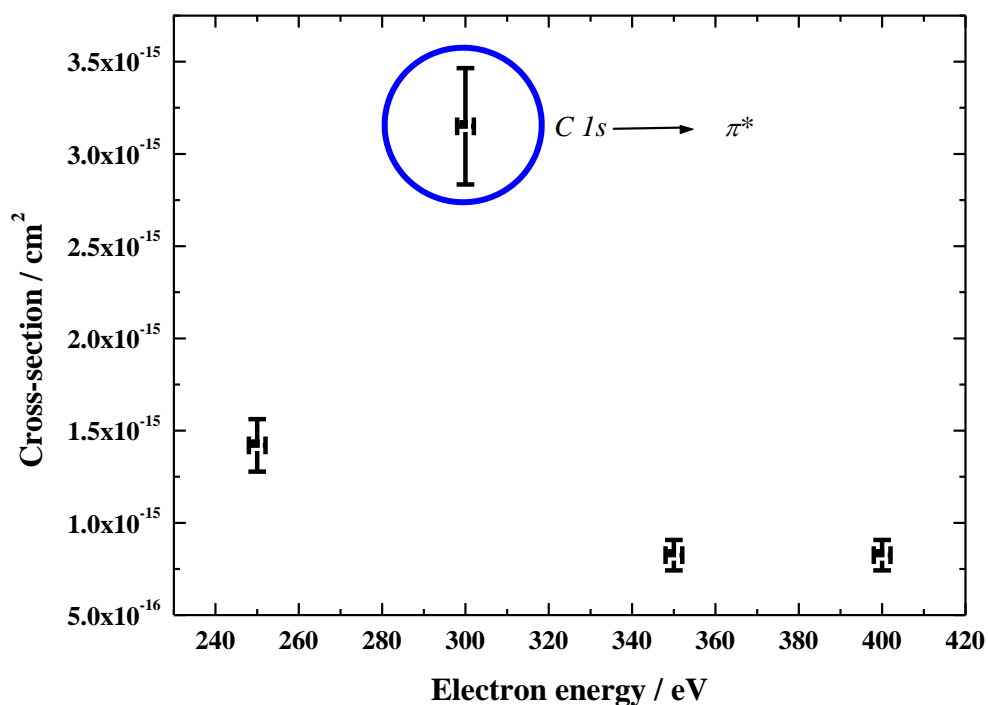


Figure 5.9: Total cross-sections for the $C\equiv N$ loss as a function of the electron energy. The circled point is discussed in detail in the text.

Table 5.1: Total cross-section for CH₃CN electron-promoted desorption for a 200 L (28 nm) film of solid CH₃CN as a function of the incident electron energy. The origin of error estimates is given in the text.

Electron energy / eV	Electron flux / electron cm ⁻² s ⁻¹	Electron-cross section / cm ²
250	1.2(±0.1)×10 ¹²	1.4(±0.1)×10 ⁻¹⁵
300	1.1(±0.1)×10 ¹²	3.2(±0.1)×10 ⁻¹⁵
350	1.6(±0.1)×10 ¹²	0.8(±0.2)×10 ⁻¹⁵
400	1.4(±0.1)×10 ¹²	0.8(±0.2)×10 ⁻¹⁵

5.4.1.3 Interactions of Solid CH₃CN with Low Energy Electrons

For the energies used, an inelastic mean free path, λ , for the low energy electrons in solid H₂O and CH₃CN has been estimated from the following equation [60]:

$$\lambda(nm) = \frac{538a}{E^2} + 0.41a^{2/3}E^{1/2} \quad (5.3)$$

where E is the energy in eV and a is the mean atomic diameter of the scattering material, given by **equation (5.4)**:

$$a = \left(\frac{M}{1000\rho N_A} \right) \quad (5.4)$$

where M is the molar mass, ρ is the density of the scattering material (0.78 g cm⁻³ and 0.87 g cm⁻³ for solid CH₃CN and H₂O respectively) and N_A is Avogadro's number. Calculated a values were used in **equation (5.3)** to calculate the inelastic mean free path λ of electrons in solid CH₃CN and H₂O.

Figure 5.10 shows the values of the inelastic mean free paths of the electrons in solid CH₃CN and H₂O as a function of the electron energy. In the 200 - 400 eV energy range, the inelastic mean free path lies between 1.2 – 2.4 nm in solid CH₃CN, and 1.0 – 1.5 nm in H₂O ice. These mean free paths are used to quantify the penetration

depth of electron irradiation with CH₃CN and H₂O ices up to 200 L thick with **equation (5.5)**:

$$\frac{S}{S_0} = \exp\left(\frac{d}{\lambda(E) \cos \theta}\right) \quad (5.5)$$

where S/S_0 is the ratio of the intensity of the electron beam to its initial value, d is the thickness of the film in nm, estimated from the exposure in L, and θ is the incidence angle of the electron beam to the surface normal (45° in this work). **Figure 5.11** shows the penetration of electrons in CH₃CN and H₂O solid films as a function of the film thickness. The penetration of energetic particles in ice depends on the type of particles used to perform the irradiation, the surface temperature, and the composition of the ice. For instance, UV photons penetrate the ice deeply, resulting in decomposition, formation of new species, surface changes (*e.g.* amorphisation of crystalline ices), and / or desorption [61-64]. Protons at keV energies can do likewise but low energy electrons cannot. However, the impact of UV photons on ices is less than that of ions (*e.g.* protons).

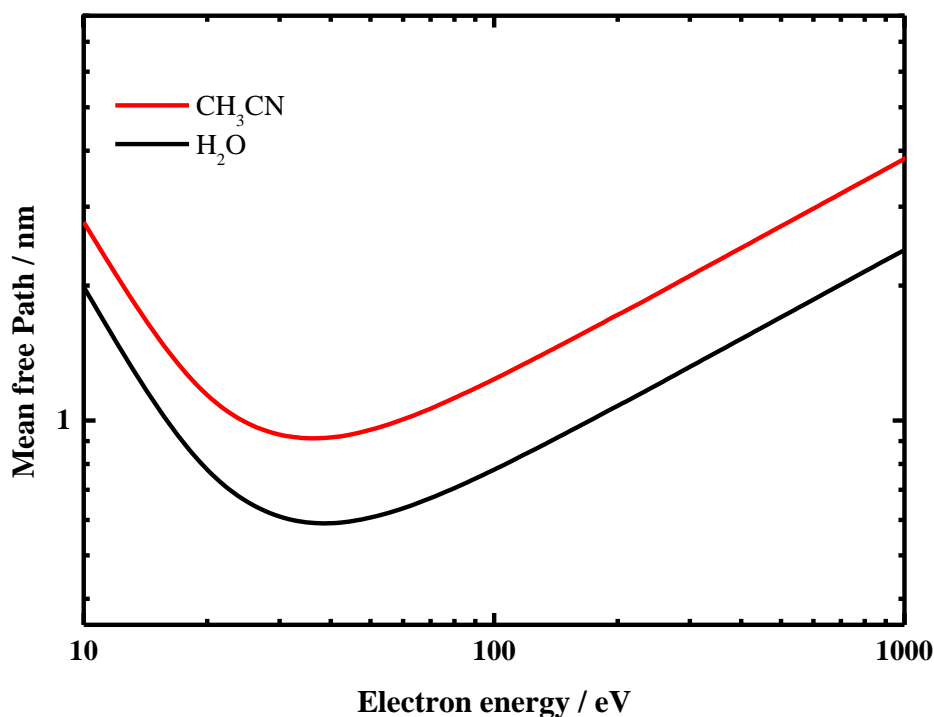


Figure 5.10: Calculated mean free paths for electrons in CH₃CN and H₂O films.

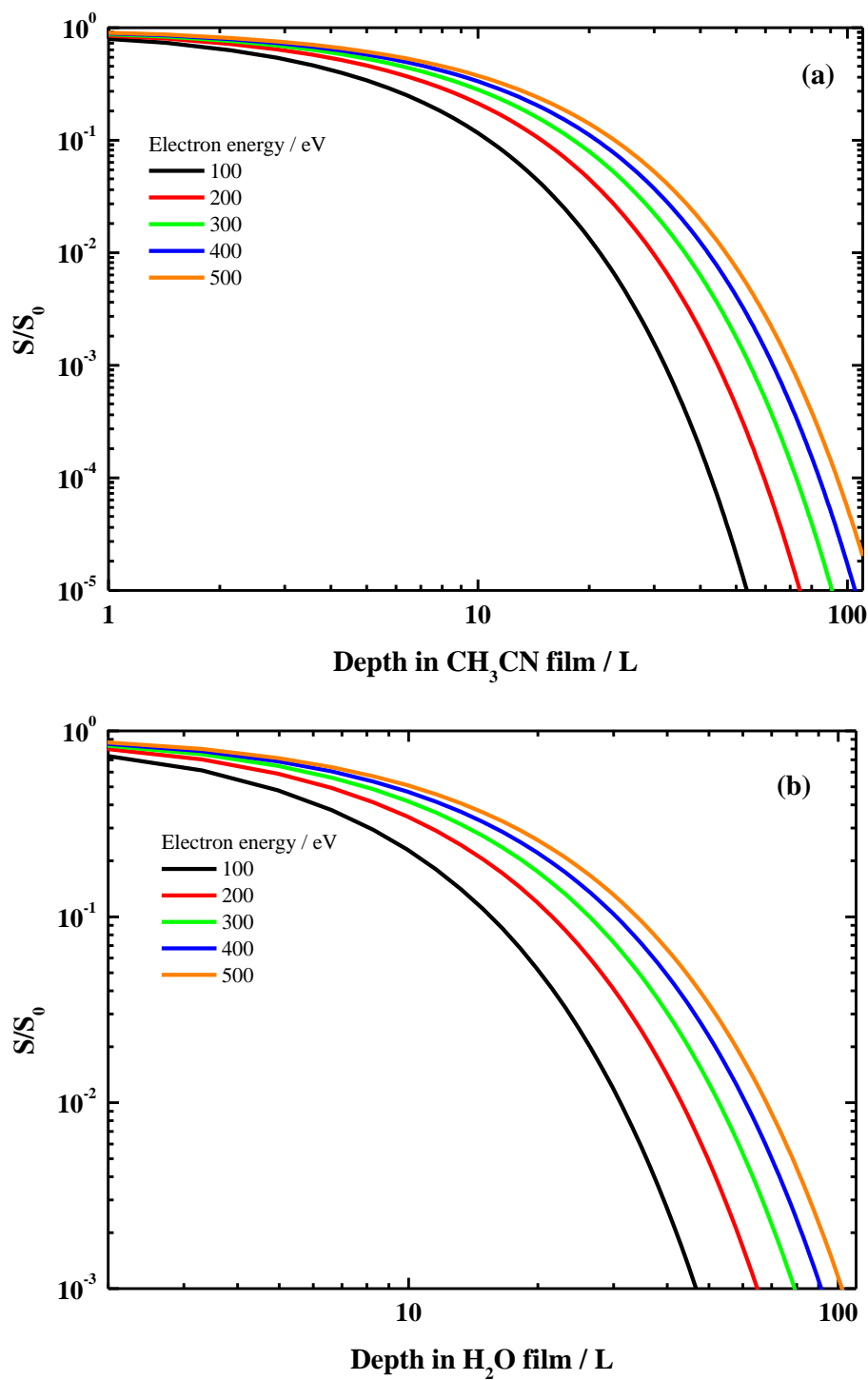


Figure 5.11: Calculated electron penetration through (a) 200 L CH_3CN films and (b) 200 L H_2O films, for the electron energies 100, 200, 300, 400, and 500 eV. The penetration depths are reported in dose equivalent units to aid comparison with the previously presented data.

Ruiterkamp and co-workers compared the effect of UV photon and ion irradiation on C₆H₆. They found that UV photons ($E_{photons}=7.41 \pm 0.23$ eV, $\varphi_{UV} = 10^{14}$ photons cm⁻² s⁻¹) induced the destruction of C₆H₆ and formed dehydrogenated benzene, methyl acetylene (C₃H₄) and acetylene (C₂H₂), but 300 times less efficiently than protons ($E_{H^+} = 0.8$ MeV, $\varphi_{H^+} = 4 \times 10^{12}$ protons cm⁻² s⁻¹) [65]. The penetration depth in the pure C₆H₆ film is lower for electrons than for ions or UV photons. From the penetration depth curves of the present work (see **Figure 5.11**), the electrons cannot completely penetrate the organic matter because there is a limit (*i.e.* the stopping power of electrons within the organic matter). This will be described in more detail in **Section 5.4.2**.

Few electrons are likely to penetrate the H₂O film corresponding to an H₂O exposure of 150 L. The consequence of the electron passage through the H₂O film is ionization and generation of secondary electrons. The secondary electron cascade has been calculated for a 500 eV Auger electron [66] in ice, where 25 secondary electrons were found to be released after about 100 fs. Thrower *et al.* in the investigations of the EPD of benzene (C₆H₆) adsorbed on a solid H₂O surface observed that there are fast and slow desorption channels [52]. These desorption channels are also tentatively thought to be present in the EPD of CH₃CN adsorbed on water ice.

Accordingly, upon bombardment with low energy electrons, an electronic excitation of the CH₃CN molecules can be suggested as a possible desorption mechanism of CH₃CN from the surface, as described in **equations (5.6) and (5.7)**:



The solid CH₃CN molecules are electronically excited to produce intermediate CH₃CN* species, which no longer hold strongly to the solid surface and desorb as gaseous molecules, carrying off some of the excess energy deposited by the electron.

Indeed, CH_3CN molecules tend, in this work, to desorb from two different surface structures (see **Figure 5.12**): from the CH_3CN islands adsorbed on the ASW surface (**Figure 5.12a**) and from bulk CH_3CN films (**Figure 5.12b** and **Figure 5.12c**). H_2O molecules may also desorb from the ASW free surface located between the CH_3CN islands. Such surface behaviour was observed for C_6H_6 adsorbed on an ASW surface [53]. In the second structure, CH_3CN molecules desorb from the thick layer of CH_3CN adsorbed on the ASW surface (see **Figure 5.12b**). This structure assumes that CH_3CN covers the whole ASW surface, which means that the H_2O molecules cannot desorb during irradiation. The interactions of electrons with low energy with CH_3CN adsorbed on a bare silica surface are presented in **Figure 5.12c**. Irradiation of structures in **Figure 5.12b** and **Figure 5.12c** is similar.

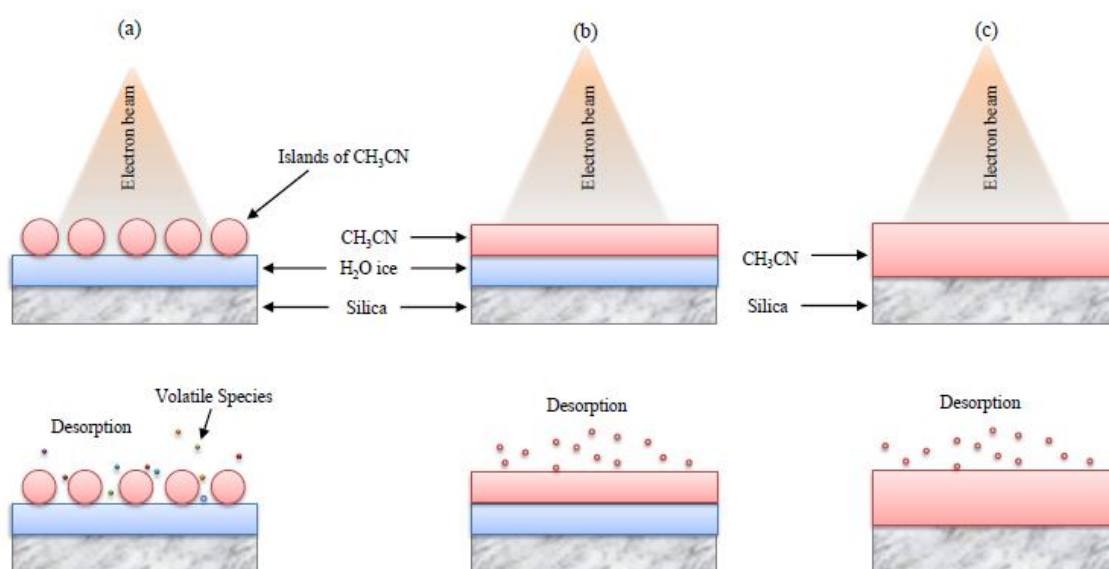


Figure 5.12: Cartoon showing the interaction of electrons with low energy on solid CH_3CN adsorbed on H_2O and on silica: (a) islands of CH_3CN on the ASW surface, (b) a thick layer of CH_3CN adsorbed on an ASW surface, and (c) electron irradiation of CH_3CN adsorbed on bare silica.

5.4.2 Proton Processing of CH₃CN

Prof. M. E. Palumbo and Dr. F. Islam from Osservatorio Astrofisico di Catania are acknowledged for providing the data in this part of this work. In these experiments (see **Section 5.3.2**), Palumbo and co-workers irradiated a thick film of solid CH₃CN (approximately 260 nm), capped with a 100 nm film of Argon (Ar) with 200 keV protons at 15 K [20]. IR spectroscopy revealed new IR features belonging to new products; CH₃NC, HCN, HCCCN, and H₂CCNH were observed (see **Figure 5.13**). This demonstrates that interactions involving fragmentation, rearrangement and conjugation took place in the irradiated film. **Table 5.2** shows the IR assignments and the column densities of the new products, obtained from the band strength values (see also **Figure 5.14**).

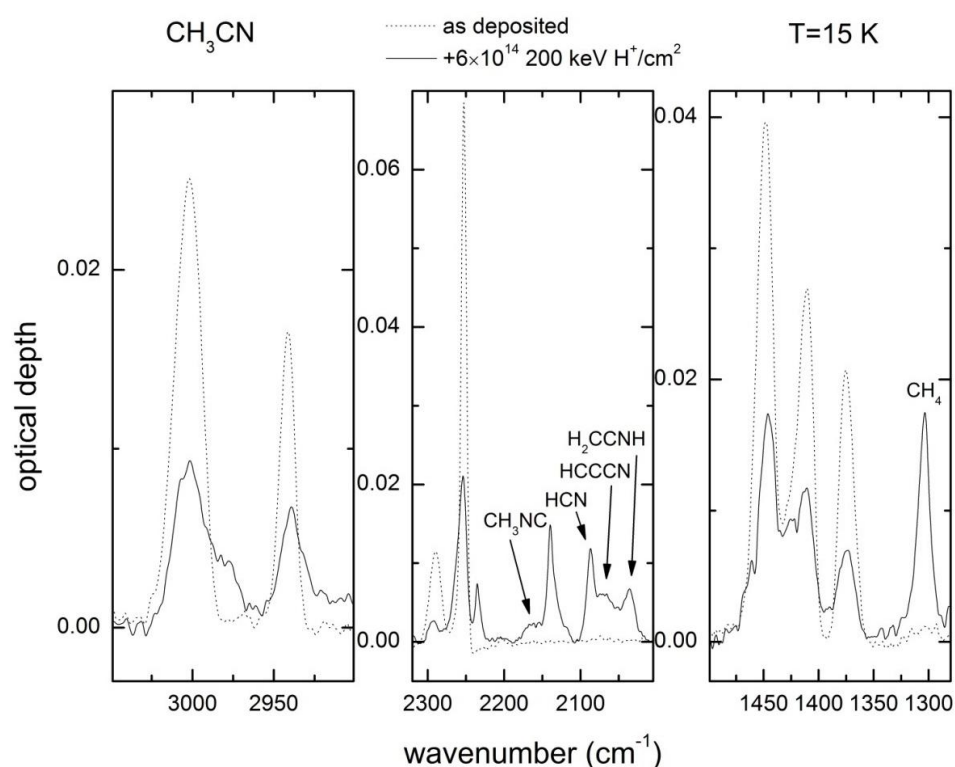


Figure 5.13: Transmission IR spectra (P polarization) of 260 nm film of CH₃CN adsorbed on crystalline silicon at 15 K. The IR spectra were taken before and after irradiation with 6×10^{14} 200 keV H⁺ cm⁻² [19].

Table 5.2: IR assignments and column densities of the newly-formed molecules from ion processing on CH₃CN [19].

Molecule	Peak position / cm ⁻¹	Column density / cm molecule ⁻¹	Reference
CH ₃ CN	2252	2.2×10^{-18}	[31]
CH ₃ NC	2168	2.2×10^{-18}	[31]
HCN	2087	5.1×10^{-18}	[31]
H ₂ C=C=NH	2035	7.2×10^{-17}	[31]
HCCCN ^(a)	2066	1.0×10^{-17}	

^(a) The band strength has not been measured. The value is estimated based on the average value of other similar species.

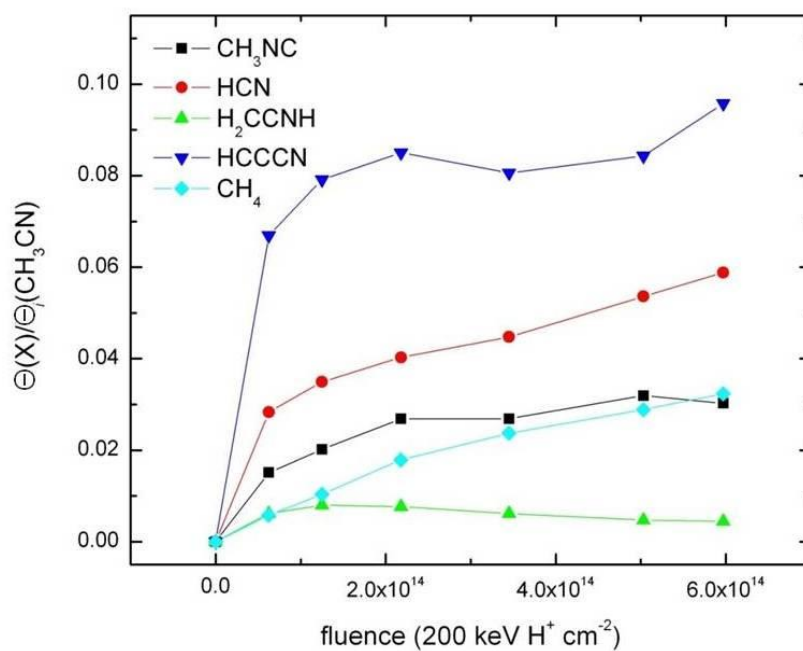


Figure 5.14: The product column densities $\Theta(X)$ as a function of the fluence of the protons (200 keV H⁺ cm⁻²). The column density $\Theta(X)$ is divided by the initial column density of CH₃CN [19].

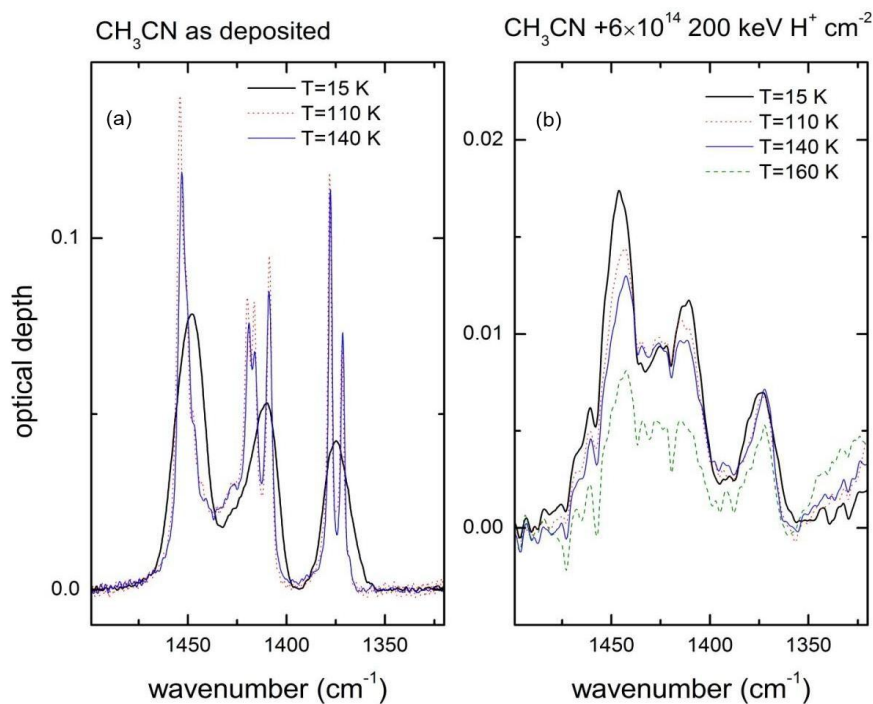


Figure 5.15: Transmission IR spectra of CH₃CN deposited at 15 K: (a) CH₃CN warmed up to 110 K and 140 K, (b) CH₃CN after deposition at 15 K followed by irradiation with 200 keV protons and subsequent heating to 110 K, 140 K and 160 K. The irradiated ices have not sublimated by 160 K [19].

The effect of warming up the CH₃CN after irradiation with protons was investigated as well. The ices were warmed up to 110 K and to 140 K (see **Figure 5.15**). There are no significant differences in the transmission IR bands at 110 K and 140 K, indicating that no change in the ice structure occurs after heating. Furthermore, pure CH₃CN sublimates after heating to 150 K. However, CH₃CN is still present at 160 K after irradiation (see **Figure 5.16**). This is due to the presence of a refractory organic residue [11, 22] that plays a trapping role and hinders escape of volatile molecules from the solid surface. The structure of the residual refractory material remains unknown.

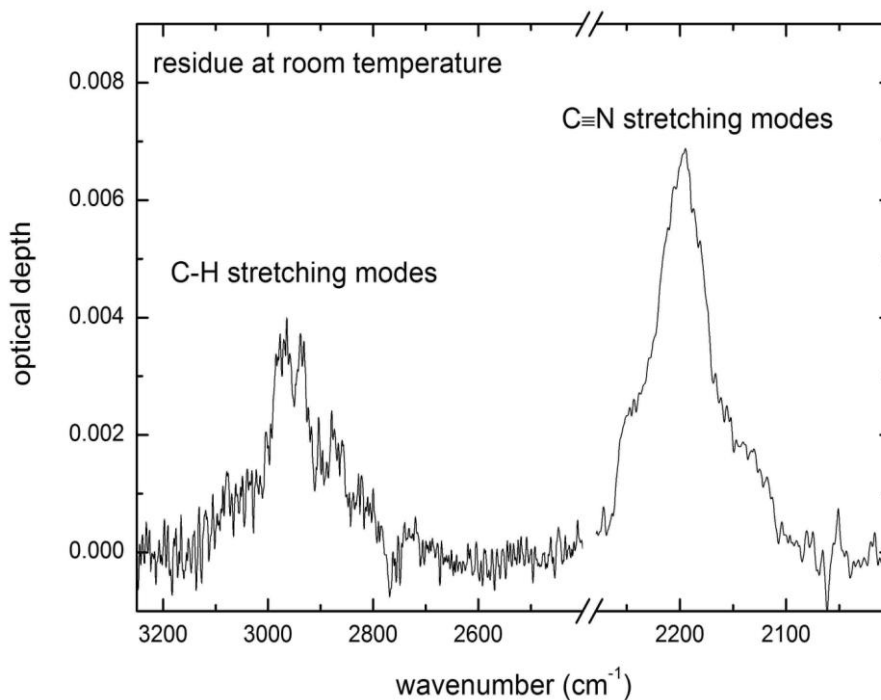


Figure 5.16: Transmission IR spectrum of the refractory residue at room temperature on the substrate, after ion irradiation of CH_3CN at 15 K. The spectrum has been taken the day after the bombardment experiment, after the sample has been left at room temperature under vacuum overnight [19].

When charged particles such as protons or electrons pass through solids, they lose part of their energy. A combination of nuclear and electron scattering mechanisms (*Stopping* in the language of nuclear material science) is responsible for the energy loss of protons in solids. The loss of energy can be represented by the total rate constant for this loss, k_{loss} . Thus, the total rate constant for the loss of CH_3CN can be written in terms of a nuclear loss term, k_{nuc} , and an electronic loss term, k_{elec} , given the parallel nature of these processes:

$$k_{loss} = k_{nuc} + k_{elec} \quad (5.8)$$

where k_{nuc} and k_{elec} reflect the nature of the processes promoted by the nuclear and electron stopping channels respectively. The SRIM code [32] has been used to estimate the stopping power for both channels. From the SRIM code, the stopping

power, which is expressed for convenience in eV/Å units, is defined by the following form:

$$S = \frac{dE}{dx} \quad (5.9)$$

where nuclear, S_N , and electron, S_e , stopping powers are distinguished, and E represents the energy of a particle moving in the x direction in a medium. The stopping powers in this work are 4.29 eV/Å and 5.95×10^{-3} eV/Å for electron and nuclear stopping channels, respectively. Since the nuclear stopping is small, this work will focus only on the issue of the processes associated with electron stopping.

Electrons in the energy range typical of secondary electrons promoted by proton irradiation tend to interact strongly with solids, so that the electrons lose energy to the surrounding solid. The amount of energy initially carried by the electron affects the energy loss to an enormous extent. For organic solids, secondary electrons are scattered inelastically during collisions inside the solid. Typically, the stopping power of such organic materials is 3 to 4 eV/Å for 200 - 500 eV electrons [67]. With a typical molecular scale of *ca.* 2 to 3 Å, this corresponds to excitation energies of *ca.* 6 to 12 eV, implying sufficient energy to excite many molecules from their ground electronic state to an excited state [68]. Such excitation might promote simple physical (*e.g.* desorption) or complex chemical (*e.g.* dissociation, isomerisation... *etc.*) processes. The electron-promoted CH₃CN loss rate, k_{elec} , is thus given by **equation (5.10)**:

$$k_{elec} = k_{ephys} + k_{echem} \quad (5.10)$$

where k_{echem} and k_{ephys} represent the loss rates of CH₃CN *via* chemical and physical electron-promoted processes, respectively.

The cross-section for CH₃CN loss in the proton irradiation experiments on CH₃CN was calculated from exponential function fitting to the integrated optical depths of the CH₃CN C≡N stretch at 2252 cm⁻¹ as a function of proton fluence. This gives a

cross section for the loss of CH₃CN, σ_{loss} , of $1.47(\pm 0.03) \times 10^{-15}$ cm² (see **Figure 5.17**). The impact of proton irradiation has also been studied on a CH₃CN sample deposited at 77 K. In this case the CH₃CN was not capped with argon. The experimental results plotted in **Figure 5.17** show that, within error limits, the decrease of the intensity of the C≡N stretch band depends neither on the temperature of the sample nor on the presence of the argon cap. The presence of the argon (Ar) cap should limit the proton-promoted desorption of CH₃CN. Since the cross-section for CH₃CN loss does not increase in the absence of the Ar cap, the proton-promoted desorption of CH₃CN must have a negligible influence on the loss of CH₃CN, which means here,

$$k_{elec} = k_{e^{-}chem} \quad (5.11)$$

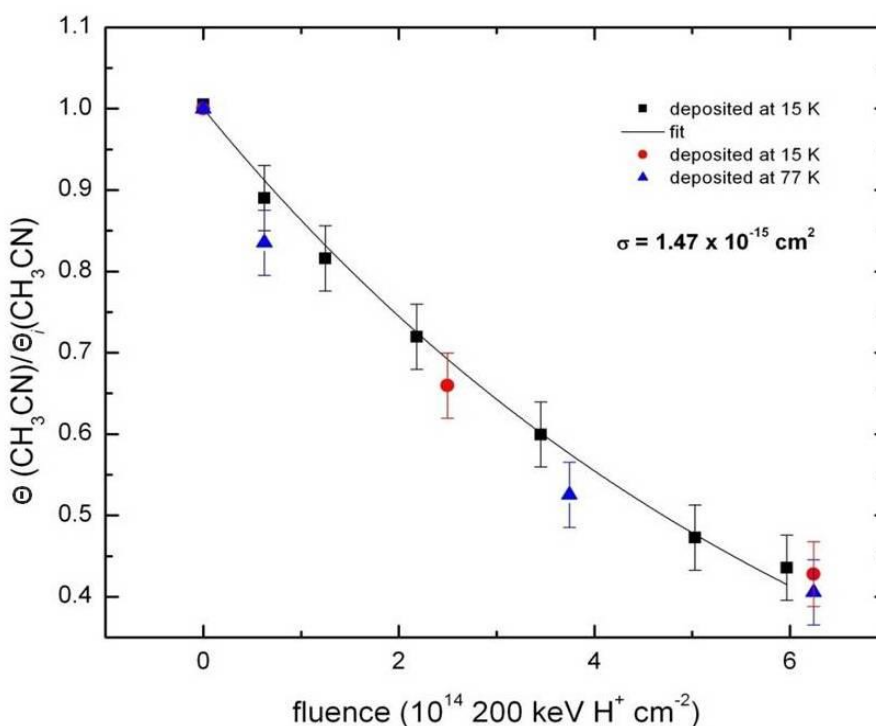


Figure 5.17: Fitted exponential curve of the destruction of CH₃CN as a function of the ion fluence (10^{14} 200 keV H^+ cm^{-2}) in an Ar-sandwiched CH₃CN film at 15 K (red dots) and in CH₃CN without the Ar-sandwich at 77 K (blue triangles), The exponential fit to obtain destruction cross section for CH₃CN deposited at 15 K (black squares) [19].

Therefore, the measured cross-section for CH₃CN loss is actually the cross-section for proton-promoted chemistry, σ_{H^+chem} .

In terms of the proton cross-section, the rate constant k_{e^-chem} can be expressed as:

$$k_{e^-chem} = \sigma_{H^+chem} \varphi_{H^+} \quad (5.12)$$

where φ_{H^+} is the proton flux of $1 \times 10^{12} \text{ cm}^{-2} \text{ s}^{-1}$. The k_{e^-chem} takes a value of $1.47(\pm 0.03) \times 10^{-3} \text{ s}^{-1}$ in the present experiments. The error value of this measurement provides an upper limit on the rate constant for electron-promoted physical processes (*i.e.* $k_{e^-phys} < 3 \times 10^{-5} \text{ s}^{-1}$).

The rate constant, k_{e^-chem} , can also be expressed in terms of a secondary electron cross section, $\sigma_{e_s^-chem}$, and a secondary electron flux, $\varphi_{e_s^-}$, both of which are energy dependent:

$$k_{e^-chem} = \int \sigma_{e_s^-chem} \varphi_{e_s^-} dE \quad (5.13)$$

In proton scattering experiments, the energies of the protons employed excite both valence and core electrons, releasing them from their molecular orbitals and producing an internal flux of secondary electrons within the solid. Using the SRIM code, the yield of secondary electrons (φ_{e^-}) can be calculated from **equation (5.14)**:

$$\varphi_{e^-} = \frac{S}{W} \quad (5.14)$$

where S is the stopping power of ions in $\text{eV } \mu\text{m}^{-1}$, and W is the typical energy deposited per ionization event. This value is usually around 2 - 3 times the ionization potential (IP) of the molecule being ionized [69]. For CH₃CN, the IP is 12.2 eV [70] and then W is 24.2 eV. For a 200 keV proton, the yield of secondary electrons (φ_{e^-}) is calculated to be in the range of $1.17 \times 10^3 - 1.76 \times 10^3 \mu\text{m}^{-1}$. The ionisation

process results in a broad distribution of secondary electron energies, from a few eV to several hundreds of eV with a maximum around 100 to 300 eV [71, 72]. For a proton flux, φ_{H^+} , of $1 \times 10^{12} \text{ cm}^{-2} \text{ s}^{-1}$, the resulting effective secondary electron flux generated throughout the 260 nm thick film and integrated over this broad distribution, $\varphi_{e_s^-}$, is $3.8(\pm 0.8) \times 10^{14} \text{ cm}^{-2} \text{ s}^{-1}$. Thus, the value of $\sigma_{e_s^-, chem}$ integrated over this energy range is $4(\pm 1) \times 10^{-18} \text{ cm}^2$.

5.4.3 *Impact of Electron and Proton Irradiation on Solid CH₃CN*

The advantage of using SRIM calculations in this work is the ability to demonstrate that the impact of proton irradiation on the CH₃CN ice is predominantly realised by the interaction of the secondary electrons produced by the proton interactions with the solid. Therefore, the proton irradiation and electron irradiation experiments should induce the same phenomenon. However, during electron irradiation of CH₃CN, only desorption is observed, whereas during proton irradiation, only chemical reaction is evident. It is therefore necessary to explain the apparently contradictory results of the two experiments.

Irradiated molecules in the first surface layer of a film, and possibly the next one or two layers below, can be desorbed. However, excited molecules deeper within the film are prevented from escaping by the layers above them. There are several mechanisms by which excitation events deeper within the film could contribute to EPD. In radiation science, the concept of the exciton is used to describe a mobile concentration of energy in a solid crystal formed by an excited electron and an associated hole. In this work, excitons, generated by low energy electron stimulation, have been shown to diffuse through considerable thicknesses of amorphous water ice [73, 50]. Although excitons will be generated within CH₃CN ice, a greatly reduced diffusivity in this medium is expected. Another energy transfer mechanism in solids has been described by Arnolds and co-workers [74]. They reported that excitation of interfacial C₆H₆ on a Pt(111) surface by hot electrons generated by 800 nm fs laser excitation promoted a ‘‘Newton’s Cradle’’-style transfer of energy and desorption [74]. With more energy to remove from the system and smaller masses, a much less ordered behaviour would result in the CH₃CN islands, especially if too thick to allow desorption [54].

The concept of “selvedge” will be introduced to aid discussing electron and proton irradiation processing in more detail. The selvedge is the near surface region of the film which is of relevance to a surface specific phenomenon such as desorption [21]. The depth of the selvedge can be measured with respect to several factors. If the efficiency of the energy transfer mechanisms discussed above is low, the selvedge may be restricted to the first few molecular layers, and therefore will be of the order of a few Å. If the energy transfer mechanisms have intermediate efficiency, they themselves can be used to determine the depth of the selvedge. If they have high efficiency, then the penetration depth of the incident electron and/or proton will determine the depth of the selvedge. The penetration depth of 200 keV protons is much greater than the thickness of the CH₃CN film, and in fact our calculations assume a flux of secondary electrons that does not vary with depth. With respect to the inelastic mean free path of electrons (0 – 500 eV) in the solid CH₃CN (1.2 – 2.4 nm), the electrons can give up 6 to 12 eV of energy per interaction, then, in the electron irradiation experiments, an incident electron could potentially penetrate the full depth of the 28 nm film investigated. However, since the path of inelastically scattered electrons is random, the bulk of the energy of the incident electron beam is expected to be deposited within the top 5 nm of the film [21].

For CH₃CN ice with a film thickness of 28 nm, observing the EPD with first order kinetics is unexpected. The results of these experiments imply that the entire film is part of the selvedge. This is possibly due to the morphology of the silica substrate, which has been found in previous studies to have roughness in the order of 40 nm [52, 53]. The TPD results show that all of the exposures subjected to electron irradiation (5 – 200 L) fall within the multilayer desorption regime. However, TPD investigates the structure of the film at the temperature of desorption (~135 K). There is some capacity for the film roughness at deposition (110 K) to be annealed during the temperature ramp prior to desorption. Since the penetration depth of 200 keV protons is high (greater than the sample thickness), the proton-promoted chemistry of CH₃CN is a bulk process. Therefore, there is no selvedge for chemistry, and the rate of CH₃CN loss by chemical transformation follows first order kinetics. As a consequence of the absence of any desorption in the proton irradiation experiment, the selvedge for proton-promoted desorption must be small compared to the thickness of the film. The upper limit for the rate constant for proton-promoted

desorption, $k_{e\text{phys}}$, can be used to calculate an upper limit for the depth of the selvedge. The rate of proton-promoted desorption, r_{H^+des} , can be expressed in terms of either the EPD or proton-promoted desorption cross sections:

$$r_{H^+des} = \sigma_{e^-des} \varphi_{e^-,selv} \Theta_{selv} = k_{e\text{phys}} \Theta_s \quad (5.15)$$

where both the secondary electron flux within the selvedge, $\varphi_{e^-,selv}$, and the surface concentration of CH₃CN within the selvedge, Θ_{selv} , depend on the selvedge depth, d_{selv} :

$$\varphi_{e^-,selv} = \varphi_{H^+} \eta d_{selv} \quad (5.16)$$

$$N_{selv} = \rho_M d_{selv} \quad (5.17)$$

where η is the yield of secondary electrons in μm^{-1} , and ρ_M is the molecular density of solid CH₃CN in molecules cm^{-3} . When the initial thickness of the ion irradiated film, d , is 260 nm, the concentration of CH₃CN is expressed as:

$$\Theta_s = \rho_M d \quad (5.18)$$

Solving the equations gives an upper limit on the selvedge depth of 1.7 nm. Further experiments are necessary to provide a more accurate constraint.

First order EPD was evident for the 200 L film (mean thickness of 28 nm) during electron irradiation. This further emphasises the impact on the desorption behaviour of the roughness of the silica substrate used in the electron irradiation experiments. The cross-section for chemical transformation of the CH₃CN film by secondary electrons, σ_{e^-chem} , of $4(\pm 1) \times 10^{-18} \text{ cm}^2$ measured during proton irradiation is lower than the upper limit of $3.5 \times 10^{-17} \text{ cm}^2$ estimated during electron irradiation. This suggests that the rate of formation of products is expected to be below the limit of detection during the electron irradiation experiment. In similar investigations of water/methane mixtures [75], products were not observed by infrared spectroscopy

when the deposited mixed film was irradiated, due to the rapid EPD of methane, although when the film was irradiated during deposition, reaction products such as methanol were trapped and could be detected.

5.5 Conclusions and Astrophysical Implications

The interactions of electrons (250 – 400 eV) and protons (200 keV H⁺) on CH₃CN ices in an astrophysical regime have been investigated. **Figure 5.18** summarises the results and the implications of these investigations in the interstellar medium (ISM). For electron irradiation experiments, the interaction with electrons was performed within two different environments, on H₂O ice and on silica. Interactions of electrons with low energy on CH₃CN condensed on H₂O ice showed no evidence for reaction products (they may be volatile species) at 110 K (see **Figure 5.18b**). However, electrons promote significant desorption of CH₃CN ices. During desorption of solid CH₃CN from the H₂O surface, there was evidence for amorphisation of crystalline CH₃CN in a broadening of the C≡N stretching band in the IR around 2248 cm⁻¹ region. EPD data also tentatively imply the presence of two components of desorption, known as slow and fast desorption channels, *cf.* C₆H₆ [52, 53]. This suggests there may be a universal mechanism for desorption of species bonded to H₂O *via* hydrogen bonding.

In the silica environment, electrons also promote desorption of CH₃CN, under the same experimental conditions. The cross section for desorption of CH₃CN during electron irradiation of thin films, $\sigma_{e^- des}$, was estimated to lie in the range 0.82 - 3.2×10⁻¹⁵ cm². No reaction products were detected, which is likely to be due to their volatility at the working temperature.

The chemical destruction of CH₃CN films under irradiation with 200 keV protons occurs with a cross section, $\sigma_{H^+ chem}$, of 1.47(±0.03)×10⁻¹⁵ cm², forming species such as CH₃NC, HCN, H₂CCNH, HCCCN and CH₄ (see **Figure 5.18a**). Proton-promoted desorption of CH₃CN was not detected. Warming up the proton-irradiated film produces an organic residue, which can trap CH₃CN beyond its normal sublimation temperature, and is stable at room temperature. The residue remains unidentified. SRIM calculations show that the effects of proton irradiation are predominantly

realised by electron stopping and the consequent generation of secondary electrons. By estimating the secondary electron yield, a calculation of the cross-section for secondary electron-promoted chemistry, $\sigma_{e^-, chem}$, gives a value of $4(\pm 1) \times 10^{-18} \text{ cm}^2$.

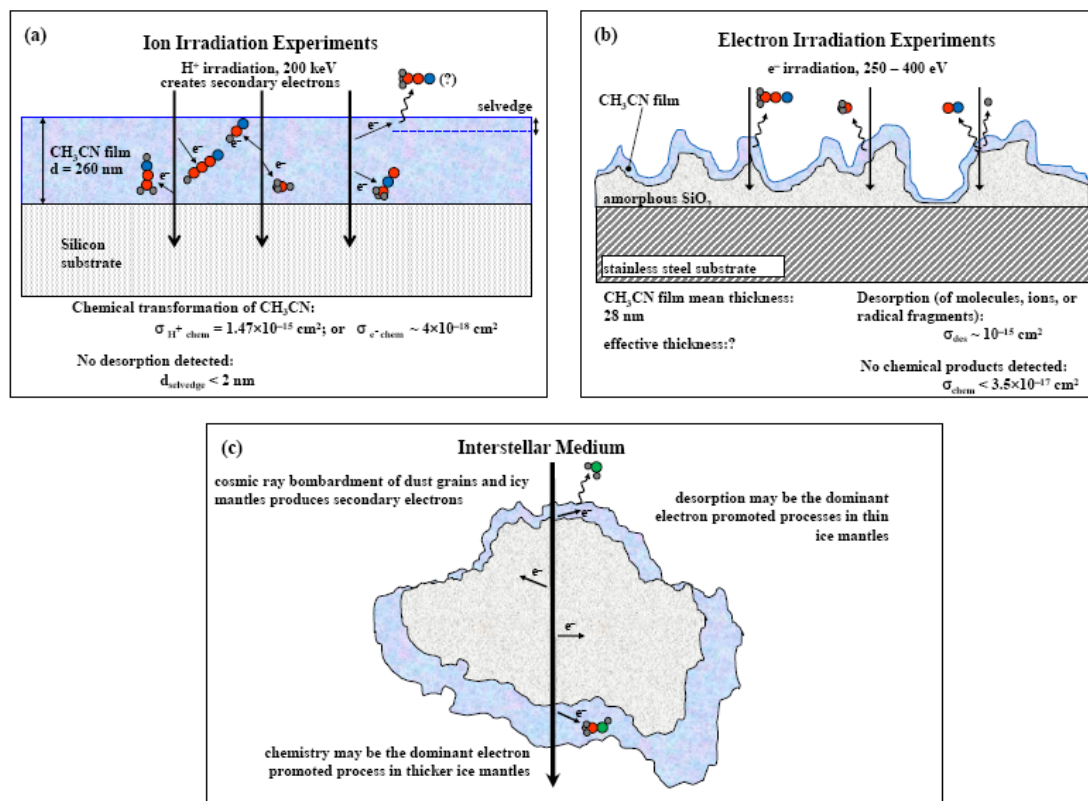


Figure 5.18: Cartoon illustrating the results of (a) proton, (b) electron irradiation processes, and (c) the implications of these processes in the interstellar medium [19].

The cross-section for desorption of CH₃CN during electron irradiation of thin films, $\sigma_{e^-, des}$, was determined to fall in the range $0.82 - 3.2 \times 10^{-15} \text{ cm}^2$. No reaction products were detected, which is likely to be due to their rapid desorption under the electron irradiation. Secondary electron-promoted chemical reaction of CH₃CN is found to be a bulk process, occurring throughout the full depth of the film, whereas electron-promoted desorption is a surface process, restricted to the selvedge. This finding explains the difference between the observations of the proton and electron irradiation experiments and has important consequences for understanding of the balance of the two processes in interstellar environments.

In terms of astrophysics, if these processes are considered to take place in the ISM, the processes would have two implications: (i) in the regions where thick ices are dominant (*i.e.* the centre of dense clouds) and at temperatures as low as 10 K, electron-promoted chemistry will dominate processes on grain surfaces, and a complex solid phase chemistry within ices, involving reactions between the products of grain processing, will proceed, and (ii) in the regions where the ices remain thin, EPD is the dominant process occurring on grain surfaces and the composition of the ice may more strongly reveal re-adsorption of the products of gas phase chemistry. **Figure 5.18c** shows how cosmic rays can ionise the icy mantles where secondary electrons were produced. These electrons do not travel away but drive other process within the ices (mainly desorption).

5.6 References

- [1] P. Ehrenfreund and M. A. Sephton, *Faraday Discuss.*, 2006, **133**, 277.
- [2] C. D. Neish, A. Somogyi, and M. A. Smith, *Astrobiology*, 2010, **10**, 337.
- [3] J. Cui, R.V. Yelle, and V. Vuitton, J. H. Waite Jr., W. T. Kasprzak, D. A. Gell, H. B. Niemann, I. C. F. Müller-Wodarg, N. Borggren, G. G. Fletcher, E. L. Patrick, E. Raaen, and B. A. Magee, *Icarus*, 2009, **200**, 581.
- [4] V. Vuitton, R. V. Yelle, and P. Lavvas, *Phil. Trans. R. Soc. A*, 2009, **367**, 729.
- [5] A. J. T. de Laat, J. A. de Gouw, J. Lelieveld, and A. Hansel, *J. Geophys. Res.*, 2001, **106**, 28469.
- [6] M. Suto and L.C. Lee, *J. Geophys. Res.*, 1985, **90**, 13037.
- [7] F. Edard and M. Tronc, *J. Phys. B.*, 1987, **20**, L265.
- [8] Ph. Parent, C. Laffon, and F. Bournel, *J. Chem. Phys.*, 2000, **112**, 986.
- [9] D. Ascenzi, P. Tosi, P. Franceschi, D. Catone, S. Turchini, and K. C. Prince, *Chem. Phys.*, 2012, **398**, 269.
- [10] R. L. Hudson and M. H. Moore, *Icarus*, 2004, **172**, 466.
- [11] R. L. Hudson, M. H. Moore, J. P. Dworkin, M. P. Martin, and Z. D. Pozun, *Astrobiology*, 2008, **8**, 771.
- [12] W. Sailer, A. Pelc, P. Limão-Vieira, N.J. Mason, J. Limtrakul, P. Scheier, M. Probst, and T.D. Märk, *Chem. Phys. Lett.*, 2003, **381**, 216.
- [13] I. Ipolyi, W. Michaelisw and P. Swiderek, *Phys. Chem. Chem. Phys.*, 2007, **9**, 180.
- [14] A. D. Bass, J. H. Bredehöft, E. Böhler, L. Sanche, and P. Swiderek, *Eur. Phys. J. D.*, 2012, **66**, 53.
- [15] J. E. Schaff, and J. T. Roberts, *Langmuir*, 1999, **15**, 7232.
- [16] C. Mair, Z. Herman, J. Fedor, H. Lezius, Z. Herman, and T.D. Märk, *J. Chem. Phys.*, 2003, **118**, 1479.

- [17] S. Bahr and V. Kempter, *J. Chem. Phys.*, 2009, **130**, 214509.
- [18] Hyperchem Release 8.0.2, Molecular Modelling System, © 2007, Hypercube Inc.
- [19] A. G. M. Abdulgalil, D. Marchione, J. D. Thrower, M. P. Collings, and M. R. S. McCoustra, F. Islam, M. E. Palumbo, E. Congiu, and F. Dulieu, *Phil. Trans. R. Soc. A*, 2013, **371**, 20110586.
- [20] G. Strazzulla, G. A. Baratta, and M. E. Palumbo, *Spectrochim. Acta A*, 2001, **57**, 825.
- [21] G. A. Baratta, G. Leto, and M. E. Palumbo, *Astron. Astrophys.*, 2002, **384**, 343.
- [22] M. E. Palumbo, G. Ferini, and G. A. Baratta, *Adv. Space Res.*, 2004, **33**, 49.
- [23] P. A. Gerakines, W. A. Schutte, and P. Ehrenfreund, *Astron. Astrophys.*, 1996, **312**, 289.
- [24] M. J. Loeffler, G. A. Baratta, M. E. Palumbo, G. Strazzulla, and R. Baragiola, *Astron. Astrophys.*, 2005, **435**, 587.
- [25] D. Fulvio, B. Sivaraman, G. A. Baratta, M. E. Palumbo, and N. J. Mason, *Spectrochim. Acta. A*, 2009, **72**, 1007
- [26] G. A. Baratta and M. E. Palumbo, *J. Opt. Soc. Am. A*, 1998, **15**, 3076.
- [27] M. E. Palumbo, G. A. Baratta, M. P. Collings, and M. R. S. McCoustra, *Phys. Chem. Chem. Phys.*, 2006, **8**, 279.
- [28] D. M. Hudgins, S. A. Sandford, L. J. Allamandola, and A. G. G. M Tielens, *Astrophys. J. Supp. Ser.*, 1993, **86**, 713.
- [29] P. A. Gerakines, W. A. Schutte, J. M. Greenberg, and E. F. van Dishoeck, *Astron. Astrophys.*, 1995, **296**, 810.
- [30] P. Modica, and M. E. Palumbo, *Astron. Astrophys.*, 2010, **519**, A22.
- [31] K. I. Öberg, H. J. Fraser, A. C. A. Boogert, S. E. Bisschop, G. W. Fuchs, F. W. van Dishoeck, and H. Linnartz, *Astron. Astrophys.*, 2007, **462**, 1187.

- [32] J. F. Ziegler, J. P. Biersack, and M. D. Ziegler, *The Stopping and Range of Ions in Solids*, (Pergamon Press, New York, 2008), see also <http://www.srim.org/>.
- [33] I. Engquist, I. Lundström, B. Liedberg, A. N. Parikh, and D. L. Allara, *J. Chem. Phys.*, 1997, **106**, 3038.
- [34] A. B. Horn, M. A. Chesters, M. R. S. McCoustra, and J. R. Sodeau, *J. Chem. Soc. Faraday Trans.*, 1992, **88**, 1077.
- [35] B. Rowland, N. S. Kadagathur, J. P. Devlin, V. Buch, T. Feldman, and M. J. Wojcik, *J. Chem. Phys.*, 1995, **102**, 8328.
- [36] L. M. Sverdlov, M. A. Kovner, and E. P. Krainov, *Vibrational Spectra of Polyatomic Molecules*, (John Wiley & Sons, New York, 1974).
- [37] J. P. Camplin, J. C. Cook and E. M. McCash, *J. Chem. Soc. Faraday Trans.*, 1995, **91**, 3563.
- [38] S. Raunier, T. Chiavassa, A. Allouche, F. Marinelli, and J. Aycard, *Chem. Phys*, 2003, **288**, 197.
- [39] S. Raunier, T. Chiavassa, F. Marinelli, A. Allouche, and J. Aycard, *J. Phys Chem. A.*, 2003, **107**, 9335.
- [40] P. Theule, F. Duvernay, A. Ilmane, T. Hasegawa, O. Morata, S. Coussan, G. Danger, and T. Chiavassa, *Astron. Astrophys.*, 2011, **530**, A96.
- [41] I. Reva, L. Leszek, and R. Fausto, *J. Mol. Struct.*, 2010, **976**, 333.
- [42] J. N. Crowley and J. R. Sodeau, *J. Phys. Chem.*, 1989, **93**, 3100.
- [43] M. E. Jacox, and D. E. Milligan, *J. Chem. Phys.*, 1964, **40**, 2457.
- [44] J. B. Burkholder, A. Sinha, P. D. Hammer, and C. J. Howard, *J. Mol. Spectrosc.*, 1987, **126**, 72.
- [45] M. Nezu, T. Amano, and K. Kawaguchi, *J. Mol. Spectrosc.*, 1998, **192**, 41.
- [46] A. G. Maki and G. Ch. Mellau, *J. Mol. Spectrosc.*, 2001, **206**, 47.

- [47] P. Babineca and J. Leszczynskia, *J. Mol. Struct.(Theochem)*, 2000, **501-502**, 277.
- [48] K. Yamada, *J. Mol. Spectrosc.*, 1965, **79**, 438.
- [49] K. Jensen, M. Due, and A. Holm, *Acta Chem. Scand.*, 1965, **19**, 438.
- [50] N. G. Petrik and G. A. Kimmel, *J. Chem. Phys.*, 2005, **123**, 054702.
- [51] J. Bergeld and D. Chakarov, *J. Chem. Phys.*, 2006, **125**, 141103.
- [52] J. D. Thrower, *PhD Thesis*, (Heriot-Watt University, Edinburgh, 2009).
- [53] J. D. Thrower, M. P. Collings, F. J. M. Rutten, and M. R. S. McCoustra, *Chem. Phys. Lett.*, 2011, **505**, 106.
- [54] A. G. M. Abdulgalil, D. Marchione, A. Rosu-Finsen, M. P. Collings, and M. R. S. McCoustra, *J. Vac. Sci. Technol. A*, 2012, **30**, 041505-1.
- [55] G. Strazzulla, G. A. Baratta, G. Leto and G. Foti, *Europhys. Lett.*, 1992, **18**, 517.
- [56] M. Famá, M. J. Loeffler, U. Raut, and R. A. Baragiola, *Icarus*, 2010, **207**, 314.
- [57] A. P. Hitchcock, M. Tronc, and A. Modelli, *J. Phys. Chem.*, 1989, **93**, 3068.
- [58] Ph. Parent, and C. Laffon, *J. Chem. Phys.*, 2000, **112**, 986.
- [59] T. M. Orlando and M. T. Sieger, *Surf. Sci.*, 2003, **528**, 1.
- [60] G. Attard and C. Barnes, *Surfaces*, (Oxford University Press, Oxford, 2008).
- [61] J. M. Greenberg, *Adv. Space. Res.*, 1983, **3**, 19.
- [62] R. Briggs, G. Ertem, J. P. Ferris, J. M. Greenberg, P. J. McCain, C. X. Mendoza-Gomez, and W. Schutte, *Orig. Life. Evol. Biosph.*, 1992, **22**, 287.
- [63] H. Cottin, M.C. Gazeau, and F. Raulin, *Planet. Space. Sci.*, 1999, **47**, 1141.
- [64] G. Leto and G. A. Baratta, *Astron. Astrophys.*, 2003, **397**, 7.
- [65] R. Ruiterkamp, Z. Peeters, M. H. Moore, R. L. Hudson, and P. Ehrenfreund, *Astron. Astrophys.*, 2005, **440**, 391.

- [66] N. Timneanu, C. Caleman, J. Hajdu, and D. van der Spoel, *Chem. Phys.*, 2004, **299**, 277.
- [67] J. C. Ashley, *IEEE Trans. Nucl. Sci.*, 1980, **27**, 1453.
- [68] L. Amiaud, F. Dulieu, J. H. Fillion, A. Momeni, and J. L. Lemaire, *J. Chem. Phys.*, 2007, **127**, 144709.
- [69] W. F. Schmidt and E. Illenberger, *Nukleonika*, 2003, **48**, 75.
- [70] J. E. House, *Inorganic Chemistry*, (Academic Press, New York, 2008).
- [71] K. A. Long and H. G. Paretzke, *J. Chem. Phys.*, 1991, **95**, 1049.
- [72] M. E. Rudd, Y. K. Kim, D. H. Madison, and J. W. Gallagher, *Rev. Mod. Phys.*, 1985, **57**, 965.
- [73] N. G. Petrik and G. A. Kimmel, *Phys. Rev. Lett.*, 2003, **90**, 166102.
- [74] H. Arnolds, C. Rehbein, G. Roberts, R. J. Levis, and D. A. King, *J. Phys. Chem. B.*, 2000, **104**, 3375.
- [75] A. Wada, N. Mochizuki, and K. Hiraoka, *Astrophys. J.*, 2006, **644**, 300.

CHAPTER – 6 Conclusions

Contents

6.1	Introduction.....	202
6.2	Summary	202
6.2.1	<i>Chapter 3</i>	202
6.2.2	<i>Chapter 4</i>	203
6.2.3	<i>Chapter 5</i>	204
6.3	Future Outlook.....	205
6.4	References.....	207

6.1 Introduction

The work presented in this thesis has described thermal and non-thermal desorption experiments on H₂O, and CH₃CN ice samples. The experiments were performed at astrophysically relevant conditions. The experimental results were compared with the observations from simulations to explain the behaviour of certain molecules, such as water (H₂O) and acetonitrile (CH₃CN). This chapter highlights the key findings in this thesis and the suggested future work for further understanding of the astrochemistry of nitriles and perhaps polycyclic aromatic hydrocarbons (PAHs), which may have a link to the origin of amino acids.

6.2 Summary

The overall conclusions are summarised in the following key points from each chapter.

6.2.1 Chapter 3

The thermal desorption reported in this chapter has two important results; (1) the desorption of water from the model interstellar dust (*i.e.* amorphous silica) follows zero-order desorption kinetics for all surface exposures, with marked shifting to higher temperature as the surface exposure increases (350 L of H₂O ice desorbs at 180 K). Since the interaction between H₂O molecules themselves (*via* hydrogen bonding) is greater than that of H₂O molecules with the silica surface, they bind together to form H₂O clusters or islands. The analysis of TPD data concluded the values of E_{des} to be 42.1 ± 1 kJ mol⁻¹ and 49.3 ± 1 for c-ASW and CSW, respectively, which is consistent with those in the literature [1-4]. (2) The presence of the two peaks at 150 K is attributed to crystallisation of H₂O ices at surface exposures larger than 3.5 L. Indirect desorption of H₂O *via* a non-thermal route was investigated by using mass spectrometry and RAIRS. Low energy electrons were employed to promote desorption of H₂O ice. No evidence for any chemical product was found during electron irradiation of low surface coverages of H₂O. However, significant desorption of H₂O was observed. The large cross-section of H₂O desorption ($\sim 10^{-16}$

cm²) suggests that excitons form within the H₂O layer, which then migrate to the vacuum interface, resulting in H-bond cleavage and H₂O desorption.

In the final part of **Chapter 3**, a simple model of H₂O ice desorption was modified by including a re-adsorption step [5, 6]. This model was built in an effort to predict the concentration of H₂O in the molecular cloud Barnard 68 with different values of A_v (0, 2, 4, and 6) and conditions of low temperature (typically 10 K). At the centre of the cloud, in which $A_v=6$, most of the H₂O in this model adsorbs onto dust grain surfaces. The calculations showed that up to 8×10^{17} molecules cm⁻² are condensed onto the surfaces. Moreover, EPD has a crucial role in producing H₂O in gas at $A_v = 6$ (*i.e.* in the cloud core, where the temperature is typically 10 K or less). Furthermore, the high concentration of H₂O in the gas phase at the edge of the cloud was investigated by including the thermal processing in this model. This implies that under thermal conditions the re-adsorption step is an unimportant process.

6.2.2 Chapter 4

The surface structure of CH₃CN was investigated by studying TPD and RAIRS on bare silica and on H₂O/silica surfaces. Firstly, desorption of CH₃CN from the silica surface was observed to follow first order kinetics for sub-monolayer coverages and zero order kinetics for multilayer coverages. Analysis using leading edge analysis and CKS modelling showed the desorption energy to be 38.2 ± 1 kJ mol⁻¹ and the pre-exponential factor, $8 \times 10^{28 \pm 1}$ molecules cm⁻² s⁻¹. From the sub-monolayer analysis, it was concluded that CH₃CN molecules require more energy to be liberated from the surface (*ca.* $E_{des} > 40$ kJ mol⁻¹). This was explained as being due to the interactions between the sub-monolayer and the silica. However, the increase of the surface coverage to the multilayer level resulted in a decreased interaction ability of CH₃CN molecules with the surface (*i.e.* CH₃CN molecules interact with themselves). Therefore, less energy (*ca.* $E_{des} < 40$ kJ mol⁻¹) was required to release CH₃CN molecules from the surface.

The RAIR spectra of CH₃CN on a SiO₂ surface showed no evidence of new features and were consistent with the literature [7, 8]. For CH₃CN adsorbed onto a H₂O/ SiO₂ system, the RAIRS of low surface coverages of CH₃CN (~2.5 L) showed evidence of

the presence of hydrogen bonding. The hydrogen bond resulted in transfer of some of the electron density from the N atom to form $C\equiv N\cdots H-O$, leading to an increase of the $C\equiv N$ stretching frequency [8, 9]. Computational calculations confirmed the hydrogen bond between the N atom of the CH_3CN and the oxygen atom of H_2O .

The RAIR spectra of the annealed CH_3CN on both SiO_2 and H_2O/SiO_2 surfaces showed complete desorption of CH_3CN after 160 K. The results of an annealed mixture of $H_2O:CH_3CN$ (approximately 2:1) showed evidence of a H_2O crystalline phase, whereas CH_3CN desorbed.

6.2.3 Chapter 5

The interactions of electrons (250 - 400 eV) and protons (200 keV H^+) with CH_3CN ices under astrophysically relevant conditions were investigated [10]. RAIRS was used to probe the changes on the surface. Firstly, the interactions with electrons were carried out within two different environments, on H_2O ice and on silica. The results obtained from low energy electron irradiation of CH_3CN condensed on H_2O ice showed no evidence for new products. If it does produce these, then they must be volatile species at the experimental temperature of 110 K. However, electrons promote significant desorption of CH_3CN ices. During desorption of thin films of solid CH_3CN from the H_2O ice surface, there was evidence of amorphisation, in a broadening of the 2248 cm^{-1} region. In the silica environment, electrons also promote desorption of CH_3CN , under the same experimental conditions. The cross section for desorption of CH_3CN during electron irradiation of thin films, $\sigma_{e^- des}$, was measured and found to lie in the range $0.8 - 3.2 \times 10^{-15}\text{ cm}^2$.

Secondly, the results showed that the chemical destruction of CH_3CN films under proton irradiation (typically 200 keV) occurs with a cross section, $\sigma_{H^+ chem}$, of $1.47(\pm 0.03) \times 10^{-15}\text{ cm}^2$. The interaction with protons leads to new species, such as CH_3NC , HCN , H_2CCNH , $HCCCN$ and CH_4 . Proton-promoted desorption of CH_3CN was not detected. Warming up the proton-irradiated film produces an organic residue which can trap CH_3CN beyond its normal sublimation temperature, and is stable at room temperature.

Secondary electron-promoted chemical reaction of CH₃CN is found to be a bulk process occurring throughout the full depth of the film, whereas EPD is a surface process restricted to a selvedge. This conclusion explains the difference between the observations of the proton and electron irradiation experiments and has important consequences for understanding the balance of the two processes in interstellar environments. Accordingly, the results obtained from this thesis clearly illustrate; how molecules such as H₂O and CH₃CN will behave under charged particle irradiation (*i.e.* electrons and protons) mimicking conditions in astrophysical environments.

6.3 Future Outlook

This thesis has highlighted many possibilities for future research, some of which are developed here. In order to gain more understanding about the astrochemistry of nitriles, because of their importance as possible precursors of amino acids, it is desirable to study the interactions driven by different energetic particles (such as ions, electrons and UV photons) on nitriles within mixtures containing other molecules relevant to the ISM. In such mixtures, one should consider adding molecules such as H₂O, CO, H₂CO, CH₃OH, and O₂; molecules containing a CO group will be of particular interest in the perspective of investigating the formation of amino acids. Additionally, the ratio between left and right enantiomeric forms of the produced amino acids should be monitored with gas phase chromatography [11, 12], in order to shed light on the possible exogenous origin of life. Such studies will increase our understanding of the processes occurring in dense regions of the ISM. This would be achieved by determining the reaction pathways, physical and chemical conditions in which the amino acids can form, linking these with the astronomical observations, and providing constraints to the astrochemical models. Moreover, to gain knowledge on both the formation and the destruction routes of amino acids in the ISM, it is worth investigating the destruction of prototypical amino acids (*e.g.* glycine, alanine...*etc.*) by ions, electrons, or UV photons under astrophysically relevant conditions (for example, on bare or ice-covered silica).

Furthermore, to gain knowledge about the structure of molecules adsorbed on surfaces, core-level and valence band photoemissions (*e.g.* XPS/UPS), and scanning

tunnelling microscopy (STM) experiments can give us clear insight on the electronic structure of the adsorbed molecules. This study can open a window which allows for the investigation of other molecules, ranging from simple to more complex compounds such as amino acids or polycyclic aromatic hydrocarbons.

6.4 References

- [1] R. J. Speedy, P. G. Debenedetti, R. S. Smith, C. Huang and B. D. Kay, *J. Chem. Phys.*, 1996, **105**, 240.
- [2] H. J. Fraser, M. P. Collings, M. R. S. McCoustra and D. A. Williams, *Mon. Not. R. Astron. Soc.*, 2001, **327**, 1165.
- [3] A. S. Bolina, A. J. Wolff, and W. A. Brown, *J. Phys. Chem. B.*, 2005, **109**, 16836.
- [4] D. M. Murphy and T. Koop, *Quart. J. Roy. Meteor. Soc.*, 2005, **131**, 1539.
- [5] J. D. Thrower, *PhD Thesis*, (Heriot-Watt University, Edinburgh, 2009).
- [6] J. D. Thrower, A. G. M. Abdulgalil, M. P. Collings, M. R. S. McCoustra, D. J. Burke, W. A. Brown, A. Dawes, P. D. Holtom, P. Kendall, N. J. Mason, F. Jamme, H. J. Fraser, and F. J. M. Rutten, *J. Vac. Sci. Technol. A*, 2010, **28**, 799.
- [7] N. Russo and R. Khanna, *Icarus*, 1996, **123**, 366-395.
- [8] J. E. Schaff and J. T. Roberts, *Langmuir* 1999, **15**, 7232.
- [9] S. Bahr and V. Kempter, *J. Chem. Phys.*, 2009, **130**, 214509.
- [10] A. G. M. Abdulgalil, D. Marchione, J. D. Thrower, M. P. Collings, and M. R. S. McCoustra, F. Islam, M. E. Palumbo, E. Congiu, and F. Dulieu, *Phil. Trans. R. Soc. A*, 2013, **371**, 20110586.
- [11] M. P. Bernstein, J. P. Dworkin, S. A. Sandford, G. W. Cooper, and L. J. Allamandola, *Nature*, 2002, **146**, 401.
- [12] G. M. Muñoz Caro, U. J. Meierhenirch, W. A. Schutte, B. Barbier, A. Arcones Segovia, H. Rosenbauer, W. H. -P. Thiemann, A. Barck, and J. M. Greenberg, *Nature*, 2002, **146**, 403.